MULTICORRELATOR TECHNIQUES FOR ROBUST MITIGATION OF THREATS TO GPS SIGNAL QUALITY

A DISSERTATION SUBMITTED TO THE DEPARTMENT OF MECHANICAL ENGINEERING AND THE COMMITTEE ON GRADUATE STUDIES OF STANFORD UNIVERSITY IN PARTIAL FULFILLMENT OF THE REQUIREMENTS FOR THE DEGREE OF DOCTOR OF PHILOSOPHY

Robert Eric Phelts

June 2001

I certify that I have read this thesis and that in my opinion it is fully adequate, in scope and in quality as a dissertation for the degree of Doctor of Philosophy.

_____

Prof. Per K. Enge, Principle Advisor

I certify that I have read this thesis and that in my opinion it is fully adequate, in scope and in quality as a dissertation for the degree of Doctor of Philosophy.

_____

Prof. Thomas W. Kenny

I certify that I have read this thesis and that in my opinion it is fully adequate, in scope and in quality as a dissertation for the degree of Doctor of Philosophy.

_____

Prof. Stephen M. Rock

Approved for the University Committee on Graduate Studies:

_____

Abstract

Many applications that utilize the Global Positioning System (GPS) demand highly accurate positioning information. Safety-critical applications such as aircraft navigation require position solutions with not only high accuracy but also with high integrity. Two significant threats to GPS signal quality exist which can make meeting both of these requirements a difficult task.

Satellite signal anomalies, or "evil waveforms," can result from soft failures of the signal generating hardware onboard the GPS satellite. These subtle anomalies cause distortions of the signal, which if undetected may pose an integrity risk to an aircraft relying on GPS. Signal Quality Monitoring (SQM) is required to reliably detect these anomalies and thereby protect airborne users from this integrity threat. Multipath, or undesired reflected signals from the ground or other obstacles, also distorts the desired GPS signal. In addition to making evil waveforms more difficult to detect, multipath—an ever-present error source—also degrades nominal performance. Multipath mitigation techniques attempt to reduce or eliminate this threat.

This thesis introduces novel signal processing techniques for addressing these twin concerns. First, a comprehensive method for designing a robust signal quality monitor to detect evil waveforms in the presence of multipath is described. This method is used to specify a practical multiple-correlator configuration for the SQM receiver that satisfies the requirements for Category I precision approaches for landing aircraft. Second, a new

multipath mitigation approach is introduced that leverages “multipath invariant” properties of the GPS signals. A real-time Tracking Error Compensator (TrEC) algorithm is experimentally shown to provide significant accuracy improvements over existing techniques for low-end (or “narrowband”) receivers. Additionally, it is shown that TrEC may have at least comparable multipath mitigation performance to that of a high-end (or “wideband”) receiver technique.

Acknowledgements

There are many people who have contributed greatly to the completion of this work and the writing of this thesis. First and foremost among them is my research advisor, Professor Per Enge. From the very start of my work under his guidance until now, I have continued to benefit from his vast knowledge and skill as a mentor, a scholar, a professor, and also a technical and professional leader. He gave me wide lattitude to excersise creativity in this research that I found refreshing. Still, he kept me focused and making rapid progress toward completion.

I also owe a tremendous debt of gratitude to my other readers. Even before I had a thesis advisor, Professor Thomas Kenny, served as my departmental advisor. In all, he has served as a guide for my qualifying exams, as an examiner for my thesis defense, and now, finally, as a reader of this thesis. Professor Kenny has always provided much needed advise and support when I needed it most. Professor Stephen Rock has also seved as an examiner and graciously gave this thesis a thorough reading on relatively short notice. His helpful comments should greatly contribute to its readability. Although not an official reader, Fiona Walter, too, helped greatly to this end. Her comments and suggestions were much more thororogh than I could have ever hoped for, and were exactly what this thesis needed to make the writing clearer for future readers.

I would like to thank the Federal Aviation Administration for funding this work. Without their generous support, our research labs would surely grind to a halt. The Department of

Mechanical Engineering (ME) and the Department of Aeronautics and Astronautics (Aero/Astro) also deserve thanks. Particularly, Judith Haccou (ME), Sally Gressens (Aero/Astro), and Yasmeen Husain (Aero/Astro) have greatly assisted in making things run more smoothly for me as a Ph.D. student.

I would also like to thank my many colleagues on the Wide Area Differential GPS Laboratory and the Local Area Augmentation System Laboratory. If there is one sure thing I will miss most about being a Ph.D. student at Stanford, it will be being surrounded with many of the best and the brightest minds I have known so far in my life. Most significantly among them is, Dr. Todd Walter, whose technical leadership is truly something to behold. His guidance was critical in the production of the results of some of this thesis.

Also of significant importance were the countless formal and informal discussions—technical and otherwise—that let to an extremely productive and supportive environment for research. These were held with numerous colleagues. Among these are Dr. Christopher Comp, Dr. Awele Ndili, Dr. Dennis Akos, Dr. Sam Pullen, Dr. Jae-Woo Jung, Dr. Richard Fuller, Dr. Andrew Hansen, Dr. Keith Alter, Dr. Donghai Dai, Dr. Sharon Houck, Dr. Andrew Barrows, Demoz Gebre-Egziabher, Sherman Lo, Jonathan Stone, Chad Jennings, Alexander Mitelman, Konstantin Gromov, Roger Hayward, Shau-Shiun Jan, Gabriel Elkaim, and Frank Bauregger. Of special note are Dr. Christopher Comp and Dr. Dennis Akos, who shared their invaluable experience and insights on the inner workings of receivers, signal processing techniques, and multipath. Dr. Akos and Dr. Pullen also deserve special thanks for their significant contributions to the Signal Quality Monitoring research portions of this thesis.

Finally, on a more personal note, I would like to thank my parents, Louise and Eddie Phelts, my brother, Michael Phelts, and my friends. They have all believed in me and supported me from afar, even when the work made it so I lost touch from time to time. Last but not least I would like to thank my wife, Maria. For each of the many sacrifices I made to complete this work, I believe she has made two—one for each of us. Still, through it all, she has remained patient, supportive, and loving. No one could ask for anything more. I dedicate this thesis to her.

Table of Contents

List of Tables

List of Figures

List of Acronyms

2OS	2nd-Order Step Threat Model
6oB	6th-Order Butterworth
A/D	Analog-to-Digital
ASIC	Application-Specific Integrated Circuit
AWGN	Additive White Gaussian Noise
C/A	Civilian Access
CAI	Carrier Aiding
CCS	Cross-Channel Smoothing
CONUS	Continental United States or contiguous United States
CP	Corrections Processor
CSM	Carrier Smoothing
CW	Continuous Wave
DC	Direct Current
DCO	Digitally Controlled Oscillator
DGPS	Differential GPS
DLL	Delay-Lock Loop
DOP	Dilution of Precision
E-L	Early-Minus-Late
EWF	Evil Waveform
FAA	Federal Aviation Administration
FIR	Finite Impulse Response

FLL	Frequency-Lock Loop
FS	Fibonacci Search
GAD	General Accuracy Designator
GDOP	Geometric Dilution of Precision
GEO	Geostationary Satellite
GLS	GPS Landing System
GNSS	Global Navigation Satellite System
GPS	Global Positioning System
GS	Gradient Search
HMI	Hazardously Misleading Information
HPA	High Power Amplifier
HPL	Horizontal Protection Level
ICAO	International Civil Aviation Organization
ICP	Integrated Carrier Phase
IF	Intermediate Frequency
IIR	Infinite Impulse Response
IPA	Intemediate Power Amplifier
LAAS	Local Area Augmentation System
LADGPS	Local Area Differential GPS
LGF	LAAS Ground Facility
LHCP	Left-Hand Circular Polarization
LNAV	Lateral Navigation
LO	Local Oscillator
LOS	Line-of-Sight
MCS	Master Control Station
MDE	Minimum Detectable Error
MEDLL	Multipath Estimating Delay Lock Loop
MERR	Maximum Error Range Residual (or Maximum Tolerable Error)
MET	Multipath Elimination Technology
MEWF	Most Evil Waveform
MLA	Multipath Limiting Antenna

MP	Multipath
MPI	Multipath Invatiant (or Multipath Invariance)
MRDLL	Modified Rake Delay Lock Loop
MSE	Mean Square Error
NBR	Narrowband Receiver
NDU	Navigation Data Unit
PASL	Peak-Adjacent Sidelobe
PCBw	Precorrelation Bandwidth
PDF	Probability Density Function
PDOP	Position Dilution of Precision
PFSL	Peak-Flush Sidelobe
PIT	Predetection Integration Time
PLL	Phase-Lock Loop
PR	Pseudorange
PRN	Pseudorandom Noise
PRE	Pseudorange Error
RABF	Radiofrequency Antenna Beam Forming
RAIM	Receiver Autonomous Integrity Monitoring
RF	Radiofrequency
RFI	Radiofrequency Interference
RHCP	Right-Hand Circular Polarization
RMS	Root Mean Square
SARPS	Standard and Recommended Practices
SigGen	GPS Signal Generator
SMR	Signal-to-Multipath Ratio
SNR	Signal-to-Noise Ratio
SP	Safety Processor
SPS	Standard Positioning Service
SQM	Signal Quality Monitoring
SU	Stanford University
SV	Space Vehicle

STNA	Service Technique de la Navigation Aerienne
TM	Threat Model
TrEC	Tracking Error Compensator
TTA	Time-to-Alarm
UDP	Undetected Point
VAL	Vertical Alert Limit
VNAV	Vertical Navigation
WAAS	Wide Area Augmentation System
WADGPS	Wide Area Differential GPS
WMS	WAAS Master Station
WRE	WAAS Reference Equipment
WRS	WAAS Reference Station

Chapter 1:

Introduction

> *Moore's Law:*
> *The observation made in 1965 by Gordon Moore, co-founder of Intel, that the number of transistors per square inch on integrated circuits had doubled every year since the integrated circuit was invented. Moore predicted that this trend would continue for the foreseeable future. In subsequent years, the pace slowed down a bit, but data density has doubled approximately every 18 months, and this is the current definition of Moore's Law, which Moore himself has blessed. Most experts, including Moore himself, expect Moore's Law to hold for at least another two decades.*
>
> - Webopedia

Moore's Law has been prophetic not only in the computer industry but also in advances in communications (and navigation) receiver technology as well. Rapidly decreasing costs of application-specific integrated circuits (ASICs) and other silicon-based receiver components have led to the introduction of many novel digital signal processing (DSP) techniques for improving signal tracking performance. Specifically, many of these receivers have in recent years witnessed the introduction of numerous so-called "multicorrelator" (i.e., high-resolution sampling) DSP techniques used to reduce or eliminate signal tracking errors. As costs continue to decrease, multicorrelator signal processing techniques will no doubt become the standard means for mitigating signal tracking errors in receivers used for wireless communication and navigation.

1.1 The Global Positioning System (GPS)

The Global Positioning System (GPS) is a satellite-based radio navigation system used to compute precise time and three-dimentional positions anywhere on the earth [Kaplan]. An illustration is provided in Figure 1-1 below. GPS position solutions are accomplished by obtaining time-of-arrival (TOA) measurements, or pseudoranges (PR), from a minimum of four GPS satellites. These raw pseudoranges are the measured distances along the line-of-sight (LOS) of the signals broadcast by each of the satellites. The PR, ρ, for each satellite, k, is simply

$$\rho^k = \sqrt{\left(X^k - x_u\right)^2 + \left(Y^k - y_u\right)^2 + \left(Z^k - z_u\right)^2} + c \cdot b_u \quad k = 1,2,3,...,K \qquad K \geq 4 \tag{1.1}$$

where X^k, Y^k, Z^k are the Earth-centered, Earth-fixed (ECEF) coordinates for satellite k. The subscript, u, represents the user, and x, y, and z are the user ECEF coordinates. The user clock bias, b_u, is required to compute precise (GPS) time. This equation is subsequently linearized and iteratively solved for the user position and clock bias using a least-squares computation [Kaplan].

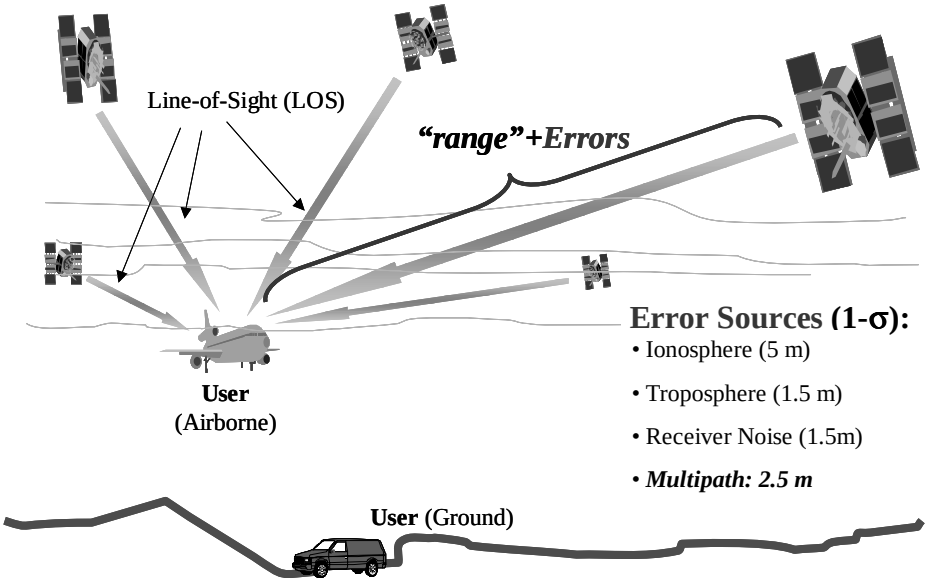

Figure 1-1 Navigation Using the Global Positioning System (GPS)

The users clock bias is a time-varying term that consists of all the common mode effects present on all pseudoranges. To the receiver, these may include the following:

- Local oscillator drift and bias
- System filter (analog and digital) propagation delays
- Antenna and receiver channel line biases

Because these biases are *common mode* to all pseudoranges, they only affect the magnitude of the bias, b_u. This translates to a timing error. It does not, however, affect the position solution contained in the x_u, y_u, and z_u terms.

1.1.1 GPS Error Sources

In the absence of pseudorange errors, highly accurate position solutions may be obtained by solving the system of equations described in (1.1) above. However, in general, there are several primary error sources to GPS. Two of these include unknown atmospheric errors, or delays, introduced by the ionosphere and troposphere. These effects cause the line-of-sight (LOS) signal to actually "arrive" later than predicted by Equation (1.1). ([Kaplan] and [Klobuchar] discuss ionosphere, troposphere, and other error sources in greater detail.)

Multipath (MP) is another primary pseudorange error source. MP signals are (usually undesired) signal reflections from the ground or other nearby obstacles. (See Figure 1-2.) These are simply amplitude-scaled (reduced) and time-delayed replicas of the nominal incoming signal or LOS. MP signals combine with the LOS and effectively distort the received signal. As opposed to the atmospheric effects, which directly affect the LOS signal TOA, MP causes the GPS receiver to make erroneous measurements of the TOA of the signal.

Satellite failures—far less common error sources for GPS than the aforementioned effects—may also cause distortion of the received (and generated) GPS signal. Such a failure may cause an anomalous signal, or "evil waveform" (EWF), to be generated by the

satellite. Like multipath, this mechanism causes TOA measurement errors by the receiver. If undetected, such anomalous signals could cause unacceptably large errors for GPS users in high-integrity applications such as aviation.

1.1.2 Differential GPS (DGPS)

Local-area differential GPS (LADGPS) attempts to correct for many of the dominant error sources in GPS. It accomplishes this by placing a reference station at a known location in the vicinity of a user, or where high accuracy navigation is required. Equipped with a GPS receiver, the reference station measures the ranges to each of the GPS satellites in view. It subsequently computes true ranges to the same satellites using the known reference station location. As illustrated in Figure 1-2 below, the reference station then broadcasts (scalar) corrections for each of those pseudorange (PR) measurements to local users via a datalink. LADGPS makes it possible to achieve position accuracies of several centimeters or less. (See [Parkinson95] for more details.) LADGPS is only effective, however, when correcting for common mode, spatially correlated errors such as the ionosphere and troposphere delays. MP-induced errors are not common to both the reference station and the user.

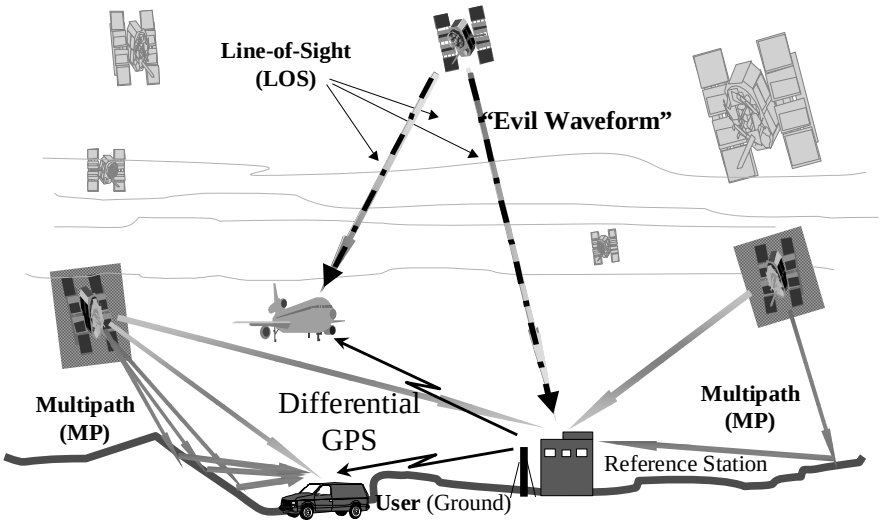

Figure 1-2 Two Threats to GPS Signal Quality: Multipath and Evil Waveforms

EWFs are generated by the satellite and as a result are effectively spatially correlated. In other words, both the user and the reference station may observe the same distorted signal independent of their separation. Nevertheless, since the user and reference station receivers are not identical, LADGPS cannot reliably correct for these errors.

1.1.3 GPS Augmentation Systems for Improving Flight Operations

GPS augmentation systems utilize DGPS techniques in addition to integrity monitoring algorithms to achieve the accuracy, availability, integrity and continuity required to continuously provide robust, safe navigation for aircraft in all phases of flight. These four requirements answer the following questions, respectively:

- How correct is the user position estimate? (Accuracy)
- What is the largest the user position error can ever become without detection? (Integrity)
- How often can a user use this system and have the desired accuracy and integrity? (Availability)
- What is the probability that an operation, once commenced, can be completed? (Continuity)

Notably, for landing aircraft these requirements become particularly difficult to meet. Category I (Cat I) precision approaches, for instance, propose to guide an aircraft on final approach down to a vertical height of 200 feet above the ground. Specifically, for a Cat I approach, should any pseudorange errors cause a user's vertical position error to exceed 10 meters, the ground facility (or reference station) must alert the user to abort the landing within 6 seconds. The Federal Aviation Administration (FAA) defines this as the Cat I 6-second time-to-alarm (TTA) requirement. If the landing system cannot meet the TTA requirement, a user may receive hazardously misleading information (HMI) from the augmentation system. In this case, the system may incorrectly inform the user that all errors are within acceptable bounds. This scenario constitutes an integrity risk.

(The reference station may use only a fraction of the 6-second TTA because the user will require some of the allocated TTA to receive and process the message.)

Local Area Augmentation System (LAAS)

Local Area Augmentation System (LAAS) is a LADGPS system tailored to meet the stringent requirements on accuracy, integrity, availability, and continuity for landing commercial aircraft using GPS. LAAS is referred to as a Ground-Based Augmentation Systems (GBAS), since it proposes to meet these requirements by placing a reference station, or LAAS Ground Facility (LGF), at each airport. The LGF monitors the GPS signal and must alert the users before they experience HMI.

The current goal for LAAS is to meet the FAA requirements for Cat I precision approaches. As always, multipath corrupts the GPS signal for LAAS users and degrades the system accuracy, while EWFs affect the system's ability to guarantee high integrity for this phase of flight. It follows that LAAS requires signal quality monitoring (SQM) to detect EWFs in order to meet the Category I integrity requirements. (Note that Cat II and Cat III approaches provide aircraft guidance to lower minimum heights, and accordingly have significantly more stringent requirements.)

Wide Area Augmentation System (WAAS)

The Wide Area Augmentation System (WAAS) corrects for GPS nominal pseudorange errors over a wide geographical area. It accomplishes this using a network of 29 WAAS Reference Stations (WRS) distributed all over the United States. While LAAS position solutions are extremely accurate for users located close to the LGF, WAAS-corrected position solutions are less accurate. However the accuracy remains relatively constant with respect to user distance from the WRS. WAAS is a so-called Satellite-Based Augmentation System (SBAS) since it uses a geostationary satellite (GEO) to broadcast corrections to WAAS users. Although not as accurate as LAAS, WAAS will eventually provide the accuracy, integrity, availability, and continuity for Cat I precision approaches.

1.2 GPS Signal Structure

The nominal incoming GPS signal is composed of (sinusoidal) carrier wave centered at two frequencies: f_{L1}=1575.42MHz and f_{L2}=1227.6MHz. The carrier at f_{L1} from each satellite is modulated by two pseudorandom noise (PRN) codes: the Civilian Access or C/A code and the military's Precision or P(Y) code. (The f_{L2} signal is modulated only by the P(Y) code.) The Civilian Access (C/A) code is composed of a sequence of 1023 bits or chips. This PRN code sequence is different for each satellite and repeats every 10^{-3} second (i.e., a chipping rate of 1.023 chips per second). The nominal broadcast power of the C/A code is -160dBW. Figure 1-3 illustrates the basics of the C/A signal. The nominal (civilian) signal has a power of –160dBW and is not normally detectable using a spectrum analyzer. The military signal or P(Y) code is also present on the L1 signal. It has a chipping rate of 10.23Mcps and is broadcast at a power of –163dBW [Spilker94a]. The C/A and P(Y) codes on L1 are in phase quadrature (i.e., 90° out of phase) with respect to each other.

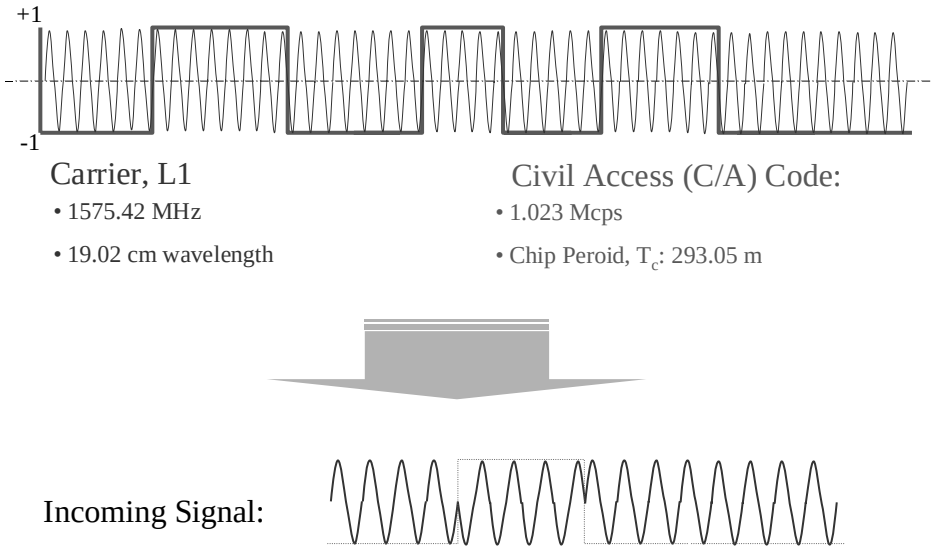

Figure 1-3 Basic Structure of Civil GPS Signal

The GPS signal that carries the C/A code may be expressed as

$$s_0(t) = AC(t)\,X(t)\sin(\omega_0 t) \tag{1.2}$$

In the above expression, A is the amplitude of the incoming signal and $C(t)$ equals ±1 corresponding to the sign of the C/A code chip. $X(t)$ represents the sign of the navigation data bit [Braash95]. A navigation data bit consists of 20 C/A code epochs. The details of the complete GPS navigation message and also the military P(Y) code and signal structure can be found in [Spilker94a].

To acquire and track the incoming signal, the receiver uses a process known as correlation. This process multiplies the incoming signal by an internally generated replica of the PRN code corresponding to a specific satellite and averages the result. The correlation equation is given as

$$\overline{s_0(t)s_1(t)} = R(\tau - \tau_0)\cos(\omega_0 t + \theta_0) \tag{1.3}$$

where $R(\tau)$ is the ideal autocorrelation function of the incoming signal code with the replica PRN code. Note that code tracking is almost solely based on the shape of the correlation peak, and distortion of the correlation function is the primary way in which MP signals and EWFs degrade the performance of GPS receivers.

1.3 Correlation Functions

The convolution of a given PRN code with itself forms the autocorrelation function, $R_{\text{nom}}(\tau)$. If $x_{nom}(t)$, is the nominal, ideal incoming PRN code, this operation is given as

$$R_{\text{nom}}(\tau) = x_{\text{nom}}(t) * x_{\text{nom}}(t) = \left\langle x_{\text{nom}}(t), x_{\text{nom}}(t-\tau) \right\rangle \tag{1.4}$$

Some also refer to the correlation process (as it occurs in GPS) as matched filtering since "matching" it to an internally stored replica of that signal filters the incoming signal. This process despreads the GPS (spread spectrum, CDMA) signal. Matched filters optimally filter the incoming signal since they possess *a priori* knowledge of the signal (i.e., pulse shape) [Carlson]. The double-sided normalized power spectrum for the C/A code autocorrelation function is shown below in Figure 1-4, and is equivalent to the magnitude response of the C/A code matched filter.

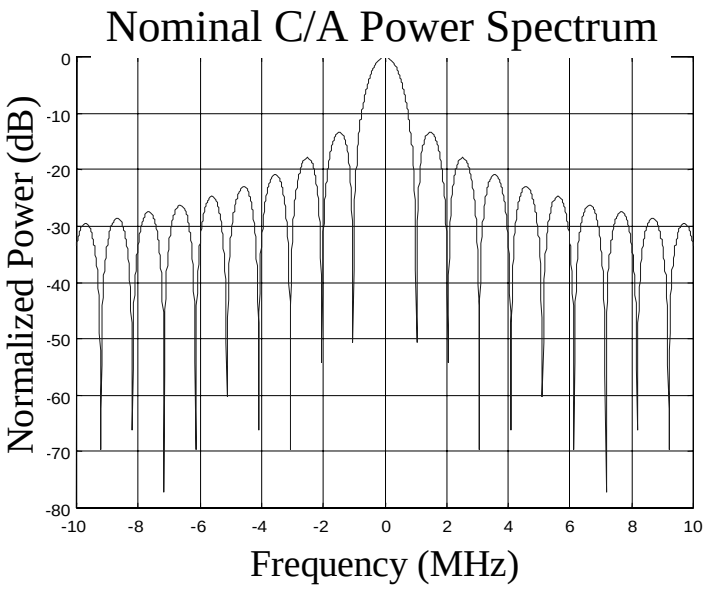

Figure 1-4 Normalized Power Spectral Density of GPS C/A Code (at Baseband)

GPS signals are designed to yield a maximum correlation output when the codes are perfectly aligned. Conversely, zero correlation output is desired when the codes are misaligned. This case is illustrated in Figure 1-5 below. This ideal case models the incoming signal as a single bit or pulse. During acquisition, a receiver processing this pulse attempts to align its internal replica of that pulse to that signal. For the partial alignment shown, only partial correlation is possible. Again, the receiver maximizes the correlation output by aligning the two pulses. Note that although the entire correlation peak is pictured, the only "observation" point for the alignment shown in Figure 1-5 would be the location of the downward arrow. In other words, a receiver would only measure this relatively low correlation (signal) power corresponding to the alignment of the incoming and replica signal pulses.

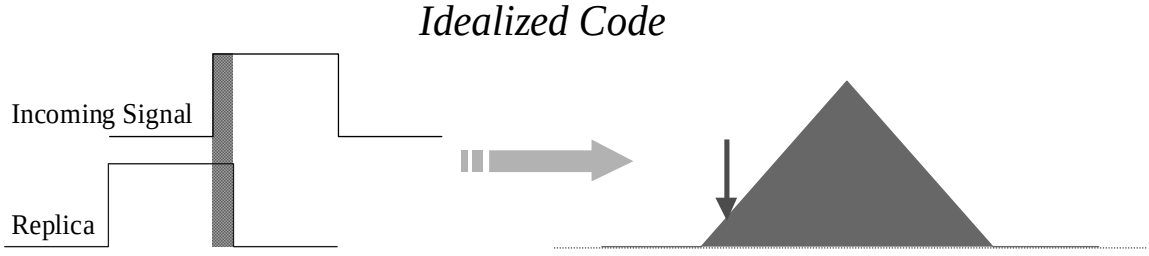

Figure 1-5 Ideal Autocorrelation Process

1.4 Pseudorandom Noise (PRN) Codes

Maximum-length pseudorandom noise (PRN) codes are called *m*-sequences and are nearly orthogonal to each other [Spilker94a], [Glisic]. The autocorrelation function of an orthogonal code appears much like the ideal autocorrelation. They have a single correlation peak when perfectly aligned and have constant, negligibly small correlation when the codes are misaligned by more than a single chip. Figure 1-6 illustrates the autocorrelation and cross-correlation functions for two (ideal) *m*-sequences.

The actual GPS C/A codes are taken from the Gold Codes. These PRN codes have a maximum length of only 1023 chips and are non-orthogonal. Consequently, their autocorrelation functions are not minimal for code offsets greater than one chip. Their cross correlation properties, too, are non-minimal. The Gold Codes do, however, guarantee uniformly low cross-correlation properties between the 1025 sequences in the Gold family of length 1023. (GPS currently uses only 36 of these 1025 possible sequences [Misra].) More importantly, because the code lengths are short, relatively rapid acquisition is made possible.

C/A code correlation functions, like *m*-sequences, possess a single, relatively large main lobe when the codes are perfectly aligned. However, at offsets greater than or equal to 1 chip, these functions also possess characteristic sidelobes. (One C/A code chip, or 1-T_c code period, is approximately equivalent to 1μ-second or 293.05 meters in range.) Figure 1-7 shows the autocorrelation and cross-correlation functions for two C/A codes normalized by the maximum (main peak) value of each function. The height of the main peak is nominally 1023 samples. The minimum plateau height, –1, is the desired correlation level for large code offsets and for cross-correlation. The minor lobes may be as large as +64 or –65.

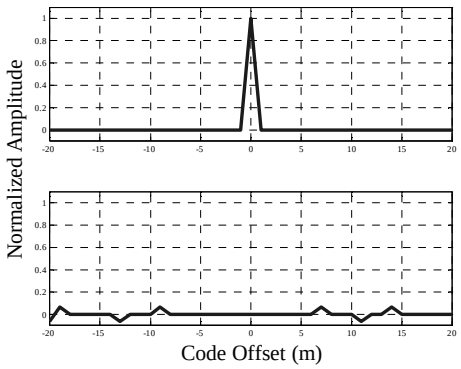

Figure 1-6 Normalized Correlation Functions for *m*-sequences (Top: Autocorrelation; Bottom: Cross-correlation)

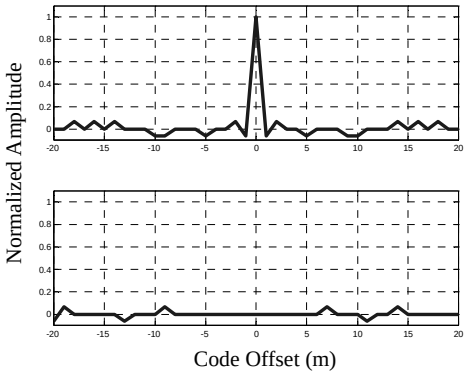

Figure 1-7 Normalized Correlation Functions for CA code (Top: Autocorrelation; Bottom: Cross-correlation)

For simplified analysis, a triangle exactly models the ideal normalized correlation peak, $R(\tau)$, defined in Equation (1.4). Equation (1.5) generalizes this according to

$$R(\tau) = \begin{cases} b, & |\tau| > \mathrm{T_c} \\ a_s - \dfrac{|(1+b)\cdot\tau|}{\mathrm{T_c}}, & |\tau| \le \mathrm{T_c} \end{cases} \tag{1.5}$$

where a_s=1.0, a_s=64/1023, or a_s=-65/1023 for the main peak, and the positive and negative sidelobes, respectively. The normalized (base) plateau height, b, nominally equals -1/1023, unless a sidelobe lies flush against the peak. (See Section 3.6 of Chapter 3.)

1.5 Code Tracking

A (spread spectrum) GPS receiver uses a minimum of two code replicas to acquire and track the GPS signal. These replicas, or correlators, align and convolve with the incoming code. They are normally held at fixed offsets, or correlator spacings, relative to each other. One is called the "Early" (E) correlator and the other is called the "Late" (L) correlator. Sometimes a third replica, the "Prompt" (P) correlator, is placed in the center of the E and L correlators. The standard E-to-L correlator spacing, $d_{\text{E-L}}$, is $1\mathrm{T_c}$.

After acquisition, the standard receiver code tracking loop, called a delay-lock loop (DLL), "tracks" the signal by slewing the correlators until the E and L correlator outputs are balanced. This subtraction (E-L=0) forms the standard DLL discriminator. (See Figure 1-8 below.) In the absence of thermal noise, multipath, filtering effects, and any other correlation peak distortions, when the discriminator is zeroed, the code tracking errors are also zero regardless of correlator spacings, $d_{E\text{-}L}$. (See Chapter 2, Section 2.2.2.)

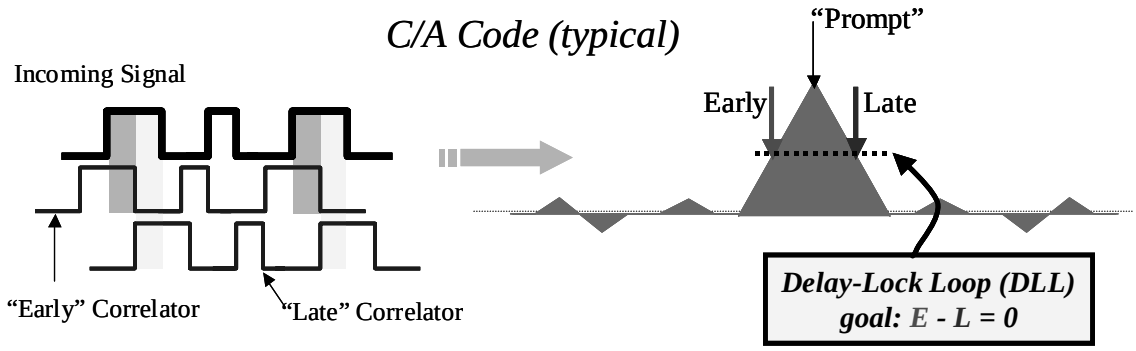

Figure 1-8 Correlation and Conventional Code Tracking in a GPS Receiver

1.6 Threats to GPS Signal Quality

Evil Waveforms

Evil waveforms may result from failures of the signal generating hardware on GPS satellites. These failures introduce anomalous distortions onto the correlation peak as illustrated in Figure 1-9. Consequently, when a conventional DLL balances the E and L correlators, although E-L=0, the tracking errors remain non-zero and unknown. Reference stations cannot, in general, correct for these errors because the correlator spacings of the reference stations and airborne (user) receivers generally differ. If such distortions are present on a satellite signal being tracked by an avionics receiver, this could pose a severe threat to the *integrity* of that airborne user.

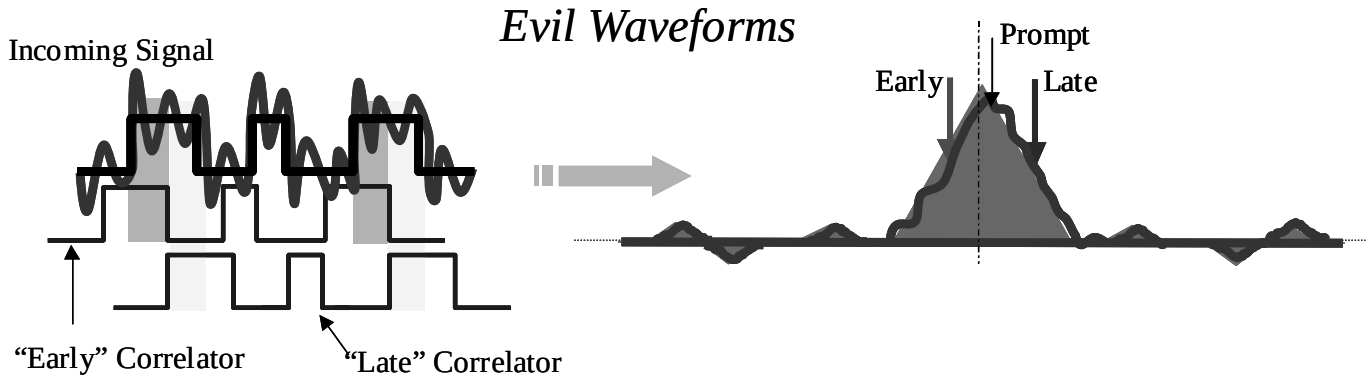

Figure 1-9 Effect of Evil Waveforms on Code Tracking

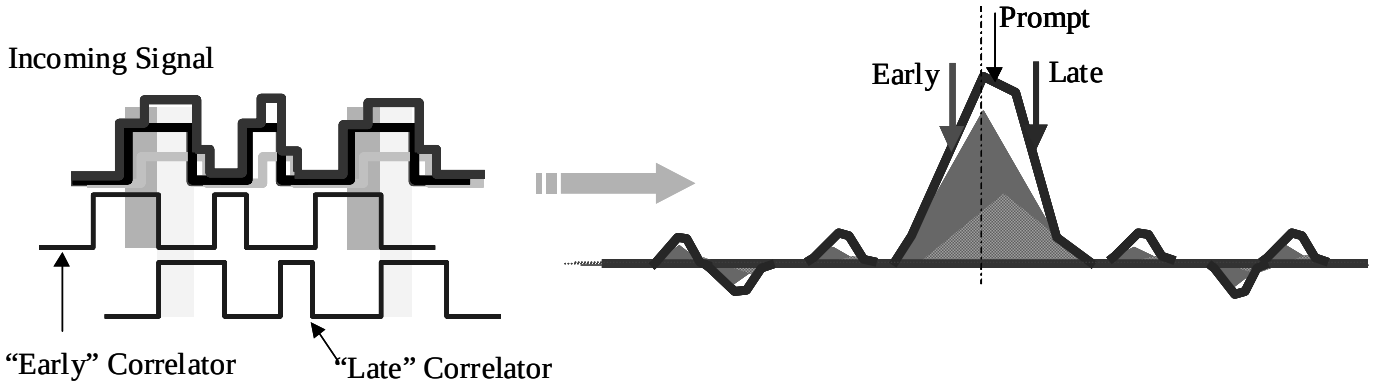

Figure 1-10 Effect of Multipath on Code Tracking

Multipath

Multipath also causes significant distortion to the correlation peak. Figure 1-10 illustrates a type of distortion caused by a single reflected MP signal. The MP is a (usually) reduced-amplitude copy of the direct signal; it arrives "later than" the direct signal. Since the relative delay, amplitude, and other MP parameters are generally unknown, the superposition of these signals produces an unknown distortion of the correlation peak. MP distortions are always present to some degree and primarily threaten to degrade user position *accuracy*.

Problem statement:

Use multiple correlators to mitigate these threats to GPS signal quality.

This thesis proposes and analyzes several multicorrelator techniques for signal quality monitoring (SQM), or detection of evil waveforms, and for mitigating (code phase) multipath in GPS receivers in order to protect integrity in aviation applications and to improve general GPS accuracy.

1.7 Current Efforts And Contributions to Signal Quality Monitoring Research

Much of the research in SQM has occurred between 1997 (at FAA request) to present and has taken place at Stanford University. There are currently four primary areas of this research: EWF Threat Model development, Minimum Detectable Error (MDE) determination, SQM Design, and SQM Experimental Validation. This section describes the research and contributions in each of these areas.

1.7.1 Threat Models

Several candidate threat models were initially proposed to explain the SV19 phenomenon. (These are discussed in greater detail in Chapter 3.) Of these, the Most Evil Waveform Threat Model (MEWF) first explored the set of anomalous signals that induced a certain (maximum) differential pseudorange error (PRE) in the presence of SQM. Theoretical

MEWFs result from the analysis of a waveform that could pass undetected through a prescribed multicorrelator EWF detection technique and result in the maximum user PREs. The MEWF analysis, however, is very complex. In addition, MEWFs are not realizable. Note that [Mitelman98] first used the term "evil waveform."

Contributions:

This thesis develops the 2nd-order Step (2OS) Threat Model, which characterizes the most plausible EWF failure modes. This practical model captures the essential signal threats of concern to aviation users. This thesis also derives analytical equations for the EWF signals (codes) and the corresponding anomalous correlation peaks.

1.7.2 Minimum Detectable Errors (MDEs)

Minimum detectable errors (MDEs), or the SQM detection thresholds, quantify the nominal distortions of correlation peak measurements due to multipath and thermal noise. Accordingly MDEs are equivalent to the smallest EWF-distortions that can be measured by a particular multicorrelator SQM. Several individuals and organizations analyzed the MDEs. The initial analysis assumed *n* independent tracking loops per channel in a given receiver. From these independent tracking loops, the monitor formed *n*-1 pseudorange differences. From these, [Brenner], [Shively99a] generated standard deviations for each pseudorange difference as a function of elevation angle using a model (simulation) for typical reference station multipath and receiver thermal noise. Also, [Shively99a], [Van Dierendonck00] computed a multiplier generated to guarantee detection of EWFs with high integrity and low false-alarm probability.

Contributions:

This thesis analyzes the MDEs on a satellite-by-satellite basis. More specifically, it derives thresholds based on a specific PRN code of a given satellite. It is shown that the detection thresholds must adjust for the small variations in correlation peak shape caused by the location of the sidelobes.

1.7.3 SQM Design

Various multicorrelator SQM techniques propose to solve the EWF detection problem. The first of these utilized the pseudorange difference measurements used to determine the SV19 failure. [Mitelman98] computed user PREs as a function of number of correlators used to form these differences to detect MEWFs.

Contributions:

This thesis develops a selection and analysis methodology for validating SQM implementations in the case of steady-state EWF failures for the 2OS threat model. Also using the 2OS analysis, it constructs and analyzes new tests to provide improved steady-state detection performance for both LAAS and WAAS based on differences and ratios of direct samples of the correlation peak. Additionally, this thesis presents a transient LAAS SQM performance analysis methodology, and proposes SQM tests that provide improved transient EWF detection performance. Since the introduction of these analysis techniques, [Shively99a], [Van Dierendonck00], and [Macabiau00] have subsequently validated and extended many of these results.

1.7.4 SQM Experimental Validation

The performance of a specific SQM implementation has been experimentally validated under several different conditions. [Macabiau00b] used an analog filter to generate a single 2^{nd}-order Step EWF. Using actual receiver measurements, they showed that the resulting correlation peak distortion matched well to the theoretical model prediction. In addition, [Akos00a] designed and tested an (arbitrary) EWF generator capable of producing any EWF, including MEWFs. [Mitelman00] investigated several hazardous EWFs and demonstrated the first real-time SQM detection performance. No experimental validation contributions are given this thesis.

1.8 Previous Research and Contributions in Multipath Mitigation

Previous research in (code) multipath mitigation for GPS falls into two primary categories: receiver-external approaches and receiver-internal approaches. Receiver-external approaches attempt to mitigate multipath by preventing it from ever entering the receiver. Accordingly, they utilize methods that do not require changes to the receiver hardware or software configuration. Conversely, receiver-internal approaches are primarily multicorrelator signal processing techniques. They make little or no attempt to alter the incoming GPS signal. Note, however, that both of these classes of techniques may be used simultaneously to reduce MP-induced position errors as well.

1.8.1 Receiver-External Approaches

Antenna Design

Antenna gain patterns use shaped reception gain patterns to attenuate reflected signals from low elevation angles. For example, a choke-ring antenna utilizes concentric rings surrounding the antenna. This effectively increases the surface area of the ground plane from which the multipath reflects [Bartone]. The Multipath Limiting Antenna (MLA) uses a combination of two antennas to provide high gain for low elevation satellites while maintaining a sharp cutoff for angles below the (5°) horizon [Brenner].

Multiple antennas can steer nulls—regions of low gain—in the direction of the multipath [Moelker]. Conversely they can steer the maximum antenna gain in the direction of the desired signal. Use of multiple antennas—connected to multiple, respective receivers—may provide additional signal information (e.g., MP-dependent SNR and carrier phase differences between antennas) for subsequent, receiver-internal processing to remove MP effects [Ray99b].

Antenna Siting

Careful antenna siting (i.e., placement the antenna away from buildings or other large obstacles) can prevent multipath from entering the antenna and subsequently distorting the signal.

Ranging Signal Design

Higher code chipping rates also mitigate multipath. The military signal (P-code) has a chipping rate 10 times higher than that of the C/A code. As a result, for a single strong (3dB less strong than the LOS) MP reflection, the maximum multipath pseudorange errors for a conventional receiver code tracking loop are only $1/10^{th}$ the size of the C/A code [Braasch96]. The new civil signal, L5, will be broadcast with this rate [Hegarty].

Alternatively, [Weill] suggested selection of a second civil carrier frequency modulated by the same (C/A) code to reduce multipath tracking errors to sub-meter levels. Note that this method implies redesign of the actual transmitted GPS signal and was only a modification proposal for the L5 signal. In addition, the processing requires computationally intensive minimum mean-square estimation and processing of the correlation peak using multiple correlators.

1.8.2 Receiver-Internal Approaches

Measurement Processing: Calibration

The GPS satellites return to their positions in the sky approximately every 23 hours and 56 minutes. Accordingly, for stationary users (e.g., reference stations) the multipath errors also repeat with the same frequency. Calibration (and removal) of these repeated effects implies measuring, recording, and subtracting these time-varying pseudorange errors from future measurements [Braasch95]. For dynamic users and/or multipath conditions that change unpredictably, of course, this mitigation technique becomes significantly less useful—perhaps even risky.

Measurement Processing: Carrier Smoothing

Carrier smoothing effectively (low pass) filters the pseudorange measurements. Single frequency (L1 only) receivers perform this smoothing over relatively short time windows due to code-carrier divergence caused by the ionosphere. Dual-frequency or differential GPS receivers, however, are able to remove this effect and may smooth for indefinite periods of time. Carrier smoothing is most effective at reducing random pseudorange errors (e.g., thermal noise) and multipath errors that change rapidly. Multipath, however, may have significant bias components, which cannot be eliminated by smoothing alone [van Nee92a], [Montalvo].

Measurement Processing: SNR and Pseudorange Estimation

Changing satellite geometry causes multipath conditions to change as well. Variations observed in the pseudorange measurements correspond to variations in SNR measurements reported by a receiver. To the extent these variations are distinguishable from elevation-dependent ones, estimation algorithms can filter these measurements and form error corrections to be applied to the pseudoranges [Axelrad], [Breivik], [Sleewaegen]. Note that signals from multiple antennas (as discussed in Section 1.8 above under *Antenna Siting*) may also combine with these receiver observables to help better estimate the multipath pseudorange errors [Ray99b]. All of these techniques, however, have substantial difficulty removing errors caused by barely-observable MP signals such as those that are weak (i.e., they have low signal power) relative to one or more dominant reflections.

Signal Processing: Multicorrelator Techniques

The last several years have witnessed the development of numerous multicorrelator multipath mitigation techniques. Most of these have at least two things in common. First, they concentrate almost exclusively on extracting information from the peak of the autocorrelation function. This is intuitive since most of the signal power is concentrated here. For orthogonal code sequences, the main lobe theoretically contains all the information of the signal. Although the C/A codes are not orthogonal, the sidelobes of the autocorrelation function are for the most part ignored. Second, today's multicorrelator techniques tend to perform well against long-delay multipath, with relatively strong signal-

to-noise ratios (SNR). However, when faced with low-SNR multipath and/or multipath with relatively short delays (e.g., less than 30 meters) their performance degrades to that of a conventional, 1-chip spacing DLL.

Many current approaches attempt to track only the LOS signal and thereby reduce or eliminate the effects of the multipath. They essentially attempt to separate the LOS and MP signals. Several of these include: Narrow Correlator [Van Dierendonck92], [van Nee92b], E1-E2 Tracker [Mattos], Edge Correlator [Garin96], ΔΔ-Correlators [Garin96], [Garin97], [Hatch], [McGraw], [Weill], [Zhadanov], etc. Alternatively, other approaches attempt to estimate the parameters of the LOS and/or MP signals, and approximate their combined effect on the tracking errors. Several of these estimation-based techniques are as follows: MEDLL [van Nee94a], [van Nee94b], [Townsend95], MET [Townsend94], MRDLL [Gadallah], [Laxton], Deconvolution Approach [Kumar], Adaptive Filter [Nelson], Transition Points [Enge97], etc. Further, [Cahn] and others have also done some combination separation and estimation-based techniques to form corrections for the code tracking error.

All of the above methods rely on an ability to somehow distinguish the multipath from the line-of-sight. This is most readily accomplished using special multicorrelator sampling of the autocorrelation functions and/or discriminator curves. The most widely used of these techniques are illustrated below in Figure 1-11. Additional correlators (i.e., more than the usual Early, Late and sometimes Prompt correlators) and often a wider bandwidth are frequently employed for this purpose. A fundamental limitation these methods must overcome is their sensitivity to the changing characteristics of the multipath. For example, the closer the MP parameters match those of the LOS, the more difficult it becomes to either separate or estimate one from the other. This explains the characteristic degradation in performance these techniques suffer when the MP relative delays are very short or when the number or strength of the MP signals increases.

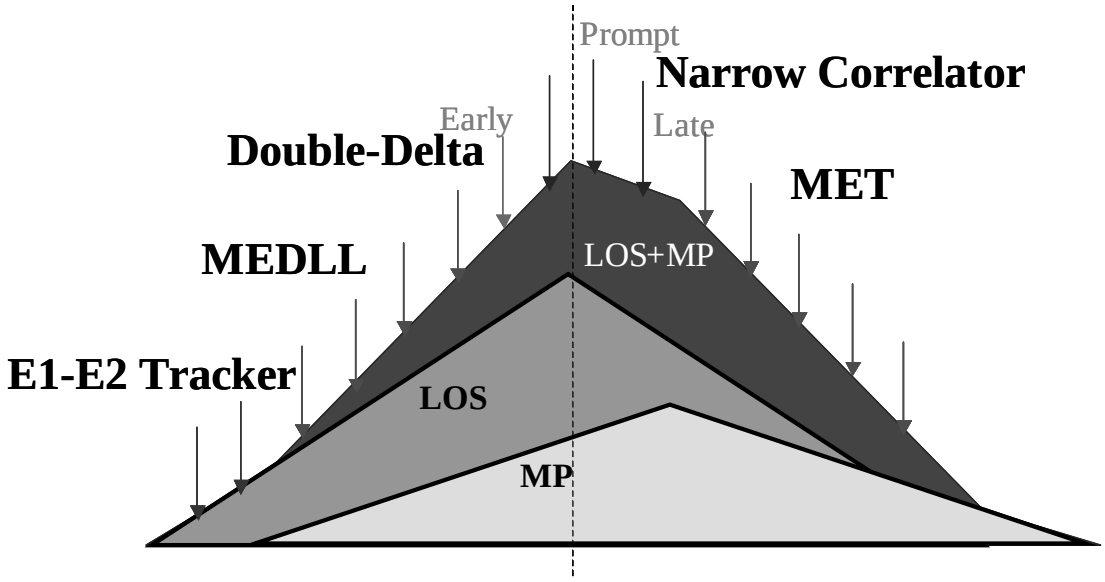

Figure 1-11 Current Multicorrelator Multipath Mitigation Techniques

The E1-E2 Tracker differs somewhat from the others, and most closely approaches the technique introduced in this thesis. It controls the receiver correlators to obtain samples of the earliest, relatively "undelayed" portions of the main lobe of the autocorrelation function [Mattos]. The difference between the sampled slope and ideal, expected slope of this low-SNR region of the main lobe is used to dynamically adjust the code tracking loop. However, like many others, it ignores the effect of multipath from sidelobes at long relative MP delays. For best performance, it also requires a maximum receiver precorrelation bandwidth (e.g., 20MHz) for accurate estimates of the slope of the leading edge of the primary peak [Peterson]. It performs best against medium and long-delay multipath only. Also, because it uses samples near the base of the main correlation peak it has received a somewhat dishonorable mention because of its poor noise performance [Van Dierendonck95].

Contributions:

This thesis introduces the concept of multipath invariance (MPI). It asserts and proves that there are properties of the correlation function that do not change as a function of

multipath. Using this concept, it develops the Tracking Error Compensator (TrEC)—a multicorrelator mitigation technique.

The analysis reveals TrEC theoretical performance provides superior mitigation for arbitrary receiver precorrelation bandwidth. The analysis also reveals TrEC operation is virtually independent of the multipath parameters, and the number of multipath reflections.

This thesis describes a Fibonacci Search optimization method adapted to locate "MPI points" on the correlation functions using a single correlator pair. Additionally, it proposes several multicorrelator implementations. These combine to compute theoretical performance bounds for arbitrary receiver configurations. Real-time, experimental results validate TrEC performance on a low-end, narrowband receiver and a single additional correlator pair. These experiments provided results from actual GPS signals generated using both a GPS signal generator and live GPS satellites.

1.9 Thesis Outline

Chapter 2 gives the reader some fundamentals on how GPS receivers operate and briefs the reader on the salient signal and threat mitigation terminology used in this thesis. Chapter 3 develops the story and theory behind evil waveforms and Chapter 4 discusses how best to detect them. Chapter 5 details the selection and design of a robust multicorrelator signal quality monitoring (SQM) implementation for LAAS. Chapter 6 introduces the concept of Multipath Invariance (MPI) and the Tracking Error Compensator (TrEC) and derives the multipath mitigation performance advantages and limitations of using TrEC. Chapter 7 discusses the extensive experimental validation of MPI and TrEC under various signal conditions. Finally, Chapter 8 presents the many conclusions of this thesis and several possible topics for further research.

Chapter 2:

GPS Receiver Basics

Figure 2-1 illustrates the basic structure of a single GPS receiver channel.

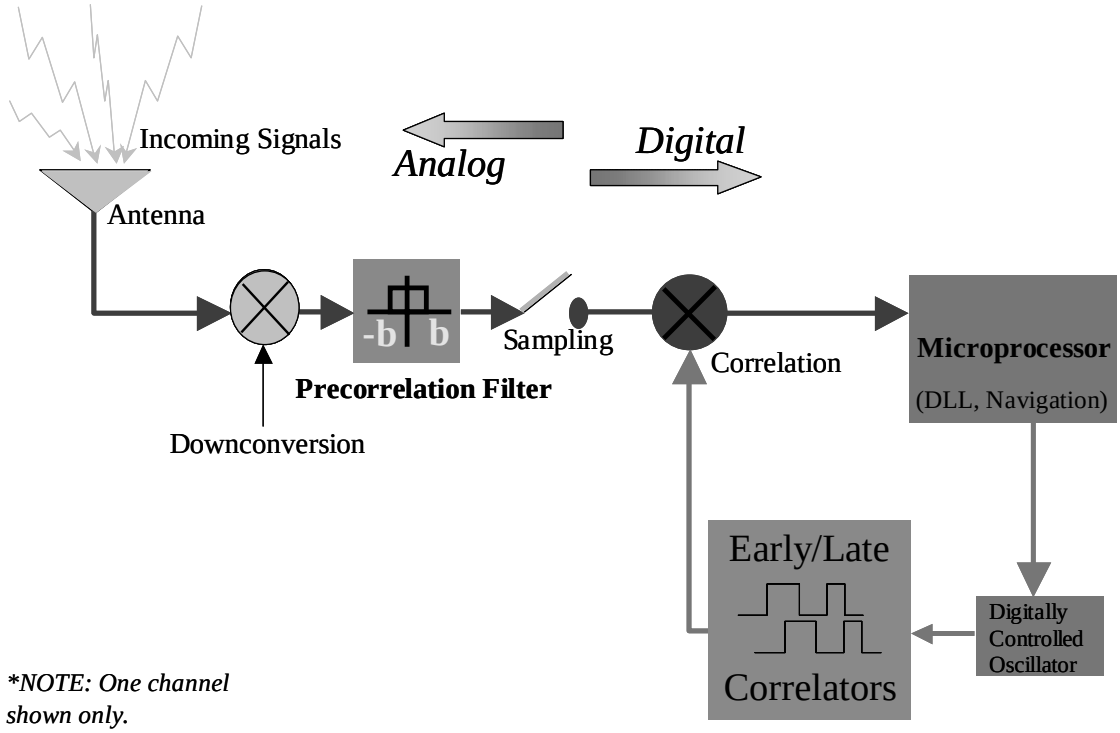

Figure 2-1 Simplified Block Diagram of a Basic GPS Receiver Channel

To understand this thesis it is necessary to gain a familiarity with the basic operation of GPS receivers. This chapter describes the essential elements of a receiver tracking channel

and how signal tracking is performed in a conventional GPS receiver. Section 2.1 describes the receiver analog front-end. Sections 2.2 and 2.3 describe the digital processing aspects including code and carrier tracking fundamentals, and subsequent processing of the code measurements. Section 2.4 outlines the ways in which EWF and MP threats to signal quality manifest themselves in GPS receivers, where the multicorrelator mitigation attempts to take place, and what characteristics determine the nominal performance or response of the receiver.

2.1 Analog Processing: Receiver Front-end

The analog portion of the receiver consists of the antenna, the mixers and local oscillators, and precorrelation filters. All of these subsystems precondition the signal and affect how well the signal is subsequently tracked. The operations of each of these stages are briefly summarized below. (Refer to Figure 2-1.)

2.1.1 Antenna

Incoming GPS signals enter through a left-hand circularly polarized (LHCP) GPS antenna. Depending on the arrival angle of the signal and the antenna design, the antenna gain pattern either amplifies or attenuates these signals. Recall from Section 1.2 of Chapter 1 that the civilian GPS signal has a nominal power of –160dBW. The standard GPS antenna—a (omnidirectional) patch antenna—typically amplifies signals arriving from zenith by approximately 3dB. Conversely, the antenna frequently attenuates signals arriving from the horizon (0° elevation angle) or below by 3dB or more. This is desirable since most undesired signal reflections (multipath) arrive from low elevation angles.

A low-noise radiofrequency (RF) amplifier subsequently amplifies the signal. The noise figure for this first stage amplifier, NF_1, when added to the ambient noise temperature-dependent figure, essentially prescribes the worst case thermal noise figure, N_0, for the receiver [Van Dierendonck95]. Conservative assumptions yield a receiver noise figure (power loss in decibels) approximated by

$$N_0 = -204\text{dBW/Hz} + \text{NF}_1(\text{dB}) \tag{2.1}$$

The maximum C/A signal power, when measured in a 20MHz bandwidth, is approximately 14.9dB below the noise floor [Spilker94a].

2.1.2 Downconversion and Sampling

Downconversion refers to the process which translates the signal from a high nominal center frequency (at f_{L1}) to baseband or pseudo-baseband (usually less than 10MHz) [Kaplan]. Several stages of local oscillator (LO) mixing to intermediate frequencies (IF) and alternate filtering stages accomplish this task. After passing through the precorrelation filter, an A/D converter samples the final IF signal (at a frequency at least twice the precorrelation filter bandwidth). The next two subsections describe these processes.

2.1.3 Precorrelation Filtering

The final stage IF filter determines the precorrelation bandwidth (PCBw) of the receiver. As illustrated in Figure 2-2 below, this bandwidth effectively extracts a number of central lobes of the signal power spectrum. In other words, it removes low-power, higher frequency components. Moreover, it provides substantial attenuation for some types of out-of-band RF interference (RFI) [Phelts], [Spilker95]. As shown qualitatively in Figure 2-3 and more explicitly in Figure 2-4, narrow PCBws, however, round the corners of the (ideal) correlation peak. As a result, so-called “narrowband” receivers are generally less desirable candidates for mitigating multipath and for detecting EWFs.

Narrowband receivers attempt to select only the main lobe of this spectrum and accordingly have bandwidths as narrow as 2MHz. Wideband receivers may include several lobes of the spectrum and frequently have a precorrelation bandwidth of 8MHz or more. (For civil users, the widest PCBw is approximately 20MHz. For military receivers it typically extends to 24MHz.)

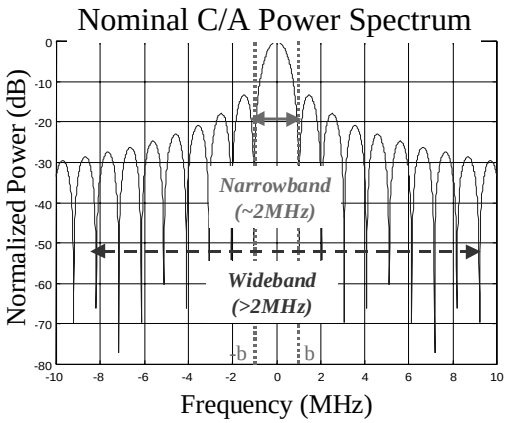

Figure 2-2 Nominal CA Power Spectrum for Wideband and Narrowband Receivers.

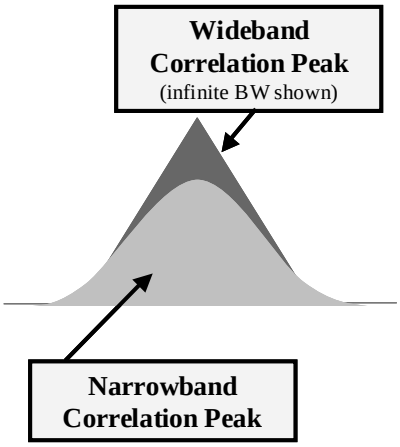

Figure 2-3 Effect of Narrow Bandwidth on the Correlation Peak

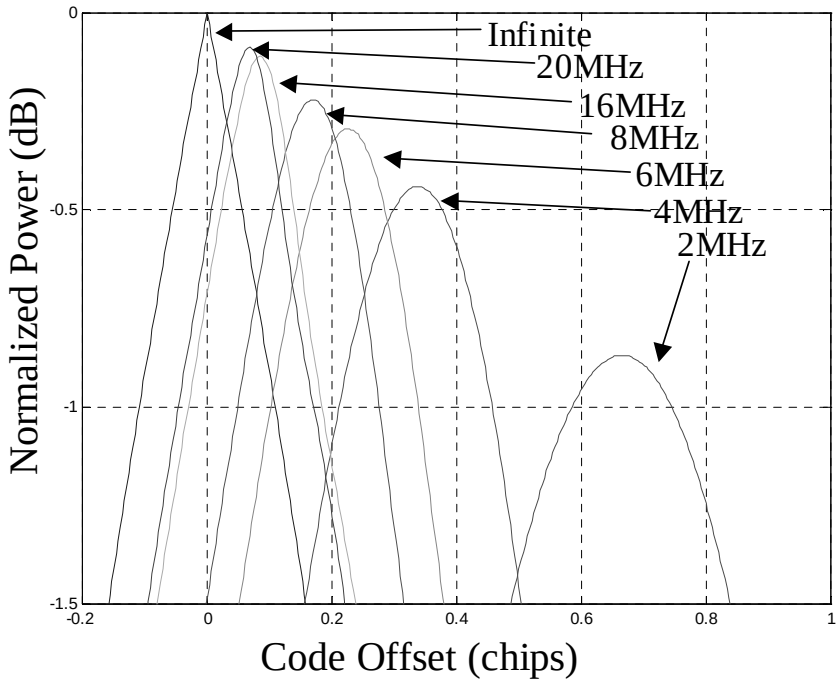

Figure 2-4 Comparison of Wideband and Narrowband Correlation Peaks

2.1.4 Precorrelation Sampling

An A/D converter (sampler) converts the analog GPS signal (at the final IF frequency) to a (baseband) digital signal using inphase (*I*) and quadrature (*Q*) sampling. To permit correlation and doppler removal, this *I,Q* sampling process samples the signal (at a prescribed sampling frequency) at two phases separated by 90° [Van Dierendonck95]. The digital signal samples, I_s and Q_s, at time step, *w*, are then described as

$$I_{sw} = \frac{A}{\sqrt{2}} C_w X_w \cos(\phi_w)$$
$$Q_{sw} = \frac{A}{\sqrt{2}} C_w X_w \sin(\phi_w) \tag{2.2}$$

where

A is the signal amplitude

ϕ_w is the phase of the digital signals at sample *w*.

C_w is the C/A code at sample *w*.

X_w is the data bit at sample *w*.

GPS receivers quantize the incoming signals using one or more bits. In general, lower signal degradation (hence, better receiver performance) results from using 3-bit quantization or more [Van Dierendonck95].

2.2 Digital Processing

The essentials of the digital portion of a receiver channel are shown in the rightmost half of Figure 2-1. Once the A/D digitizes (samples) the signal, this portion of the GPS receiver becomes solely responsible for correlation, acquisition, code and carrier phase tracking, pseudorange measurement processing, and, ultimately, generation of the navigation solution in real-time. The first four of these tasks occur for each channel and are detailed

below. (Section 1.3 of Chapter 1 briefly discusses the generation of the GPS navigation solution.)

2.2.1 Correlation and Acquisition

Sections 1.5 and 1.6 of Chapter 1 described the basic concept of correlation for GPS signals. The initial goal of the correlation process, however, is simply to acquire a specific GPS (PRN code) signal. The receiver performs a search over all possible frequency (doppler) bins and all possible code phases to acquire the combined satellite signal [Kaplan]. The digitally (or numerically) controlled oscillator (DCO) in a given channel accomplishes these tasks. The DCO outputs replicate I_{rw} and Q_{rw} samples using phase, ϕ_{rw}, in an attempt to match (align) them to the incoming signal. (The replica I and Q samples are output from the receiver's correlators discussed in Section 1.5 of Chapter 1.) The receiver measurement samples may be expressed as products of the incoming (Equation (2.2)) and replica signals as follows

$$\begin{aligned} I_{sw} &= \frac{A}{\sqrt{2}} C_k C_{rw,j} X_w \cos\left(\phi_w - \phi_{rw}\right) \\ Q_{sw} &= \frac{A}{\sqrt{2}} C_w C_{rw,j} X_w \sin\left(\phi_w - \phi_{rw}\right) \end{aligned} \tag{2.3}$$

where $C_{rk,j}$ is the replica code phase, j, at time step, w.

Acquisition search time depends on the receiver channel (thermal and cross-correlation) noise levels. The noise floor of the receiver is dictated by the power (variance) of the I and Q samples from Equation (2.3) output when no signal is present. The variance of these samples increases in the presence of the desired GPS satellite signal. The search terminates—a given satellite is presumed detected—once the received signal-to-noise ratio (SNR) from one or more of the correlators exceeds a prescribed threshold. Assuming that additive white gaussian noise (AWGN) models the channel noise with a standard deviation, σ_n, the acquisition threshold, V_t, may be determined from

$$V_t = \sigma_n \sqrt{-2 \ln P_{fa}} \tag{2.4}$$

where P_{fa} is the specified probability of false acquisition. It follows that the probability density function, p_{fa}, is simply

$$p_{fa} = e^{-\left(\frac{V_t^2}{2\sigma_n}\right)} \tag{2.5}$$

Note that performing the correlation process (i.e., integrating) over more than a single code epoch will reduce σ_n. The predetection integration time (PIT, or T_I), for N_{PIT} C/A code sequences is N_{PIT} milliseconds (where $N_{\text{PIT}} \geq$1ms). The correlators may convolve or integrate over as many as 5-20ms for reliable acquisition and tracking. More details on signal acquisition can be found in [Kaplan].

2.2.2 Code Tracking Loops

After acquisition, the standard receiver code tracking loop, called a delay-lock loop (DLL), "tracks" the signal by slewing, or "servo-ing", the correlators until the E and L correlator outputs are balanced. The difference (E-L=0) forms the standard DLL discriminator. (See Figure 2-5 below.) In the absence of thermal noise, multipath, filtering effects, and any other correlation peak distortions, when the discriminator is zeroed, the code tracking errors are also zero *independent of correlator spacings*. (See Figure 2-6.)

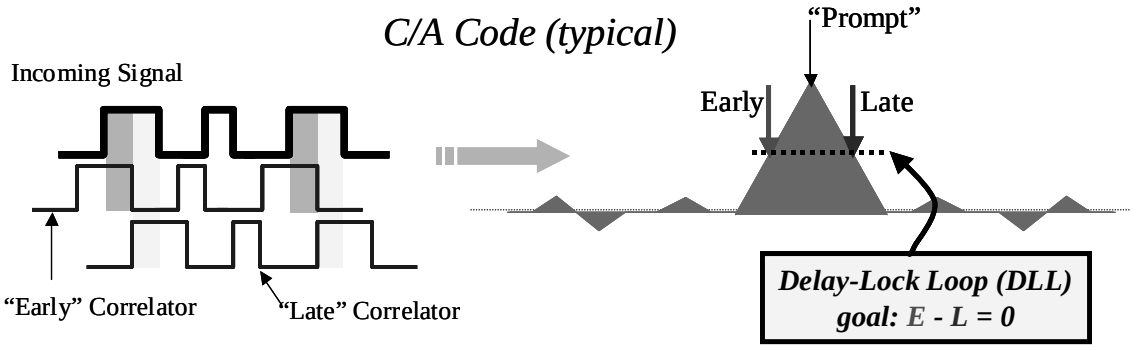

Figure 2-5 The Conventional Delay-Lock Loop

Code tracking errors translate directly into pseudorange errors. The primary task of the DLL is to keep the tracking errors as small as possible in the presence of thermal noise. Figure 2-6 shows the discriminator function for an ideal correlation peak and various correlator spacings, $d = 1T_c$, $d=0.5T_c$, $d=0.2T_c$, and $d=0.1T_c$.

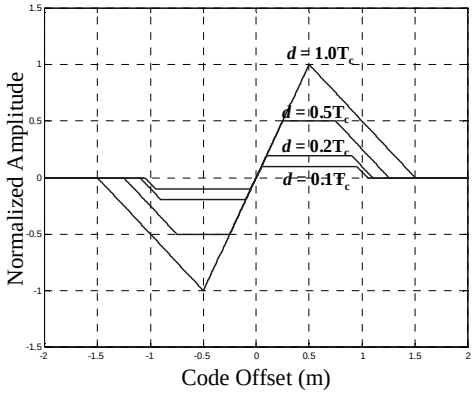

Figure 2-6 Four E-L Discriminator Functions for $d=1.0T_c$, $d=0.5T_c$, $d=0.2T_c$, and $d=0.1T_c$.

There are three basic types of code tracking loops: Early minus Late (E-L) power, dot-product and coherent DLLs. Note that both the E-L power and dot-product discriminators are noncoherent since they do not require phase tracking by the receiver. Coherent DLLs, however, provide smaller steady state tracking errors. (See Equations (2.9) and (2.10).) These three DLLs combine the in-phase and quadrature samples from each correlator in different ways. Assuming a predetection integration time (PIT) over N_{PIT} code epochs, the discriminators for each code tracking loop are expressed in Equations (2.6), (2.7), and (2.8) below.

Early Minus Late (E-L) Power:

$$\sum_{i=1}^{N_{\text{PIT}}} \left\{ \left(I_E^{\,2} + Q_E^{\,2} \right) - \left(I_L^{\,2} + Q_L^{\,2} \right) \right\} \tag{2.6}$$

Dot-Product:

$$\sum_{i=1}^{N_{\mathrm{PIT}}}\left\{\left(I_E + I_L\right)I_P - \left(Q_E - Q_L\right)Q_P\right\} \tag{2.7}$$

Coherent:

$$\sum_{i=1}^{N_{\mathrm{PIT}}}\left(I_E - I_L\right) \tag{2.8}$$

where *E*, *L*, and *P* correspond to the Early, Late, and Prompt correlators, respectively.

A code loop filter smoothes the (integrated) discriminator (E-L) measurements, and scales them by the loop gains to translate them into tracking errors. The steady-state closed-loop code tracking errors (normalized variances) due to thermal noise for coherent and noncoherent DLLs can be found using the following equations [Betz00b]:

$$\left(\frac{\sigma_\tau^{\,2}}{T_c^{\,2}}\right)_{Coherent} = \frac{B_L\left(1-0.5B_LT_I\right)\int_{-B/2}^{B/2}\mathrm{sinc}^2\left(\pi f\right)\sin^2\left(\pi f d_{\mathrm{E\text{-}L}}\right)\mathrm{d}f}{\left(2\pi\right)^2\left(C/N_0\right)\left(\int_{-B/2}^{B/2} f\mathrm{sinc}^2\left(\pi f\right)\sin\left(\pi f d_{\mathrm{E\text{-}L}}\right)\mathrm{d}f\right)^2} \tag{2.9}$$

$$\left(\frac{\sigma_\tau^{\,2}}{T_c^{\,2}}\right)_{Noncoherent} = \left(\frac{\sigma_\tau^{\,2}}{T_c^{\,2}}\right)_{Coherent}\cdot\left[1+\frac{\int_{-B/2}^{B/2}\mathrm{sinc}^2\left(\pi f\right)\cos^2\left(\pi f d_{\mathrm{E\text{-}L}}\right)\mathrm{d}f}{\mathrm{T_I}\left(C/N_0\right)\left(\int_{-B/2}^{B/2} f\mathrm{sinc}^2\left(\pi f\right)\sin\left(\pi f d_{\mathrm{E\text{-}L}}\right)\mathrm{d}f\right)^2}\right] \tag{2.10}$$

where C/N_o is the carrier (signal) to noise ratio in dB-Hz, $d_{\mathrm{E\text{-}L}}$ is the Early-Late spacing in chips, *B* is the double-sided PCBw in MHz, *f* is the frequency offset in MHz, and B_L is the single-sided code tracking loop bandwidth in Hz [Betz00b]. (B_L is designed based on the desired code tracking performance in the presence of receiver platform dynamics and thermal noise; it determines the noise bandwidth of the loop.)

The above expressions assume the thermal noise is AWGN. They are valid for any SNR (signal power) and code integration time, T_I. 1-σ pseudorange (i.e., tracking) errors for

standard users are typically between 1-2 meters. Chapter 3 addresses code tracking performance in the presence of evil waveforms and Chapter 5 discusses code tracking in the presence of multipath.

2.2.3 Carrier Tracking Loops

A frequency-lock loop (FLL) and/or a phase-lock loop (PLL) perform carrier phase (or frequency) tracking. Several possible implementations of both PLLs and FLLs exist and are detailed in [Kaplan]. FLLs generally provide more robust tracking for low C/N_0 signals and also in the presence of interference [Ndili]. FLLs attempt to achieve zero steady-state frequency errors. PLLs provide phase tracking; they attempt to zero the phase tracking errors. Although receiver acquisition processes almost universally employ FLLs, most receivers use PLLs almost exclusively for precise phase tracking. They simply transition from FLL to a PLL once the signal is (re)acquired. This thesis will presume steady state tracking conditions (i.e., the receiver of interest uses a PLL).

The phase discriminator (error), $\delta\phi$ is simply

$$\delta\phi = \text{atan}\left(\frac{Q_P}{I_P}\right) \tag{2.11}$$

Carrier phase tracking—by providing accurate doppler and phase measurements—captures user dynamics. The carrier tracking loop filters reduce any phase errors due to thermal noise while allowing a maximum range of dynamics [Kaplan]. High bandwidth loop filters permit the widest range of user dynamics, while low-bandwidth filters most significantly attenuate the thermal noise tracking errors. Regardless of the loop bandwidth, however, the 1-σ carrier-phase tracking errors are on the order of 20° (1cm in range) or less for thermal noise. For multipath, provided the PLL maintains lock on the direct signal, the carrier tracking errors are always less than 90° (4.8cm in range) [Braasch95].

2.3 Measurement Processing

GPS receivers frequently refine the code and carrier phase measurements (and, hence, the pseudorange observables) to reduce nominal noise and multipath errors. The two primary methods for doing this are carrier aiding of the DLL and carrier smoothing of the pseudorange measurements.

2.3.1 Carrier Aiding (CAI)

The receiver may leverage the carrier phase dynamics to reduce the bandwidth of the DLL. A narrow tracking loop bandwidth implies reduced tracking errors due to thermal noise. A common (open-loop) transfer function for a DLL is

$$\frac{Y(s)}{X(s)} = \frac{\nu_b s + 1}{\nu_a s} \tag{2.12}$$

where $X(s)$ and $Y(s)$ are the Laplace transform representations of the input and output E-L measurements of the DLL, respectively, and ν_a and ν_b are positive constants. They determine the loop bandwidth and response [Ndili]. This implies the output discriminator of the DLL is simply an integrated version of the input E-L measurements, weighted against the current (unfiltered) E-L measurements. The equivalent time-domain filter for code tracking is given as

$$\Delta\tau_i = \Delta\tau_{i-1} + \nu_1\left(\delta\tau_i - \delta\tau_{i-1}\right) + \nu_2\left(\delta\tau_i\right) \tag{2.13}$$

where ν_1 and ν_2 are functions of ν_a, ν_b, and the loop update rate [Ndili], [GEC]. $\Delta\tau_i$ and $\Delta\tau_{i-1}$ are the current and previous closed-loop code tracking errors, respectively; $\Delta\tau_i$ and $\Delta\tau_{i-1}$ are the current and previous open-loop (discriminator) code tracking errors, respectively.

With carrier aiding, this equation becomes

$$\Delta\tau_i = \left(\Phi_i - \Phi_{i-1}\right) + \nu_3\left(\delta\tau_i - \delta\tau_{i-1}\right) + \nu_4\left(\delta\tau_i\right) \tag{2.14}$$

where ν_3 and ν_4 are also functions of ν_a, ν_b, and the loop update rate. Φ_i and Φ_{i-1} are the current and previous accumulated (i.e., integrated) carrier phase (ICP) differences computed according to

$$\begin{aligned} \Phi_i &= \int_0^{t_i} \dot{\phi}(t)\, dt \\ \Phi_0 &= 0 \end{aligned} \tag{2.15}$$

Here, the dynamics of the code tracking loop are propagated (aided) from one update to the next using the difference in accumulated carrier phase measurements. Since thermal noise (and multipath) errors on carrier measurements are much smaller than on code phase measurements, carrier aiding effectively smoothes the code tracking errors.

The constants ν_3 and ν_4 determine the degree of noise abatement (filtering). Note that when $\nu_3 = 0$ and $\nu_4 = 0$, the code tracking loop dynamics rely solely on the carrier. Such a design effectively de-weights the code measurements entirely. Weighting the ICP differences too much is generally undesirable, however, since this can sometimes introduce biases into the pseudorange measurements, which may be difficult to remove. Section 6.1 of Chapter 6 illustrates this experimentally and explains the effects in more detail.

2.3.2 Carrier Smoothing (CSM)

In addition to using CAI to produce less noisy pseudorange measurements, the relatively smooth ICP measurements usually filter the final code pseudorange measurements. In contrast to CAI, which directly affects the dynamics of the tracking loop, CSM only acts on the measurements produced by the DLL. Standard CSM smoothing is accomplished using a Hatch Filter.

$$\hat{\rho}^{\,k}(t_i) = \frac{1}{L}\tau^{\,k}(t_i) + \frac{L-1}{L}\left[\tau^{\,k}(t_{i-1}) + \left(\Phi^{(k)}(t_i) - \Phi^{(k)}(t_{i-1})\right)\right] \tag{2.16}$$

where for the *k*th satellite,

$\hat{\rho}^{k}(t_i)$ is the estimated pseudorange estimate at time t_i,

$\tau^{k}(t_i)$ and $\tau^{k}(t_{i-1})$ are the code phase measurements (code DLL-based pseudoranges) at times t_i and t_{i-1}, respectively,

$\Phi^{k}(t_i)$ and $\Phi^{k}(t_{i-1})$ are the ICP measurements at times t_i and t_{i-1}, respectively,

L is a constant that determines the smoothing time constant of the filter

The Hatch filter is equivalent to a Kalman filter with a single (velocity) state variable [Kaplan]. However, an even simpler way to describe it is simply as a first-order lowpass filter. The transfer function from raw (DLL) input smoothed (pseudorange) to the output of this filter is given as

$$\hat{\Gamma}(s) = \frac{\alpha}{s+\alpha}\mathrm{T}(s) + \frac{s}{s+\alpha}\Phi(s) \tag{2.17}$$

where $\hat{\Gamma}(s)$, $\mathrm{T}(s)$, $\Phi(s)$ are the Laplace transform representations of the pseudorange estimates, the (input) code phase and the (input) ICP measurements, respectively. α is a function of L as follows

$$\alpha = \frac{L-1}{L} \tag{2.18}$$

Note that as the frequency, *s*, approaches infinity, the pseudorange estimates become less dependent on the DLL-based measurements and rely more on the relatively noiseless, velocity-propagated ICP.

The transfer function from $\mathrm{T}(s)$ to $\hat{\Gamma}(s)$ is simply

$$\frac{\hat{\Gamma}(s)}{\mathrm{T}(s)} = \frac{\alpha}{s+\alpha} \tag{2.19}$$

which is clearly a 1st-order lowpass filter with a pole at $s=-\alpha$. The time constant for aviation receivers is 100 seconds and, for a sampling period of 1 second, is obtained by setting $L = 100$. A greater time constant may be used to provide more noise-abatement through smoothing. However single-frequency receivers (designed to track C/A at $f = f_{L1}$ only) seldom employ CSM time constants greater than about 2 minutes, because of ionospheric code-carrier divergence issues [Klobuchar]. Assuming continuous phase tracking (i.e., no phase "cycle slips" or losses of lock occur), dual-frequency receivers permit use of virtually unbounded CSM time constants.

Even for relatively small time constants, however, CSM is highly effective at reducing pseudorange errors due to thermal noise [Kaplan]. CSM is also effective at reducing PR errors due to MP if the so-called "fading" frequencies of the MP are sufficiently large. This implies the Doppler differences between the LOS and MP signals are high. However, only when the amplitudes and/or relative delays of the MP signals are small compared to the LOS will the MP-induced tracking errors closely resemble thermal (AWGN) noise errors and have nearly zero mean [Braasch95], [van Nee92a]. This is not always the case for MP tracking (and hence pseudorange) errors. Section 5.1 of Chapter 5 discusses the effects and parameters of MP in greater detail.

2.4 Multicorrelator-Based Signal Threat Mitigation

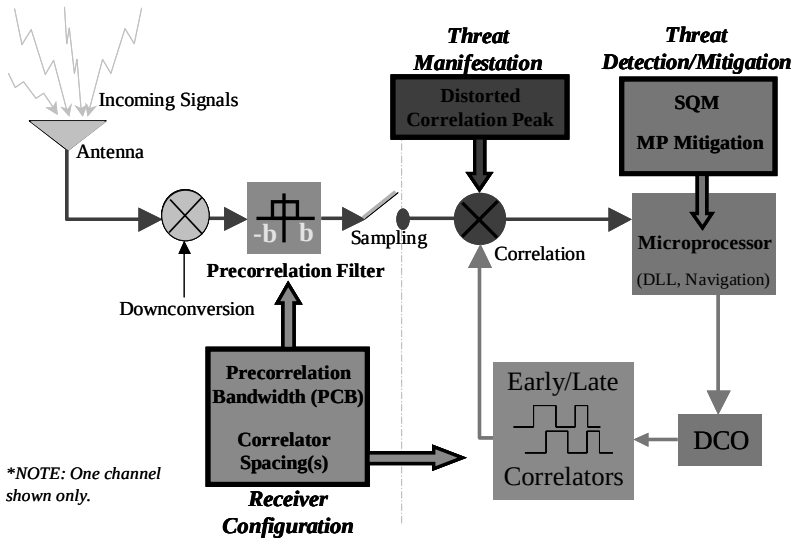

Figure 2-7 Threat Detection and Mitigation in GPS Receivers

In this thesis, the term *receiver configuration* will generally refer to the (E-L) DLL correlator spacing, d ($d_{\text{E-L}}$) and the front-end precorrelation bandwidth PCBw. The *threats* discussed—evil waveforms (EWF) and multipath (MP)—will manifest themselves as distortions of the correlation function, which introduce code tracking errors. The practical multicorrelator mitigation techniques and algorithms will reside in the microprocessor of the receiver. Figure 2-7 illustrates this scenario.

Chapter 3:

Evil Waveforms and Signal Quality Monitoring

Subtle failures of the satellite hardware may cause anomalous satellite signals that may pose an integrity threat to an airborne GPS user attempting to land. LAAS and WAAS require Signal Quality Monitoring (SQM) to protect the integrity of airborne users against the evil waveform threats. This chapter describes the development of the current theory on so-called "evil waveforms" (EWFs) and various methods of SQM. Section 3.1 and 3.2 introduce EWFs and discuss the SV19 event—the first and only known occurrence of such a GPS satellite failure. Section 3.3 describes several early candidate EWF Threat Models. Sections 3.4 and 3.5 detail the preferred model—the 2nd-Order Step Threat Model—and how to efficiently compute these waveforms. Section 3.6 describes several Signal Quality Monitoring approaches and justifies the use of multicorrelator techniques.

3.1 GPS Satellite Signal Generation Payload

The GPS signal generator is a subset of the navigation payload onboard the satellite. As shown in Figure 3-1, the signal generating hardware includes a Navigation Data Unit (NDU) followed by a cascade of analog signal processing units. The NDU outputs baseband signals for the navigation data, the C/A code, and the P(Y) code. The analog

processing includes frequency upconverters, intermediate and high power amplifiers (IPA and HPA), antenna beam forming (RABF) and finally the antenna.

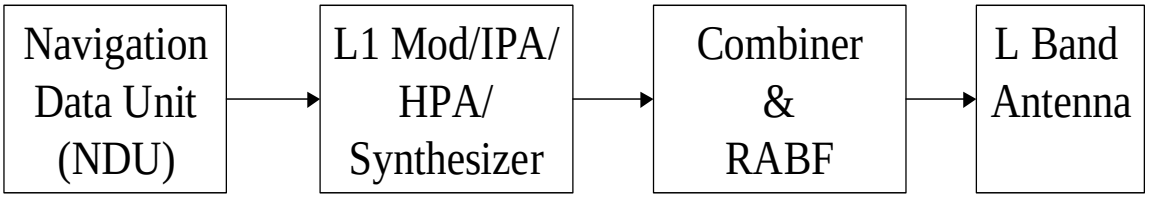

Figure 3-1 GPS Satellite Signal Generation and Transmission Hardware

An "evil waveform," (EWF) is an anomalous satellite signal that results from a failure of the analog and/or digital signal generating hardware onboard the satellite. The first and only known occurrence of an EWF failure on a GPS satellite was in 1993 on SV19 (or PRN19).

3.2 SV19

SV19 was launched on October 21, 1989 and declared operational in November of the same year. In March 1993 at the Oskosh Air Show, Trimble Navigation, Ltd. noted that differential position accuracies—based on code pseudorange measurements—without SV19 were less than 50 cm. When included in the navigation solution, position accuracies with SV19 degraded to anywhere from 2 to 8 meters [Edgar]. In July 1993, the University of Leeds measured the power spectrum of the anomalous SV19 signal. (See Figure 3-2.) The Operational Control Segment had fully resolved the problem by January of 1994 by commanding the satellite to begin using onboard redundant signal transmission hardware.

Instead of the nominal, *sinc* function trend of the main lobe, the spectral data revealed a large spike at the center frequency (L1). Recall that the receiver downconversion process translates this center frequency at L1 (1.575GHz) to baseband (0Hz). A receiver code tracking loop responds to the spectral content of the signal that resides at this center frequency. Consequently, the measured spike in the SV19 spectrum filtered through the GPS receiver essentially as a DC component.

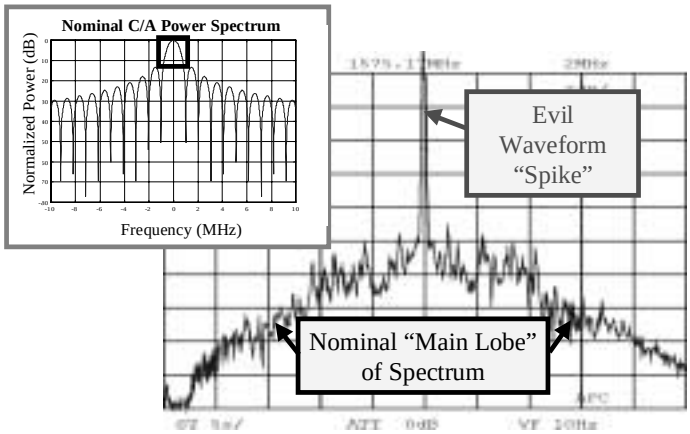

Figure 3-2 SV19 signal power spectrum measured by the University of Leeds

3.3 Early Evil Waveform Threat Models

Several candidate threat models were initially proposed to explain the SV19 event. They have spanned the range from very simple models to very complex. The most prominent of these are briefly described below.

3.3.1 Simpler Threat Models

The first proposed threat model simply added a sine wave to the nominal signal at L1. Such a model could be explained by "leak-through" of the carrier wave in the signal transmission path. This model could easily explain the SV19 spectrum measured by the University of Leeds. However, without assuming unrealistic power levels for the sine wave component, this model could not explain observed position errors as large as 3-8 meters [Enge99].

A second simplistic threat model added a delayed replica of the code to the nominal signal. Such failure could result from a mismatch in the signal transmission line, which could produce onboard reflections. Code multipath easily passes unattenuated through the receiver's front end, and could easily explain the previously observed 3-8 meter position errors. This threat model, however, could not account for the irregular power spectrum measured by the University of Leeds.

3.3.2 Most Evil Waveform (MEWF)

This threat model takes a different approach to accounting for the differential position errors observed using SV19, and the University of Leeds spectrum data. First it assumes the reference station is capable of generating pseudorange measurements using multiple correlator pairs (spacings). One of those pseudoranges forms the LAAS differential (ground reference) corrections. The others monitor for distortions caused by satellite failures. Second, it assumes that a user receiver generates a single pseudorange using (in general) a different correlator spacing precorrelation filter. The most evil waveform (MEWF) is the waveform that will produce the largest differential pseudorange error (PRE) for a particular user, while appearing completely benign (undetectable) to the reference station monitor receiver. [Mitelman98] and [Enge99] describe MEWFs in greater detail. Further, the MEWF is the topic of Mitelman's thesis dissertation.

The waveforms generated by this threat model, could result in maximum differential position errors in airborne receivers. These waveforms, however, are not causal; they originate before a code chip transition. In addition, they are intentionally phase and amplitude modulated to elude the monitor correlator pairs yet still produce large pseudorange errors for the user. Also, the International Civil Aviation Organization (ICAO) and aviation community found this threat model somewhat implausible, since it is highly unlikely that the signal generating hardware onboard the satellite is capable of generating such a waveform.

The MEWF analysis, however, did lead to the identification of three primary threats to GPS signal quality. Specifically, threats manifested themselves in the form of an anomalous correlation peak. Each of the following may result in HMI for the airborne user.

- Deadzones: "Flat spots," or plateaus atop the correlation peak, are regions of zero discriminator gain. The airborne and reference receiver correlator pairs may "track" in different portions of this region.

- Distortions: Asymmetries caused by underdamped oscillations in the correlation function may affect the airborne receivers differently than the reference station. Even using multiple correlators, monitor receivers may not detect these distortions.

- False peaks: Significant distortion of the correlation peak may cause some receivers to lock onto (i.e., track) the EWF-induced peak—a raised oscillation—instead of the true one.

3.4 2nd-Order Step Threat Model

The preferred threat model—the "2nd-order Step" (2OS) Threat Model—is capable of generating deadzones, distortions, and false peaks on the receiver correlation peak. It also explains the University of Leeds SV19 spectrum data and 3-8 meter differential position errors. (See Figure 3-2.) It uses only three parameters and is accordingly relatively simple to simulate and test. In addition, the 2nd-order Step model generates causal waveforms, which are more plausible candidates for future failure modes of the real satellite signal generating hardware.

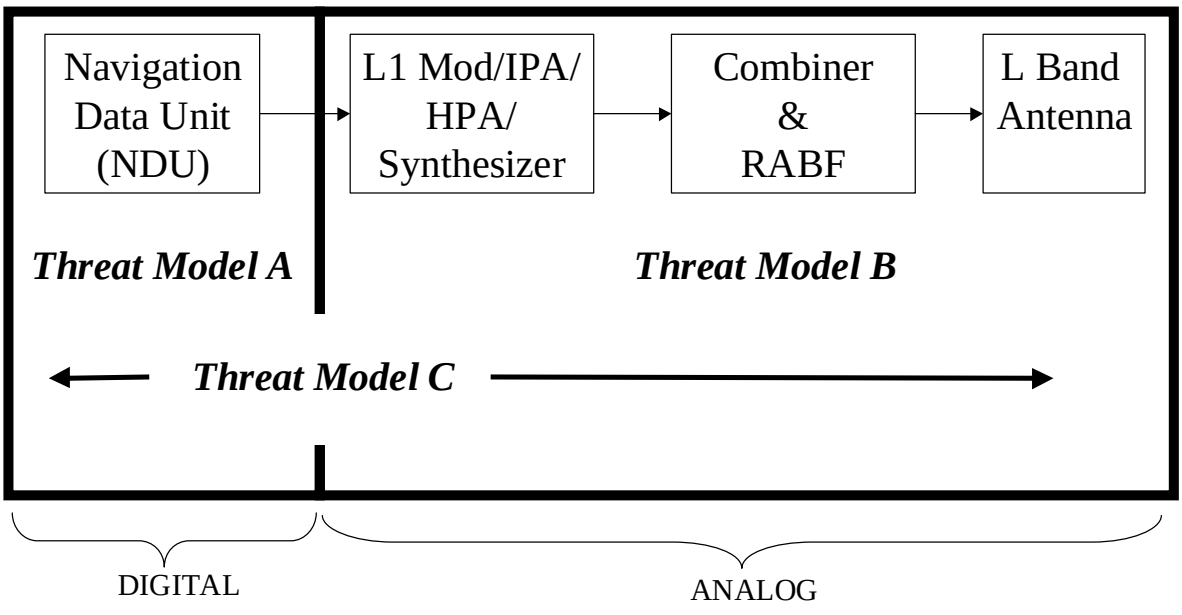

Figure 3-3 GPS Satellite Signal Generation and Transmission Hardware with Threat Models A, B and C

The 2OS models three specific classes of failure modes: digital, analog, and combination (analog and digital) failure modes. The names Threat Model A (TM A), Threat Model B (TM B), and Threat Model C (TM C) refer to each of the respective failure modes. Figure 3-3 illustrates where these failure modes would occur inside the GPS navigation payload.

3.4.1 Threat Model A: Digital Failure Mode (Lead/Lag Only)

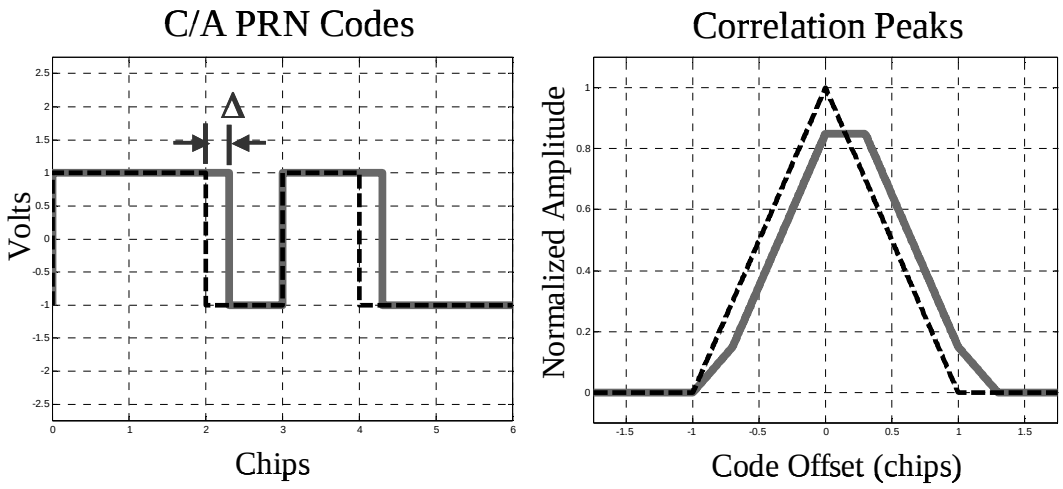

Figure 3-4 Threat Model A: digital failure mode (Ideal <dashed> and Evil <solid> Waveforms (Lag) Shown.)

A digital failure mode occurs inside the NDU. Threat Model A (TM A) models this failure as either an advance (lead, $\Delta < 0$) or a delay (lag, $\Delta > 0$) in the falling edge of the C/A code chip, which occurs independently of the analog subsystem. This failure mode creates deadzones. For illustration purposes, Figure 4 depicts a (large) lag of 30% of a chip period ($\Delta = 0.3T_c$) and its effect on the correlation peak. The entire peak is shifted, or delayed, by the lag. A lead of 30% would advance the entire peak in the opposite direction, by the same amount. Accordingly lead and lag are symmetric. (The analytical expressions for obtaining these EWF correlation functions directly are derived in Section 3.6.1.) The proposed range of the single TM A parameter Δ, is ±12% of a C/A code chip, since larger values produce waveforms that are easily detectable by multicorrelator signal quality monitors (discussed in Section 3.7).

3.4.2 Threat Model B: Analog Failure Mode (Amplitude Modulation Only)

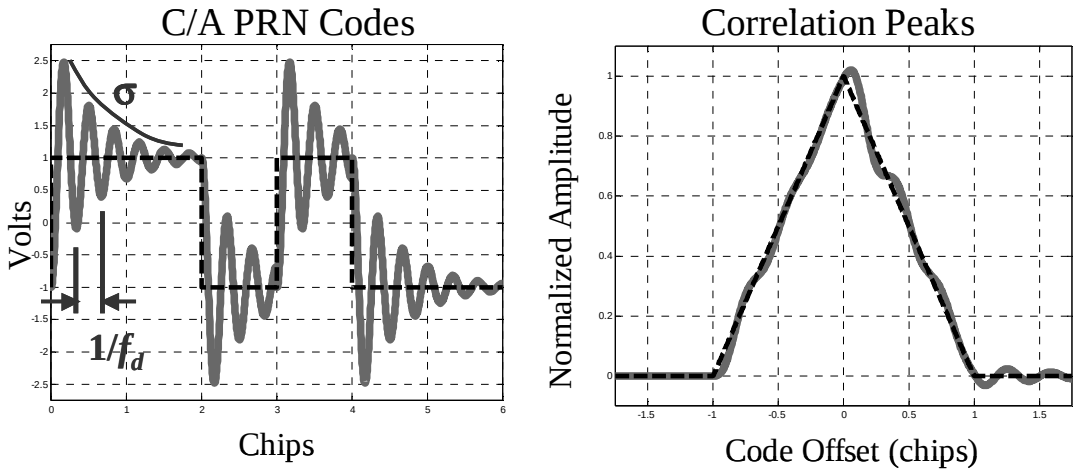

Figure 3-5 Threat Model B: Analog Failure Mode (Ideal <dashed> and Evil <solid> Waveforms Shown.)

Threat Model B (TM B) models an analog failure mode of the incoming signal as amplitude modulation or "ringing" only that occurs independent of a digital failure. TM B uses two parameters to describe this ringing as a damped second-order response. As shown in Figure 3-6, this corresponds to a second-order system with a pair of complex-conjugate poles in the left half plane at $\sigma \pm j2\pi f_d$. The two parameters of TM B are the damped frequency of oscillation, f_d (MHz), and the damping factor, σ (Mnepers/second), respectively. (This equates to an amplitude attenuation rate of about $20\sigma\log_{10}(e)$ dB/chip). It follows that each chip transition can be described by the unit step response of this second order-system, given by

$$e(t) = \begin{cases} 0 & t \le 0 \\ 1 - \exp(-\sigma t)\left[\cos\omega_d t + \dfrac{\sigma}{\omega_d}\sin\omega_d t\right] & t \ge 0 \end{cases} \qquad (3.1)$$

$$\omega_d = 2\pi f_d$$

Figure 3-5 illustrates a TM B EWF, corresponding to f_d = 3MHz and σ = 0.8 Mnepers/second, which causes significant distortion of the correlation peak.

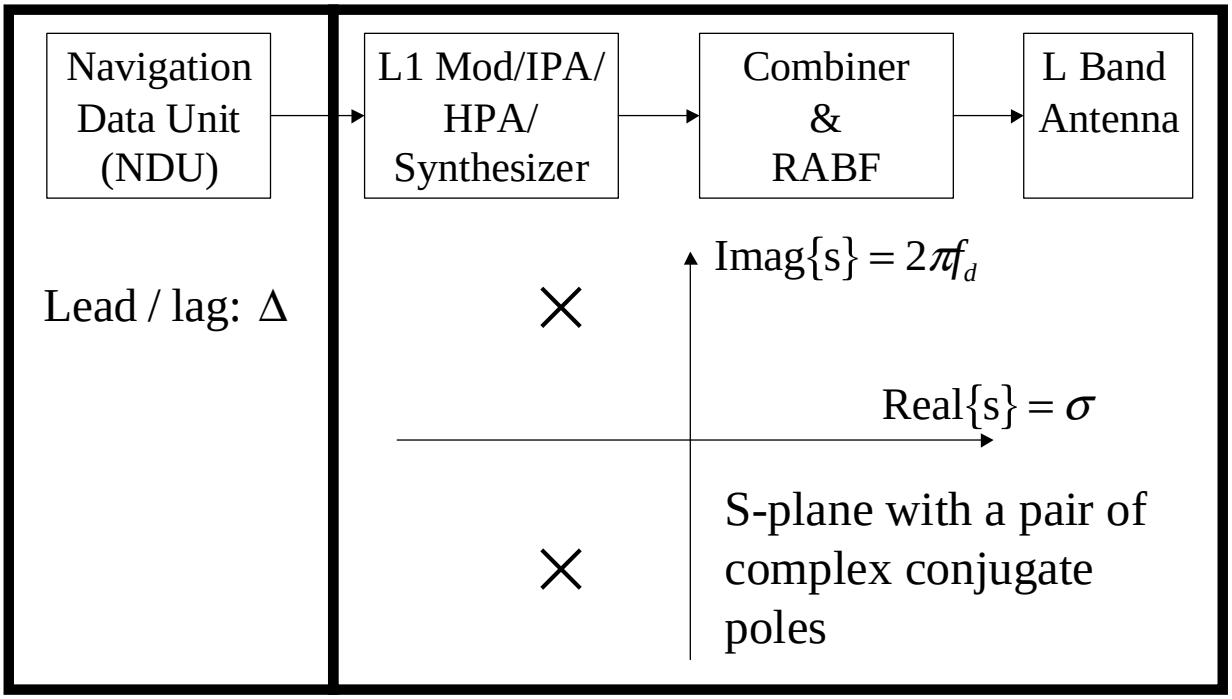

Figure 3-6 GPS Satellite Signal Generation and Transmission Hardware, with TM A and TM B Parameters

For TM B, f_d ranges from 4 to17 MHz and σ ranges from 0.8 to 8.8 Mnepers/second. f_d only extends as low as 4MHz since lower frequencies would impact the military signal (P(Y) code), which is more closely monitored than the C/A code. Frequencies above 17MHz would be difficult for the satellite signal hardware to generate. Also, the satellite bandpass filter would attenuate modes above 17MHz. (Recall that the P(Y) code has a chipping rate of 10.23MHz, compared to the C/A code rate of 1.023.) A large damping factor range permits analysis of essentially undamped analog failures along with those that have heavy damping. A lower sigma ($\sigma < 0$) would unrealistically result in unstable oscillations on the code chips. Larger values of σ ($\sigma > 8.8$) would not introduce additional constraints on the avionics since this would further attenuate the oscillations.

3.4.3 Threat Model C: Combination Failure Mode (Lead/Lag and Amplitude Modulation)

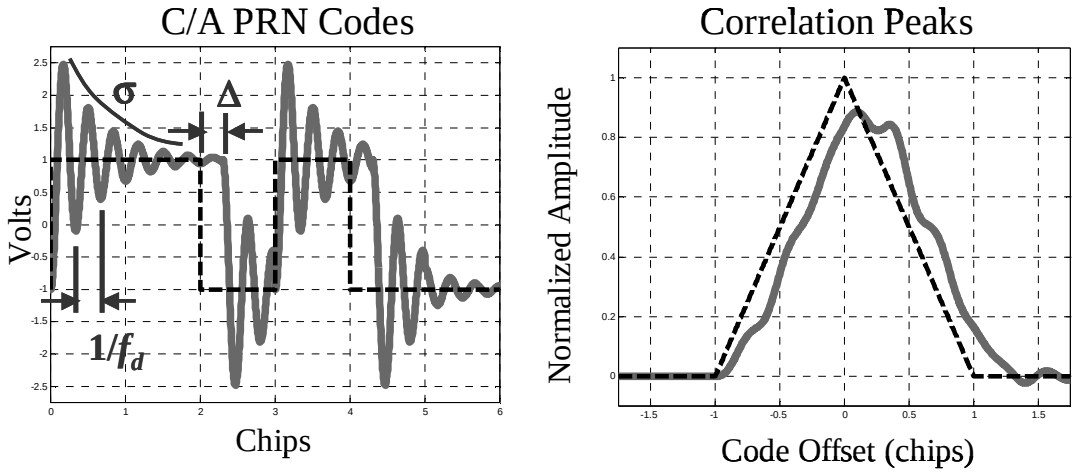

Figure 3-7 Threat Model C: Combination of Analog and Digital Failure Modes (Ideal <dashed> and Evil <solid> Waveforms Shown.)

Threat Model C (TM C) models an EWF that is a combination of simultaneous analog and digital failure modes. Although many of the details remain unknown, the SV19 event is believed to be a result of a TM C EWF. Figure 3-7 depicts such a waveform (for $\Delta = 0.3$, $f_d = 3$, and $\sigma = 0.8$). It illustrates that this threat model is capable of at once producing deadzones, distortion and false peaks.

The (3-dimentional) parameter space for TM C, however, is not a direct combination of those from TM A and TM B. For this threat model, the lead/lag parameter, Δ, is bounded by the same limits as for TM A ($\pm 0.12T_c$), and the damping factor, σ, has the same bounds as for TM B ($0.8 \leq \sigma \leq 8.8$Mnepers/second). For TM C the damped frequencies of oscillation, however, only range from 7.3 to 13MHz since the likelihood of a simultaneous analog and digital failure is relatively small. (The parameters for SV19 fell within the TM C range.)

The parameter (threat) space for all three threat models is summarized below in Figure 3-8. TM A uses only a single parameter (Δ) and represents a line in the threat space. TM B uses

two parameters (f_d,σ) and is a plane. Similarly, TM C is a 3-dimentional cube comprised of all three parameters (Δ, f_d,σ). The cube depicted in Figure 3-8 shows where TM A and TM B intersect with TM C. Also pictured are several "undetected" points (UDPs) in each respective threat space to illustrate EWFs that may not be detectable by the multicorrelator signal quality monitors discussed in Chapter 4.

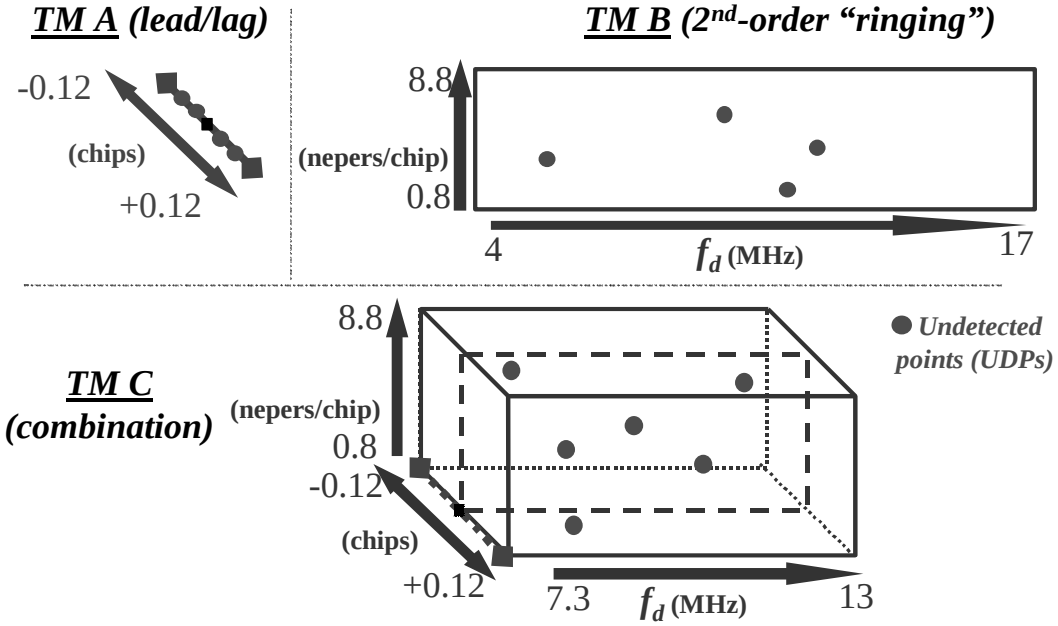

Figure 3-8 EWF parameter threat space for 2nd-Order Step Threat Models A, B, and C

3.5 Correlation Functions for the Three 2OS Threat Models

Modifying the nominal incoming signal (code sequence), $x(t)$, and correlating the new signal with the (delayed) replica of this nominal signal, $x_{nom}(t-\tau)$, allows computation of the correlation functions for each threat model. When this is done, the (ideal) nominal correlation function given by

$$R_{\text{nom}}(\tau) = \langle x_{\text{nom}}(t), x_{\text{nom}}(t-\tau) \rangle \tag{3.2}$$

becomes

$$R_{\mathrm{EWF}}(\tau) = \left\langle x_{\mathrm{EWF}}(t), x_{\mathrm{nom}}(t-\tau) \right\rangle \tag{3.3}$$

where

$R_{EWF} = R_{lead}, R_{lag}, R_A, R_B, R_C$

$x_{EWF} = x_{lead}, x_{lag}, x_A, x_B, x_C$.

(The subscripts, *lead* and *lag* refer to the digital failure modes within Threat Model A. Subscripts *A*, *B*, and *C* correspond to Threat Models A, B, and C, respectively.) Figure 3-9 below summarizes how each of the Threat Models acts to modify the nominal incoming GPS signal.. It illustrates how only the 2nd-order filter acts on the nominal code to produce TM B, while either a lead or lag (TM A) may accompany this analog failure for TM B.

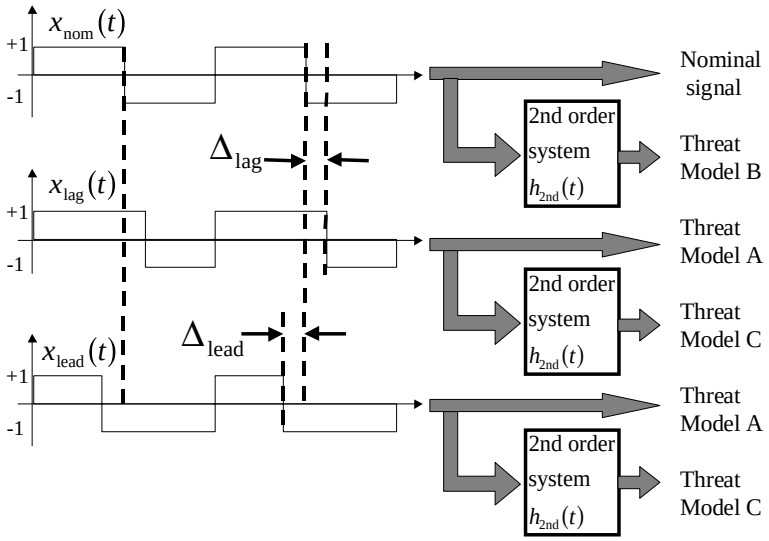

Figure 3-9 Summary of the Preferred Threat Model

Figures 3-4, 3-5, and 3-7 above depict (with dashed lines) the nominal incoming signal and resulting correlation peak for PRN5. The general expression for a normalized (i.e., elevation angle-independent) nominal correlation function, $R(\tau)$, is

$$R(\tau) = \begin{cases} b, & |\tau| > T_c \\ 1 - \dfrac{|(1+b)\cdot\tau|}{T_c}, & |\tau| \le T_c \end{cases} \tag{3.4}$$

In this expression, b is the height of the main peak at its base. For most PRNs, b = -1/1023. For SQM, however, we may assume b = 0 without significant loss of accuracy.

Recall that the actual (complete) correlation functions for the GPS signals have non-zero sidelobes, which may lie near and sometimes adjacent to the peak. In these instances, b may be non-negligible. (See Appendix E.) Section 4.3.2 of Chapter 4 discusses the effects these sidelobes may have on prescribing thresholds for detecting EWFs. For modeling EWF correlation peaks, however, these sidelobes have negligible effect.

Analytical equations can compute the EWF correlation functions directly. Figure 3-10 shows two equivalent cascades of linear systems. The top cascade models the physical reality. The baseband signals, $x_{\text{nom}}(t)$, $x_{\text{lead}}(t)$ and $x_{\text{lag}}(t)$, are generated in the satellite navigation data unit. They pass though the analog sections of the satellite that may or may not be degraded. If degraded, these sections simply become equivalent to a second order system with impulse response, $h_{\text{2nd}}(t)$. If these sections are not degraded, the signal bypasses the second order system. After transmission, the signal propagates to the receiver antenna where the receiver's front end processes it. As shown, the front end is simply another linear system with impulse response, $h_{\text{pre}}(t)$. Finally, the signal is correlated with a delayed replica of the nominal signal $x_{\text{nom}}(t-\tau)$.

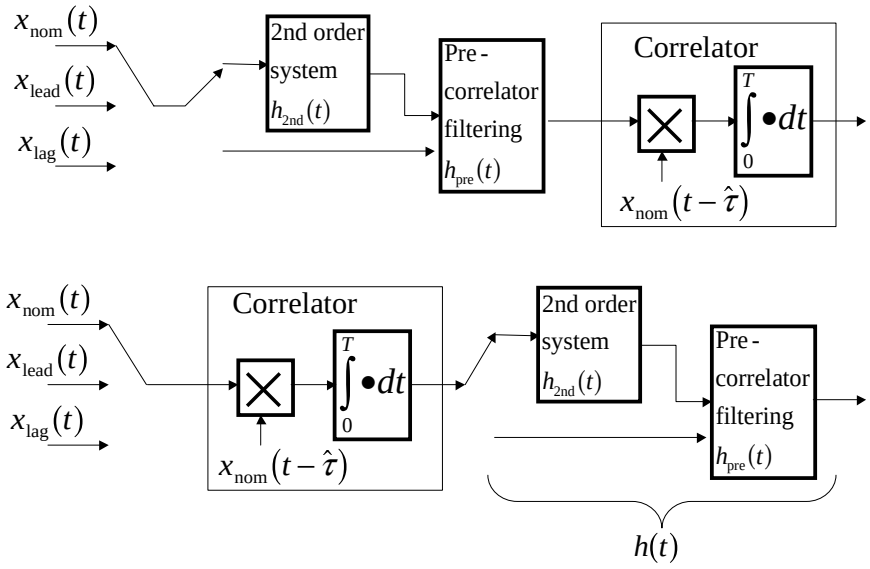

Figure 3-10 Exchanging the Order of Linear Operations

The bottom cascade in Figure 3-10 depicts a system that is mathematically equivalent to the top, but much more convenient computationally. In this case, the correlator first processes the baseband signals, then $h_{2nd}(t)$ and finally $h_{pre}(t)$. The top and bottom systems in Figure 3-10 simply exchange the order of linear systems and are equivalent. (This is apparent since, in the frequency domain, convolution and correlation operations are simply multiplications; these multiplications commute.) The bottom cascade is more convenient, because closed form expressions exist for all of the relevant correlation functions (R_{nom}, R_{lag}, R_{lead}, R_A, R_B and R_C) identified in Equations (3.5) through (3.7). Recall that R_A, R_B and R_C are simply convolved with the impulse responses for the pre-correlation filters, $h_{pre}(t)$, in the ground and air receivers.

The correlation functions for the lead and lag waveforms are

$$\begin{aligned} R_{lag}(\tau) &= \left\langle x_{lag}(t), x_{nom}(t-\tau) \right\rangle \\ R_{lead}(\tau) &= \left\langle x_{lead}(t), x_{nom}(t-\tau) \right\rangle = R_{lag}(\tau + \Delta T_C) \\ R_A(\tau, \Delta) &= \begin{cases} R_{lag}(\tau) & \Delta \geq 0 \\ R_{lead}(\tau) & \Delta \leq 0 \end{cases} \end{aligned} \tag{3.5}$$

The next subsection derives closed form expressions for R_{lag} and R_{lead}, and it also shows that R_{lag} is simply a delay of R_{lead}. (Consequently, R_{lead} is an advance of R_{lag}.) As shown, the correlation function for TM A, R_A, is simply set equal to either R_{lag} or R_{lead}.

The correlation functions for the other two threat models, TM B and TM C (shown in Figure 3-5 and Figure 3-7) are given by

$$R_B(\tau, \sigma, f_d) = h_{2nd}(\tau, \sigma, f_d) * R_{nom}(\tau) \tag{3.6}$$

and

$$R_C(\tau, \sigma, f_d, \Delta) = \begin{cases} h_{2nd}(\tau, \sigma, f_d) * R_{lag}(\tau) & \Delta \geq 0 \\ h_{2nd}(\tau, \sigma, f_d) * R_{lead}(\tau) & \Delta \leq 0 \end{cases} \tag{3.7}$$

where * denotes convolution. Closed form expressions for R_B and R_C are also derived below.

3.5.1 Threat Model A Correlation Function

Threat Model A has only one parameter (Δ), which is the lead $(\Delta < 0)$ or lag $(\Delta > 0)$ of the falling edge of the positive chips in the C/A code. The corresponding correlation function (for a lag) is given by

$$\begin{aligned} R_{\text{lag}}(\tau) &\equiv \left\langle x_{\text{lag}}(t), x_{\text{nom}}(t-\tau) \right\rangle \\ &= \left\langle x_{\text{lag}}(t) - x_{\text{nom}}(t) + x_{\text{nom}}(t), x_{\text{nom}}(t-\tau) \right\rangle \\ &= \left\langle x_{\text{lag}}(t) - x_{\text{nom}}(t), x_{\text{nom}}(t-\tau) \right\rangle + \left\langle x_{\text{nom}}(t), x_{\text{nom}}(t-\tau) \right\rangle \\ &= \left\langle x_{\text{lag}}(t) - x_{\text{nom}}(t), x_{\text{nom}}(t-\tau) \right\rangle + R_{\text{nom}}(\tau) \end{aligned} \tag{3.8}$$

The lagging edge shown in Figure 3-12 causes the perturbation, $x_{\text{lag}}(t) - x_{\text{nom}}(t)$. Figure 3-12 also shows the perturbation caused by a leading edge $\left(x_{\text{lead}}(t) - x_{\text{nom}}(t)\right)$.

The correlation between the lag perturbation and the nominal waveform (plotted in Figure 3-11) combines with the nominal correlation function to yield $R_{\text{lag}}(\tau)$ as shown in Figure 3-12. The corresponding equation is

$$R_{\text{lag}}(\tau) = \begin{cases} 0 & \tau \le -T_C \\ \frac{N}{2}(\tau + T_C) & -T_C < \tau \le -T_C + \Delta T_C \\ N\tau + NT_C(1 - \Delta/2) & -T_C + \Delta T_C < \tau \le 0 \\ NT_C(1 - \Delta/2) & 0 < \tau \le \Delta T_C \\ -N\tau + NT_C(1 + \Delta/2) & \Delta T_C < \tau \le T_C \\ \frac{-N}{2}(\tau - T_C(1+\Delta)) & T_C < \tau \le T_C + \Delta T_C \\ 0 & T_C + \Delta T_C < \tau \end{cases} \tag{3.9}$$

If the falling edge lags by Δ, then the correlation function acquires a flat top, or plateau, with width Δ and the resulting discriminator function has a dead zone with width Δ.

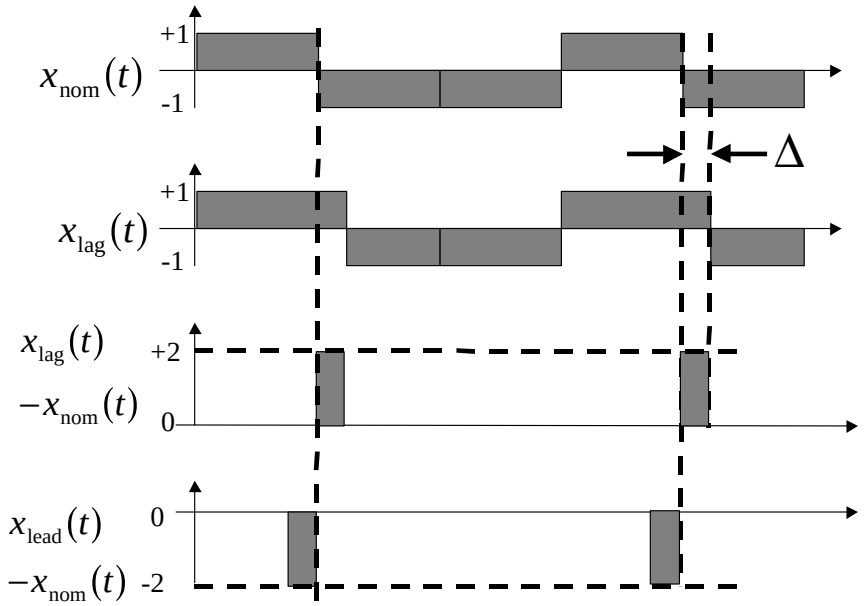

Figure 3-11 Difference Between Nominal Signal and Signals with Lead and Lag

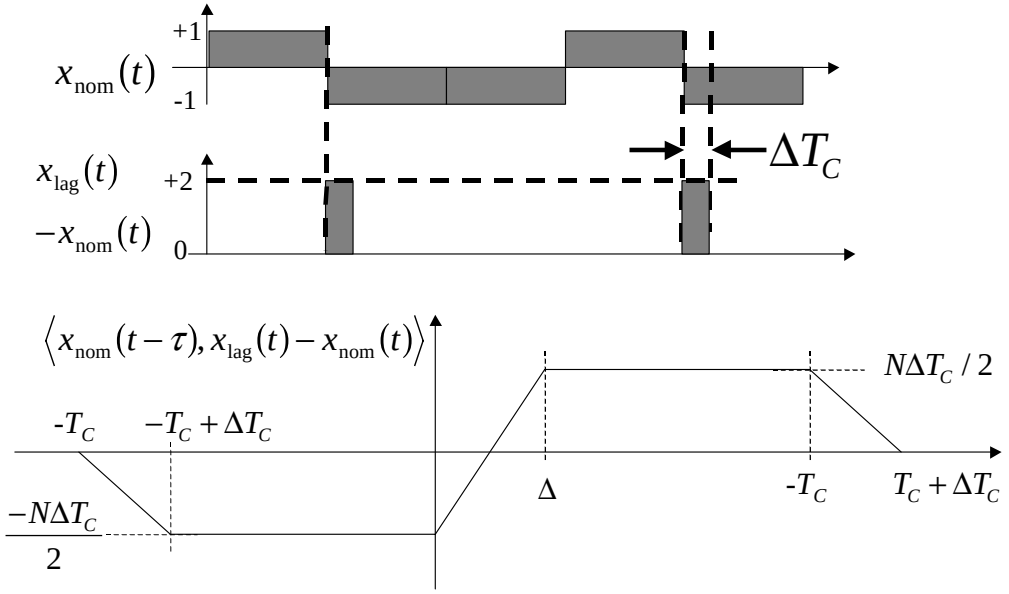

Figure 3-12 Correlation Between Nominal Signal and Lag Difference Signal

The process outlined above for the lag perturbation can also derive the correlation function for the lead perturbation ($R_{\text{lead}}(\tau)$). Figure 3-11 and 3-12 summarize this derivation and

imply that the correlation for lead is simply a time advance of the correlation for lag $\left(R_{\text{lead}}(\tau) = R_{\text{lag}}\left(\tau + \Delta T_C\right)\right)$. (Note also that the amplitude of the lead "pulse," or difference, is the same as for the lag but with the opposite sign.) This time shift appears both at the reference receiver and the airborne receiver, and so it may be ignored, as differential processing removes this difference. The HMI effects generated by either lead or lag are adequate to characterize both, and $R_{\text{A}}(\tau, \Delta)$ may be set to either.

3.5.2 Threat Model B Correlation Function

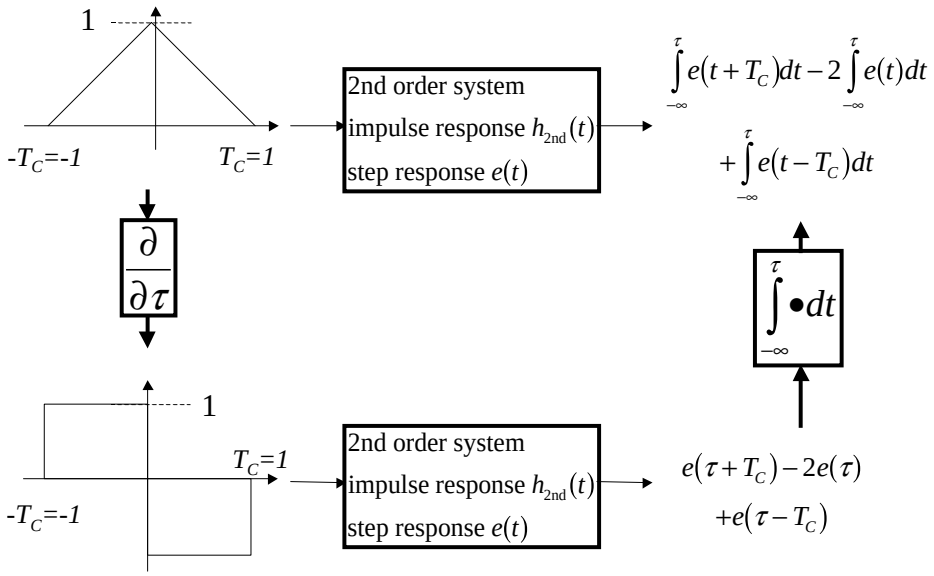

Figure 3-13 Nominal Correlation Peak and Its Derivative

As shown in Figure 3-6, TM B models the degraded satellite subsystem as a linear system dominated by a pair of poles located at $\sigma \pm j2\pi f_d$. Figure 3-13 illustrates the strategy to find R_{B}. The derivative of R_{nom} is input to the second order system and the resulting step response is integrated to find the response to R_{B}. The derivative and its response are given by

$$\frac{\partial R_{\text{nom}}(\tau)}{\partial \tau} = u\left(\tau + T_C\right) - 2u\left(\tau\right) + u\left(\tau - T_C\right) \tag{3.10}$$

$$h_{2\text{nd}}(\tau) * \frac{\partial R_{\text{nom}}(\tau)}{\partial \tau} = e(\tau + T_C) - 2e(\tau) + e(\tau - T_C) \tag{3.11}$$

The correlation function of interest, R_B, is the integral of this last expression and is simply

$$R_B(\tau, \sigma, f_d) = h_{2\text{nd}}(\tau, \sigma, f_d) * R_{\text{nom}}(\tau) = E\big|_0^{\tau+T_C} - 2E\big|_0^{\tau} + E\big|_0^{\tau-T_C} \tag{3.12}$$

where E is the integral of the unit step response (Equation (3.1)) given by

$$\begin{aligned} E(t) &= \int_0^t e(\alpha) d\alpha \\ &= \begin{cases} 0 & t \le 0 \\ t - \dfrac{2\sigma}{\sigma^2 + \omega_d^2} + \dfrac{\exp(-\sigma t)}{\sigma^2 + \omega_d^2}\left[2\sigma \cos \omega_d t + \left(\dfrac{\sigma^2}{\omega_d} - \omega_d \right) \sin \omega_d t \right] & t \ge 0 \end{cases} \end{aligned} \tag{3.13}$$

3.5.3 Threat Model C Correlation Function

TM C passes $x_{\text{lead}}(t)$ or $x_{\text{lag}}(t)$ through the second order system and has three parameters (σ, f_d, Δ). The same strategy that was used for R_B may be used to find R_C. In this case,

$$\begin{aligned} \frac{\partial R_{\text{lag}}(\tau)}{\partial \tau} = \frac{\partial R_{\text{lead}}(\tau)}{\partial \tau} &= \frac{1}{2}u(\tau + T_C) + \frac{1}{2}u(\tau + T_C - \Delta) - u(\tau) \\ &\quad - u(\tau - \Delta) + \frac{1}{2}u(\tau - T_C) + \frac{1}{2}u(\tau - T_C - \Delta) \end{aligned} \tag{3.14}$$

$$\begin{aligned} h_{2\text{nd}}(\tau) * \frac{\partial R_{\text{lag}}(\tau)}{\partial \tau} = h_{2\text{nd}}(\tau) * \frac{\partial R_{\text{lead}}(\tau)}{\partial \tau} &= \frac{1}{2}e(\tau + T_C) + \frac{1}{2}e(\tau + T_C - \Delta) \\ &\quad - e(\tau) - e(\tau - \Delta) + \frac{1}{2}e(\tau - T_C) + \frac{1}{2}e(\tau - T_C - \Delta) \end{aligned} \tag{3.15}$$

The responses due to the original correlation functions are the integrals of these step responses.

$$R_{\mathrm{C}}(\tau,\sigma,f_d,\Delta) = h_{\mathrm{2nd}} * R_{\mathrm{lag}} = \frac{1}{2}E\big|_0^{\tau+T_C} + \frac{1}{2}E\big|_0^{\tau+T_C-\Delta} - E\big|_0^{\tau} - E\big|_0^{\tau-\Delta} + \frac{1}{2}E\big|_0^{\tau-T_C} + \frac{1}{2}E\big|_0^{\tau-T_C-\Delta} \tag{3.16}$$

where E is still given by Equation (3.13). Note that this expression is also valid for TM B ($\Delta = 0$). In addition, the lead response is still a time shift of the lag response. Accordingly, TM C need only consider either lead or lag failures alone.

3.6 Signal Quality Monitoring (SQM)

To date, a satellite failure like SV19 has only occurred once. However, recall that LAAS (Category 1 Precision Approach) requires that a user have a vertical error less than 10 meters. In addition, it specifies a total "time to alarm" (TTA) of 6 seconds. In other words, if, while attempting to land, an airplane's vertical errors ever exceed 10 meters, the LAAS ground facility (LGF) must detect this potentially hazardous condition within $\mathrm{TTA}_{\mathrm{lgf}}$ of 3 seconds. This provides the user an additional 3 seconds to receiver, process, and respond to the alarm message. These requirements, in addition to the *unknown, nonzero probability of a future satellite failure* means some kind of signal quality monitoring is needed.

Differential GPS alone is unable to correct for the pseudorange errors caused by these failures. In general, the receiver configurations of the airborne user and the reference station are not the same. Differences in receiver precorrelation filter and code tracking loop implementations may result in tracking errors that cannot be corrected using differential GPS. Figure 3-14 illustrates this for the case of a distorted correlation peak, being tracked using different correlator spacings (multiple correlator pairs). The asymmetry of the peak could induce significant error for some receivers, and cause relatively small errors for others.

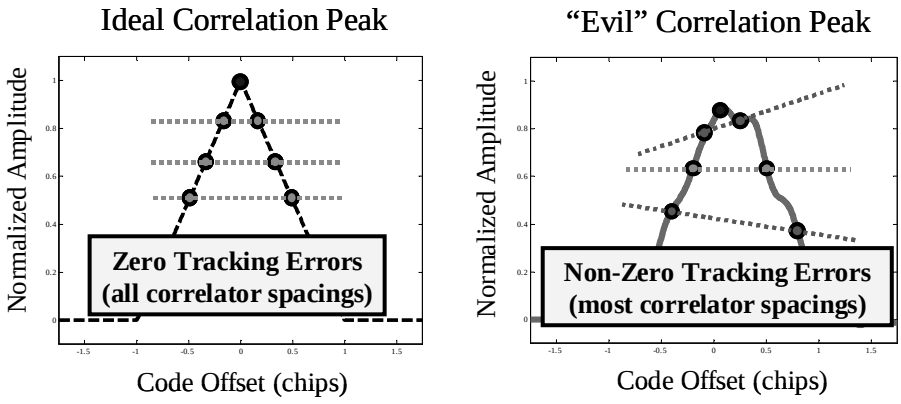

Figure 3-14 Effects of Evil Waveforms on Received Correlation Peaks

3.6.1 Receiver Autonomous Integrity Monitoring (RAIM)

In the presence of EWFs, the code tracking (or pseudorange) error state at the reference station receiver does not necessarily indicate the level of the error experienced by the users. Recall that if the ground and airborne receivers were configured identically, EWFs would not induce any pseudorange errors for LAAS users. Receiver manufacturers and users, however, design and select their receivers based on more than the EWF threat. Hence, LAAS cannot constrain the airborne users to use the same receiver configuration as the LGF.

Consistency checks—comparing position solutions with and without a potentially "failed" satellite—may be a practical form of monitoring for some applications. An example of this is a form of Receiver Autonomous Integrity Monitoring (RAIM). This would entail placing receivers of various configurations at the LGF to monitor and compare the pseudorange and position observables. For SQM, however, this approach would require a large number of receivers. Alternatively, if the airborne receivers were to perform these checks themselves, it would place the difficult and costly burden of integrity monitoring on the users.

3.6.2 Multicorrelator Techniques

Multicorrelator signal processing techniques provide a more practical means of safeguarding user integrity against evil waveforms. They can be performed using a single receiver located at a single reference station. (Note that for redundancy both LAAS and WAAS reference stations come equipped with multiple receivers.) The reference station hardware and equipment may have greater complexity and cost; however, there are substantially fewer reference stations than there are would-be users. Since the FAA must certify all avionics and landing hardware, and the LGF and/or manufacturers must, install, check, and maintain this equipment for proper operation, the cost savings could be substantial.

Chapter 4:

Multicorrelator Techniques for EWF Detection

Signal quality monitoring is best performed using multiple correlators to detect anomalous asymmetries of the correlation peak. Section 4.1 discusses two multicorrelator SQM techniques and introduces several test metrics for detecting EWFs. Section 4.2 analyzes the Minimum Detectable Errors (MDEs) and thresholds that ultimately determine the sensitivity of the detection metrics.

4.1 Symmetry Tests

Multiple receiver correlators can be used to detect EWFs. Using observables obtained from these measurements, GPS receivers can perform symmetry tests on the nominal correlation peak of a received signal. Recall that the ideal, infinite bandwidth correlation peak, $R(\tau)$, is perfectly symmetric independent of receiver correlator spacings, d_m. As observed from the previous sections, EWFs make the peak asymmetric. SQM aims to detect these asymmetries.

The precorrelation filter itself, however, also distorts the correlation peak. In fact, $\tilde{R}(\tau)$—the precorrelation filtered correlation peak—is in general asymmetric. This asymmetry does not introduce errors for either standard GPS users (e.g., reference stations alone) or for differential users (e.g., the aircraft using LAAS) since the errors are common across all satellites. (Recall from Chapter 1, Section 1.1 that such common-mode errors are interpreted as clock bias errors, and do not affect the position solution accuracy.) This asymmetry, however, could impede the detection capability of multicorrelator signal quality monitors. Assuming the mean, nominal symmetry test outputs for each correlator (and receiver), may be estimated and stored, these values may be subtracted from the respective real-time measurements to make the monitor more sensitive to EWFs. (Section 4.2.2 describes how to remove these effects.)

In addition, SQM must be performed in the presence of the nominal distortion of the correlation peak caused by a combination of multipath and thermal noise. Using measurements from live satellite and statistical analyses, the nominal errors introduced by multipath and noise may be quantified. These quantities determine the minimum detectable EWF-induced errors (MDEs) on the correlation peak by a particular multicorrelator symmetry test. Section 4.3 describes the computation of the MDEs in greater detail.

The following two sections discuss the two primary observables used in multicorrelator SQM techniques: pseudorange (tracking error) differences and correlator values.

4.1.2 Pseudorange Differences

If multiple correlator pairs (each with a different early-to-late correlator spacing, *d*) are used independently to track the correlation peak, a single receiver may compute correlation peak symmetry tests in the pseudorange domain. Differences between pairs of measurements may form pseudorange differences, $\Delta\tau(d_1, d_2)$; one independent pseudorange measurement corresponds to each correlator pair. For a nominal incoming signal, $\Delta\tau_{\text{nom}}(d_1, d_2)$ is computed as follows:

$$\Delta\tau_{\text{nom}}\left(d_1,d_2\right)=\tau_{\text{nom}}\left(d_1\right)-\tau_{\text{nom}}\left(d_2\right) \tag{4.1}$$

where

$$\tau_{\text{nom}}\left(d\right)=\arg_{\tau}\left\{\tilde{R}_{\text{nom}}\left(\tau+d/2\right)-\tilde{R}_{\text{nom}}\left(\tau-d/2\right)=0\right\} \tag{4.2}$$

and the filtered correlation peak, $\tilde{R}_{\text{nom}}$, is defined as

$$\tilde{R}_{\text{nom}}=h_{\text{pre}}*R_{\text{nom}} \tag{4.3}$$

In contrast, $\Delta\tau_{\text{a}}\left(d_1,d_2\right)$ represents the pseudorange differences measured in real-time while tracking the anomalous waveform. It is defined analogously to Equation (4.1) as

$$\tau_{\text{a}}\left(d\right)=\arg_{\tau}\left\{\tilde{R}_{\text{a}}\left(\tau+d/2\right)-\tilde{R}_{\text{a}}\left(\tau-d/2\right)=0\right\} \tag{4.4}$$

where $\tilde{R}_{\text{a}}\in\left\{h_{\text{pre}}*R_{\text{A}},h_{\text{pre}}*R_{\text{B}},h_{\text{pre}}*R_{\text{C}},\right\}$. In these equations, the subscripts "*nom*" and "*a*" denote nominal and anomalous measurements, respectively.

For each independent pseudorange difference, the (constant) nominal values subtract from the anomalous ones and are normalized by the corresponding minimum detectable error (MDE). (MDEs are defined and discussed in greater detail in Section 4.2.) Once performed, assuming C_p independent correlator pairs (C_p-*1* independent pseudorange differences) are used, the SQM detectability metric, β_{PR}, becomes

$$\beta_{PR}=\max\begin{bmatrix}\dfrac{\Delta\tau_{\text{a}}\left(d_1,d_2\right)-\Delta\tau_{\text{nom}}\left(d_1,d_2\right)}{MDE\left(d_1,d_2\right)}\\ \dfrac{\Delta\tau_{\text{a}}\left(d_1,d_3\right)-\Delta\tau_{\text{nom}}\left(d_1,d_3\right)}{MDE\left(d_1,d_3\right)}\\ \vdots\\ \dfrac{\Delta\tau_{\text{a}}\left(d_1,d_C\right)-\Delta\tau_{\text{nom}}\left(d_1,d_C\right)}{MDE\left(d_1,d_C\right)}\end{bmatrix}\geq 1 \tag{4.5}$$

Accordingly, an EWF is only detectable when β_{PR} (i.e., at least one of the symmetry tests in Equation (4.5)) is greater than unity.

As stated previously, a signal quality monitor based on pseudorange differences requires that all the monitor correlator pairs track the satellite signal independently. Most GPS receivers, however, possess only a single independent tracking loop per channel. As a result, performing SQM using pseudorange difference measurements requires multiple receivers. Provided each receiver is configured with a different correlator spacing, the number of independent pseudorange differences possible would equal the number of receiver pairs available. Clearly, if the number of differences required is very large, this option becomes both costly and complex.

4.1.2 Correlator Values

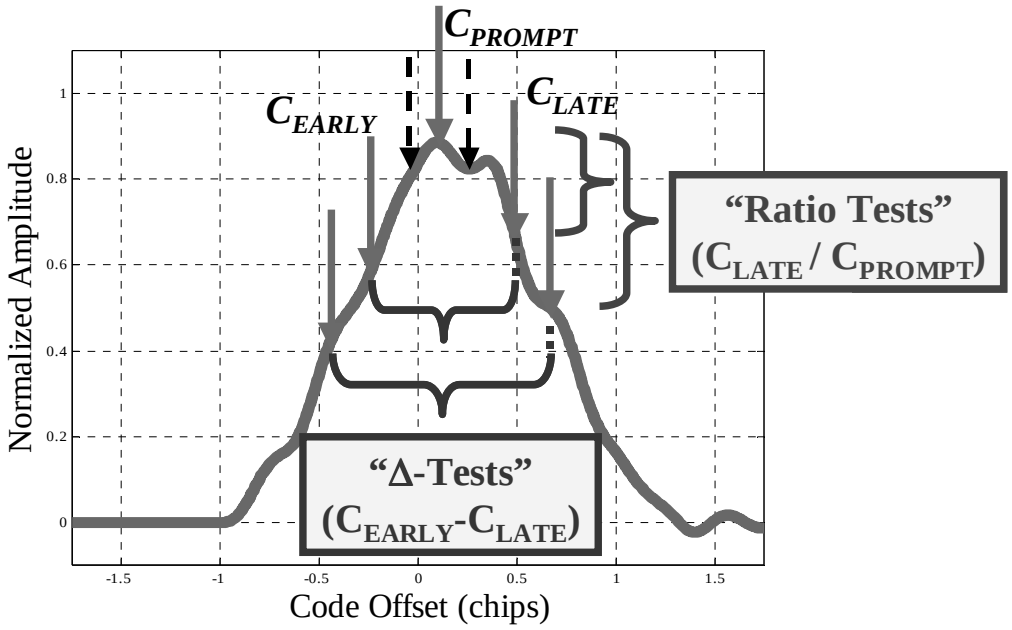

Figure 4-1 Multicorrelator Symmetry Tests for Detecting Evil Waveforms Using Correlator Values

A more practical SQM approach utilizes the actual correlator values output form a receiver that possesses multiple correlators per channel. Provided the total number of correlator pairs is reasonable (from a cost standpoint), this approach is preferable to using

pseudorange differences. (See Section 5.5 of Chapter 5.) In this configuration, only a single correlator pair (per receiver channel) tracks the correlation peak. The other correlator pairs, or monitors, remain at fixed offsets relative to the tracking pair. Conventional pseudorange measurements are derived only from the tracking pair. (Recall that the tracking loop attempts to null the difference between each correlator value for this pair. The monitor pairs serve only to measure the distortion of the correlation peak, relative to the tracking pair.)

Delta Tests

The first configuration of correlator measurements is referred to as a "delta test" (Δ-test). A simple E-L correlator value difference—the difference of the two measurements output from each correlator in a correlator pair—forms a Δ-test given by the following equations:

$$\Delta_m = \tilde{R}\left(\tau\left(d_{\text{ref}}\right) - d_m / 2\right) \tag{4.6}$$

$$\tau\left(d_{\text{ref}}\right) = \arg_{\tau}\left\{\tilde{R}\left(\tau + d_{\text{ref}} / 2\right) - \tilde{R}\left(\tau - d_{\text{ref}} / 2\right) = 0\right\} \tag{4.7}$$

(Refer to Figure 4-1.) Assuming the carrier loop is completely phase-locked, all the quadrature samples of the code loop are negligible ($Q \approx 0$). The delta test correlator measurements may then be expressed solely in terms of the in-phase samples, *I*, as

$$\Delta_m = \frac{\tilde{I}_{early,m} - \tilde{I}_{late,m}}{2 \cdot \tilde{I}_{prompt}} \tag{4.8}$$

$\tilde{I}_{early,m}$, $\tilde{I}_{late,m}$, and $\tilde{I}_{prompt}$ correspond to the (filtered) $\tilde{R}\left(\tau_{ref} - d/2\right)$, $\tilde{R}\left(\tau_{ref} + d/2\right)$, and $\tilde{R}\left(\tau_{ref}\right)$ correlator values for correlator pair *m*, respectively. Note that the I_{prompt} measurement normalizes the ideal correlation peak to have a maximum value of one. The factor of 2 is the slope of the discriminator function (the discriminator gain) for the ideal peak with a correlator spacing, $d = 1T_c$. This factor effectively translates the early-minus-late difference, Δ, into an equivalent change in tracking error or pseudorange. In fact, using

correlator values is in many ways equivalent to using pseudorange differences. (Appendix C discusses SQM for WAAS, which uses pseudorange differences to detect peak asymmetries.)

Assuming a total of C_p correlator pairs per channel, C_p-1 delta tests may be formed. After removing the nominal filter effects and normalizing by the appropriate MDEs, the detectability, γ_Δ, is then given by

$$\gamma_\Delta = \max \left[\begin{array}{c} \dfrac{\left(\Delta_{\mathrm{a},1} - \Delta_{\mathrm{a},ref}\right) - \left(\Delta_{\mathrm{nom},1} - \Delta_{\mathrm{nom},ref}\right)}{MDE\left(\Delta_{1,ref}\right)} \\ \dfrac{\left(\Delta_{\mathrm{a},2} - \Delta_{\mathrm{a},ref}\right) - \left(\Delta_{\mathrm{nom},2} - \Delta_{\mathrm{nom},ref}\right)}{MDE\left(\Delta_{2,ref}\right)} \\ \vdots \\ \dfrac{\left(\Delta_{\mathrm{a},C\text{-}1} - \Delta_{\mathrm{a},ref}\right) - \left(\Delta_{\mathrm{nom},C\text{-}1} - \Delta_{\mathrm{nom},ref}\right)}{MDE\left(\Delta_{C\text{-}1,ref}\right)} \end{array} \right] \geq 1 \tag{4.9}$$

The delta test detects any EWF that makes γ_Δ greater than one.

Ratio Tests

Ratio tests attempt specifically to detect the presence of deadzones (flat correlation peaks) and abnormally sharp or elevated correlation peaks. These tests are computed using the ratios of the correlator value measurements ($\tilde{I}_{early,m}$ and $\tilde{I}_{late,m}$) to $\tilde{I}_{prompt}$ as illustrated in Figure 4-1. (Note that as with the delta tests, these relations implicitly assume coherent code tracking.) For a receiver that has a true prompt correlator available, the average ratio tests are defined as

$$\mathrm{R}_{avg,\,P} \equiv \frac{I_{early} + I_{late}}{2 \cdot I_{prompt}} \tag{4.10}$$

Without a true prompt measurement, a pair of correlators with very narrow spacing, *d*, may still form the ratios. Denoting the narrowly spaced correlator measurements, $\tilde{I}_{early,n}$ and $\tilde{I}_{late,n}$, the average ratio test equation becomes

$$\mathrm{R}_{avg_m,\, avg_n} \equiv \frac{I_{early,m} + I_{late,m}}{I_{early,n} + I_{late,n}} \tag{4.11}$$

For increased sensitivity to distortions affecting only a single side of the correlation peak, individual correlator values may also be used to form single-sided tests. With an available prompt correlator, these tests may be expressed as

$$\mathrm{R}_{early_m,\, prompt} \equiv \frac{I_{early_m}}{I_{prompt}} \tag{4.12}$$

and

$$R_{late_m,\, prompt} \equiv \frac{I_{late_m}}{I_{prompt}} \tag{4.13}$$

for the early and late correlator values, respectively. For C_p correlator pairs in a given receiver channel, the combined average and single-sided ratios permit a total of $3C_p$ independent tests.

Without a prompt, the same tests are computed as

$$\mathrm{R}_{early_m,\, avg_n} \equiv \frac{2 \cdot I_{early_m}}{I_{early_n} + I_{late_n}} \tag{4.14}$$

and

$$\mathrm{R}_{late_m,\, avg_n} \equiv \frac{2 \cdot I_{late_m}}{I_{early_n} + I_{late_n}} \tag{4.15}$$

yielding a total number of $3C_p$-1 ratio tests.

Accounting for the nominal (filtered) ratio values and normalizing by the corresponding MDEs yields the following for the ratio test EWF detectability, γ_R:

$$\gamma_R = \max_{t=1,2,3} \begin{bmatrix} \dfrac{\left({}_t\mathrm{R}_{a,1} - {}_t\mathrm{R}_{nom,1}\right)}{MDE\left(\mathrm{R}_1\right)} \\ \dfrac{\left({}_t\mathrm{R}_{a,2} - {}_t\mathrm{R}_{nom,2}\right)}{MDE\left({}_t\mathrm{R}_2\right)} \\ \vdots \\ \dfrac{\left({}_t\mathrm{R}_{a,C} - {}_t\mathrm{R}_{nom,C}\right)}{MDE\left({}_t\mathrm{R}_C\right)} \end{bmatrix} \geq 1 \qquad (4.16)$$

where *t = 1, 2,* 3 corresponds to the *average*, *early*, and *late* ratio tests, respectively. An EWF is detected if it causes any of these tests to exceed unity.

4.2 Minimum Detectable Errors

Minimum detectable errors (MDEs) are the amount of correlation peak distortion or variation required to guarantee a given symmetry test will detect the EWF with a probability of false alarm less than $1.5\text{x}10^{-7}$ (per test decision per critical satellite), and a missed detection probability of 10^{-3}. The one-sided missed detection probability is given for a Category I precision approach interval of 150 seconds. The false (or fault-free) alarm probability applies to each test decision for each critical satellite. [Van Dierendonck00], [Shively99a], [Shively99b], and [Shively00] provide a detailed explanation of how these values are computed.

To obtain the MDEs, measurement analyses must quantify the standard deviations of each individual symmetry test, or σ_{test}, of the peak due to multipath and thermal noise. The MDEs are simply a multiple of σ_{test} by a constant. That scale factor is the sum of the two multipliers, K_{ffd} and K_{md}, computed to produce the required fault-free detection probability

and false alarm probability, respectively. Accordingly, the equation for computing the MDEs is given by

$$\mathrm{MDE} = \left(\mathrm{K}_{ffd} + \mathrm{K}_{md}\right) \cdot \sigma_{test} \tag{4.17}$$

Assuming the noise and MP variations are gaussian, $\mathrm{K}_{ffd} = 5.26$ yields a fault-free alarm probability less than or equal to $1.5\text{x}10^{-7}$, and $\mathrm{K}_{md} = 3.09$ guarantees a missed-detection probability no greater than 10^{-3}.

The noise is assumed to have a gaussian distribution with a mean of zero. In general multipath does not have zero mean, however, for small multipath—which is typical of reference stations—this assumption is adequate [van Nee92a]. Conversely, the mean values of each multicorrelator symmetry test may be significant and nonzero. Note the delta test biases result from finite precorrelation bandwidth only. The ratio tests have nonzero nominal values even for the infinite bandwidth case. Measurement processing must calibrate and remove these post-correlation biases.

4.2.1 Test Statistic Standard Deviation, σ_{test}

The MDE analysis utilized a combination of theoretical models, simulation and experimental data to compute and validate σ_{test}. For LAAS, it validated this statistic using the pseudorange difference tests [Enge99], [Shively99a], [Akos00a] in addition to the correlator value tests. The ICAO eventually adopted experimental, correlator value-based MDEs as the standard for design of a multicorrelator signal quality monitor.

[Akos00a] measured the actual distortion of the correlation peak due to thermal noise and multipath using Stanford University's (SU) LAAS testbed. A specially configured receiver, equipped with 24 correlator pairs (48 individual correlator measurements) on a single channel, was connected to a single choke-ring antenna atop a building on the campus of SU. This receiver had a double-sided precorrelation bandwidth of 16MHz. Figure 4-2 illustrates the distribution of the correlator pairs along the normalized, filtered correlation

peak. Live data obtained while tracking a single, high-elevation satellite provided correlation peak measurements. Subsequent processing averaged these measurements from up to five separate passes of the same satellite. The "tracking pair" had a $0.1T_c$ spacing, and the prompt (at the peak) was in the center of this pair. All other correlators were kept at fixed offsets from the prompt. Note that the receiver configuration grouped correlators more densely near the peak to obtain more useful σ_{test} measurements at relatively narrow correlator spacings [Akos00a].

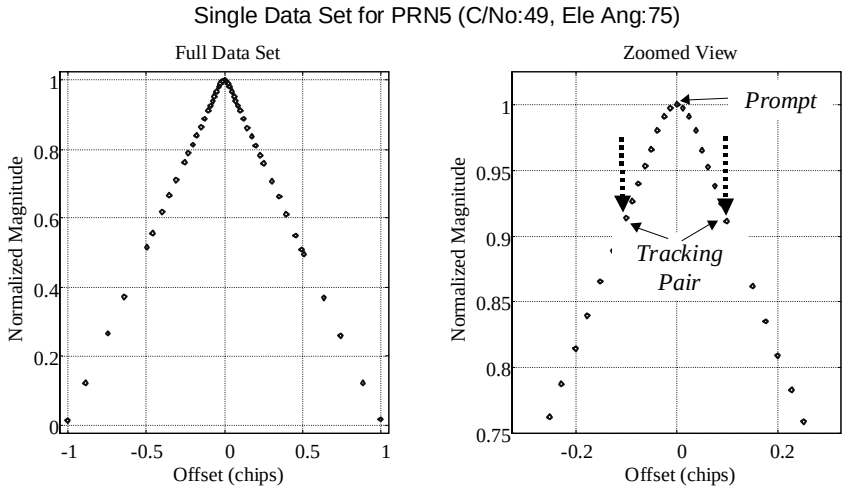

Figure 4-2 Correlation Peak Observation Points for σ_{test} Measurements

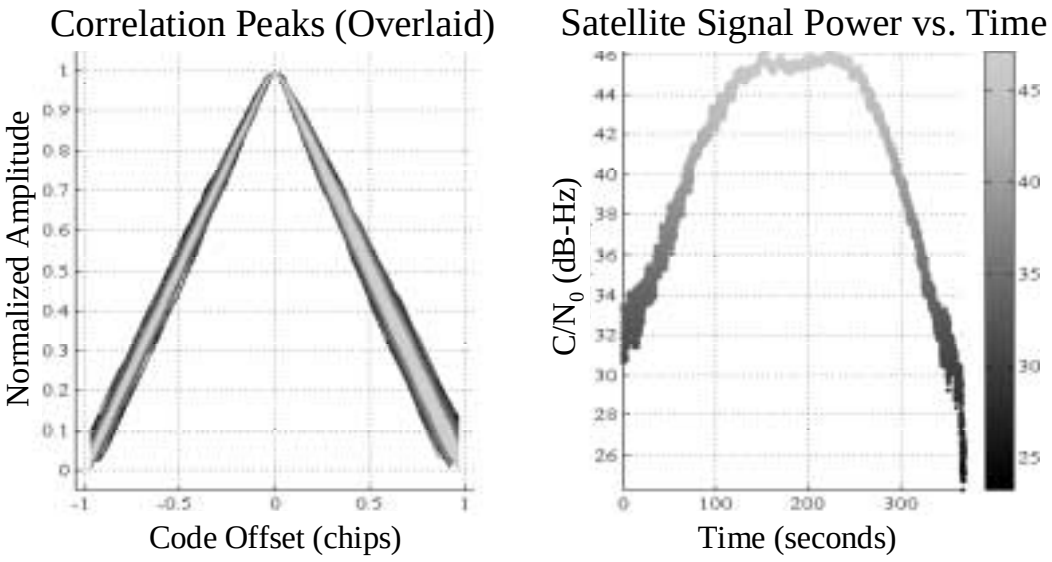

Figure 4-3 Distortion of Received Correlation Peak Due to Multipath (Static Reference Station Data Taken Over a Single Satellite Pass from Live SV)

The analysis first recorded live correlation measurements for various satellites over multiple passes. Figure 4-3 shows the deviations of the (normalized) received correlation peak for a single satellite pass [Akos00b]. The accompanying plot shows the satellite signal power (carrier-to-noise ratio, C/N_0) as a function of time. The light and dark shading corresponds to high-elevation (high signal power) and low-elevation (low signal power) information, respectively.

Figure 4-3 illustrates two key points. First, the largest nominal distortion of the peak occurs when the satellite is at low elevation angles and low signal power. In general, the dispersion of the correlation peak when a satellite is at high elevation is significantly less than the variation of the peak when the same satellite is at low elevation angles. This implies that σ_{test} (and hence, the MDEs) are elevation angle-dependent.

Second, the noise and multipath distortions are smallest near the top of the correlation peak. This implies the MDEs will be smaller for symmetry tests taken near the peak (i.e., with narrow correlator spacings). Indeed [Van Dierendonck92] describes why narrow correlator spacings are used in many modern GPS receivers and details their noise abatement and multipath mitigation capabilities. (Section 5.2 of Chapter 5 discusses these advantages in more detail.) For these reasons [Akos00a] configured the 48-correlator spacing arrangement as pictured above in Figure 4-2.

Sample statistics of the correlation peak variations of three different SV's—corresponding to three different satellite passes—are shown below in Figure 4-4. The figure shows histograms for "late," or right-side-of-peak, correlators only. The first (top-left) histogram corresponds to the late correlator at a code offset of $+0.05T_c$. (This is also the late half of the tracking pair.) The last histogram (bottom-right) is the late correlator at $0.92T_c$. At the top of each plot, two pairs of values are shown. The first pair indicates the code offset and the (expected) ideal normalized amplitude of the function. The second pair gives the mean and vertical standard deviation, respectively, of the correlation peak. Note that the means are nonzero.

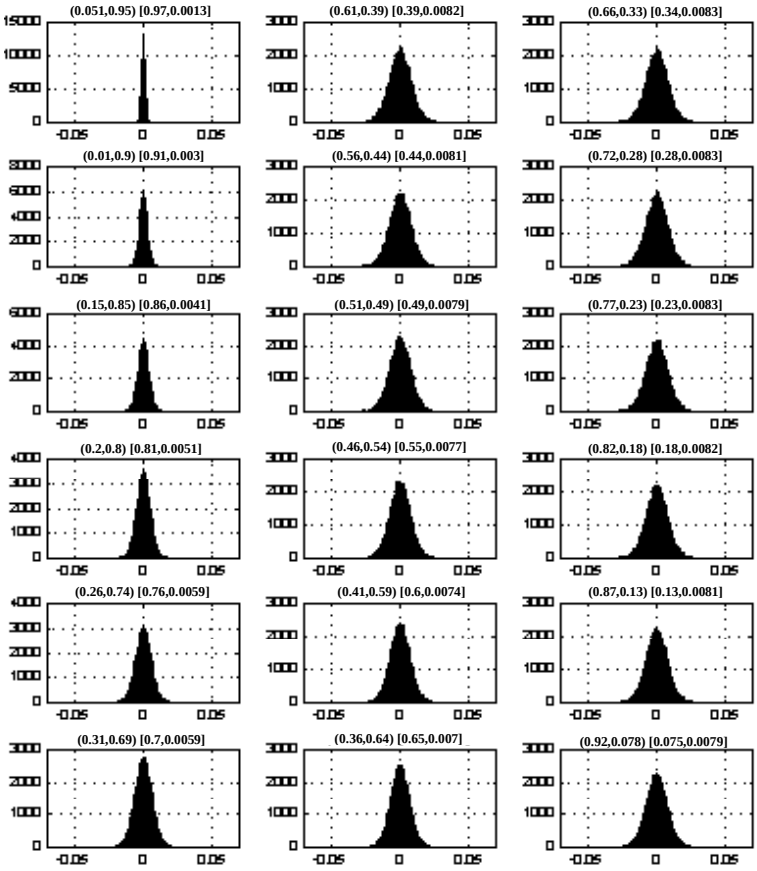

Figure 4-4 Resulting Correlation Peak Measurement Histograms for Three Satellite Passes

4.2.2 Nominal Symmetry Test Biases

Finite Precorrelation Bandwidth (PCBw)

The rounding of the received correlation peak due to finite PCBw is apparent from Figure 4-5. Other more subtle effects of bandlimiting are also evident from the nonzero means of the histograms in Figure 4-4. As stated previously, the precorrelation filter (i.e., finite PCBw) renders the received correlation peak asymmetric. These pre-existing asymmetries can cause σ_{test} to have nonzero mean. Any multicorrelator SQM must record and store the nominal means offline and subsequently subtract them from real-time correlation peak measurements.

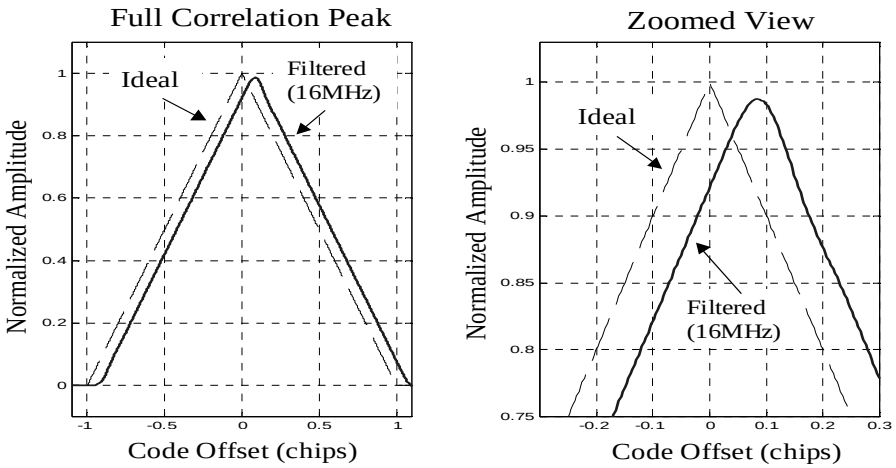

Figure 4-5 Comparison of Ideal and Filtered Correlation Peaks. Precorrelation Filter Model: 6th-order Butterworth (PCBw = 16MHz)

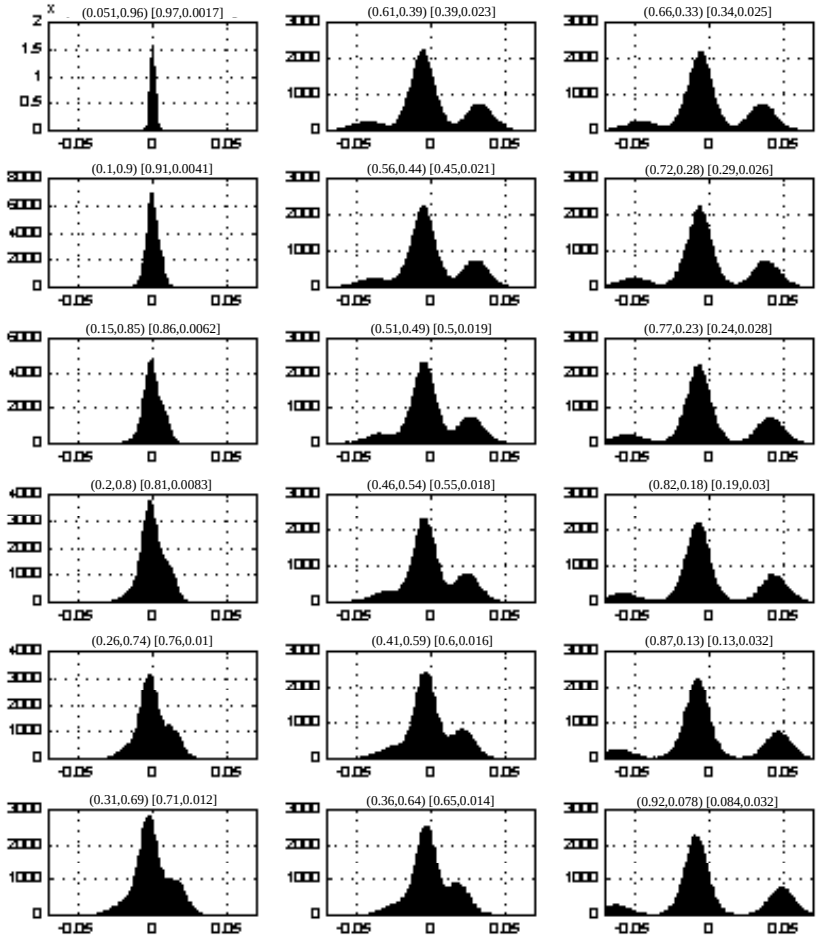

Figure 4-6 Resulting Correlation Peak Measurement Histograms for Five Satellite Passes. (Data for one negative (low) PFSL and one positive (high) PFSL are included in the statistics.)

Peak-flush and Peak-Adjacent Sidelobes

Peak-flush sidelobes (PFSL) are sidelobes of a particular PRN that occur at ±1 chip offset from the main lobe. Accordingly, they appear "flush" against the side (base) of the peak. If unaccounted for, signals from these satellites result in histograms like those pictured in Figure 4-6. For the two satellites shown, the histograms contain significant (positive and negative) biases.

PFSLs modify the nominal, ideal slope of the ideal main peak. Positive (or "high") PFSLs have a nominal (normalized) height of +64/1023. They decrease the slope of the ideal peak, widening it. Negative (or "low") PFSLs are nominally –65/1023. These increase the slope of the main peak and narrow it slightly. An example of this situation is shown below in Figure 4-7. The correlation function for SV8 contains two low PFSLs—one on each side.

Note that peak-adjacent sidelobes (PASLs), conversely, do not modify the ideal correlation peak slope. (See Figure 4-8.) Also, each of these peaks can be modeled using Equation (3.4) from Chapter 3, where b = 64/1023 and b = -65/1023 for the high and low PFSLs, respectively. Of course, for PASLs, b = -1/1023 (as in the ideal case).

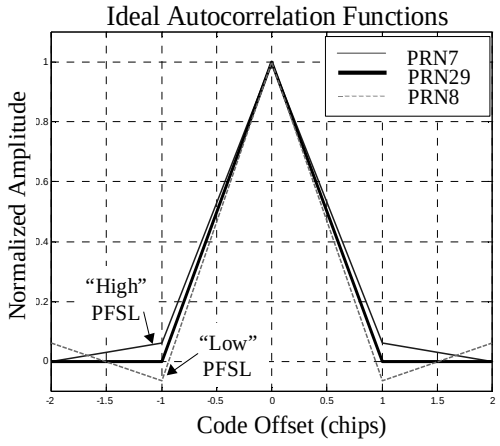

Figure 4-7 Peak-Adjacent Sidelobe (PASL) Correlation Peaks

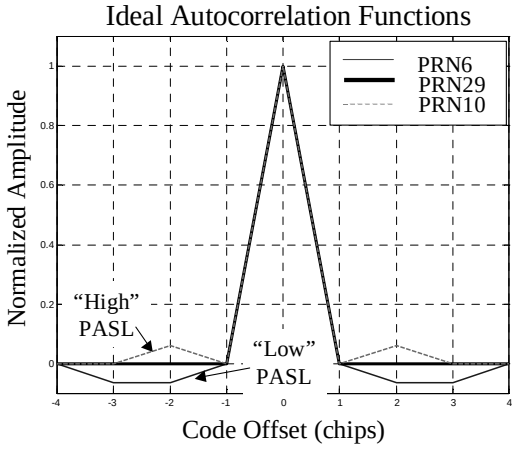

Figure 4-8 Peak-flush Sidelobe (PFSL) Correlation Peaks

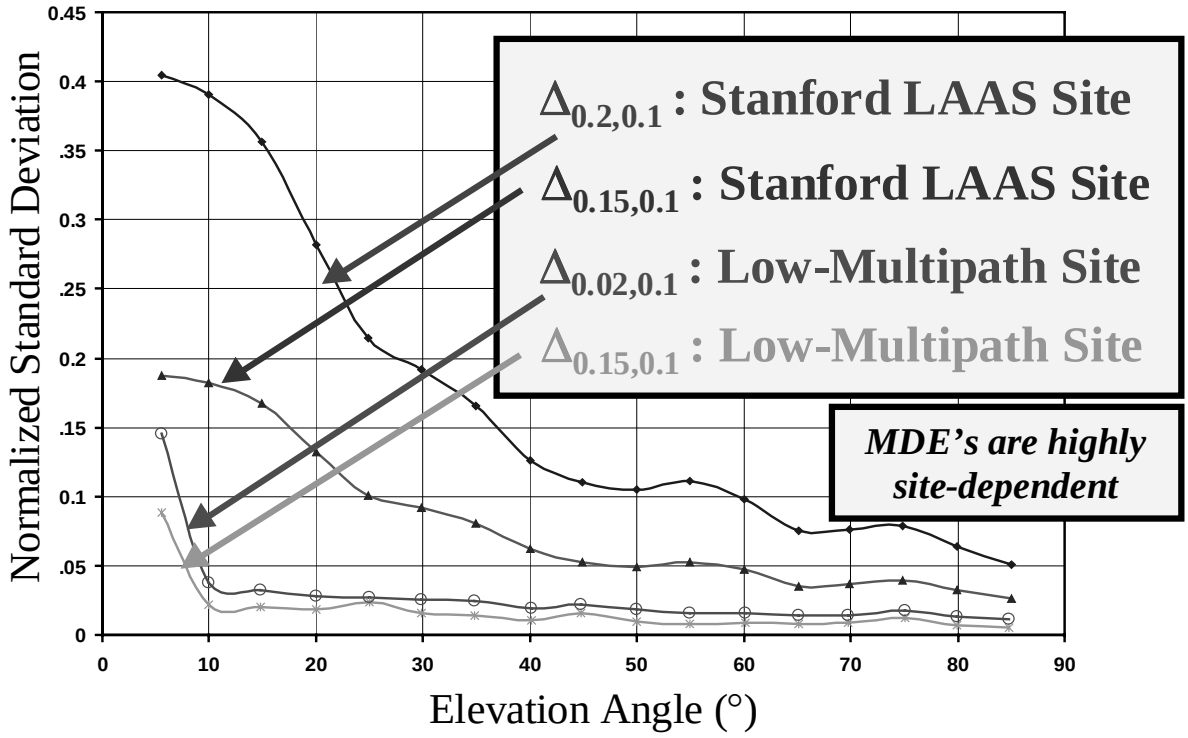

Figure 4-9 Measured Δ-Test Standard Deviations as a Function of Elevation Angle [Van Dierendonck00]

4.2.3 SU MDEs

After accounting for the correlation peak sidelobe effects and precorrelation filter asymmetries, Equations (4.9) and (4.16) compute MDEs for all the delta tests and ratio tests. The analysis used the SU-measured data to obtain σ_{test} (filtered by a 100-tap rectangular window FIR filter—a moving average taken over 100 seconds). [Akos00c] and [Akos00b] validated the MDEs by comparing them to a model for thermal noise and multipath. In addition, these MDEs agreed with data taken by others at an actual airport [Macabiau00c]. The International Civil Aviation Organization (ICAO) has since adopted the SU MDEs as the standard for GPS-LAAS SQM validation.

Standard deviation (σ_{test}) measurements corresponding to two Δ-tests are shown in Figure 4-9. The top two curves represent the preferred, more conservative data taken at Stanford University. For comparison, the bottom two curves correspond to the same tests, taken at a

relatively multipath-free site. Since only the multipath is site-dependent, its severity may vary significantly from one location to the next. Clearly, multipath is the dominant factor in the determination of the MDEs.

To reduce the influence of site-specific multipath at a given elevation angle, a polynomial may be fit to these MDEs according to

$$\mathrm{MDE} = a_3\theta^3 + a_2\theta^2 + a_1\theta + a_0 \tag{4.18}$$

where

θ = Elevation angle in degrees

a_0, a_1, a_2, a_3 = 3^{rd} –order polynomial coefficients

For any specific symmetry test of interest, once the fit coefficients are obtained, Equation (4.18) above can compute useful MDEs at arbitrary elevation angles. Chapter 5 describes the selection of a multicorrelator SQM and uses this equation to evaluate its detection performance against 2OS EWFs.

Chapter 5:

Robust Signal Quality Monitor Design

A robust signal quality monitor is able to protect airborne users against hazardous EWFs in the presence of noise, multipath and ground-air receiver configuration differences. Recall that noise and multipath distort the received correlation peak and thereby make EWFs more difficult to detect. Receiver configuration differences result in larger differential pseudorange errors, since undetected EWFs affect the ground (reference) differently than the airborne (user) receiver. This chapter provides a methodology for specifying a practical, multicorrelator SQM technique capable of detecting EWFs that cause HMI for the users. Sections 5.1, 5.2, and 5.3 describe the basic performance criteria for the users in terms of maximum EWF-induced range errors and the maximum allowable errors. Section 5.4 describes the standard SQM evaluation plots, metrics, and assumptions used to determine the performance of a particular implementation. Section 5.5 discusses the process used to select a specific multicorrelator SQM—namely SQM2b—for further analysis. Section 5.6 describes the detailed analysis of SQM2b for robustness to variations in satellite elevation angle, user differential group delay, and user precorrelation filter transition bandwidth. In so doing, it describes the ability of SQM2b to protect all E-L receiver configurations along with a compromise made for the few "double-delta" ($\Delta\Delta$) receiver configurations that could not be protected. Section 5.8 addresses the transient

SQM problem and proves that the steady-state multicorrelator SQM design is valid even against these EWF threats.

5.1 SQM Design Analysis Summary

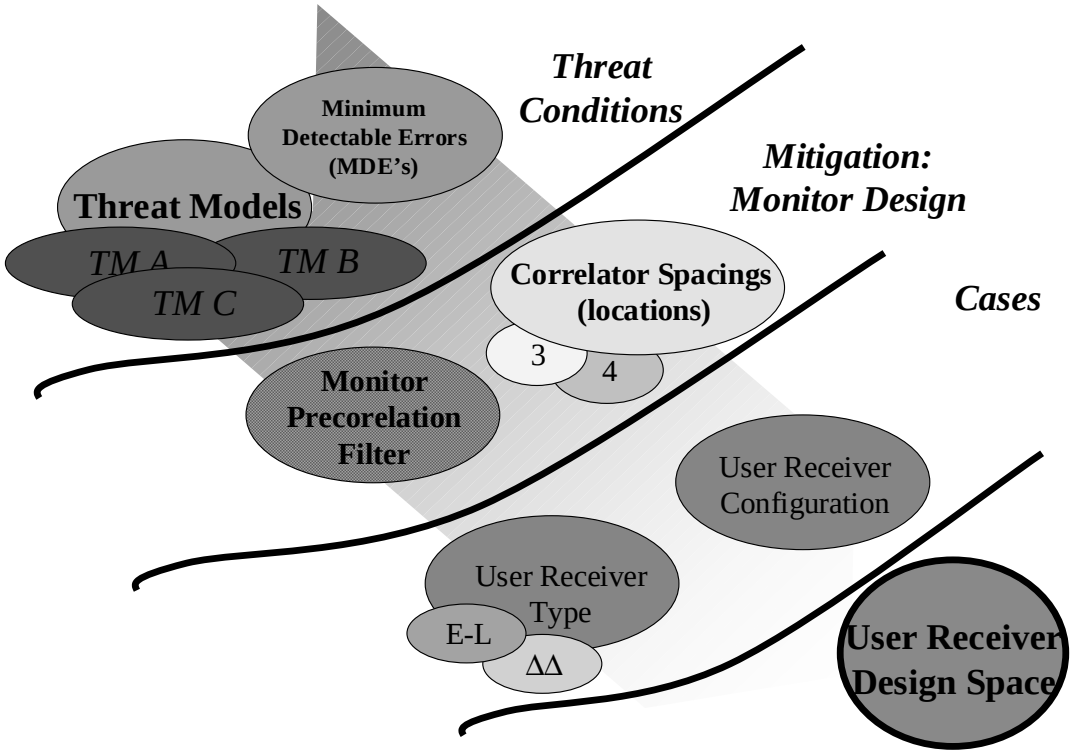

Figure 5-1 The Signal Quality Monitoring Design Problem

Figure 5-1 provides a graphical illustration of the SQM2b design problem. The previous chapter described the threat conditions. It characterized them in terms of the EWF models (Threat Models A, B, and C) and the MDEs. The goal however is to develop a multicorrelator monitoring technique to detect those waveforms that cause HMI for the airborne users. This will result in suggested designs (i.e., placement) of correlator spacings and number of correlator pairs. It may also require analysis and redesign of the monitor receiver precorrelation filter characteristics. Should all practical monitor designs prove incapable of protecting airborne users from this threat, as a last resort, some superfluous configurations will need to be removed from consideration. (Refer to the "notch"

discussion in Sections 5.7.2 and 5.7.3.) This implies that a detailed SQM analysis must evaluate, for each multicorrelator design, the differential pseudorange errors (PREs) for every current and envisioned user receiver configuration. A robust SQM implementation will ensure that errors from undetected points (UDPs) in the threat space remain within acceptable limits in the user design space, and that potentially hazardous EWFs are detected by the monitor and are removed from the user's position solution within the 6-second time-to-alarm (TTA).

The following sections present four analysis methods to design and evaluate a robust signal quality monitor for LAAS. The first compares the maximum differential pseudorange errors (PREs) to the respective maximum tolerable errors for a failed satellite at all elevation angles. The second perturbs (only) the user filter differential group delays, to investigate the sensitivity of those PREs to this variation. A third parameterizes the user filter transition bandwidth to evaluate the sensitivity of the PREs to filter magnitude response variations. Finally, the fourth examines the transient responses of the multicorrelator detection metrics and the differential PREs to ensure the monitor flags detectable EWFs within the 6-second TTA.

This design methodology resulted in several conclusions and recommendations. A practical multicorrelator SQM monitoring implementation—referred to as SQM2b—was proven using all the aforementioned analyses. E-L correlator receivers had no hazardously misleading information (HMI) due to any EWFs for all elevation angles and group delay variations (0-150ns). However, double-delta ($\Delta\Delta$) correlators required a notch in Region 2 to prevent HMI from Threat Model C EWFs at elevation angles >5°. For $\Delta\Delta$ compliance, the following recommendations were made:

- $\Delta\Delta$ Region 2 Notch Parameters: 0.07Tc, 14MHz (lower-right corner)

- Maximum Transition Bandwidth: 6th-order Butterworth

- A single squared delta test (Δ^2-test) should be used in addition to the 11 steady-state tests of Section 5.6 to ensure EWFs are detected within the TTA. (Refer to Section 5.9.)

Based on these analyses and comparable results obtained by STNA [Macabiau00c], the ICAO adopted and certified these recommendations in May of 2000. The new Region 2 for the $\Delta\Delta$ correlators was defined as in Figure 5-135. The rolloff spec was prescribed as a maximum -30dB (single-sided) precorrelation bandwidth of 13MHz, which was taken from the 6th-order Butterworth magnitude characteristic. The sections which follow discuss specifics of the above testing.

5.2 Differential Pseudorange Error (PRE)

Undetected points are denoted $\left\{(\sigma, f_d, \Delta)_n\right\}\Big|_{n=1}^{N}$ and form a subset of the entire threat space. The aircraft pseudorange error is computed for each point in this set as follows

$$\Delta\tau = \left(\tau_{\text{a,air}}\left(d_{\text{air}}\right) - \tau_{\text{a,ref}}\left(d_{\text{ref}}\right)\right) - \left(\tau_{\text{nom,air}}\left(d_{\text{air}}\right) - \tau_{\text{nom,ref}}\left(d_{\text{ref}}\right)\right) \tag{5.1}$$

where, for a standard early minus late receiver code tracking loop,

$$\begin{aligned}
\tau_{\text{a,air}}\left(d\right) &= \arg_{\tau}\left\{\tilde{R}_{\text{a,air}}\left(\tau + d/2\right) - \tilde{R}_{\text{a,air}}\left(\tau - d/2\right) = 0\right\} \\
\tau_{\text{a,ref}}\left(d\right) &= \arg_{\tau}\left\{\tilde{R}_{\text{a,ref}}\left(\tau + d/2\right) - \tilde{R}_{\text{a,ref}}\left(\tau - d/2\right) = 0\right\} \\
\tau_{\text{nom,air}}\left(d\right) &= \arg_{\tau}\left\{\tilde{R}_{\text{nom,air}}\left(\tau + d/2\right) - \tilde{R}_{\text{nom,air}}\left(\tau - d/2\right) = 0\right\} \\
\tau_{\text{nom,ref}}\left(d\right) &= \arg_{\tau}\left\{\tilde{R}_{\text{nom,ref}}\left(\tau + d/2\right) - \tilde{R}_{\text{nom,ref}}\left(\tau - d/2\right) = 0\right\}
\end{aligned} \tag{5.2}$$

and as previously defined in Chapter 3,

$$\begin{aligned}
\tilde{R}_{\mathrm{a,air}} &\in \left\{ h_{\mathrm{air}} * R_{\mathrm{A}}, h_{\mathrm{air}} * R_{\mathrm{B}}, h_{\mathrm{air}} * R_{\mathrm{C}} \right\} \\
\tilde{R}_{\mathrm{a,ref}} &\in \left\{ h_{\mathrm{ref}} * R_{\mathrm{A}}, h_{\mathrm{ref}} * R_{\mathrm{B}}, h_{\mathrm{ref}} * R_{\mathrm{C}} \right\} \\
\tilde{R}_{\mathrm{nom,air}} &= h_{\mathrm{air}} * R_{\mathrm{nom}} \\
\tilde{R}_{\mathrm{nom,ref}} &= h_{\mathrm{ref}} * R_{\mathrm{nom}}
\end{aligned} \tag{5.3}$$

Some airborne users desire receivers with so-called double-delta (ΔΔ) code-tracking loops because of their superior multipath mitigation capabilities. In contrast to the previous expressions, these receivers have a discriminator given by a linear combination of two E-L discriminators according to

$$\tau_{\mathrm{a,air}}\left(d_1, d_2\right) = \arg_{\tau} \left\{ \begin{array}{l} 2 \cdot \left[\tilde{R}_{\mathrm{a,air}}\left(\tau + d_1/2\right) - \tilde{R}_{\mathrm{a,air}}\left(\tau - d_1/2\right) \right] \\ -\left[\tilde{R}_{\mathrm{a,air}}\left(\tau + d_2/2\right) - \tilde{R}_{\mathrm{a,air}}\left(\tau - d_2/2\right) \right] = 0 \end{array} \right\} \tag{5.4}$$

where $d_2 = 2 \cdot d_1$. (An analogous equation applies for the nominal tracking errors.) The two-component correlator spacings, d_1 and d_2, are sometimes referred to as the "wide" and "narrow" correlator spacings of the ΔΔ configuration, where again $d_{wide} = 2 \cdot d_{narrow}$. The ΔΔ correlator spacing limits are specified for d_{narrow} only since this uniquely specifies d_{wide}. The E-L correlator spacing limits place an upper bound on d_{wide} as well as $d_{E\text{-}L}$.

As shown in Equations (5.1) and (5.2), the aircraft's pseudorange error, $\Delta\tau$, contains the aircraft's current measurement, $\tau_{\mathrm{a}}\left(d_{\mathrm{air}}\right)$ minus the current differential correction from the reference receiver on the ground, $\tau_{\mathrm{a}}\left(d_{\mathrm{ref}}\right)$. (In practice, the carrier phase smoothes both these real-time measurements using a Hatch filter with a 100-second time constant.) Note that the resulting error also removes the nominal difference between the aircraft and reference measurements, $\tau_{\mathrm{nom}}\left(d_{\mathrm{air}}\right) - \tau_{\mathrm{nom}}\left(d_{\mathrm{ref}}\right)$, because this common mode term will be present in the corrected measurements for the other satellites. Hence, it will cause (bias) errors in the aircraft's clock estimate but it will not affect the position estimate.

5.3 Performance Criteria

Maximum Error Range Residuals (MERRs) are the largest (differential) pseudorange errors tolerable at the user's location without producing HMI. These bounds are elevation angle-dependent and are derived based on worst-case assumptions for satellite geometry [Shively99b]. LAAS computes the MERRs as a standard deviation of the pseudorange, σ_{pr_lgf}, as measured by the LAAS ground facility. σ_{pr_lgf} is found from [LGFSpec] as

$$\sigma_{pr\_lgf}(\theta) \le c_0 \left(\sqrt{\frac{\left(\mu_0 + \mu_1 e^{-\theta_n / \theta_0} \right)^2}{M}} + (\mu_2)^2 \right) + \varpi_0 \qquad (5.5)$$

In the above expression, θ_n is the elevation angle for the n^{th} ranging source, M is the number of corrections per ranging source, μ_0, μ_1, μ_2, θ_0, ϖ_0, and c_0 are the coefficients for the appropriate ground accuracy designator (GAD) defined below for GPS satellites and SBAS (satellite-based augmentation systems or geostationary satellites) in Table 5-1 and Table 5-2. GAD B corresponds to LAAS Category I precision approach requirements. GAD C coefficients apply to Category II and III landing requirements

GAD B	μ_0 (meters)	μ_1 (meters)	μ_2 (meters)	θ (°)	ϖ_0 (meters)	c_0
GPS	0.16	1.07	0.08	15.5	0	1.0
SBAS	0.16	1.07	0.08	15.5	0.15	1.91

Table 5-1 Ground Accuracy Designator B Coefficients

GAD C	μ_0 (meters)	μ_1 (meters)	μ_2 (meters)	θ (°)	ϖ_0 (meters)	c_0
GPS $\theta_n \ge 35°$	0.15	0.84	0.04	15.5	0	1.0
GPS $\theta_n < 35°$	0.24	0	0.04	-	0	1.0
SBAS $\theta_n \ge 35°$	0.15	0.84	0.04	15.5	0.15	1.91
SBAS $\theta_n < 35°$	0.24	0	0.04	-	0.15	1.91

Table 5-2 Ground Accuracy Designator C Coefficients

Figure 5-2 below plots the MERRs for the GPS satellites as a function of elevation angle, θ, in degrees.

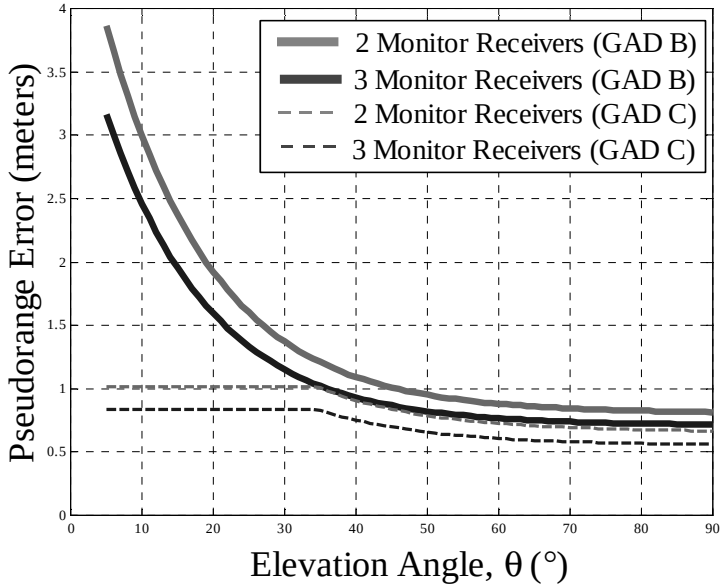

Figure 5-2 Maximum Allowable Errors vs. Elevation Angle for GAD B and C

5.4 User Design Space

If any EWFs are undetectable by a particular multicorrelator SQM configuration (i.e., the measured correlation peak distortion, it becomes necessary to determine their impact on the differential PREs of airborne users. These users may have vastly different receiver configurations since receiver manufacturers desire the freedom to implement both narrow and wide precorrelation bandwidths (PCBws) with narrow and/or wide correlator spacings. As shown in Figure 5-3 and Figure 5-4, the goal for LAAS Category I Precision Approach is to protect an L-shaped region of this two-dimensional user design space using a practical multicorrelator ground SQM scheme.

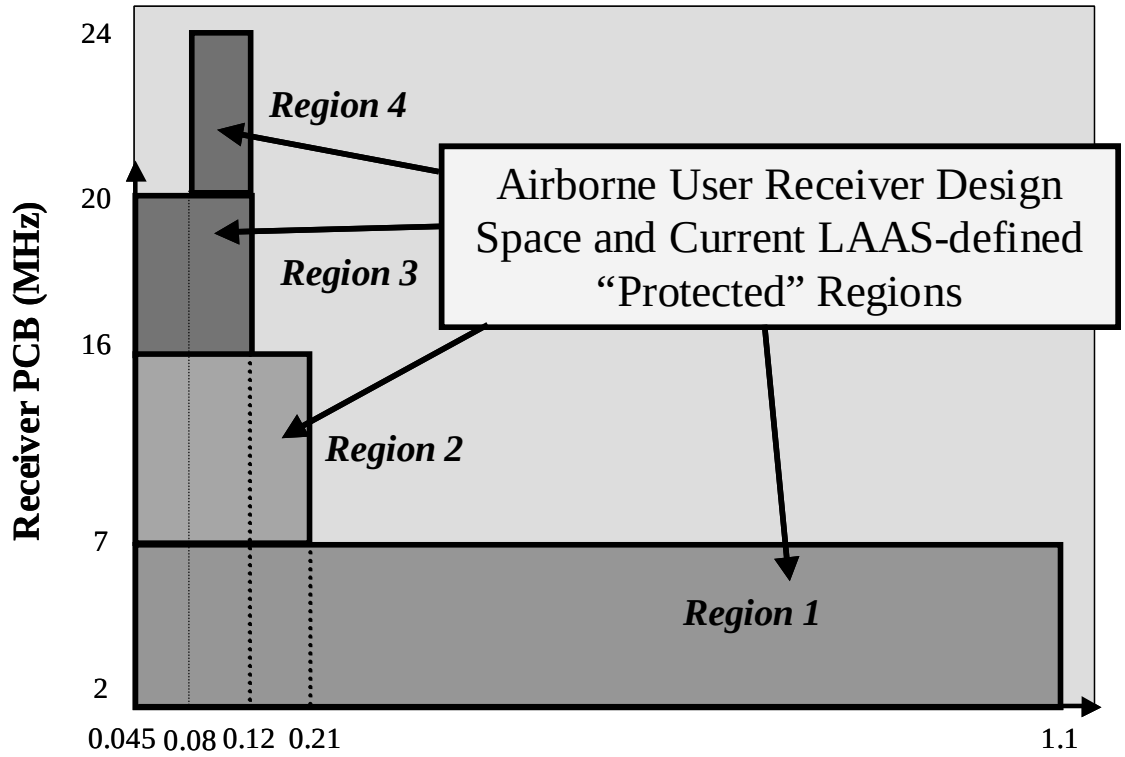

Figure 5-3 Airborne User E-L Receiver Configuration (Design) Space

There are four regions for standard E-L code-tracking loop receiver types (designs). Conversely, for ΔΔ-correlator designs, originally only the two (full) regions shown in Figure 5-4 described the feasible configuration space. As will be described in detail in the following sections, however, a rectangular "notch" was removed from the area of Region 2 of the ΔΔ configurations because the errors for a few configurations proved too difficult to protect using a practical SQM design. (Refer to Sections 5.6.2 and 5.6.3.) Table 5-3 and 5-4 summarize the original, desired bounds for each of these regions. Note that the maximum correlator spacings allowed for the ΔΔ receivers in Regions 1 and 2 are specified for d_{narrow} only and are one-half the limits of the respective E-L regions.

E-L	Region 1	Region 2	Region 3	Region 4
Precorrelation Bandwidth, PCBw (2-Sided, MHz)	2≤ PCBw≤7	7≤ PCBw≤16	16≤PCBw≤20	20≤ PCBw≤24
Average Correlator Spacings, $d=d_{e-l}$ (chips)	0.045≤ d ≤1.1	0.045≤ d ≤0.21	0.045≤ d ≤0.11	0.08≤ d ≤0.11

Table 5-3 Early Minus Late (E-L) Correlator Configuration Constraints for Airborne Receivers

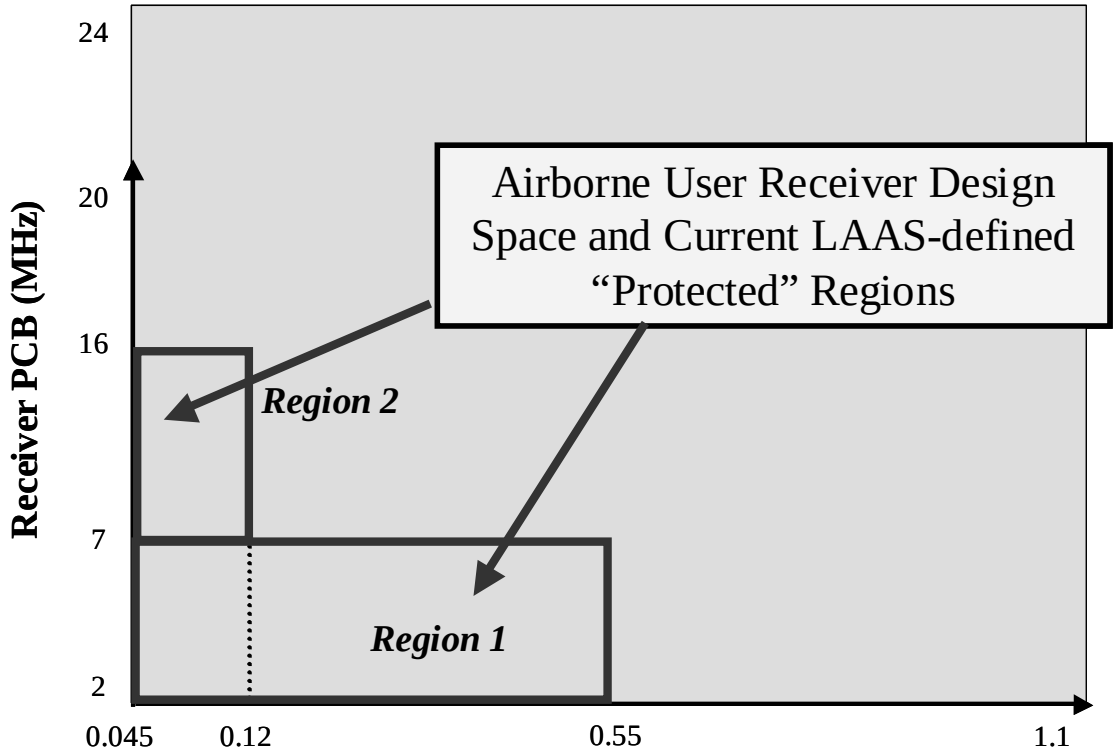

Figure 5-4 Original Airborne User ΔΔ Receiver Configuration (Design) Space

ΔΔ	Region 1	Region 2
Precorrelation Bandwidth, PCBw (2-Sided, MHz)	2≤ PCBw≤7	7≤ PCBw≤16
Average Correlator Spacings, $d=d_{narrow}$ (chips)	0.045≤ d ≤0.55	0.045≤ d ≤0.21

Table 5-4 Original Double-delta (ΔΔ) Correlator Configuration Constraints for Airborne Receivers

5.5 Signal Quality Monitor Evaluation

Computer analyses using models for nominal and anomalous correlation peaks (and also using the SU MDEs and the MERRs) can evaluate SQM designs. An illustration of this evaluation process is shown in Figure 5-5.

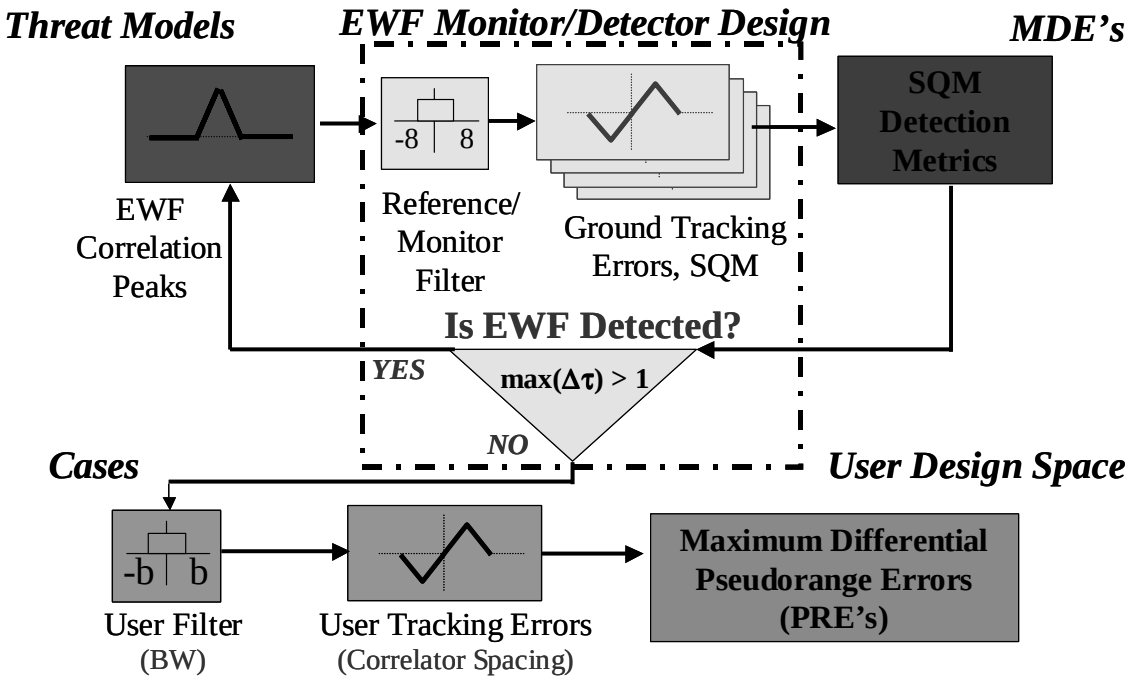

Figure 5-5 SQM Simulation and Evaluation Process

The procedure is as follows:

1) Use Equations (3.2) through (3.16) to model the anomalous correlation peaks corresponding to each EWF.

2) Filters these peaks according to the specific characteristics of the monitor receiver precorrelation filter (e.g., 16MHz bandwidth for LAAS).

3) Compute ground differential reference tracking errors for each EWF (d_{ref}=0.1T_c, 16MHz bandwidth for LAAS) using Equations (5.1) and (5.2).

4) Use a multicorrelator SQM design to sample the anomalous peak at specific locations and apply Ratio tests and Δ-tests according to Equations (4.6) through (4.16).

5) Normalize each corresponding symmetry test using the test-specific MDEs (valid for a particular elevation angle only).

6) If the monitor detects the EWF (i.e., $\gamma_\Delta \geq 1$ or $\gamma_R \geq 1$), select another EWF from the threat space and model it. (Then repeat the evaluation procedure.)

7) If an EWF is *undetected* by the monitor (i.e., $\gamma_\Delta < 1$ and $\gamma_R < 1$), compute the maximum PREs for each of the possible avionics receiver configurations—the E-L and ΔΔ L-shaped regions of Figure 5-3 and 5-4.

8) Repeat steps 1 though 7 for a new EWF; maximize the PREs in the user design space over all EWF parameters according to $\max_{\sigma, f_d, \Delta} \Delta\tau\left(d_{\text{air}}, BW_{\text{air}}\right)$.

5.5.1 Contour Plots

An effective SQM design keeps the maximum differential PREs for these users below the maximum allowable error—the MERRs—corresponding to that elevation angle. If the computed PREs ever exceed the MERR, it indicates that HMI would occur for those users. The results of this simulation and evaluation process are shown in Figure 5-6 through 5-11 for the case where there is no SQM on the ground. In this case every evil waveform passes undetected (i.e., all EWFs are UDPs) to the users and is subsequently evaluated over the entire two-dimensional design space.

As previously stated, these contours represent the maximum PREs over all EWF parameters $\left(\sigma, f_d, \Delta\right)$. For reference, closely clustered contours have been drawn at the level of an MERR of approximately 5 meters. Note from Figure 5-2 that this is greater than the maximum (5°) MERRs. The PRE contours shown below exceed even this

conservative MERR in many of the protected regions. This indicates the need for SQM to protect E-L and ΔΔ users against EWFs for satellites at any elevation angle.

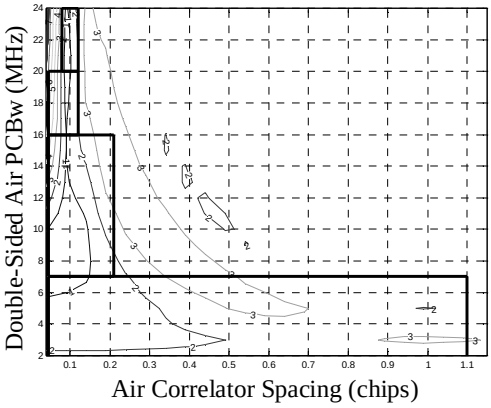

Figure 5-6 No SQM – TM A – E-L

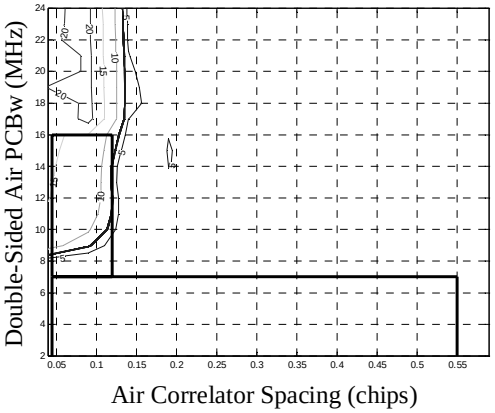

Figure 5-9 No SQM – TM A – ΔΔ

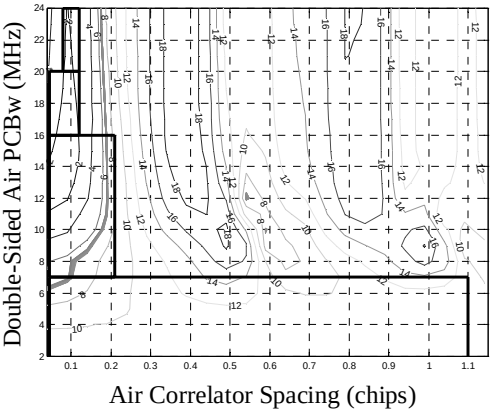

Figure 5-7 No SQM – TM B – E-L

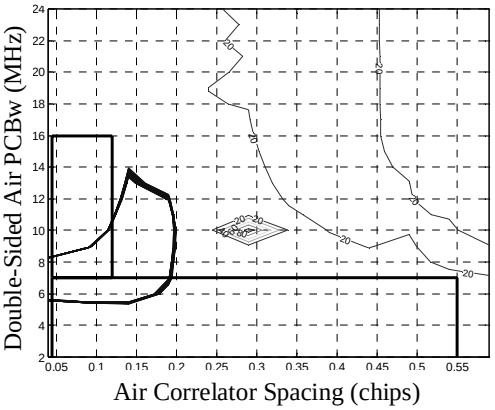

Figure 5-10 No SQM – TM B – ΔΔ

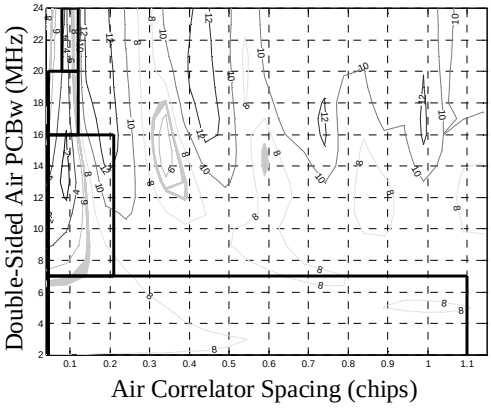

Figure 5-8 No SQM – TM C – E-L

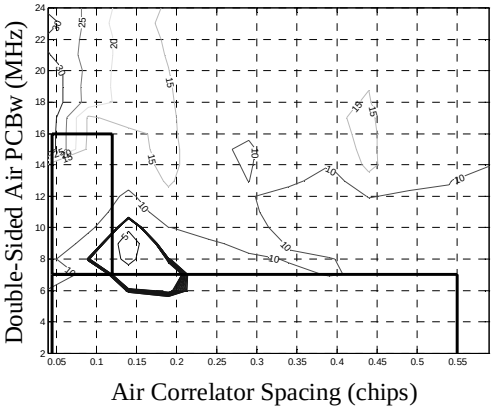

Figure 5-11 No SQM – TM C – ΔΔ

One notable exception occurs for E-L avionics configurations that are “nearly-matched” to the ground reference configuration. In all of these cases, despite the fact that all EWFs appear in the differential processing, the errors are quite small for avionics in the vicinity of 0.1Tc correlator spacing and 16MHz precorrelation bandwidth. When the ground reference and airborne receivers have identical configurations, the differential PREs are zero.

Since LAAS specifies that the ground reference corrections must come from a standard E-L receiver, no ΔΔ receivers benefit from this cancellation. In fact, the ΔΔ receiver differential PREs are generally greater than their E-L counterparts. (Refer to Section 5.5.2 below.) Since the differential errors are expected to be larger, they are fundamentally more difficult configurations to protect using the currently defined SQM techniques. If, however, the LGF differential corrections resulted from ΔΔ receiver pseudorange measurements, the opposite would be true. In that case, all the E-L airborne users would experience substantially different EWF tracking errors than would the ground receiver. Conversely, many ΔΔ users would more closely match the ground receiver configuration.

An example of the effect SQM has on the PRE contours is shown in Figure 5-12 and 5-13. Figure 5-12 shows the maximum PRE contours (for E-L correlators only) for a subset of TM B in the case where no SQM is used to detect (and remove) any EWFs. The heavy contours are drawn at approximately 3.5m, corresponding to an MERR at an elevation angle of 5° with 2 LGF (ground) monitor receivers. Figure 5-13 depicts the contours that result from only the undetected points from this threat space after a 3-correlator pair SQM is applied (using 5° MDEs). In this example, the SQM has effectively protected all the E-L users within each of the four design regions by detecting (and subsequently removing) the hazardous EWFs. (Note that the magnitudes of the errors in Figure 5-13 are much less important than the fact that they are all below the MERR.)

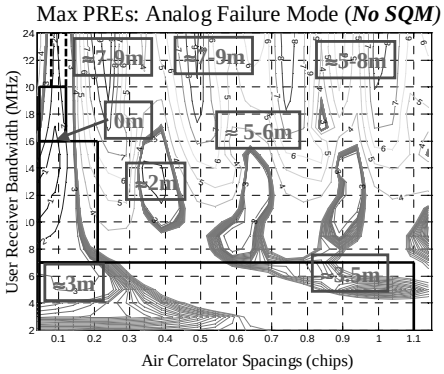

Figure 5-12 Sample "Contour Plots" of Max PREs for a Subset of TM B ($7.3 \le f_d \le 17$, $0.8 \le \sigma \le 8.8$, $\Delta=0$) without SQM (5° MERRs assumed, or ~3.5 meters)

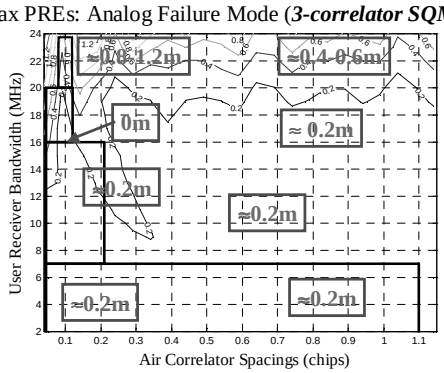

Figure 5-13 Sample "Contour Plots" of Max PREs for a Subset of TM B ($7.3 \le f_d \le 17$, $0.8 \le \sigma \le 8.8$, $\Delta=0$) with SQM (3 Correlator Spacings: d=0.1, 0.15, and 0.2 chips, 5° Elevation Angle)

5.5.2 Undetected Points (UDPs)

Figure 5-14 below shows the UDPs that caused the errors shown in Figure 5-13. Note that the number and distribution of undetected EWFs are much less important than the maximum PREs (contour plots) that result. These two are of course related. However, unacceptable errors may result for many users by a single EWF that eludes an SQM implementation that detects all others. Conversely, an SQM that detects relatively few EWFs may still more than adequately protect the entire user design space.

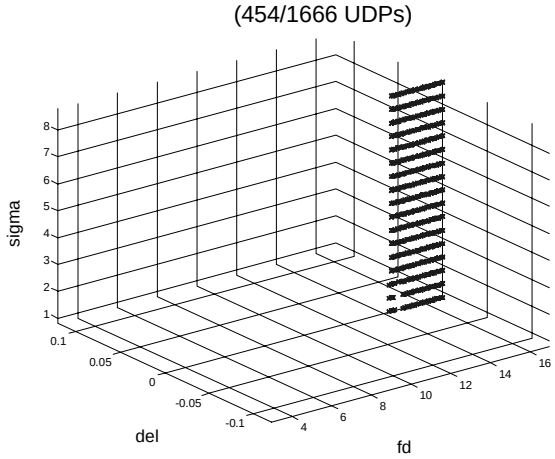

Figure 5-14 EWF Threat Space Undetected Points for Sample SQM Case of Figure 5-13

With respect to the UDPs, in general, the following is true:

- As f_d (and/or σ) increases, the EWFs become more difficult to detect, but they tend to induce smaller airborne PREs.

- As Δ increases, the EWFs become easier to detect and induce larger PREs.

These generalizations are intuitive. Recall that the amplitudes of the distortions (oscillations) vary with the EWF frequency parameter. Higher f_d implies a smaller maximum oscillation amplitude (due to the σ / ω_d factor in Equation (3.1) of Chapter 3) and, hence, a smaller distortion of the peak. Smaller distortions are, of course, more difficult to detect, but they generally induce smaller user PREs. Note that for TM B, if f_d was infinite, no distortions would occur of the main peak. Conversely, larger Δ implies larger correlation peak distortion and, accordingly, allows easier detection of the corresponding EWF.

The maximum user pseudorange errors introduced by each of the EWFs of TM A, TM B and TM C are shown in Figure 5-15 through 5-32 below. Figure 5-15, 5-16, 5-19, 5-20, 5-25, and 5-26 plot these PREs versuss the corresponding receiver configuration. The horizontal axis lists the correlator spacing. Above each column of points, the plots list the user PCBw at which the maximum error occurred in addition to the number of points in that particular column. Figure 5-17, 5-18, 5-21 through 5-24, and 5-27 through 5-32 plot the PREs versus the EWF parameters. Each point (on every plot) represents the maximum PREs over the (4 E-L and 2 $\Delta\Delta$ correlator) protected regions. (Refer to Figure 5-3 and 5-4 for the allowable configuration bounds on these receiver types.) Again, this analysis implies that all EWFs pass undetected by any ground SQM technique. It can be seen from the figures that in addition to the two generalizations above, the following statements are true:

- The maximum E-L user PREs most frequently occur for ($d_{\text{E-L}}$) correlator spacings narrower than 0.2Tc and bandwidths of 16MHz or wider.

- The maximum ΔΔ user PREs most frequently occur for (d_{narrow}) correlator spacings narrower than $0.05T_c$ and a bandwidth of 16MHz.

- Over all the EWFs within a given threat model (i.e., TM A, TM B, or TM C), the absolute maximum ΔΔ user "regional" PRE is greater than the corresponding E-L maximum PRE.

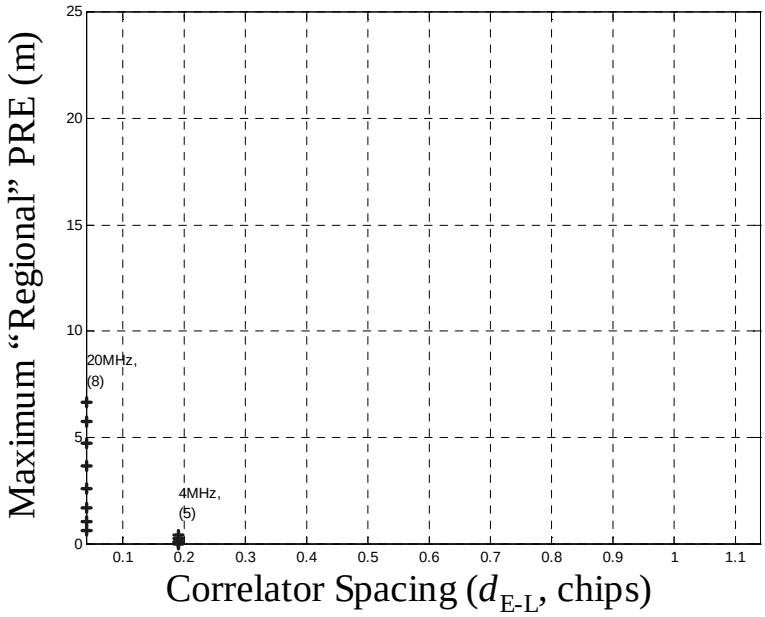

Figure 5-15 Maximum E-L User PREs Within 4 Protected Regions for TM A EWFs (13 Points Shown for Δ Varied From 0 to $0.12T_c$ in $0.01T_c$ Increments)

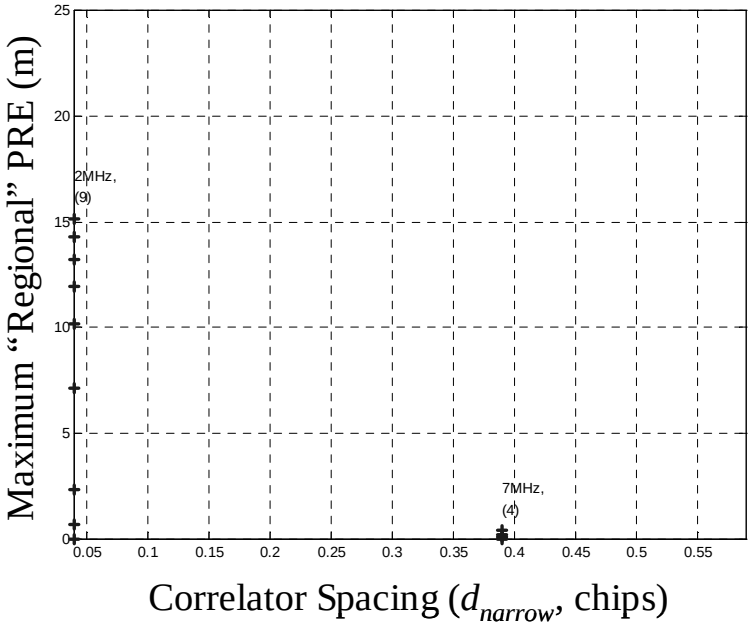

Figure 5-16 Maximum ΔΔ User PREs vs. Receiver Configuration Within 2 Protected Regions for TM A EWFs (13 Points Shown for Δ Varied From 0 to $0.12T_c$ in $0.01T_c$ Increments)

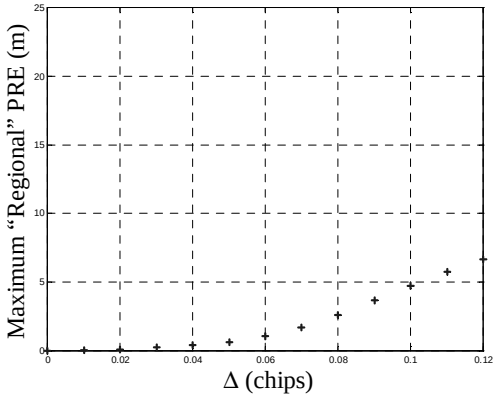

Figure 5-17 Maximum E-L User PREs Within 4 Protected Regions for TM A EWFs (13 Points Shown)

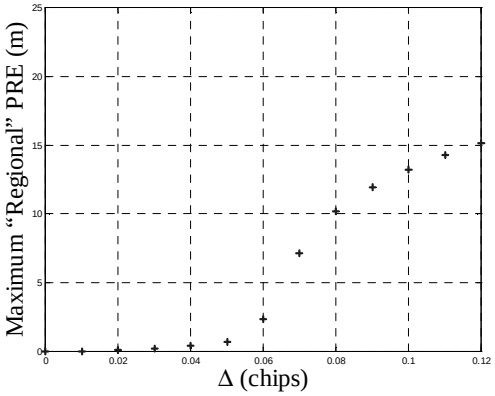

Figure 5-18 Maximum ΔΔ User PREs Within 2 Protected Regions for TM A EWFs (13 Points Shown)

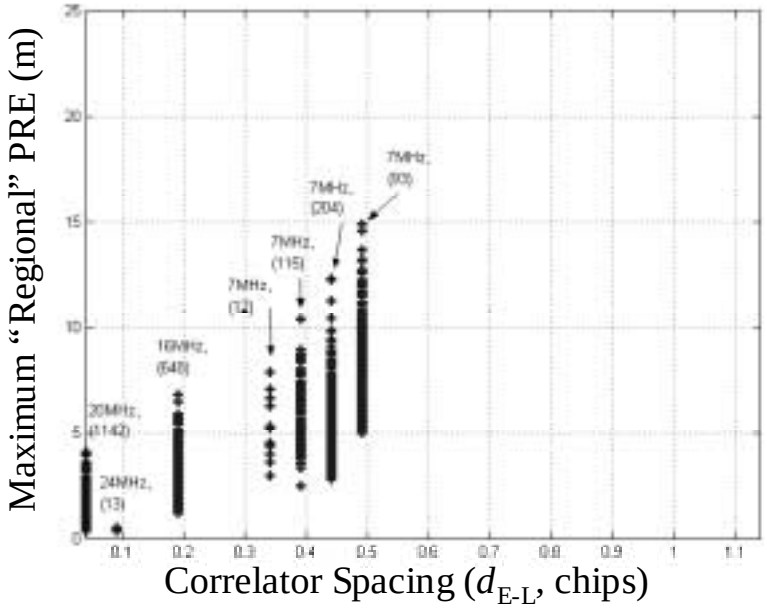

Figure 5-19 Maximum E-L User PREs Within 4 Protected Regions for TM B EWFs (2227 Points Shown for: f_d Varied From 4 to 17MHz in 1MHz Increments; σ Varied From 0.8 to 8.8Mnepers/sec in 0.5Mnepers/sec Increments)

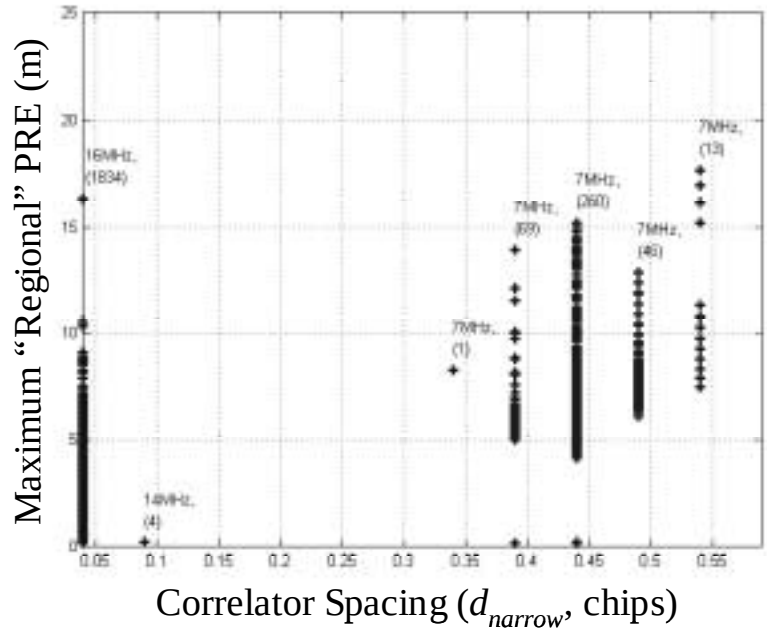

Figure 5-20 Maximum ΔΔ User PREs vs. Receiver Configuration Within 2 Protected Regions for TM B EWFs (2227 Points Shown for: f_d Varied From 4 to 17MHz in 1MHz Increments; σ Varied From 0.8 to 8.8Mnepers/sec in 0.5Mnepers/sec Increments)

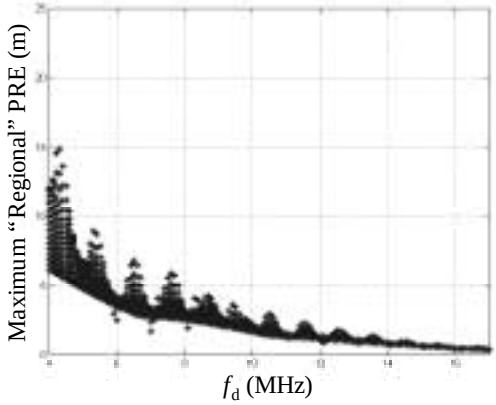

Figure 5-21 Maximum E-L User PREs vs. f_d W ithin 4 Protected Regions for TM B EWFs (2227 Points Shown)

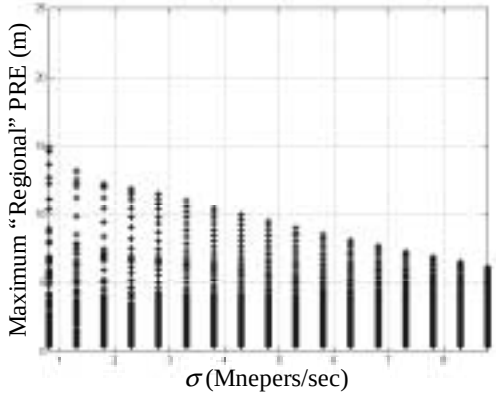

Figure 5-22 Maximum E-L User PREs vs. σ Within 4 Protected Regions for TM B EWFs (2227 Points Shown)

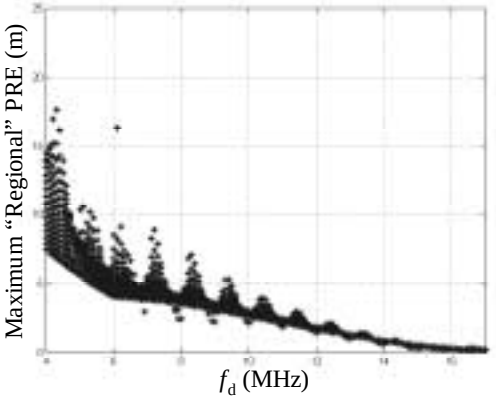

Figure 5-23 Maximum ΔΔ User PREs vs. f_d Within 2 Protected Regions for TM B EWFs (2227 Points Shown)

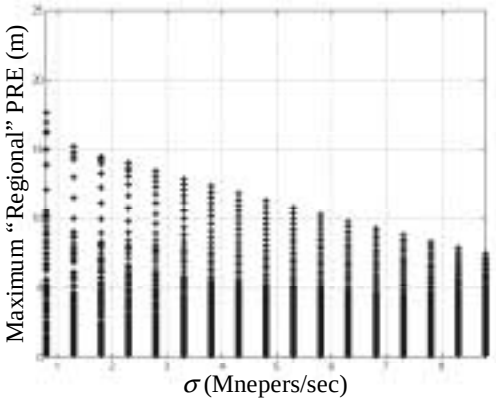

Figure 5-24 Maximum ΔΔ User PREs vs. σ Within 2 Protected Regions for TM B EWFs (2227 Points Shown)

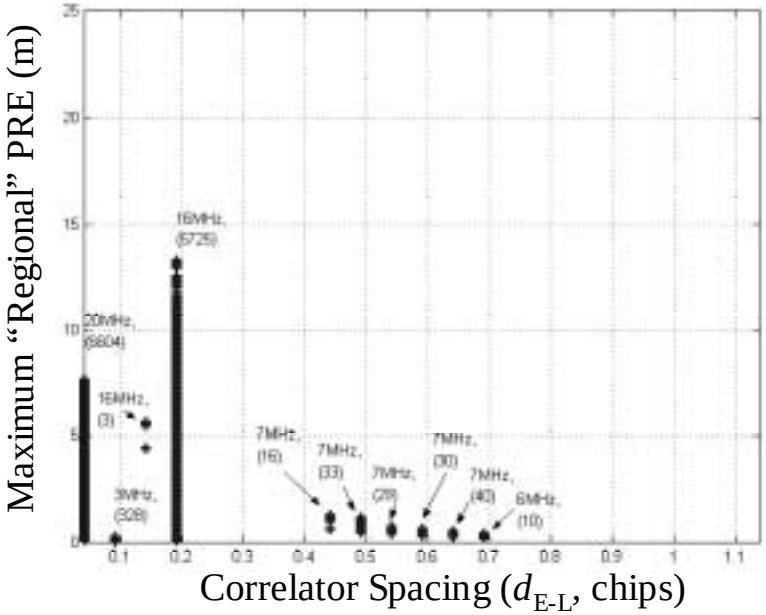

Figure 5-25 Maximum E-L User PREs Within 4 Protected Regions for TM C EWFs (12818 Points Shown for: f_d Varied From 7.3 to 13MHz in 1MHz Increments; σ Varied From 0.8 to 8.8Mnepers/sec in 0.5Mnepers/sec Increments; Δ Varied From 0 to $0.12T_c$ in $0.01T_c$ Increments)

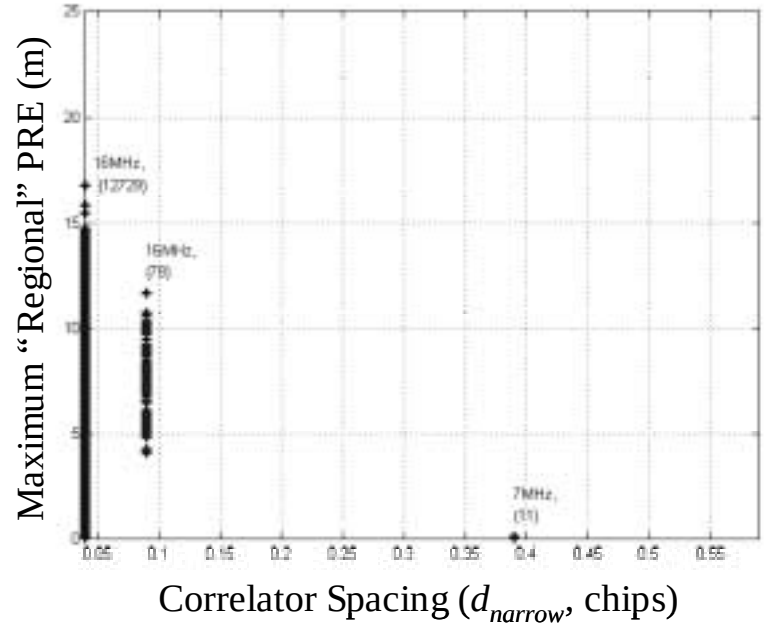

Figure 5-26 Maximum $\Delta\Delta$ User PREs vs. Receiver Configuration Within 2 Protected Regions for TM C EWFs (12818 Points Shown for: f_d Varied From 7.3 to 13MHz in 1MHz Increments; σ Varied From 0.8 to 8.8Mnepers/sec in 0.5Mnepers/sec Increments; Δ Varied From 0 to $0.12T_c$ in $0.01T_c$ Increments)

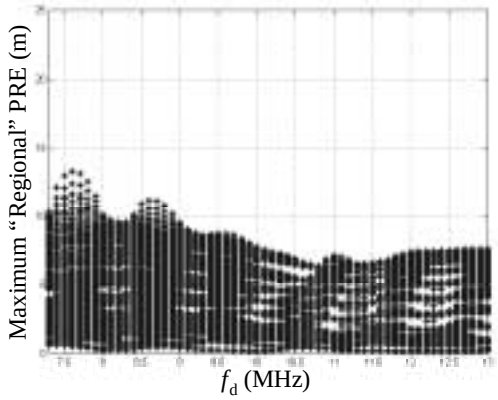

Figure 5-27 Maximum ΔΔ User PREs vs. f_d Within 4 Protected Regions for TM C EWFs (12818 Points Shown)

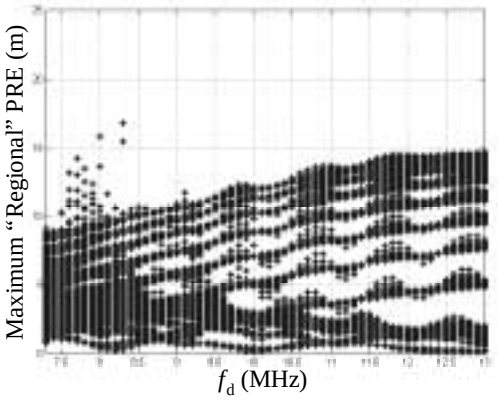

Figure 5-30 Maximum ΔΔ User PREs vs. f_d Within 2 Protected Regions for TM C EWFs (12818 Points Shown)

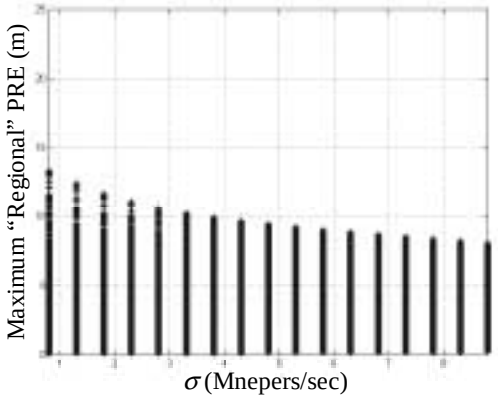

Figure 5-28 Maximum E-L User PREs vs. σ Within 4 Protected Regions for TM C EWFs (12818 Points Shown)

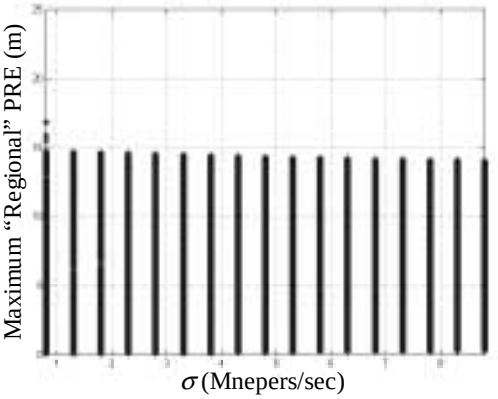

Figure 5-31 Maximum ΔΔ User PREs vs. σ Within 2 Protected Regions for TM B EWFs (12818 Points Shown)

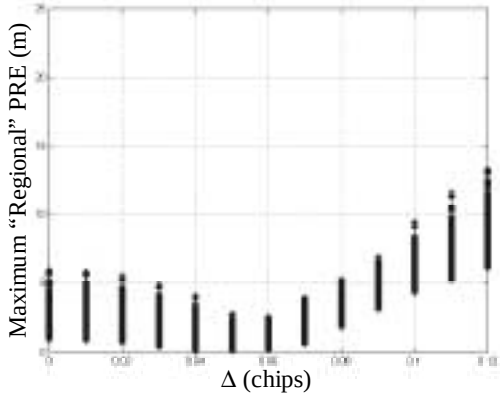

Figure 5-29 Maximum E-L User PREs vs. Δ Within 4 Protected Regions for TM C EWFs (12818 Points Shown)

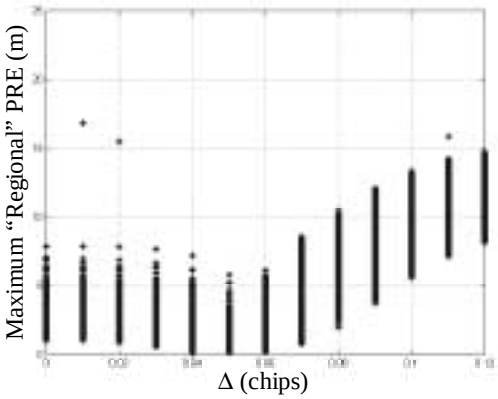

Figure 5-32 Maximum ΔΔ User PREs vs. Δ Within 2 Protected Regions for TM C EWFs (12818 Points Shown)

5.5.3 Analysis Assumptions

Unless otherwise stated, the following assumptions summarize the SQM design, selection, and evaluation process:

Threat Models

The EWF ringing parameter, f_d, varied from 7.3 to 13MHz in 0.1MHz increments. The damping parameter, σ, varied from 0.8 to 8.8Mnepers/sec in 0.5Mnepers/sec increments. The digital lead/lag, Δ, varied from 0 to $0.12T_c$ in $0.01T_c$ increments respectively.

Receiver Channel

The nominal and EWF correlation peaks used a sampling rate of 200 samples (i.e., approximately 200 MHz) per chip. This high sampling rate rendered any receiver quantization effects negligible. Coherent code tracking loops were assumed for both ground and airborne receivers. The ground and airborne E-L receivers implemented Early minus Late discriminators; the airborne $\Delta\Delta$ receivers implemented discriminators described by Equation (5.4).

A 6th-order Butterworth with a precorrelation bandwidth of 16MHz modeled ground (monitor and reference) and airborne receiver filters. User precorrelation bandwidths ranged from 2 to 24MHz bandwidth in 1 MHz increments.

SQM Evaluation

MDEs and MERRs assumed that the satellite signals arrived from a given (specified) elevation angle; MERRs were taken from GAD B curves. Selecting either two or three ground receivers (corresponding to B2 or B3 MERR curves) modeled the LGF, which presumes all observables are available from two or three independent receivers. Since these receive the satellite signal from two or three non-collocated antennas, the thermal noise and multipath from each of these receivers was assumed to be independent and gaussian. The LGF may subsequently average them to reduce the nominal standard

deviation, hence, the MDE of each measurement. Accordingly, this translated to dividing the MDEs by either $\sqrt{2}$ or $\sqrt{3}$, respectively.

SQM used samples from correlators (i.e., correlator value-based SQM) slaved to one independent DLL with an Early-Late spacing of $0.1T_c$. Ground reference (differential) corrections were based on an Early-Late spacing of $0.1T_c$. User correlator spacings ranged from 0.045 to $1.1T_c$ in $0.05T_c$ increments. Final airborne pseudorange errors were a maximum over all undetected waveforms.

5.6 SQM Design Selection

The number of possible multicorrelator implementations is actually quite large. Most practical receivers have a lower-limit of $0.05T_c$ on the spacing of any correlator pair. Some techniques, however, permit narrower spacings to be obtained. (See Chapter 7, Section 7.2). Although there is no upper bound on these spacings, few if any GPS receivers today use spacings wider than 1 chip [Van Dierendonck92]. This still leaves as many as 20 possible correlator spacings yielding anywhere from 2 to 20 possible correlator pairs.

This large number of possible implementations is computationally impractical to thoroughly model and assess. To further narrow these choices, note that Ratio tests and Δ-tests taken using very narrow correlator spacings—at or near the main peak—were more correlated [Van Dierendonck92]. As seen previously from Figure 4-3 of Chapter 4, the nominal variation (hence, the MDEs) for these spacings is relatively small. The increased correlation causes more of the thermal noise and multipath on these measurements to cancel. In addition, current equipment most-easily configures to accommodate as many as three correlator pairs per channel. Monitor receivers could employ four pairs per channel, but this option is less favorable and significantly more costly.

Several organizations initially selected candidate SQM's based on the insights gained from the preliminary simulation and analyses described above. Table 5-5 presents these five candidate multicorrelator SQM configurations (E-L chip spacings).

Candidate SQM's	Correlator Pair No.1 (chips)	Correlator Pair No.2 (chips)	Correlator Pair No.3 (chips)	Correlator Pair No.4 (chips)
Candidate No. 1 [*Service Technique de la Navigation Aerienne*]	0.1	0.15	0.3	-
Candidate No. 2 [*Stanford University*]	0.1	0.15	0.25	-
Candidate No. 2b [*Stanford University*]	0.1	0.15	0.2	-
Candidate No. 3 [*AJ Systems*]	0.05	0.1	0.2	0.3
Candidate No. 4 [*Stanford University*]	0.1	0.2	E:-0.2,L:+0.025 (offset from Prompt)	E:-0.4,L:0 (offset from Prompt)

Table 5-5 Five Candidate Multicorrelator SQM Designs

Several key observations were made to further reduce these options. Candidate 1 is similar to candidate number 2; however, it contains a slightly wider correlator spacing for the third correlator pair. This implies its MDEs will also be slightly larger and, hence, less desirable. Candidate 4 is asymmetric; the asymmetry is proposed to permit observations of a wide range of EWF distortion frequencies. The complexity of this (four-correlator pair) design, however, posed some difficult implementation issues. Candidate 2 also raised implementation issues with some receiver manufacturers. A more practical implementation of this placed the third correlator pair for this candidate at a spacing of $0.2T_c$. Henceforth, SQM2b refers to this modified version of candidate SQM No. 2.

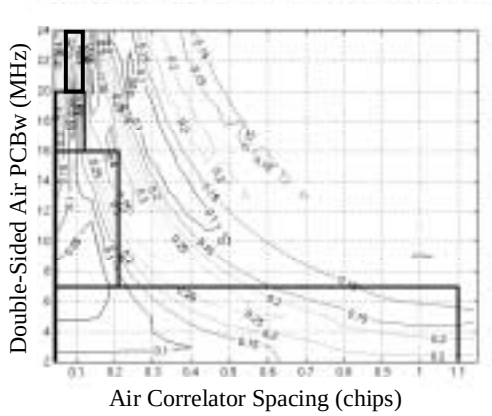

Figure 5-33 SQM3 – TM A – E-L

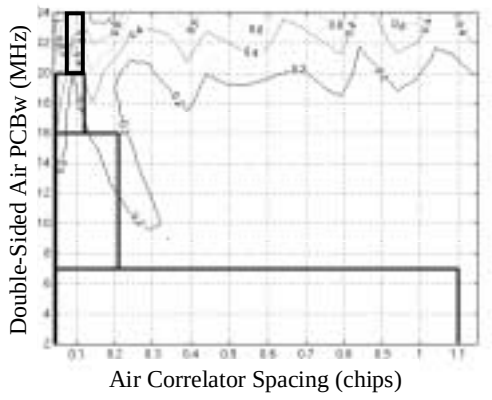

Figure 5-34 SQM3 – TM B – E-L

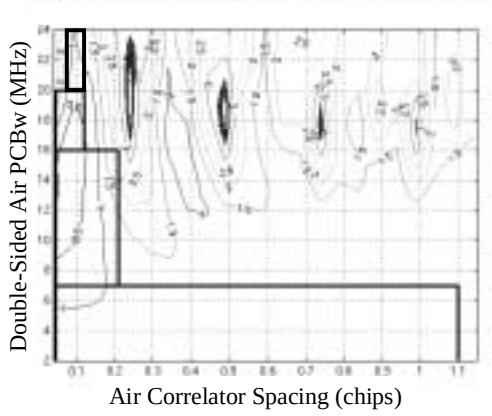

Figure 5-35 SQM3 – TM C – E-L

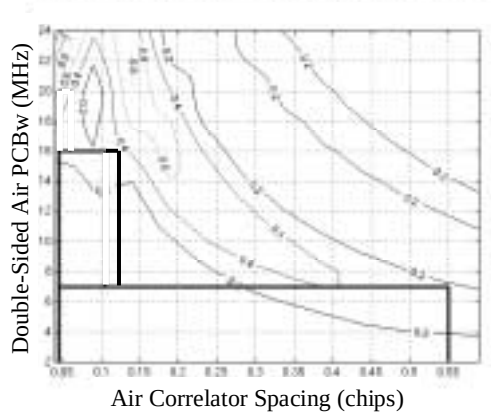

Figure 5-36 SQM3 – TM A – ΔΔ

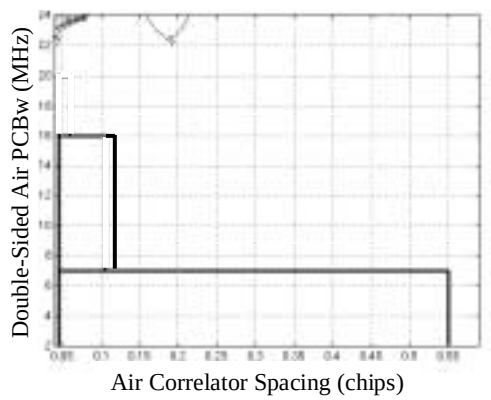

Figure 5-37 SQM3 – TM B – ΔΔ

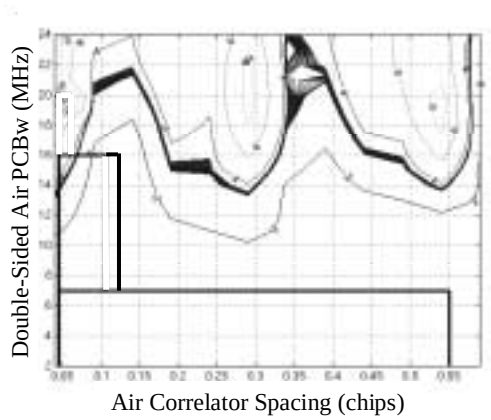

Figure 5-38 SQM3 – TM C – ΔΔ

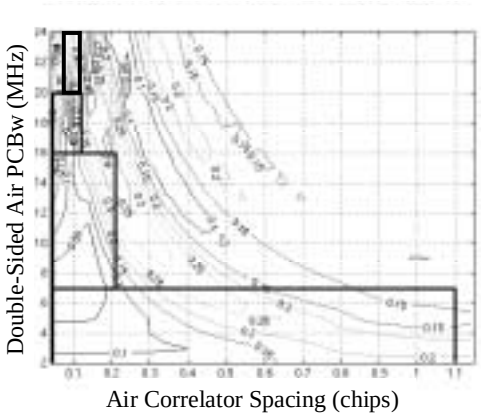

Figure 5-39 SQM2b – TM A – E-L

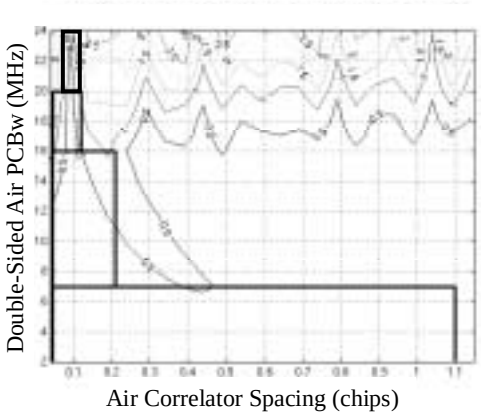

Figure 5-40 SQM2b – TM B – E-L

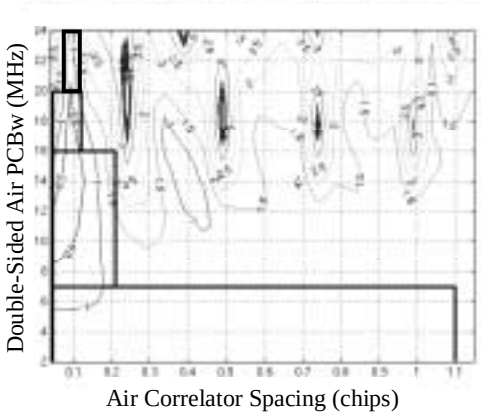

Figure 5-41 SQM2b – TM C – E-L

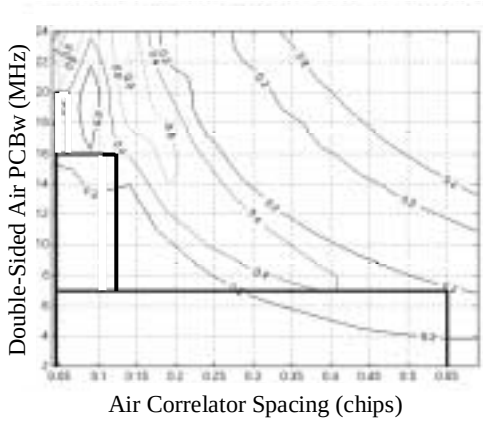

Figure 5-42 SQM2b – TM A – ΔΔ

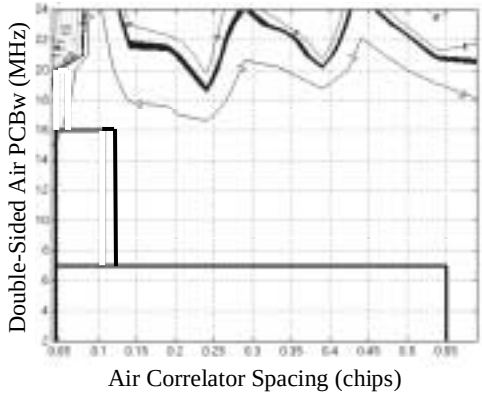

Figure 5-43 SQM2b – TM B – ΔΔ

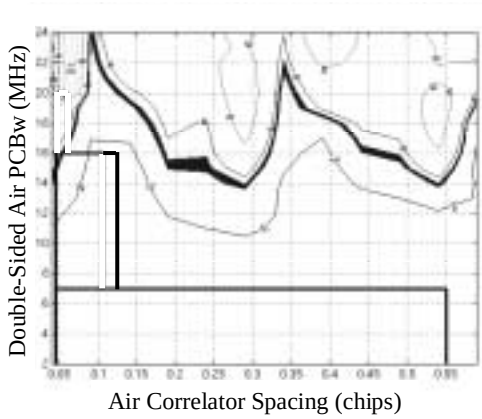

Figure 5-44 SQM2b – TM C – ΔΔ

Subsequent analysis selected SQM2b and SQM3—three and five-correlator techniques, respectively—for comparison and further investigation. Contour plots of the resulting maximum PREs obtained implementing both of these multicorrelator techniques in simulation are show below. A 5°-elevation angle was assumed for all cases. The MDEs were (conservatively) increased by 20%. Closely spaced (heavy) contours indicate the avionics designs for which the PREs met or exceeded the (5°) MERR. Figure 5-33 through 5-38 correspond to SQM3. Figure 5-39 through 5-44 correspond to SQM2b.

The above figures indicate that for a 5° elevation angle, both SQM3 and SQM2b can protect all four E-L regions for all three threat models. Note that as currently configured, both techniques, were only barely able to completely protect the upper-left hand corner of Region 2 for the ΔΔ correlators. In fact, Figure 5-45 and Figure 5-46 below show that even for less conservative (100%) MDEs this remains true. More significantly, SQM2b was at least as effective at protecting the user design space as was SQM3. For this reason, SQM2b—the more practical, three-correlator design—was selected for a more detailed analysis.

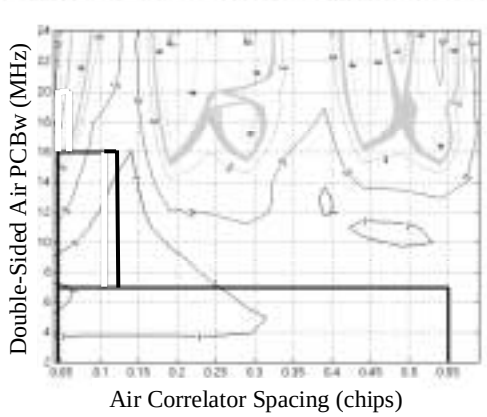

Figure 5-45 SQM3 – TM C – E-L (100% MDEs)

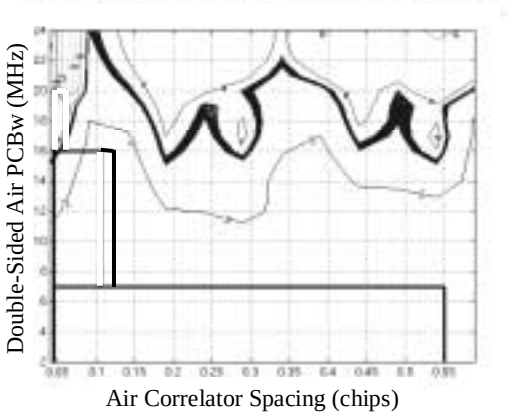

Figure 5-46 SQM2b – TM C – ΔΔ (100% MDEs)

5.7 Robust SQM Design Analysis

A "robust" SQM is able to protect the greatest number of airborne users against all hazardous EWFs despite variations in (failed) satellite elevation angle, ground multipath

conditions, and user receiver configuration. Accordingly, this section describes the evaluation of the best current evil waveform (EWF) signal quality monitor configuration, SQM2b, using a robust SQM evaluation methodology. (SQM2b is shown in Figure 5-47.) It presents the methods in three parts. First, it compares the maximum *regional* pseudorange errors (PREs), computed at varying elevation angles, to the maximum allowable pseudorange (MERR) errors. Second, it examines the sensitivity of these results to differential group delay variations of up to 150ns. Third, it discusses the sensitivity of SQM performance to variations in user filter magnitude response. (Appendix B examines the effects of monitor filter magnitude response.)

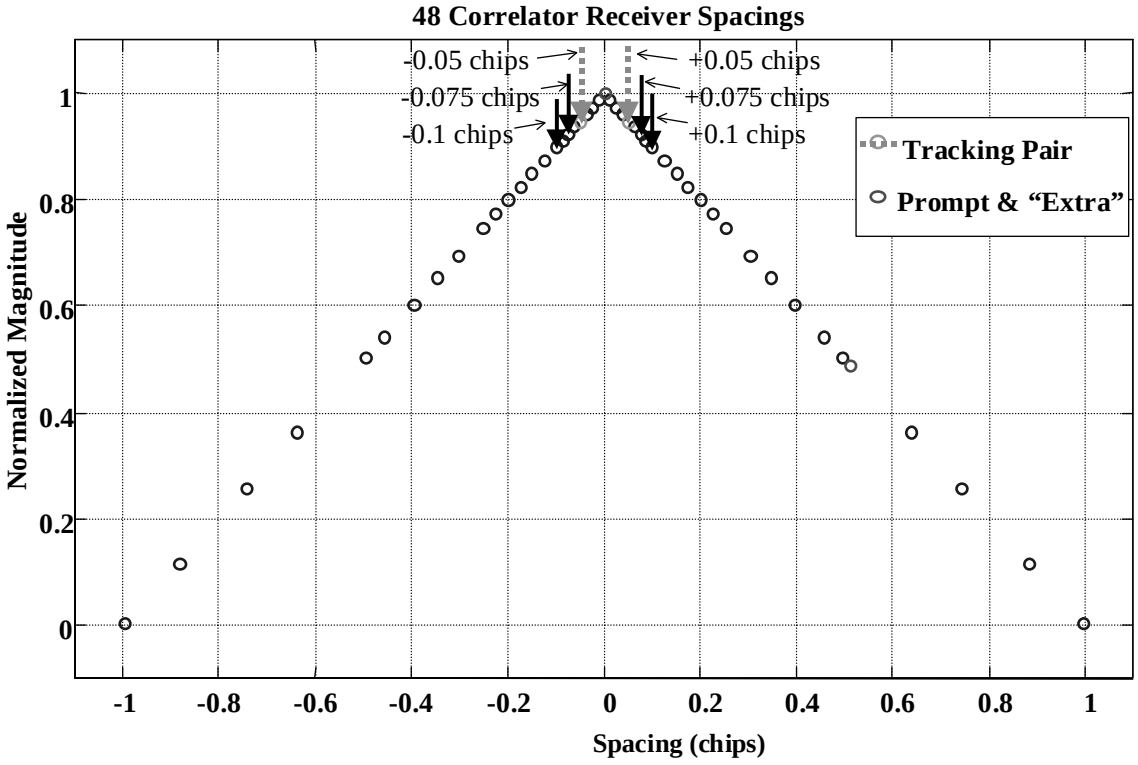

Figure 5-47 Actual correlator configuration (spacing/locations) for SQM2b used for MDE data colloction.

5.7.1 SQM2b Minimum Detectable Errors (MDEs)

For the evaluation of SQM2b, the analysis used the ICAO-standard SU MDEs for each of 11 symmetry tests—2 Δ-tests, 3 "average" ratio tests, 3 "negative" ratio tests, and 3

"positive" ratio tests. As discussed in Section 4.2.3 of Chapter 4, MDE data was taken at Stanford University (SU). More specifically, correlation peak measurements were taken for live satellite passes and were grouped into bins according to elevation angles. The analysis assumed the MDEs used for a given elevation angle corresponded to the mean elevation angle of each of the 5-degree bins from 2.5 to 87.5 degrees. Third-order polynomials were fit to the measured data according to Equation (4.18). These relations were subsequently used to compute valid MDEs for arbitrary elevation angles between 5 and 90 degrees. Tables 5-6 through 5-9 below summarize the polynomial fit coefficients. Plots of the curve fits and their residuals are given in Figure 5-48 through 5-51.

	a_3	a_2	a_1	a_0
$\Delta_{\pm 0.075, \pm 0.05}$	-5.5345e-009	1.6638e-006	-1.6604e-004	6.3401e-003
$\Delta_{\pm 0.1, \pm 0.05}$	-1.5115e-008	5.0539e-006	-3.7768e-004	1.3769e-002

Table 5-6 Polynomial Fit Coefficients for SQM2b Δ-Tests

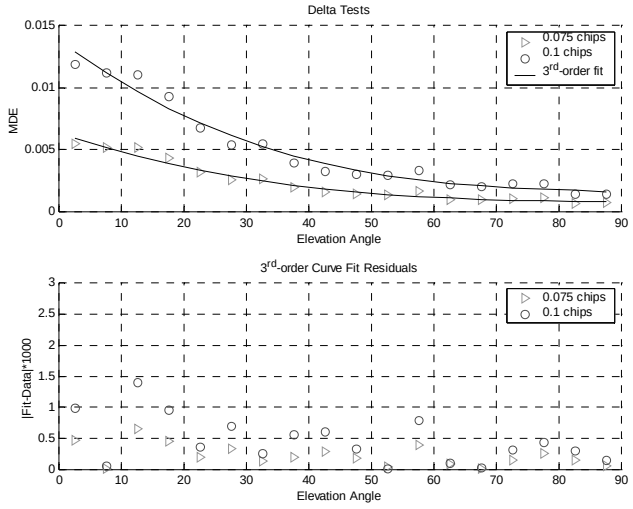

Figure 5-48 Curve Fit and Residuals for SQM2b Δ-Tests

	a_3	a_2	a_1	a_0
$\mathbf{R_{\pm 0.05av,P}}$	-1.5836e-008	3.6739e-006	-2.8795e-004	9.3079e-003
$\mathbf{R_{\pm 0.075av,P}}$	-3.2462e-008	7.0746e-006	-5.2628e-004	1.6099e-002
$\mathbf{R_{\pm 0.1av,P}}$	-3.5937e-008	8.0973e-006	-6.3291e-004	2.0298e-002

Table 5-7 Polynomial Fit Coefficients for SQM2b Average R-Tests

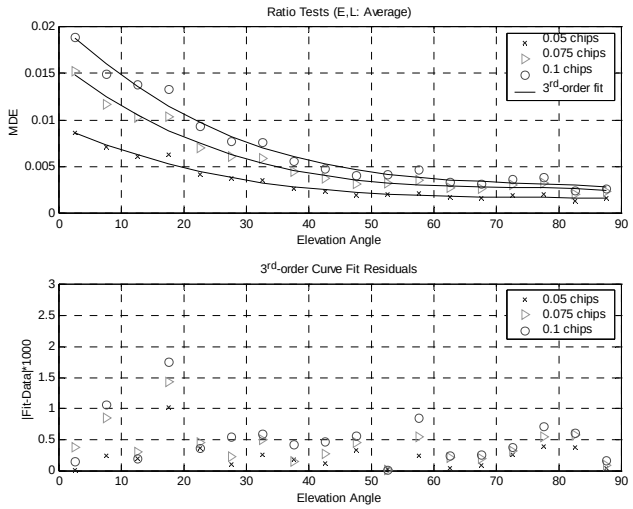

Figure 5-49 Curve Fit and Residuals for SQM2b Average R-Tests

	a_3	a_2	a_1	a_0
$\mathbf{R_{-0.05,P}}$	-9.9465e-009	2.7144e-006	-2.4363e-004	8.8196e-003
$\mathbf{R_{-0.075,P}}$	-2.0817e-008	5.5971e-006	-3.4226e-004	1.0587e-002
$\mathbf{R_{-0.1,P}}$	-1.2278e-008	3.1656e-006	-2.6544e-004	9.0253e-003

Table 5-8 Polynomial Fit Coefficients SQM2b Negative R-Tests

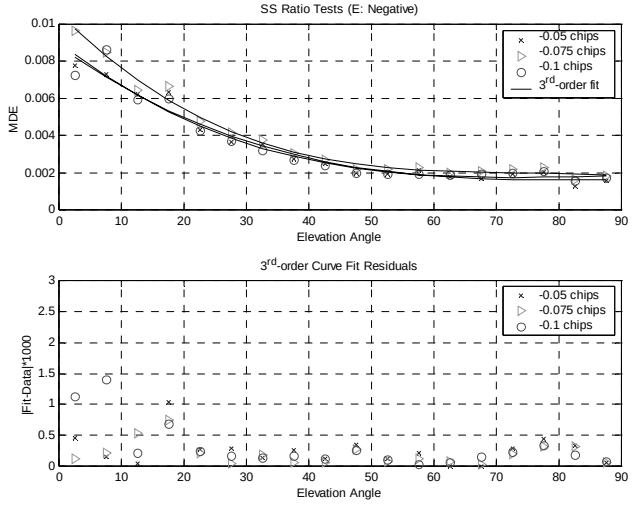

Figure 5-50 Curve Fit and Residuals for SQM2b Negative R-Tests

	a_3	a_2	a_1	a_0
$\mathbf{R_{+0.05,P}}$	-1.8875e-008	5.2323e-006	-3.2149e-004	1.0079e-002
$\mathbf{R_{+0.075,P}}$	-5.0849e-008	9.1818e-006	-7.1191e-004	2.2598e-002
$\mathbf{R_{+0.1,P}}$	-5.4957e-008	1.2696e-005	-1.0296e-003	3.4024e-002

Table 5-9 Polynomial Fit Coefficients for SQM2b Positive R-Tests

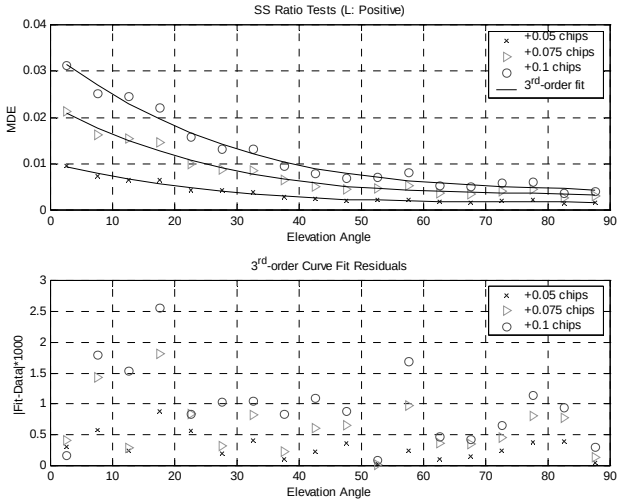

Figure 5-51 Curve Fit and Residuals for SQM2b Positive R-Tests

5.7.2 Maximum Allowable Error (MERR) Analysis

Equation (5.5) computes the MERR (σ_{pr_gf}) as a function of elevation angle for both two and three-monitor receiver cases. Because incident multipath at each of the two or three different antenna locations (one for each respective monitor receiver) is most likely independent, the analysis assumes MDE reduction factors of $\sqrt{2}$ or $\sqrt{3}$ for these cases, respectively.

Procedure

The MERR analysis implemented SQM2b as the ground monitoring correlator spacing configuration with the curve-fit (SU) MDEs. MERRs for the two and three monitor

receiver cases were compared against the respective resulting contour plots generated for each elevation angle.

The SQM2b MERR investigation proceeded as follows:

1) Computed the maximum user PREs (i.e., airborne receiver contour plots) for a given threat model and user receiver type using each elevation angle from 5° to 90° (in 5°-increments).

2) Compared the maximum PRE within any of the (4) E-L and (2) ΔΔ protected regions to the MERR corresponding to that elevation angle. This process is expressed as

$$\max_{reg_{E-L}=1,2,3,4} \left\{ \max_{\sigma, f_d, \Delta} \Delta\tau\left(d_{\text{air}}, BW_{\text{air}}\right) \right\} \tag{5.6}$$

and

$$\max_{reg_{\Delta\Delta}=1,2} \left\{ \max_{\sigma, f_d, \Delta} \Delta\tau\left(d_{\text{air}}, BW_{\text{air}}\right) \right\} \tag{5.7}$$

for standard E-L and ΔΔ correlators, respectively. (Recall that the configuration bounds for each of these regions are defined in Table 5-3 and 5-4 and depicted in Figure 5-3 and 5-4.)

3) Repeated process until maximum PREs within protected regions were below the minimum MERR (corresponding to a 90-degree elevation angle satellite) or until the elevation angle equaled 90°.

An unacceptable condition (i.e., HMI occurred for at least one user configuration) existed whenever the maximum PRE exceeded the corresponding MERR at a particular elevation angle.

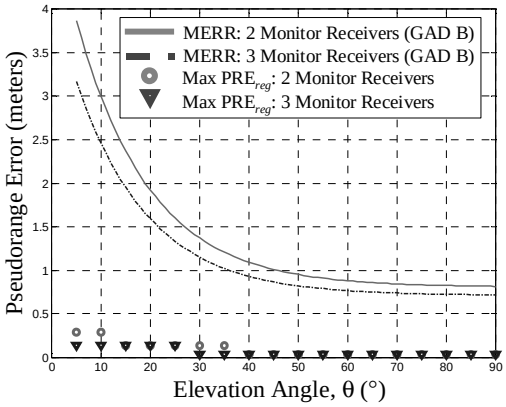

Figure 5-52 SQM2b MERR Analysis – TM A (100% MDEs) – E-L Users

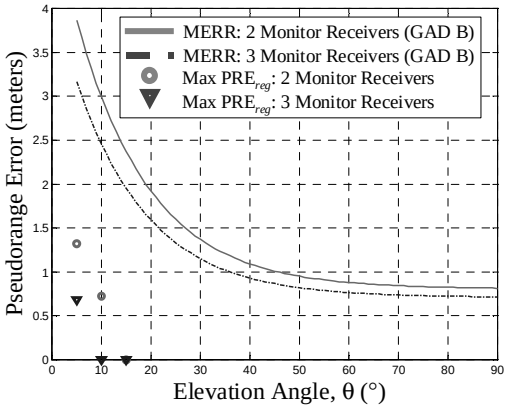

Figure 5-53 SQM2b MERR Analysis – TM B (100% MDEs) – E-L Users

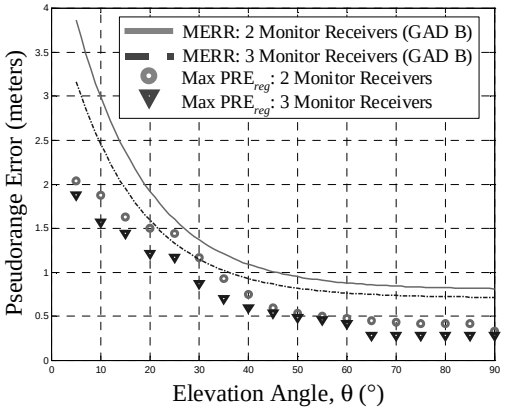

Figure 5-54 SQM2b MERR Analysis – TM C (100% MDEs) – E-L Users

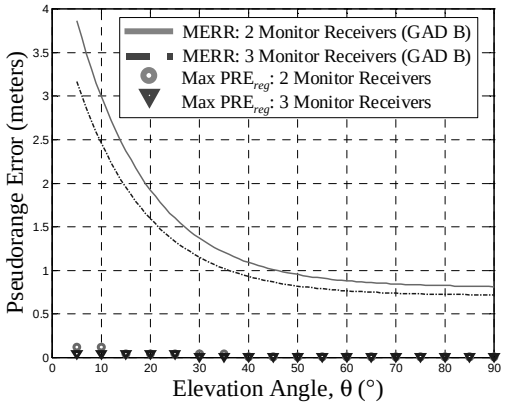

Figure 5-55 SQM2b MERR Analysis – TM A (100% MDEs) – ΔΔ Users

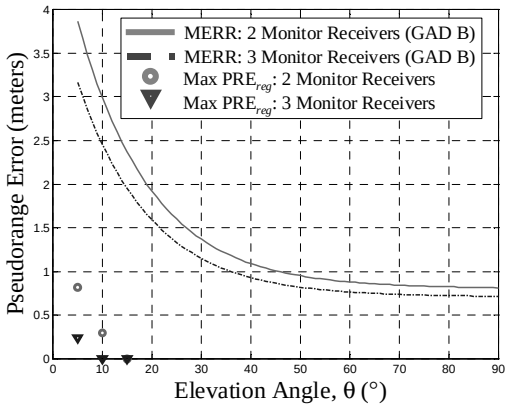

Figure 5-56 SQM2b MERR Analysis – TM B (100% MDEs) – ΔΔ Users

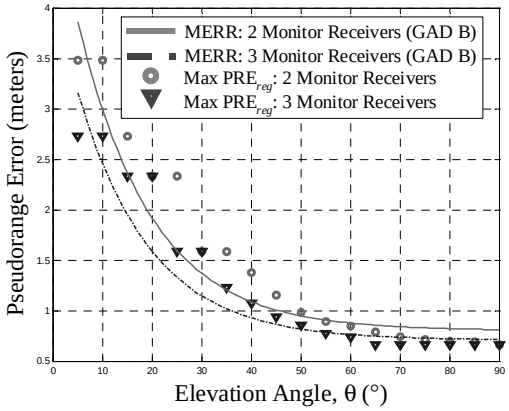

Figure 5-57 SQM2b MERR Analysis – TM C (100% MDEs) – ΔΔ Users

MERR Analysis Results: GAD B

The results for Threat models A, B, and C, assuming both two and three monitor receivers, are given below (in Figure 5-52 to 5-57) for the standard E-L and the ΔΔ correlator receivers, respectively. E-L correlator PREs remain well below the thresholds for all threat models. As shown in Figure 5-57, the ΔΔ receivers, however, were found to have unacceptably high errors when subjected to TM C EWFs (for both the two and three monitor receiver cases using 100% MDE assumptions). Consequently, these receivers (for these EWF conditions) were determined to be most critical and were subsequently singled out for more detailed analysis.

Recall that Figure 5-57 plots the maximum regional PREs, which occur at the upper left-hand corner of ΔΔ Region 2. However, this would have indicated a significant problem for the aviation community if the unacceptably large PREs had extended too far into the region and impacted current receiver designs. In other words, the receiver manufacturers and the aviation community were less concerned with a few uncommitted receiver configurations in that region of the design space. Accordingly, a small rectangular "notch" was specified in this region to exclude the few unprotected configurations from consideration. Section 5.7.3 details the specification of this notch using the differential group delay analysis.

To examine the distribution of these PREs for both E-L and ΔΔ correlators, the sample contour plots below provide results corresponding to discrete elevation angles as indicated in the captions below each figure. The five elevation angles are 7.5°, 22.5°, 37.5°, 52.5°, 67.5°, and 82.5°. The contours are shown for both the E-L and ΔΔ correlators in Figure 5-58 through Figure 5-81.

For the E-L correlators the maximum regional PREs occur for one of the following four user receiver configurations:

- 16MHz PCBw, 0.21Tc correlator spacing
- 20MHz PCBw, 0.0.045Tc correlator spacing

- 24MHz PCBw, 0.08Tc correlator spacing
- 24MHz PCBw, 0.12Tc correlator spacing

For the ΔΔ correlators the maximum PREs occur only for the upper-left corner of Region 2:

- 16MHz PCBw, 0.045Tc correlator spacing

Note that this was also true for the case where no SQM was used. (See Figures 5-6 through 5-11)

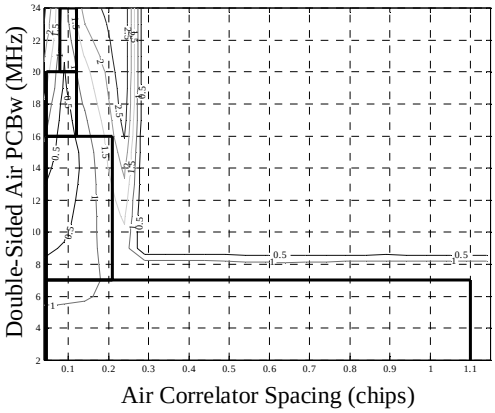

Figure 5-58 E-L Correlators – TM C - 7.5°- 2 Monitor Receivers

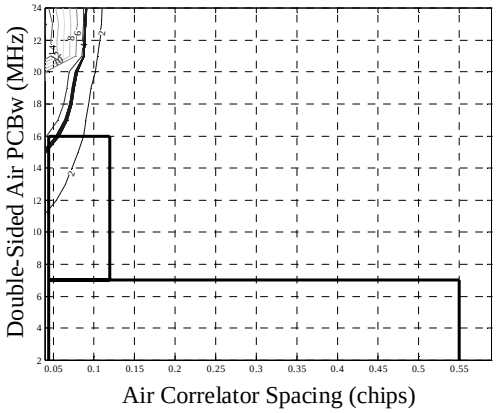

Figure 5-61 ΔΔ Correlators – TM C - 7.5°- 2 Monitor Receivers

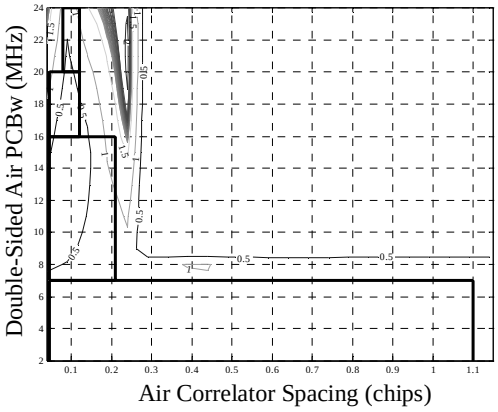

Figure 5-59 E-L Correlators – TM C - 22.5°- 2 Monitor Receivers

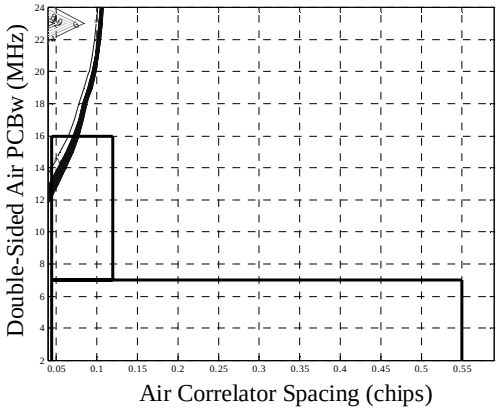

Figure 5-62 ΔΔ Correlators – TM C - 22.5°- 2 Monitor Receivers

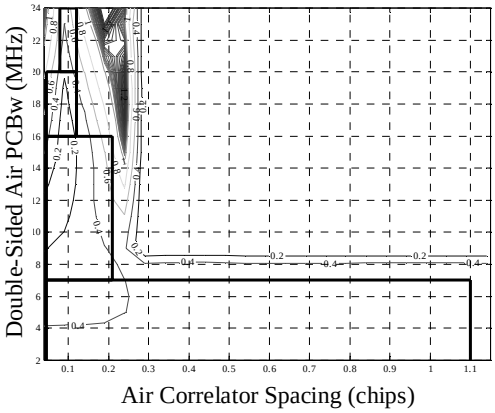

Figure 5-60 E-L Correlators – TM C - 37.5°- 2 Monitor Receivers

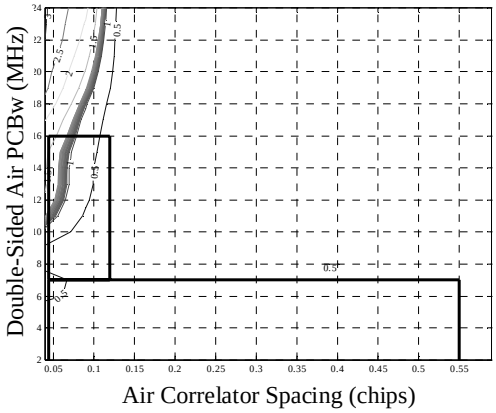

Figure 5-63 ΔΔ Correlators – TM C - 37.5°- 2 Monitor Receivers

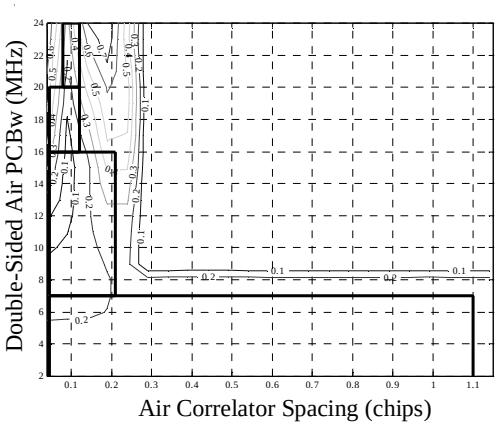

Figure 5-64 E-L Correlators – TM C - 52.5°- 2 Monitor Receivers (SQM2b)

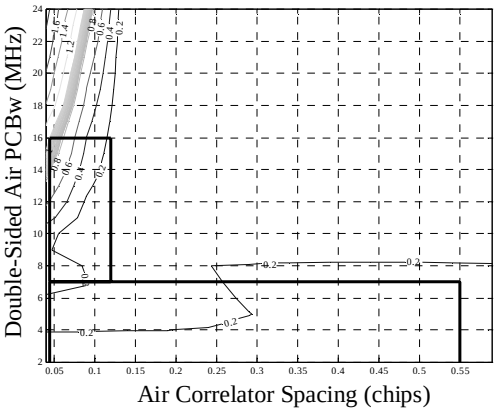

Figure 5-67 ΔΔ Correlators – TM C - 52.5°- 2 Monitor Receivers (SQM2b)

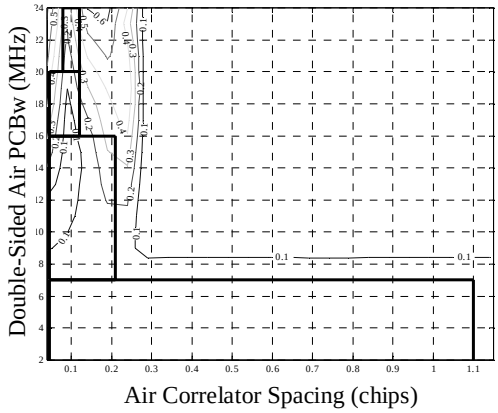

Figure 5-65 E-L Correlators – TM C - 67.5°- 2 Monitor Receivers (SQM2b)

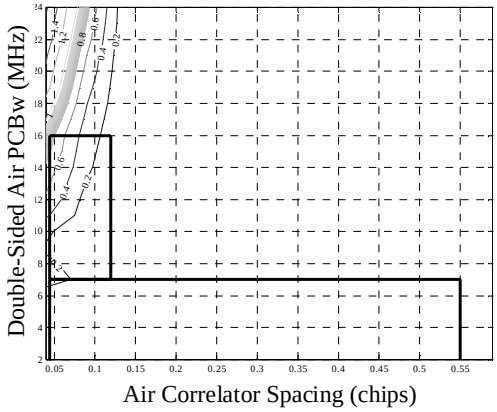

Figure 5-68 ΔΔ Correlators – TM C - 67.5°- 2 Monitor Receivers (SQM2b)

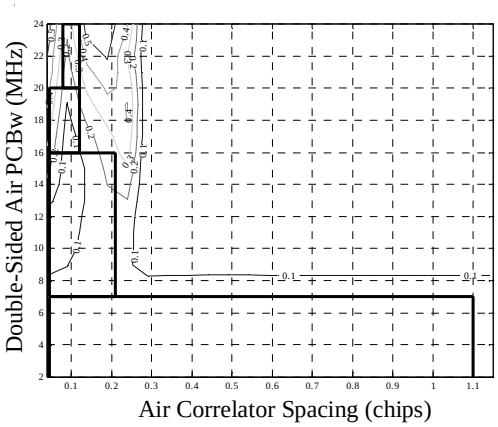

Figure 5-66 E-L Correlators – TM C - 82.5°- 2 Monitor Receivers (SQM2b)

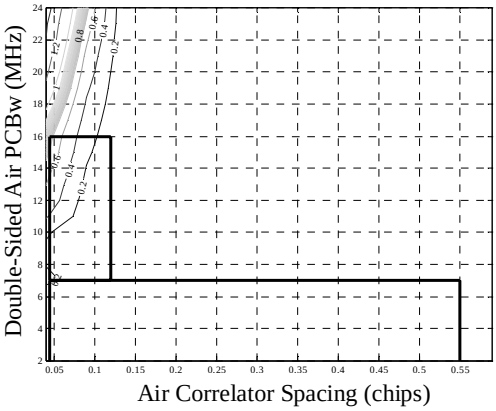

Figure 5-69 ΔΔ Correlators – TM C - 82.5°- 2 Monitor Receivers (SQM2b)

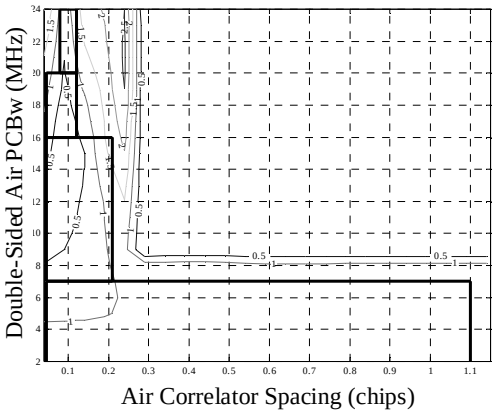

Figure 5-70 E-L Correlators – TM C - 7.5°- 3 Monitor Receivers (SQM2b)

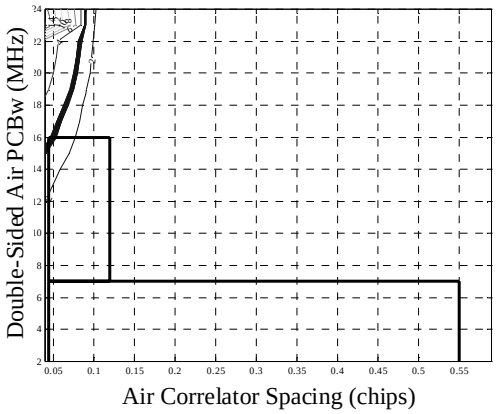

Figure 5-73 ΔΔ Correlators – TM C - 7.5°- 3 Monitor Receivers (SQM2b)

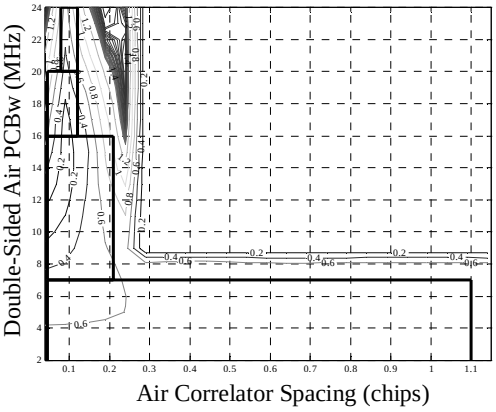

Figure 5-71 E-L Correlators – TM C - 22.5°- 3 Monitor Receivers (SQM2b)

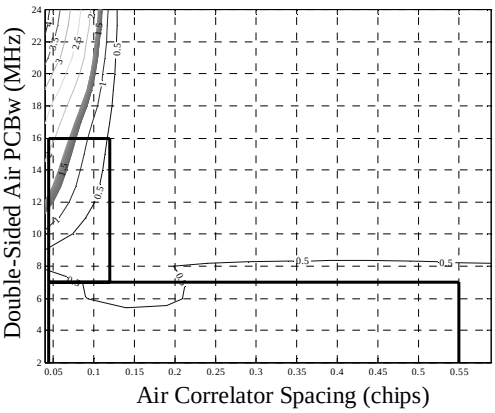

Figure 5-74 ΔΔ Correlators – TM C - 22.5°- 3 Monitor Receivers (SQM2b)

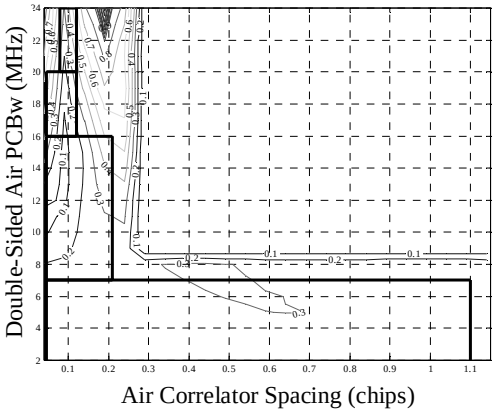

Figure 5-72 E-L Correlators – TM C - 37.5°- 3 Monitor Receivers (SQM2b)

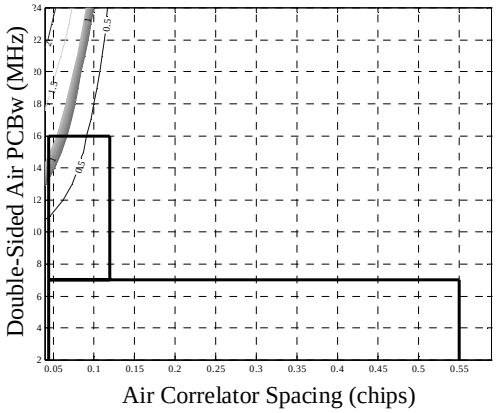

Figure 5-75 ΔΔ Correlators – TM C - 37.5°- 3 Monitor Receivers (SQM2b)

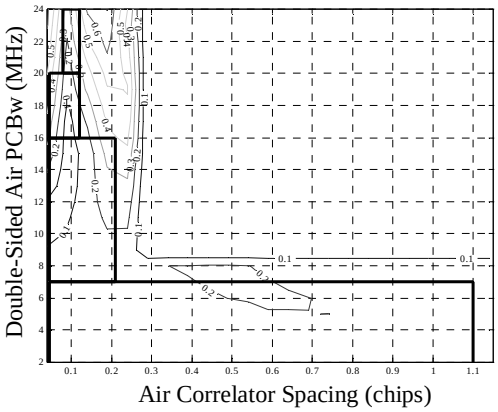

Figure 5-76 E-L Correlators – TM C - 52.5°- 3 Monitor Receivers (SQM2b)

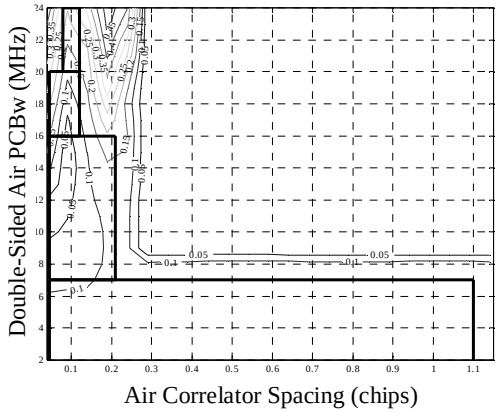

Figure 5-77 E-L Correlators – TM C - 67.5°- 3 Monitor Receivers (SQM2b)

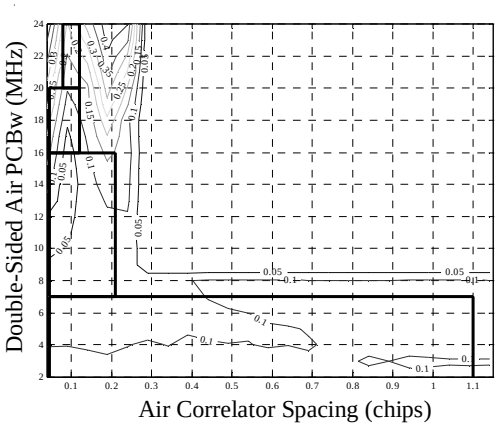

Figure 5-78 E-L Correlators – TM C - 82.5°- 3 Monitor Receivers (SQM2b)

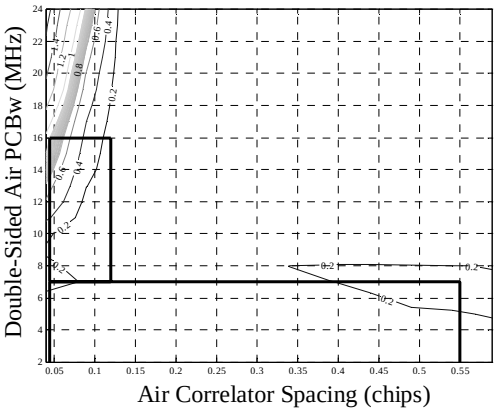

Figure 5-79 ΔΔ Correlators – TM C - 52.5°- 3 Monitor Receivers (SQM2b)

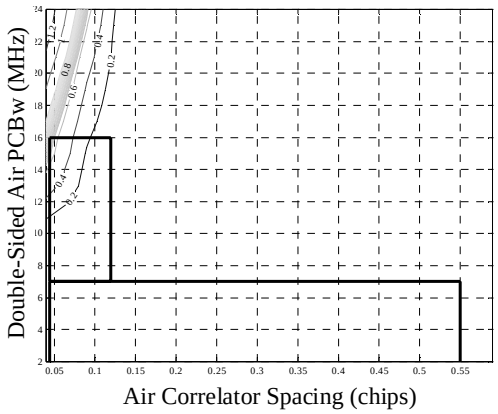

Figure 5-80 ΔΔ Correlators – TM C - 67.5°- 3 Monitor Receivers (SQM2b)

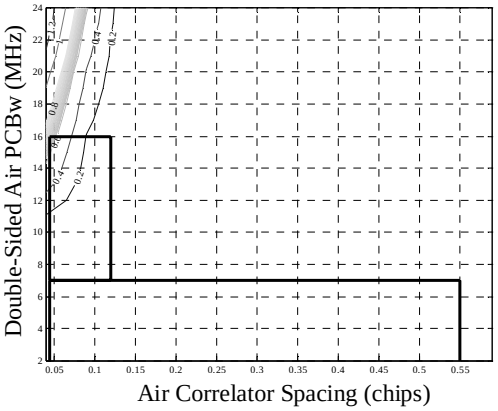

Figure 5-81 ΔΔ Correlators – TM C - 82.5°- 3 Monitor Receivers (SQM2b)

The GAD C (Category II and III) MERRs are significantly smaller than the corresponding GAD B (Category I) curves. However, meeting these error requirements presumes additional measures have been taken to mitigate the multipath at the reference station. Notably, this includes usage of the Multipath-Limiting Antenna (MLA) briefly discussed in Chapter 1, Section 1.8.1. Intuitively, such technology should improve (i.e., reduce) the MDEs at low elevation angles where the multipath correlation peak distortions are significant. At higher elevation angles significantly smaller reductions become possible, since the MP is already generally much less pronounced. Appendix B discusses the changes and modifications to the SQM monitor receiver configuration required to accommodate these more stringent MERRs at high (and low) elevation angles.

5.7.3 Differential Group Delay Analysis

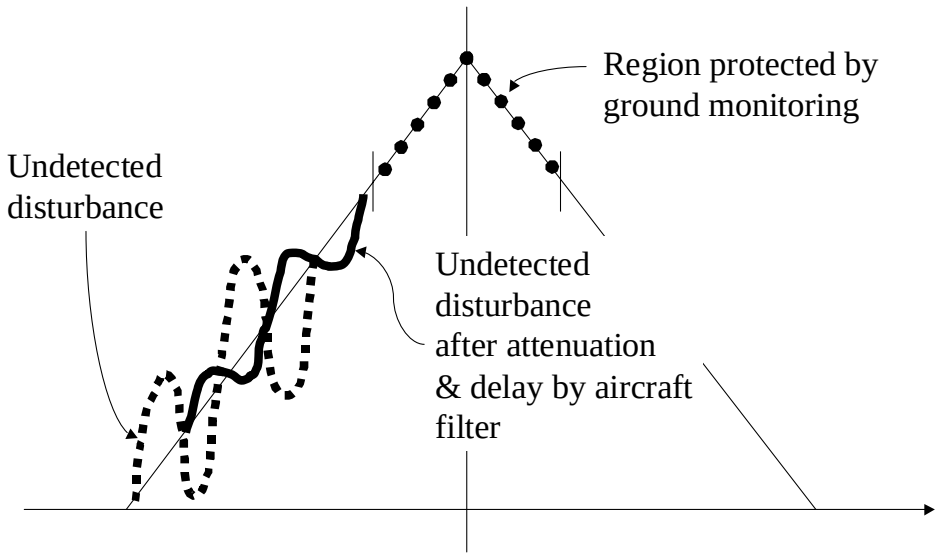

Figure 5-82 Impact of Differential Group Delay on the Aircraft Precorrelation Filter

The MERR analysis only examined the different 3dB-bandwidths of the avionics precorrelation filters. These bandwidth differences accounted for varying attenuation of EWF distortions. In general, however, user precorrelation filter implementations may also

have vastly different group delay variations. Different group delays cause the EWF distortions to have different time-offsets, or delays, which may also impact the resulting PREs. (Figure 5-82 illustrates this effect.) For this reason, a robust SQM analysis must also analyze the sensitivity of the maximum PREs (and, hence the maximum regional PREs) to this effect.

The precorrelation filter of a receiver can be described as a linear time-invariant system having both frequency-dependent magnitude, $H(\omega)$, and phase, $\phi(\omega)$, components. Such a filter may be given in the time domain as $h_{pre}(t)$. It follows that the postcorrelation filter response is simply

$$h_{post}(t) = h_{pre}(t) * R(\tau) \tag{5.8}$$

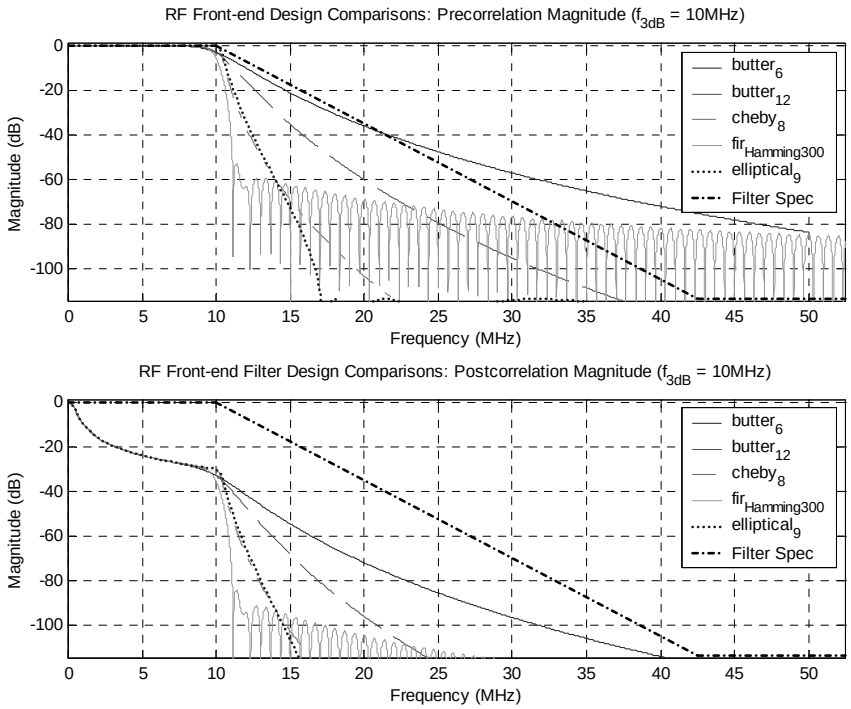

Figure 5-83 Various Filter Design Implementations

Based on Figure 5-83 compares the precorrelation and postcorrelation magnitude responses for the following filter implementations (with an 8MHz single-sided bandwidth):

- 6^{th}-order Butterworth
- 12^{th}-order Butterworth
- 8^{th}-order Tchebychev (0.5dB passband ripple)
- 9^{th}-order elliptical
- 300-tap FIR (Hamming window)

Note that of these filters, the 6^{th}-order Butterworth has the slowest rolloff (i.e., the smallest transition band attenuation rate as a function of frequency). This filter will attenuate frequencies above f_{3dB} significantly less than the other implementations. It comes closest to the minimum transition band rolloff required by LAAS. Accordingly, the 6^{th}-order Butterworth filter has a relatively conservative magnitude response. (Lower-order Butterworths will, of course have even more conservative magnitude responses. Section 5.7.4 examines SQM sensitivity to this filter characteristic.)

The group delay of the precorrelation filter described in Equation (5.8) is then

$$\mathrm{T}_{\mathrm{Gd}}(\omega) = \text{group delay}\left[H_{pre}(\omega)\right] = -\frac{\partial}{\partial\omega}\left\{\arg\left[H_{pre}(\omega)\right]\right\} = -\frac{\partial\phi}{\partial\omega}(\omega) \quad (5.9)$$

[Oppenheim].

From consideration of Figure 5-82, LAAS requires that the absolute value of the resulting differential group delay be bounded as follows

$$\left|\frac{\partial\phi}{\partial\omega}(\omega = 2\pi f_{3\mathrm{dB}}) - \frac{\partial\phi}{\partial\omega}(\omega = 2\pi f_0)\right| \le 150 \text{ nanoseconds}$$
$$f_{3\mathrm{dB}} = 3\mathrm{dB} \text{ cutoff frequency} \quad (5.10)$$
$$f_0 = \text{center frequency}$$
$$\phi(\omega) = \text{filter's phase response}$$

The maximum of the filter group relay occurs approximately at $f=f_{3dB}$. Accordingly, to bound how much the EWF perturbation can shift, the LAAS specification states that the maximum differential group delay of the (ground and airborne) receiver precorrelation filters must be no greater than 150ns. The differential group delay, $d\mathrm{T}_{Gd}$, is given by

$$d\mathrm{T}_{Gd}(\omega) = \mathrm{T}_{Gd}(\omega) - \mathrm{T}_{Gd}(\omega = 0) \tag{5.11}$$

by subtracting the filter group delay (T_{Gd} at $\omega=0$) from the group delay response at all frequencies (T_{Gd} for $\omega \geq 0$).

Figure 5-84 below shows the differential group delays corresponding to the five filters shown previously in Figure 5-83. In general, the maximum $d\mathrm{T}_{Gd}$'s increase for an infinite-impulse response (IIR) filter as it becomes sharper (i.e., has a faster rolloff). The maximum $d\mathrm{T}_{Gd}$'s increase as the order of the filter increases (while f_{3dB} remains constant) and/or the 3dB bandwidth decreases (while the filter order remains constant). Conversely, FIR filters have the (very desirable) characteristic of being linear phase. For these filters, the group delay is constant and $d\mathrm{T}_{Gd}=0$ for all frequencies, f.

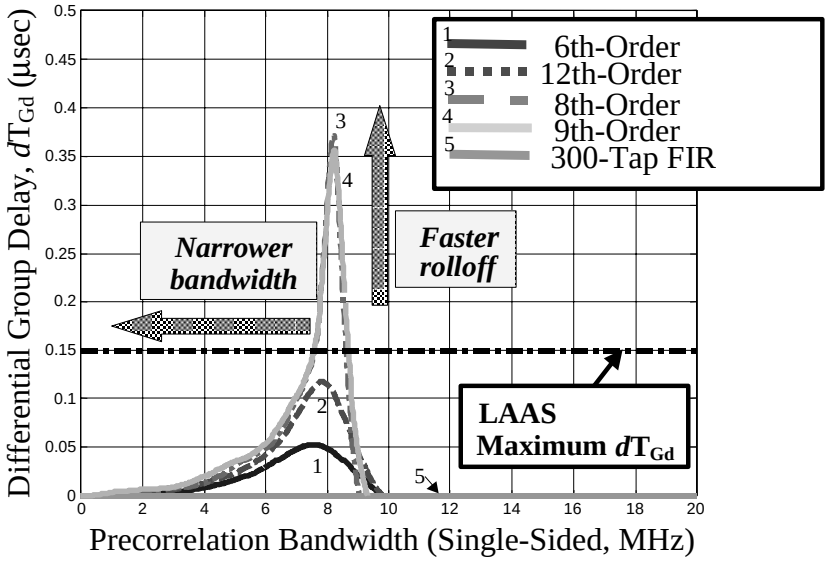

Figure 5-84 Passband Differential Group Delays of Five Different Filter Models

To isolate the differential group delay ($d\mathrm{T}_{\mathrm{Gd}}$) parameter for a sensitivity analysis, for a given 3dB bandwidth, the analysis attempted to constrain the user filter magnitude response and vary the filter $d\mathrm{T}_{\mathrm{Gd}}$ from 0 to 150ns. For this analysis, a Butterworth filter prototype was chosen as the baseline model (magnitude constraint) for the user filter implementations for the following reasons:

- Butterworth filters are simple to design and require relatively low orders for satisfactory implementations.

- Butterworth filters have minimal passband magnitude variations (i.e., a maximally flat passband magnitude response) as a function of frequency.

- Most of the SQM analysis to date (by Stanford, STNA, and others) has employed a 6^{th}-order Butterworth filter as the user filter (and on the ground). This analysis assisted in determining the generality of those results. [Macabiau00a], [Macabiau00b], [Van Dierendonck00], [Bruce00].

A 300-tap Hamming Window FIR (zero-$d\mathrm{T}_{\mathrm{Gd}}$) filter was implemented as the ground differential reference filter and the monitor receiver (16MHz) filter. This completely removed the effects of the reference and monitor filter $d\mathrm{T}_{\mathrm{Gd}}$'s from consideration.

Filter Design Procedure:

1) Design a stable digital Butterworth filter (14^{th}-order) prototype to have a single-sided bandwidth of $f=f_{3\mathrm{dB}}$ and a maximum $d\mathrm{T}_{\mathrm{Gd}}$ of 150ns.

2) Scale the group delay response of this filter to have maximum $d\mathrm{T}_{\mathrm{Gd}}$'s of 30, 60, 90, 120, and 150ns respectively.

3) For each T_{Gd} response, construct new complex filter magnitude responses. Using the magnitude responses of the original design together with new phase responses, ϕ, makes this possible. These phase responses are obtained by integrating the scaled T_{Gd}'s found in Step 2.

4) Obtain new stable transfer functions by finding the inverse frequency responses—using the inverse Fourier Transform—of the new complex magnitudes.

5) Plot filter magnitudes, phases and dT_{Gd}'s graphically to confirm they are stable and all constraints are met.

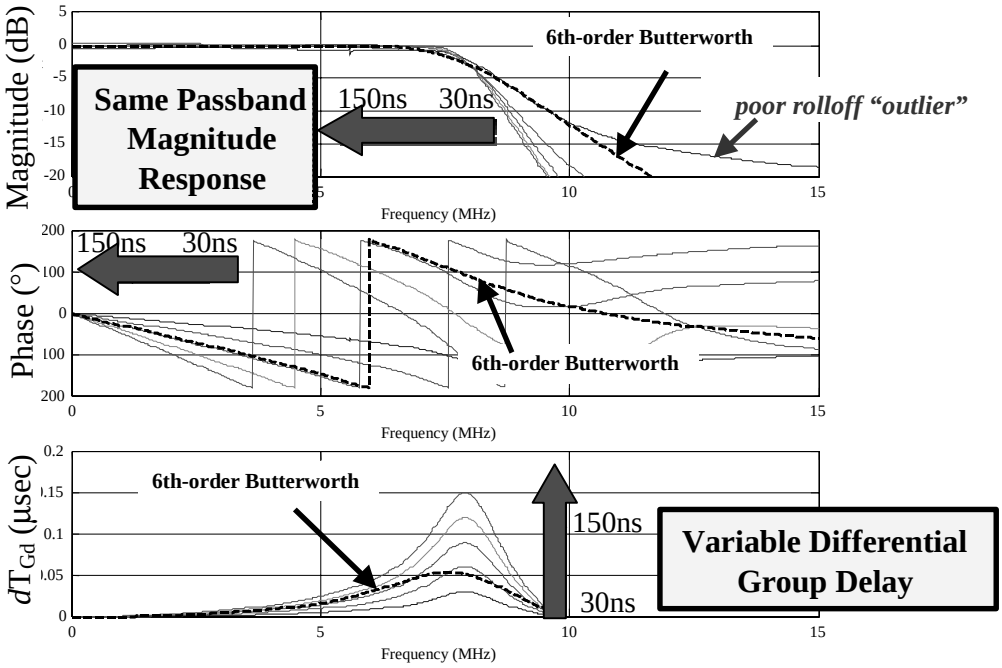

Figure 5-85 Butterworth Filter Designs with Varying Differential Group Delays

Figure 5-85 above shows the results of this design procedure. Note that the resulting filter magnitude responses were not all identical. Specifically, the original (14^{th}-order) IIR digital Butterworth designs better met the design constraints. This is due to the fact that as the dT_{Gd}'s approach zero, IIR filters become better approximated by FIR designs. Accordingly, the magnitude responses are approximately equal for all implementations except the 30ns dT_{Gd} design. This means high-frequency EWFs (e.g., those with f_d's above the 3dB bandwidth) for that filter were attenuated significantly less than for the others. The dashed curves depict the magnitude, phase, and dT_{Gd} characteristics of the 6^{th}-order Butterworth filter for comparison.

Differential Group Delay Analysis Results

The MERR analyses revealed that the largest regional PREs occur for only a localized few critical airborne receiver configurations. If user EWF-induced PREs are sensitive to $d\mathrm{T}_{Gd}$'s, they will likely affect these receiver configurations most significantly. Figure 5-86 graphically highlights each of these configurations for which the group delay variations were explored. The five critical receiver configurations (i.e., configurations having maximum differential PREs)—four E-L's and one critical ΔΔ—are given in Table 5-10:

Receiver Type	Correlator Spacing, (T_c, chips)	Precorrelation Bandwidth (MHz)
E-L	0.21	16
E-L	0.045	20
E-L	0.08	24
E-L	0.12	24
ΔΔ	0.045	16

Table 5-10 Most Sensitive Airborne Receiver Configurations Tested in $d\mathrm{T}_{Gd}$ Analysis

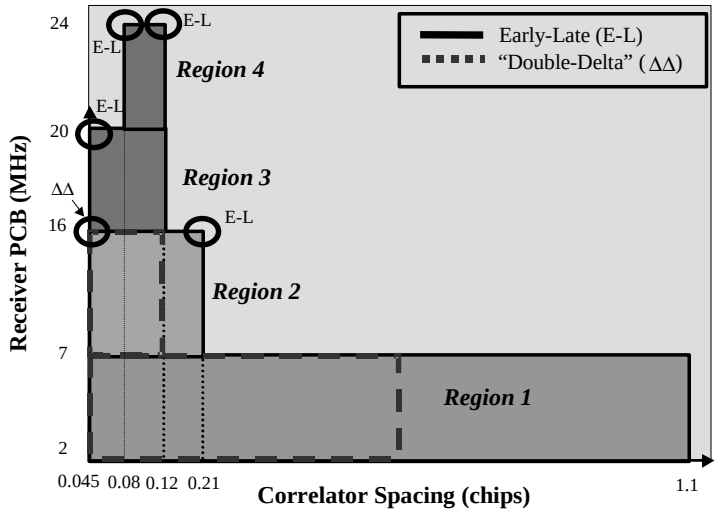

Figure 5-86 Most Sensitive Airborne Receiver Configurations Tested in $d\mathrm{T}_{Gd}$ Analysis

The next several figures plot the maximum user PREs as a function of the EWF frequency, f_d. For each EWF frequency, the analysis computed user PRE (at a selected correlator spacing and PCB). For each f_d, the analysis maximized this error over all σ and Δ. A total of six curves are shown on each plot. Each curve corresponds to a filter with a different group delay; the maximum dT$_{Gd}$'s for each filter are indicated in the legend. A vertical (dotted) line indicates the single-sided user receiver (3dB) PCBw. When SQM2b was implemented, a horizontal (dashed) line indicates the MERR corresponding to the assumed elevation angle.

Group delay analyses were performed both with and without implementing SQM2b. Without any monitoring, the results indicate maximum total PRE variations of 1-2 meters. (See Figure 5-87 to 5-91.) Also, as expected, the maximum PREs become smaller as f_d increases, even without SQM. This is because the avionics filter attenuates the effects of the EWFs. Also, as discussed in Section 5.5.2, the amplitudes of EWF oscillations—hence the differential PREs—decrease as f_d increases. Note that for the narrowest correlator spacing (0.045T$_c$) and widest bandwidths (≥20MHz) the maximum PREs do not roll off as f_d increases. This is because the lead/lag errors dominate. The flattening of the peak due to large Δ is not filtered by the user front-end bandwidth. Figure 5-92 illustrates that the PREs for the same user receiver configuration do in fact roll off when Δ is removed (i.e., TM B).

Without SQM, for almost all EWF frequencies and for both the E-L and $\Delta\Delta$ receiver configurations, the variations due to group delay alone were generally between 1-2m. Further, the largest PRE variations occur due to changes in f_d as opposed to dT$_{Gd}$. In addition, in most cases the largest PREs closely correspond to those of the 6th-order Butterworth filter. Recall that the MERR analysis used the Butterworth filter model and revealed that SQM2b protected the E-L receivers. These results in combination with the MERR analysis results indicate two things. First, using SQM2b, the E-L receivers are likely already robust to variations in user differential group delays. Second, the 6th-order Butterworth filter generally produces conservative SQM performance results.

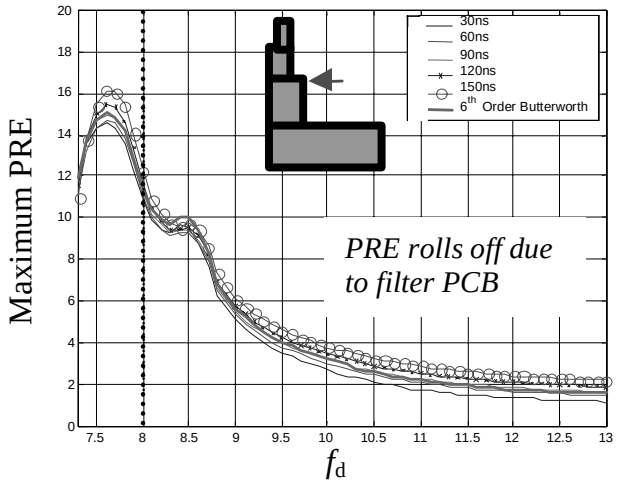

Figure 5-87 E-L Correlator dT$_{Gd}$'s (16MHz, 0.21T$_c$; no SQM)

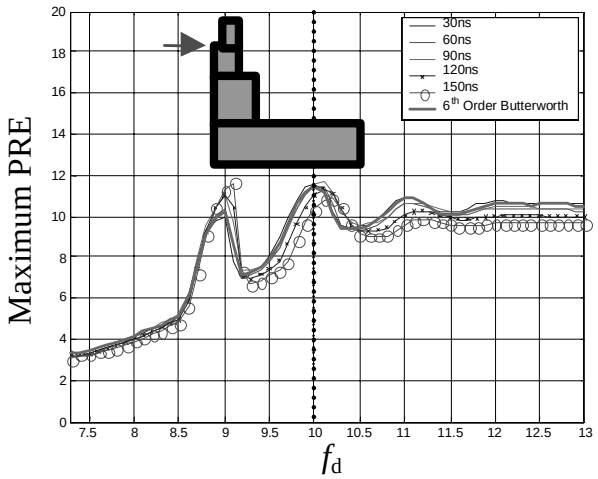

Figure 5-88 E-L Correlator dT$_{Gd}$'s (20MHz, 0.045T$_c$; no SQM)

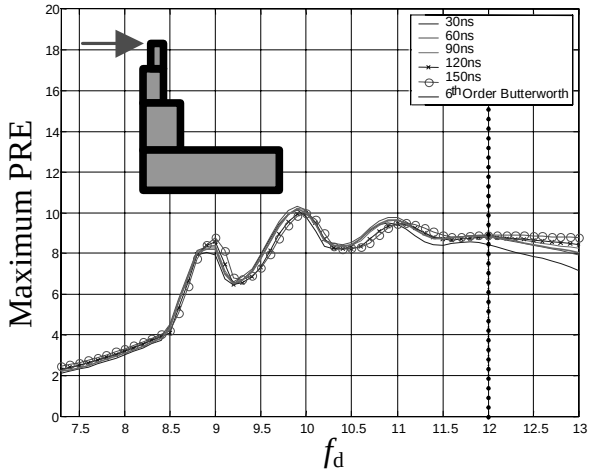

Figure 5-89 E-L Correlator dT$_{Gd}$'s (24MHz, 0.08T$_c$; no SQM)

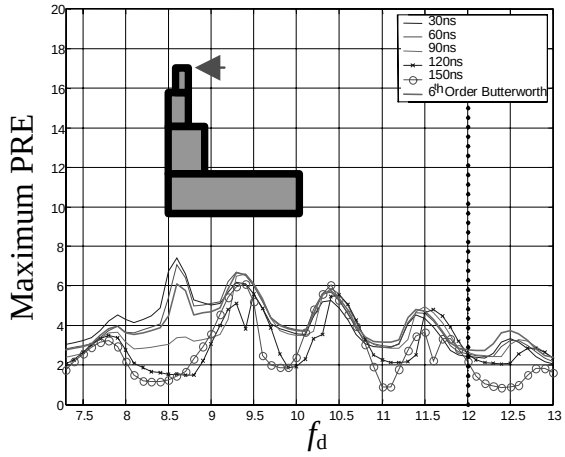

Figure 5-90 E-L Correlator dT$_{Gd}$'s (24MHz, 0.12T$_c$; no SQM)

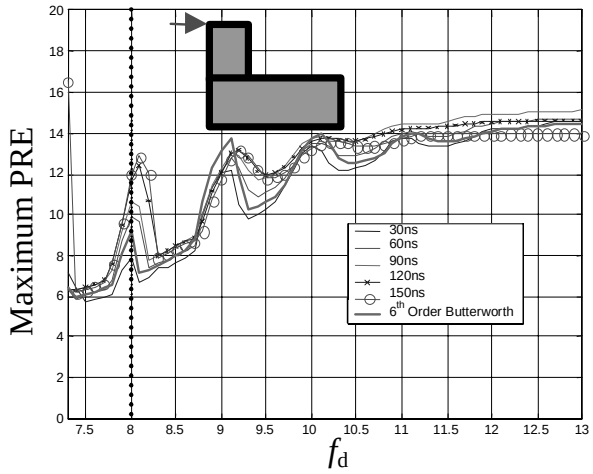

Figure 5-91 ΔΔ Correlator dT$_{Gd}$'s (16MHz, 0.045T$_c$; No SQM)

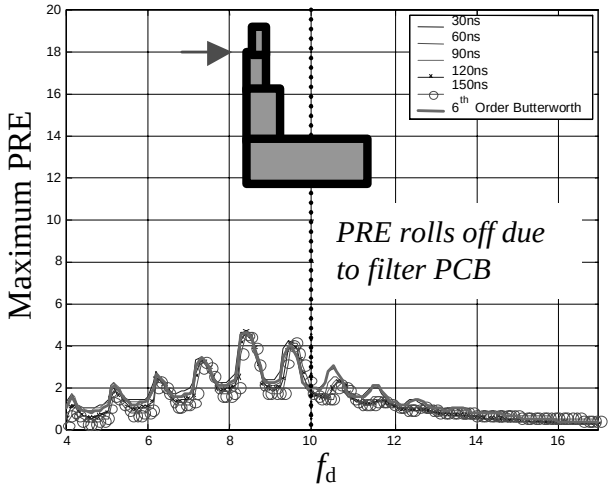

Figure 5-92 E-L Correlator dT$_{Gd}$'s (20MHz, 0.045Tc; Δ=0; no SQM)

ΔΔ Correlators - Region 2 Notch Design

Recall that the ΔΔ configurations in the 16MHz, 0.045Tc corner of Region 2 violated the MERRs (even for 100% MDEs). Had these violations occurred for the E-L correlators, it may have been necessary to redesign SQM2b (i.e., conceive and add new symmetry tests) and/or add an additional correlator pair. Since, however, the analysis presented in this section revealed that only a relatively small portion of this region violated the MERRs, the ICAO chose to modify the ΔΔ Region 2 to exclude the (relatively few) troublesome configurations.

(Note that as stated previously, the addition of an extra correlator pair may improve SQM performance, but is undesirable for practical reasons. On the other hand, additional tests may be formed using SQM2b. This is a relatively simple modification. Several additional tests were suggested to help reduce the need for the ΔΔ notch in Region 2. Appendix B describes the MERR and $d\mathrm{T}_{\mathrm{Gd}}$ analyses for these additional tests together with the 11 tests described in Section 5.7.1.)

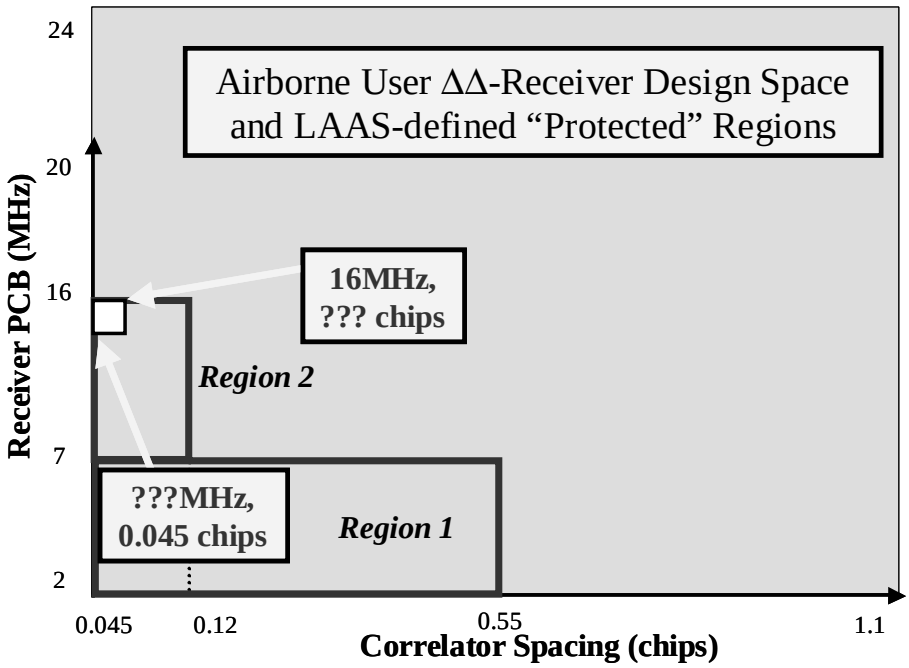

Figure 5-93 Notch Specifications and the Airborne Receiver Design Space

The specification of the excluded region, or "notch," called for the analysis of the post-SQM differential group delay sensitivity of PREs in the vicinity of these critical ΔΔ receiver configurations. (See Figure 5-93.) Conservatively, this research analyzed a square notch design. A more complicated notch shape may accommodate more ΔΔ receivers in analysis; the square notch design is able to produce a satisfactory design, and was acceptable to the receiver manufacturers.

For this analysis, recall that the maximum PREs for elevation angles between 10° and (approximately) 60° violated the MERRs. The contour plots indicate that the maximum PREs occurred for the 0.045Tc and 16MHz PCBw ΔΔ configuration. These plots also indicate that the Region 2 PREs decreased for decreasing PCBw. These maximum PREs also decreased for increasing correlator spacing (d_{narrow}). Significantly, note that the dimensions of a rectangular notch can be determined by defining the following two parameters:

- Maximum PCBw at a correlator spacing of 0.045Tc
- Minimum correlator spacing at a PCBw of 16MHz

Figure 5-94 below illustrates these configurations and the notch design process.

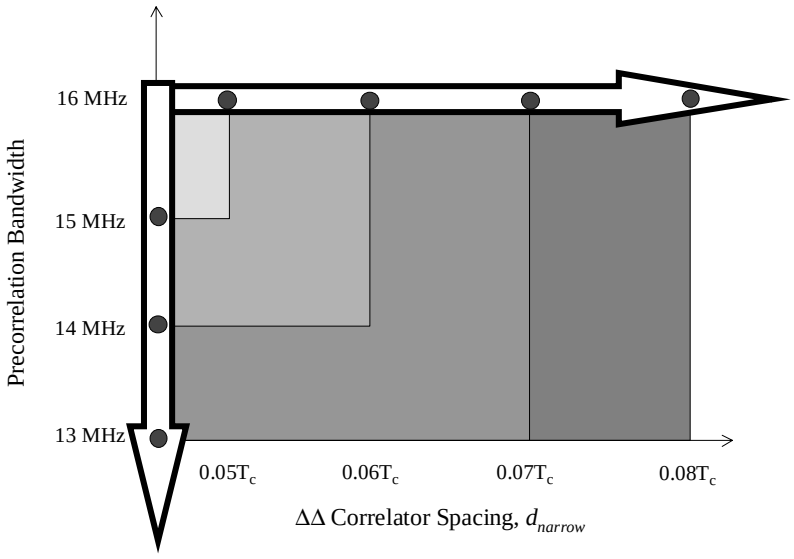

Figure 5-94 Procedure for Notch Design Analysis

To evaluate more than a few points along the edge of the notch would prove inefficient, since only a few are required to specify it. Specifying the two border configuration points uniquely determines the lower-right corner configuration. Again, the upper-left corner configuration was already seen to have unacceptably large PREs for certain elevation angles. (Also the contour plots showed that the maximum PREs decrease essentially monotonically as PCBw decreased and correlator spacing increased.) Accordingly, for both two and three monitor receivers and elevation angles between 10° and 60° (in 10-degree increments), the ΔΔ correlators were analyzed for the following configurations:

- $0.045T_c$, 15MHz
- $0.045T_c$, 14MHz
- $0.06T_c$, 16MHz
- $0.07T_c$, 16MHz

Figure 5-95 through 5-142 below show the dT_{Gd} results for these configurations. For each of these plots, the corresponding MERR appears as a horizontal line. Two important observations can be made after examining these plots. First, in every instance, *the maximum PREs occurred for the 30ns curve*. In fact, due to its extremely poor magnitude response, the 30ns curve exceeded the MERR for most elevation angles and for each configuration evaluated. (This condition is analyzed further in the following section, Section 5.7.5.) Second, for the six filters evaluated, *the 6th-order Butterworth resulted in the second-largest PREs*; it was the next most conservative filter of this suite.

Table 5-11 and 5-12 summarize these notch design results. Note that although the 6th-order Butterworth curves in these plots never exceeded the MERRs for the $0.045T_c$, 15MHz configuration, the MERR contour plot results in the previous section indicated the configurations at this correlator spacing did not meet the error requirements. This apparent discrepancy is caused by the fact that the MERR analysis used a 6th-order Butterworth filter for the monitor precorrelation filter as well as for the airborne filter. Recall that this (differential group delay) analysis implements an FIR filter as the monitor filter since it has

dT_{Gd}=0 over all frequencies. For these reasons, clearly *the safer (i.e. more conservative) choice for the notch bandwidth specification (at 0.045T_c) is the lowest possible PCBw*.

	0.045T_c, 15MHz				0.045T_c, 14MHz			
	2 Monitor Receivers		3 Monitor Receivers		2 Monitor Receivers		3 Monitor Receivers	
	Max Curve	2nd Max	Max Curve	2nd Max	Max Curve	2nd Max	Max Curve	2nd Max
10°	30ns	6oB	30ns	6oB	30ns	6oB	30ns	6oB
20°	30ns	6oB	30ns	6oB	30ns	6oB	30ns	6oB
30°	30ns	6oB	30ns	6oB	30ns	6oB	30ns	6oB
40°	30ns	6oB	30ns	6oB	30ns	6oB	30ns	6oB
50°	30ns	6oB	30ns	6oB	30ns	6oB	30ns	6oB
60°	30ns	6oB	30ns	6oB	30ns	6oB	30ns	6oB

Table 5-11 Notch Design dT_{Gd} Summary Table A (Shaded Boxes Indicate Curves which Exceeded the MERR for a Given Elevation Angle. 6oB Denotes 6th-order Butterworth.)

	0.06T_c, 16MHz				0.07T_c, 16MHz			
	2 Monitor Receivers		3 Monitor Receivers		2 Monitor Receivers		3 Monitor Receivers	
	Max Curve	2nd max	Max Curve	2nd max	Max Curve	2nd max	Max Curve	2nd max
10°	30ns	6oB	30ns	6oB	30ns	6oB	30ns	6oB
20°	30ns	6oB	30ns	6oB	30ns	6oB	30ns	6oB
30°	30ns	6oB	30ns	6oB	30ns	6oB	30ns	6oB
40°	30ns	6oB	30ns	6oB	30ns	6oB	30ns	6oB
50°	30ns	6oB	30ns	6oB	30ns	6oB	30ns	6oB
60°	30ns	6oB	30ns	6oB	30ns	6oB	30ns	6oB

Table 5-12 Notch Design dT_{Gd} Summary Table B (Shaded Boxes Indicate Curves which Exceeded the MERR for a Given Elevation Angle. 6oB Denotes 6th-order Butterworth.)

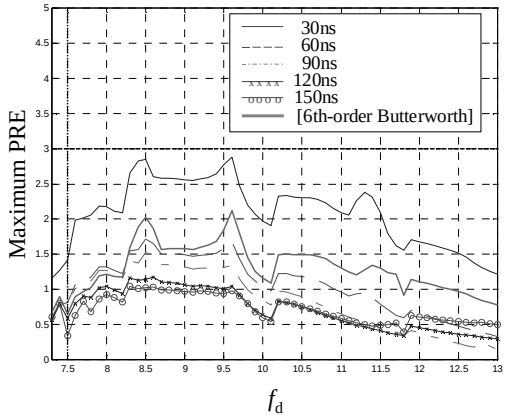

Figure 5-95 10° Elevation Angle: $0.045T_c$, 15MHz, 2 Monitor Receivers

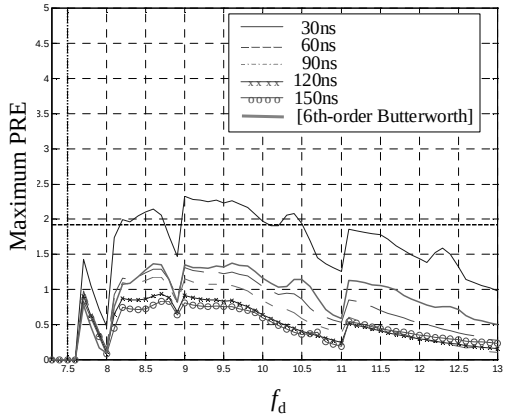

Figure 5-96 20° Elevation Angle: $0.045T_c$, 15MHz, 2 Monitor Receivers

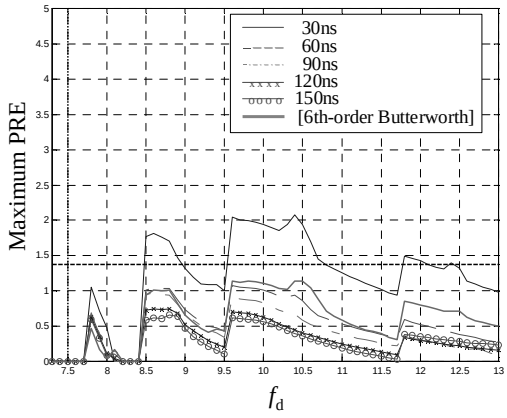

Figure 5-97 30° Elevation Angle: $0.045T_c$, 15MHz, 2 Monitor Receivers

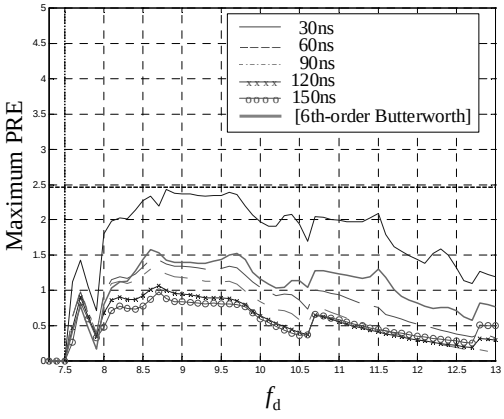

Figure 5-98 10° Elevation Angle: $0.045T_c$, 15MHz, 3 Monitor Receivers

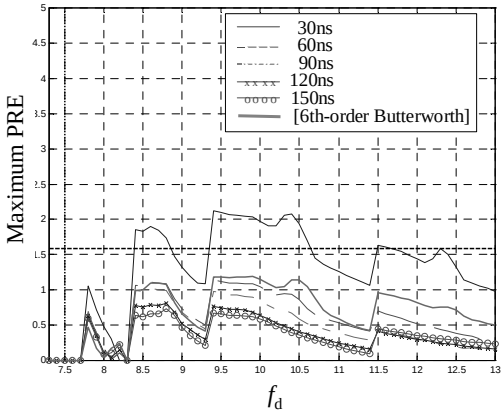

Figure 5-99 20° Elevation Angle: $0.045T_c$, 15MHz, 3 Monitor Receivers

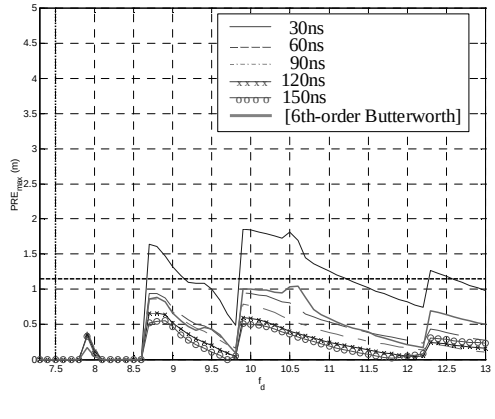

Figure 5-100 30° Elevation Angle: $0.045T_c$, 15MHz, 3 Monitor Receivers

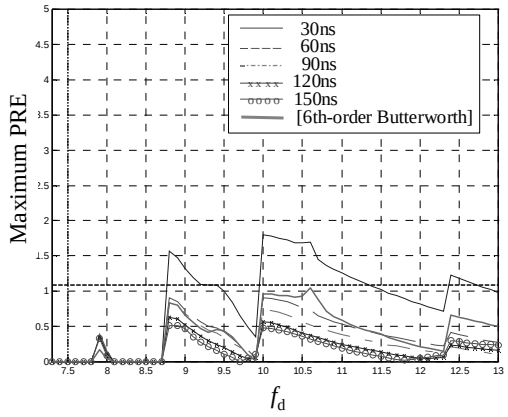

Figure 5-101 40° Elevation Angle: $0.045T_c$, 15MHz, 2 Monitor Receivers

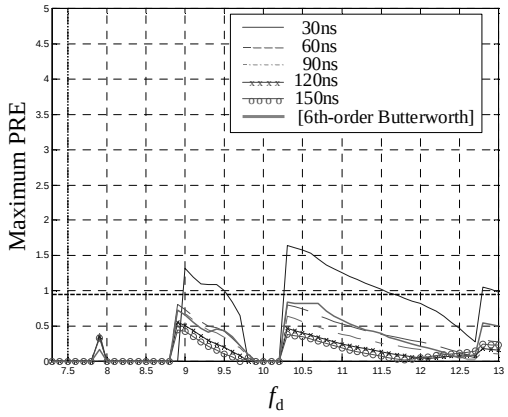

Figure 5-102 50° Elevation Angle: $0.045T_c$, 15MHz, 2 Monitor Receivers

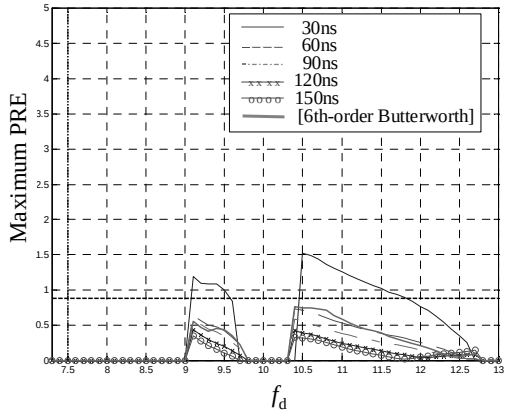

Figure 5-103 60° Elevation Angle: $0.045T_c$, 15MHz, 2 Monitor Receivers

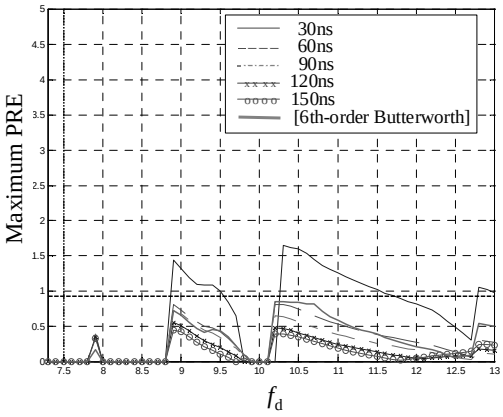

Figure 5-104 40° Elevation Angle: $0.045T_c$, 15MHz, 3 Monitor Receivers

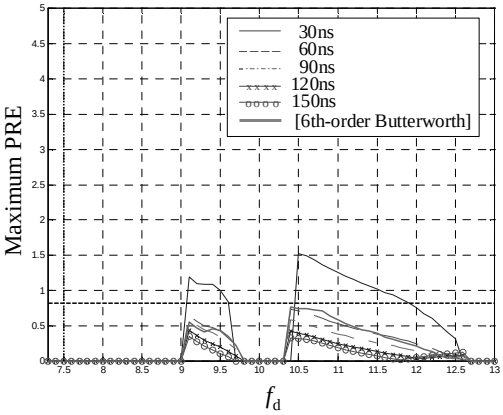

Figure 5-105 50° Elevation Angle: $0.045T_c$, 15MHz, 3 Monitor Receivers

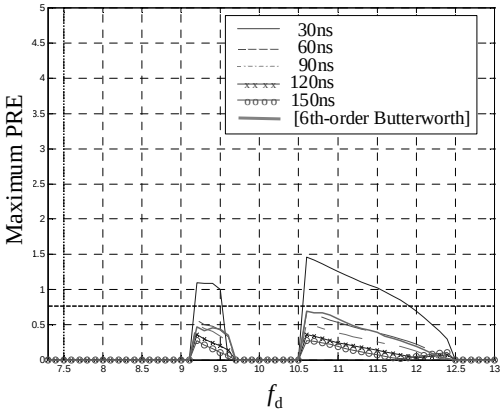

Figure 5-106 60° Elevation Angle: $0.045T_c$, 15MHz, 3 Monitor Receivers

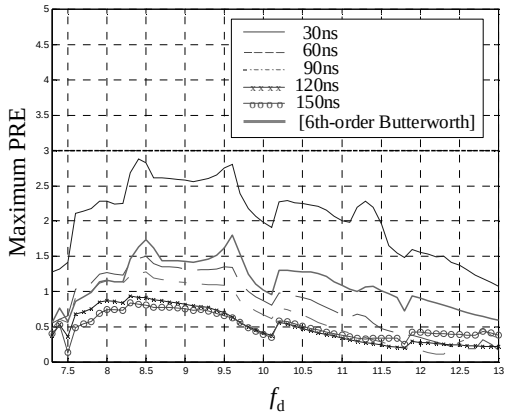

Figure 5-107 10° Elevation Angle: $0.045T_c$, 14MHz, 2 Monitor Receivers

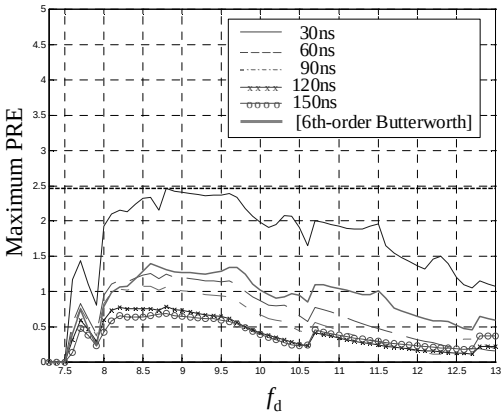

Figure 5-110 10° Elevation Angle: $0.045T_c$, 14MHz, 3 Monitor Receivers

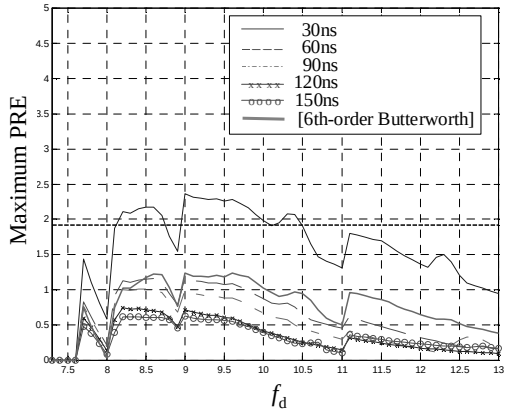

Figure 5-108 20° Elevation Angle: $0.045T_c$, 14MHz, 2 Monitor Receivers

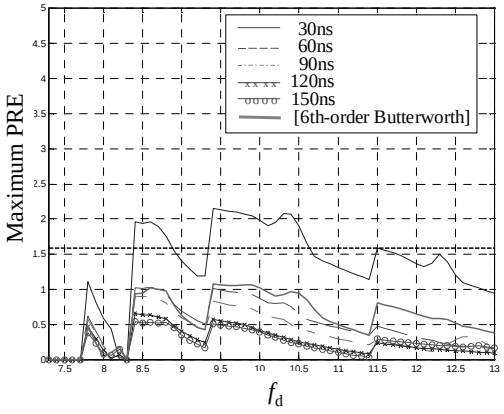

Figure 5-111 20° Elevation Angle: $0.045T_c$, 14MHz, 3 Monitor Receivers

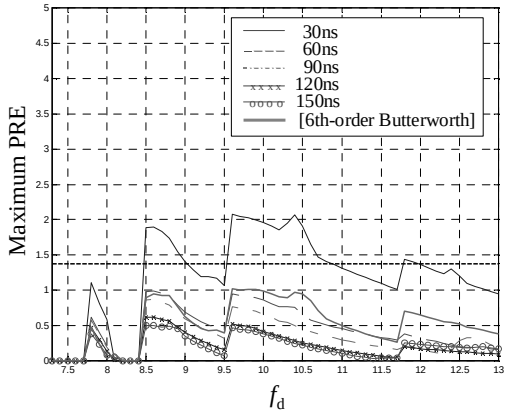

Figure 5-109 30° Elevation Angle: $0.045T_c$, 14MHz, 2 Monitor Receivers

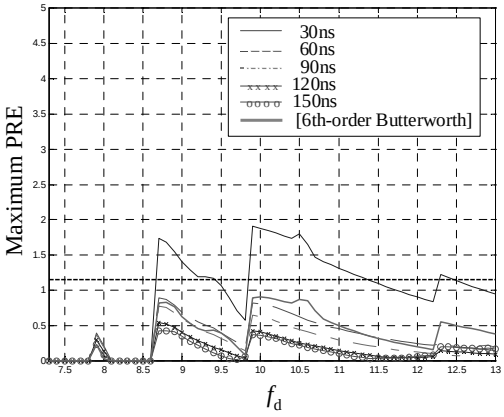

Figure 5-112 30° Elevation Angle: $0.045T_c$, 14MHz, 3 Monitor Receivers

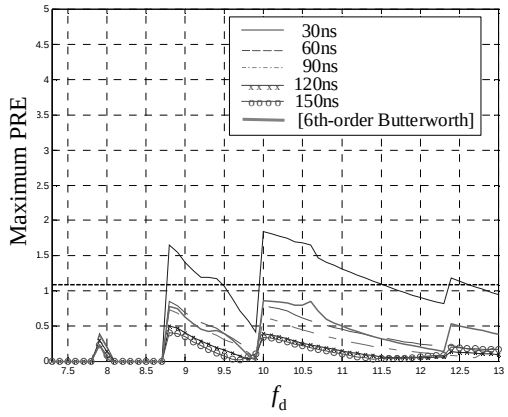

Figure 5-113 40° Elevation Angle: $0.045T_c$, 14MHz, 2 Monitor Receivers

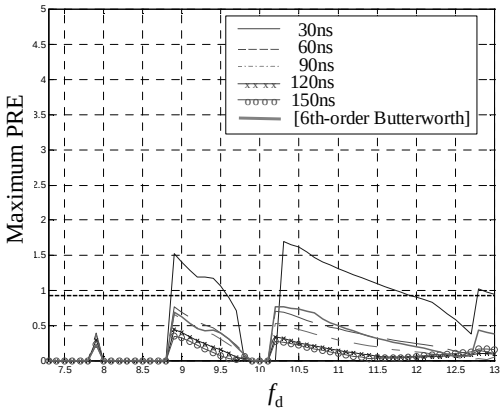

Figure 5-116 40° Elevation Angle: $0.045T_c$, 14MHz, 3 Monitor Receivers

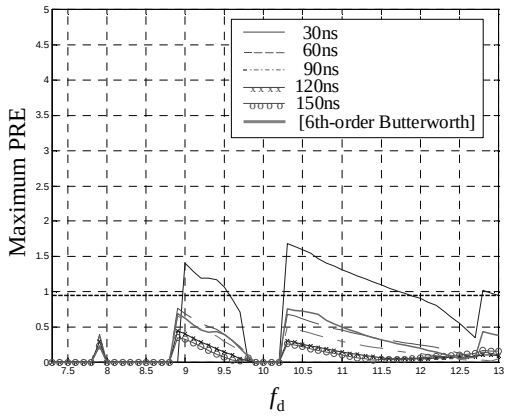

Figure 5-114 50° Elevation Angle: $0.045T_c$, 14MHz, 2 Monitor Receivers

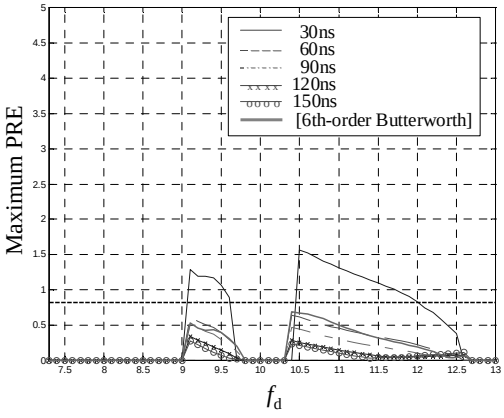

Figure 5-117 50° Elevation Angle: $0.045T_c$, 14MHz, 3 Monitor Receivers

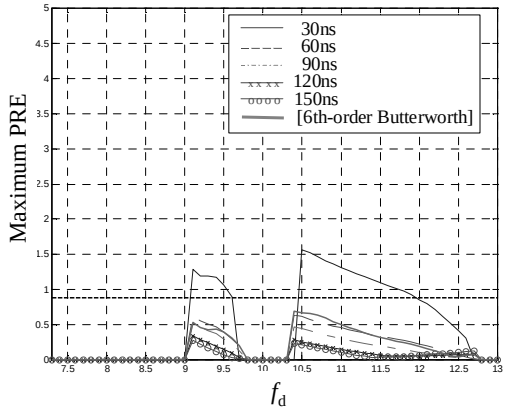

Figure 5-115 60° Elevation Angle: $0.045T_c$, 14MHz, 2 Monitor Receivers

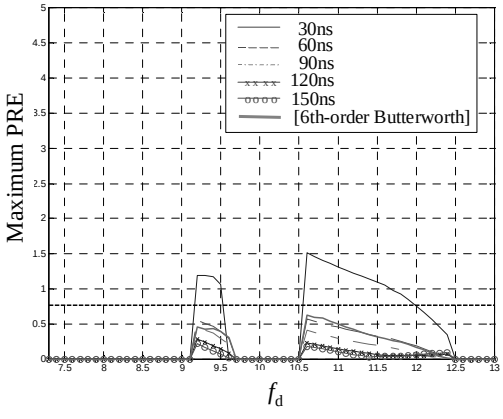

Figure 5-118 60° Elevation Angle: $0.045T_c$, 14MHz, 3 Monitor Receivers

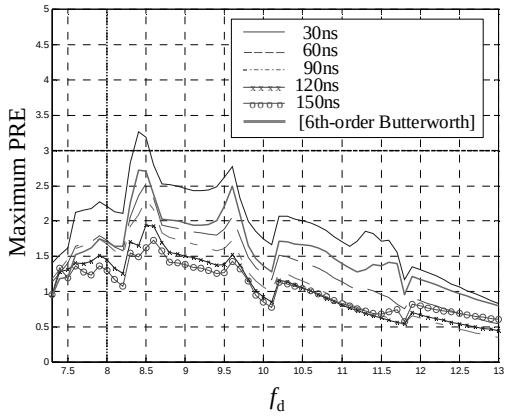

Figure 5-119 10° Elevation Angle: $0.06T_c$, 16MHz, 2 Monitor Receivers

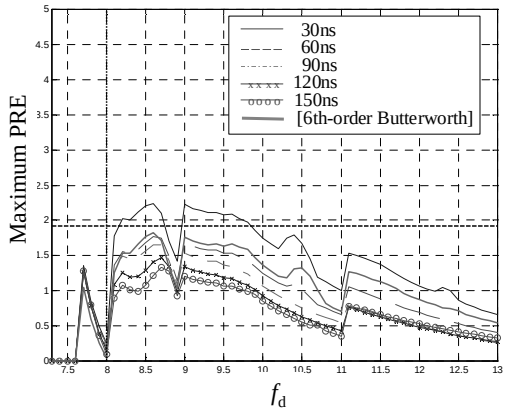

Figure 5-120 20° Elevation Angle: $0.06T_c$, 16MHz, 2 Monitor Receivers

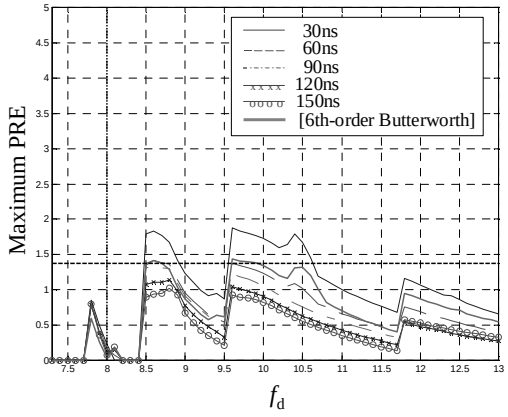

Figure 5-121 30° Elevation Angle: $0.06T_c$, 16MHz, 2 Monitor Receivers

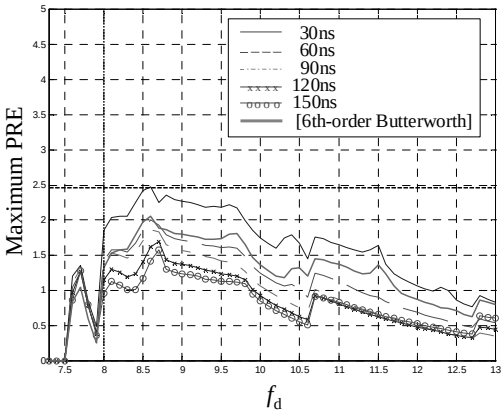

Figure 5-122 10° Elevation Angle: $0.06T_c$, 16MHz, 3 Monitor Receivers

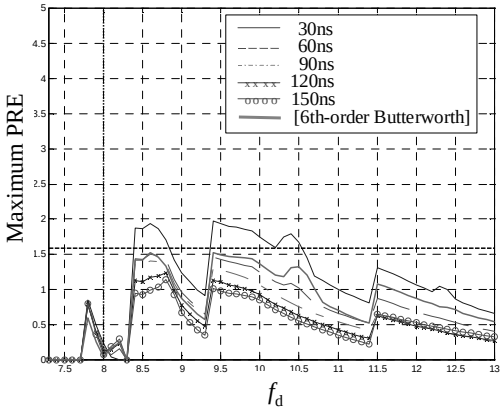

Figure 5-123 20° Elevation Angle: $0.06T_c$, 16MHz, 3 Monitor Receivers

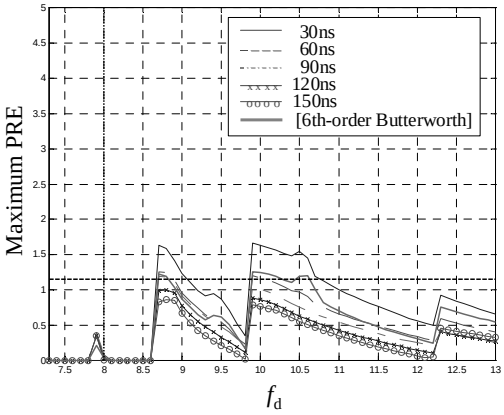

Figure 5-124 30° Elevation Angle: $0.06T_c$, 16MHz, 3 Monitor Receivers

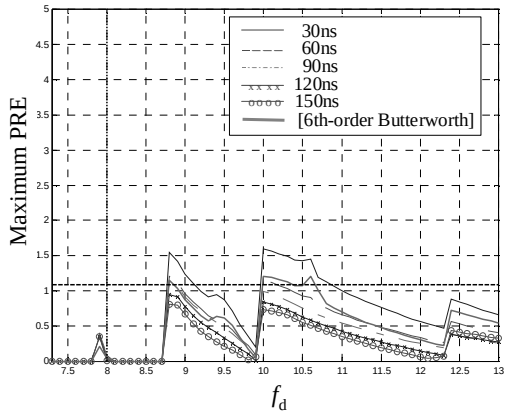

Figure 5-125 40° Elevation Angle: $0.06T_c$, 16MHz, 2 Monitor Receivers

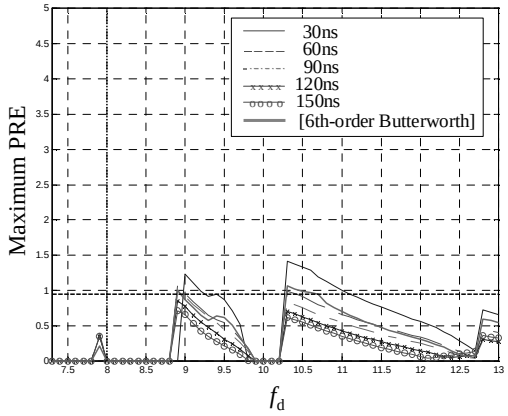

Figure 5-126 50° Elevation Angle: $0.06T_c$, 16MHz, 2 Monitor Receivers

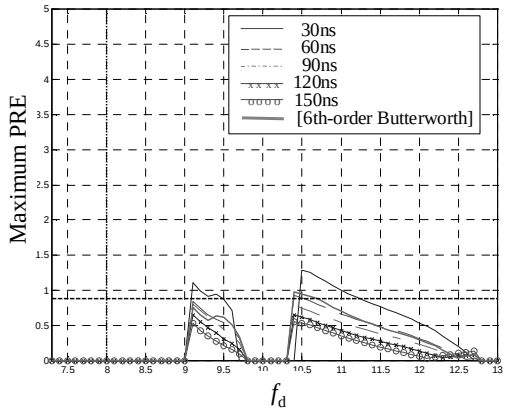

Figure 5-127 60° Elevation Angle: $0.06T_c$, 16MHz, 2 Monitor Receivers

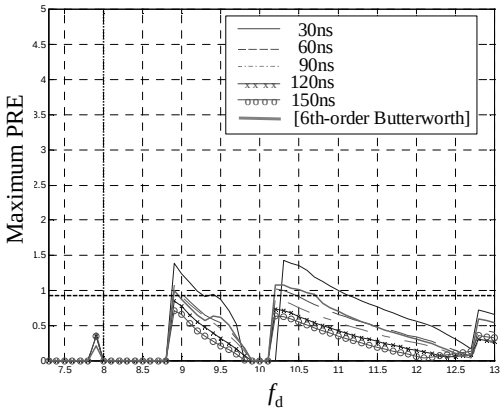

Figure 5-128 40° Elevation Angle: $0.06T_c$, 16MHz, 3 Monitor Receivers

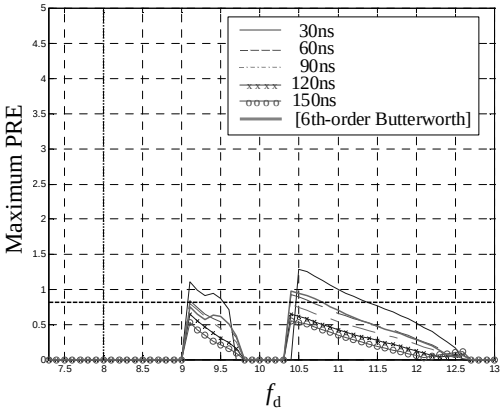

Figure 5-129 50° Elevation Angle: $0.06T_c$, 16MHz, 3 Monitor Receivers

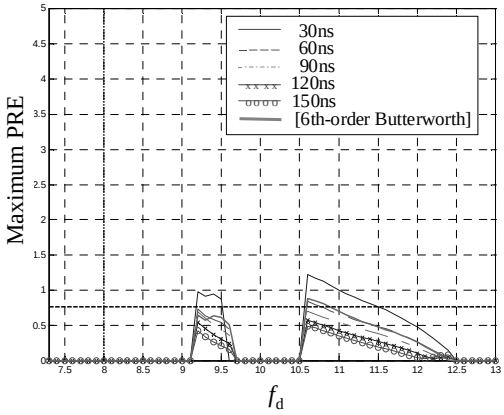

Figure 5-130 60° Elevation Angle: $0.06T_c$, 16MHz, 3 Monitor Receivers

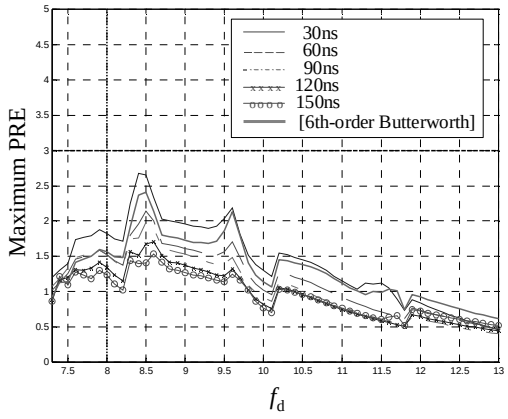

Figure 5-131 10° Elevation Angle: $0.07T_c$, 16MHz, 2 Monitor Receivers

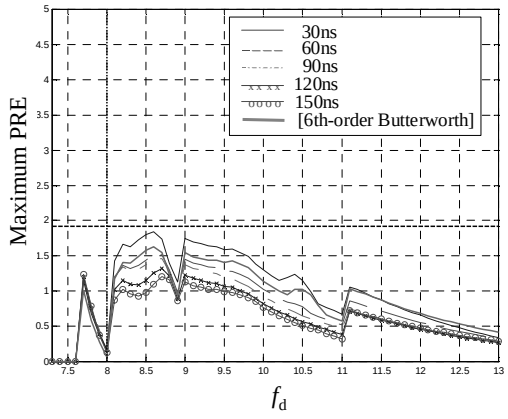

Figure 5-132 20° Elevation Angle: $0.07T_c$, 16MHz, 2 Monitor Receivers

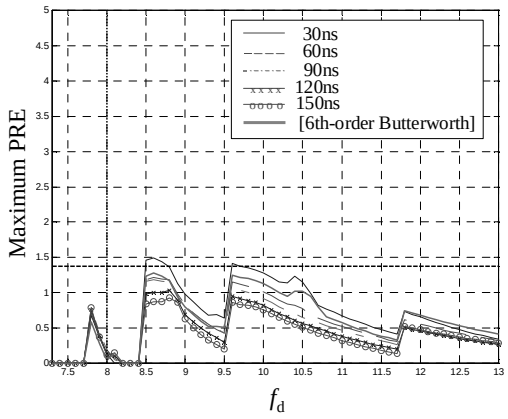

Figure 5-133 30° Elevation Angle: $0.07T_c$, 16MHz, 2 Monitor Receivers

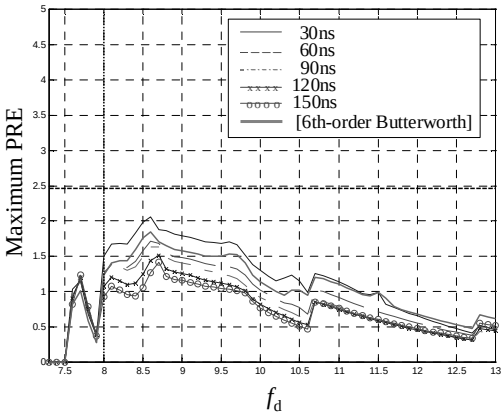

Figure 5-134 10° Elevation Angle: $0.07T_c$, 16MHz, 3 Monitor Receivers

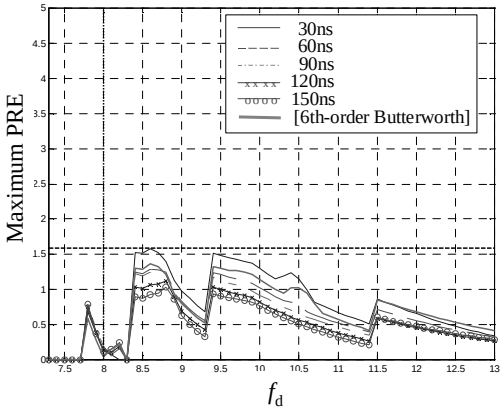

Figure 5-135 20° Elevation Angle: $0.07T_c$, 16MHz, 3 Monitor Receivers

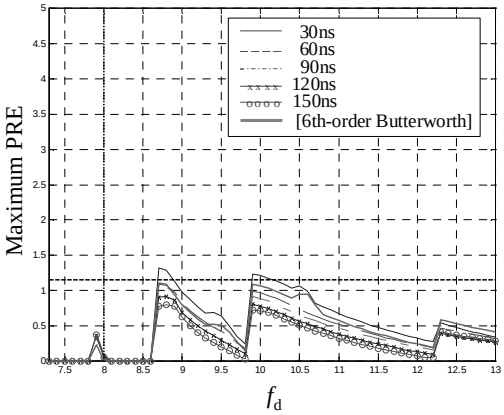

Figure 5-136 30° Elevation Angle: $0.07T_c$, 16MHz, 3 Monitor Receivers

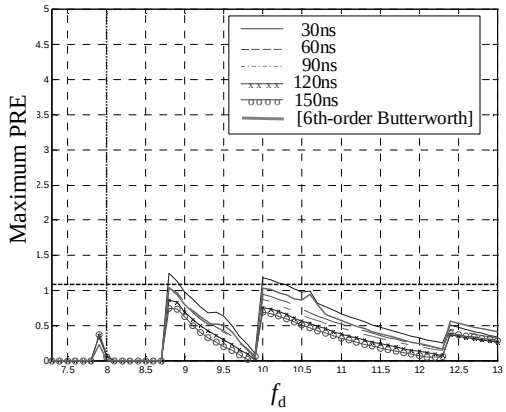

Figure 5-137 40° Elevation Angle: $0.07T_c$, 16MHz, 2 Monitor Receivers

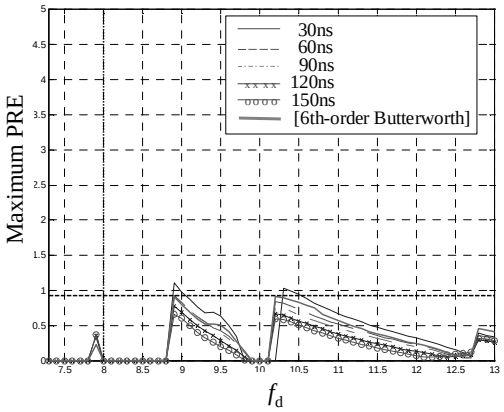

Figure 5-140 40° Elevation Angle: $0.07T_c$, 16MHz, 3 Monitor Receivers

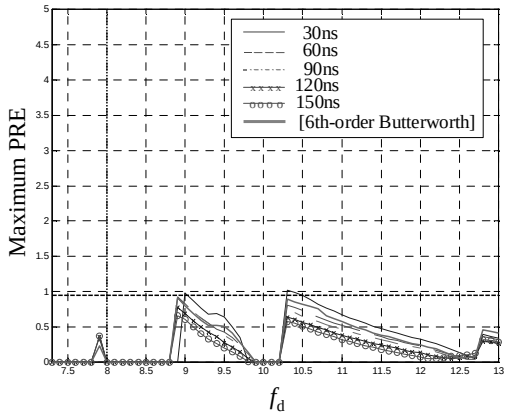

Figure 5-138 50° Elevation Angle: $0.07T_c$, 16MHz, 2 Monitor Receivers

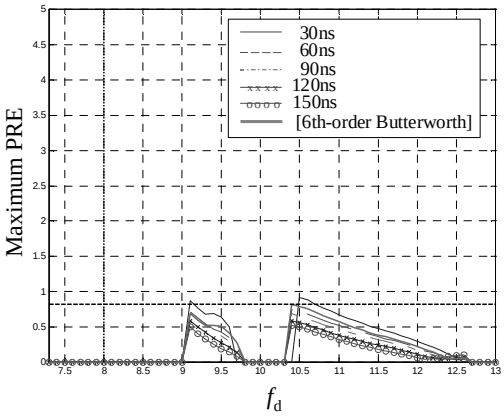

Figure 5-141 50° Elevation Angle: $0.07T_c$, 16MHz, 3 Monitor Receivers

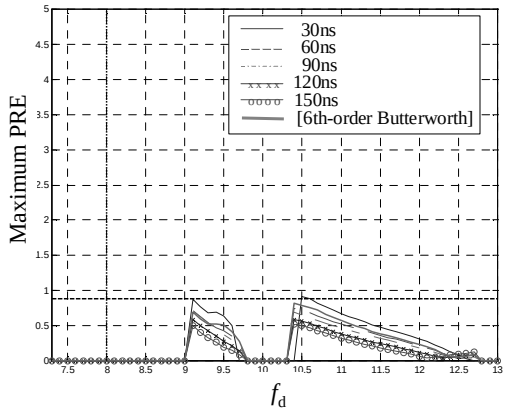

Figure 5-139 60° Elevation Angle: $0.07T_c$, 16MHz, 2 Monitor Receivers

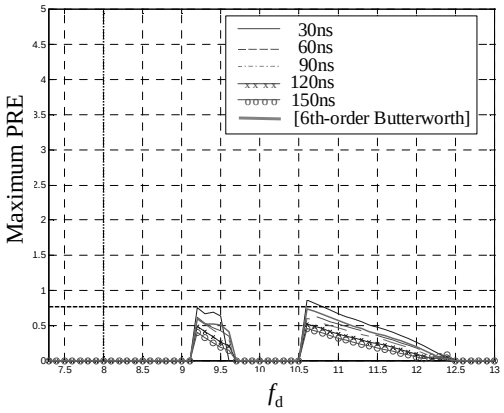

Figure 5-142 60° Elevation Angle: $0.07T_c$, 16MHz, 3 Monitor Receivers

To substantiate the assertion that the magnitude response (as opposed to small $d\mathrm{T}_{\mathrm{Gd}}$) causes the relatively poor performance of the 30ns filter, the same analysis evaluated an FIR (zero-$d\mathrm{T}_{\mathrm{Gd}}$) airborne filter. Only the result for the 14MHz, $0.05\mathrm{T}_{\mathrm{c}}$ ($\Delta\Delta$) case is shown in Figure 5-143 below. If the PREs were sensitive to small $d\mathrm{T}_{\mathrm{Gd}}$ alone, the FIR curve would be significantly higher (i.e., worse) than the 6th-order Butterworth (and also the 30ns curve shown above). Figure 5-144 shows, however, that the FIR performance here is much better than that of the 6th-order Butterworth. It results in a significantly smaller maximum PRE because the FIR filter used (300-tap Hamming window) has a much faster roll-off than the Butterworth. (See Figure 5-83 above.) Clearly, filter magnitude response in the transition band dominates the sensitivity of these curves. Based on these analysis results, the $\Delta\Delta$ Region 2 notch parameters were specified as shown in Figure 5-145. (The four E-L protected regions were left unchanged from those depicted in Figure 5-3.)

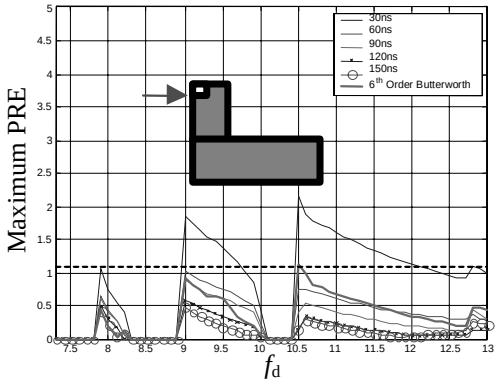

Figure 5-143 $\Delta\Delta$ Correlator $d\mathrm{T}_{\mathrm{Gd}}$'s Using SQM2b (15.0MHz, $0.05\mathrm{T}_{\mathrm{c}}$ "Narrow" Correlator Spacing; 2 Monitor Receivers, 100% MDEs; 40° Elevation Angle)

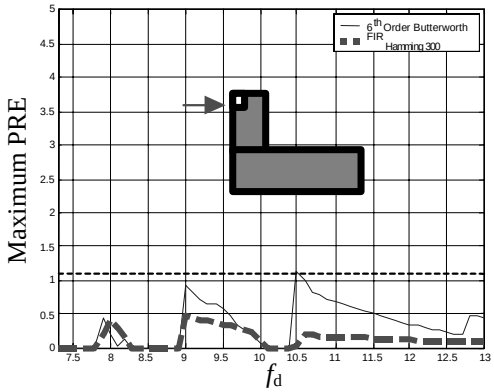

Figure 5-144 $\Delta\Delta$ Correlator $d\mathrm{T}_{\mathrm{Gd}}$'s Using SQM2b (15.0MHz, $0.05\mathrm{T}_{\mathrm{c}}$ "Narrow" Correlator Spacing; 2 Monitor Receivers, 100% MDEs; 40° Elevation Angle)

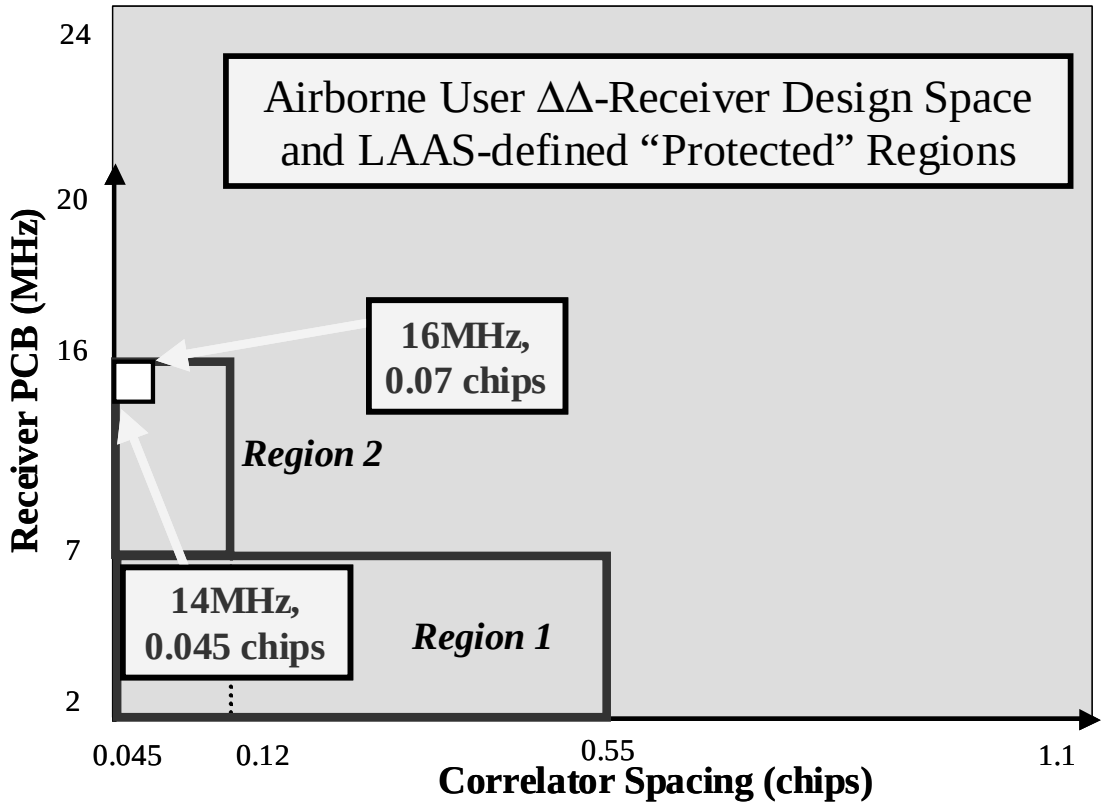

Figure 5-145 Airborne User Design Space and Recommended ΔΔ Notch Parameters

5.7.4 Magnitude Response Analysis

Figure 5-146 below shows the same suite of Butterworth filters (16 MHz PCBw) used in the differential group delay analysis compared to the LAAS interference requirement. Note that this requirement is not on the precorrelation filter responses discussed previously. Instead it also takes into account the filtering response of the correlation process itself. (A postcorrelation filter response is the product of the precorrelation filter response and the normalized power spectrum of the C/A code from Figure 2-2 of Chapter 2.)

Technically, only the postcorrelation 6^{th}-order Butterworth filters shown in Figure 5-146 completely met the LAAS specification. However, for (single-sided) frequencies higher than approximately 13MHz—the largest f_d for Threat Model C—the 60-150ns filters have magnitude responses less than or equal to that of the 6^{th}-order Butterworth. It follows that for TM C, the critical threat model under consideration, all the filters examined except the

30ns design *virtually* complied with the LAAS interference requirement, since no frequencies above 13MHz excited the system. Also note that Threat Model B has frequencies as high as 17MHz. Only TM C, however, contained EWFs that caused unacceptably large errors for a few ΔΔ receiver configurations. Had it been necessary to evaluate the notch region using TM B EWFs, few (if any) of the five $d\mathrm{T}_{\mathrm{Gd}}$ filter designs would have been acceptable.

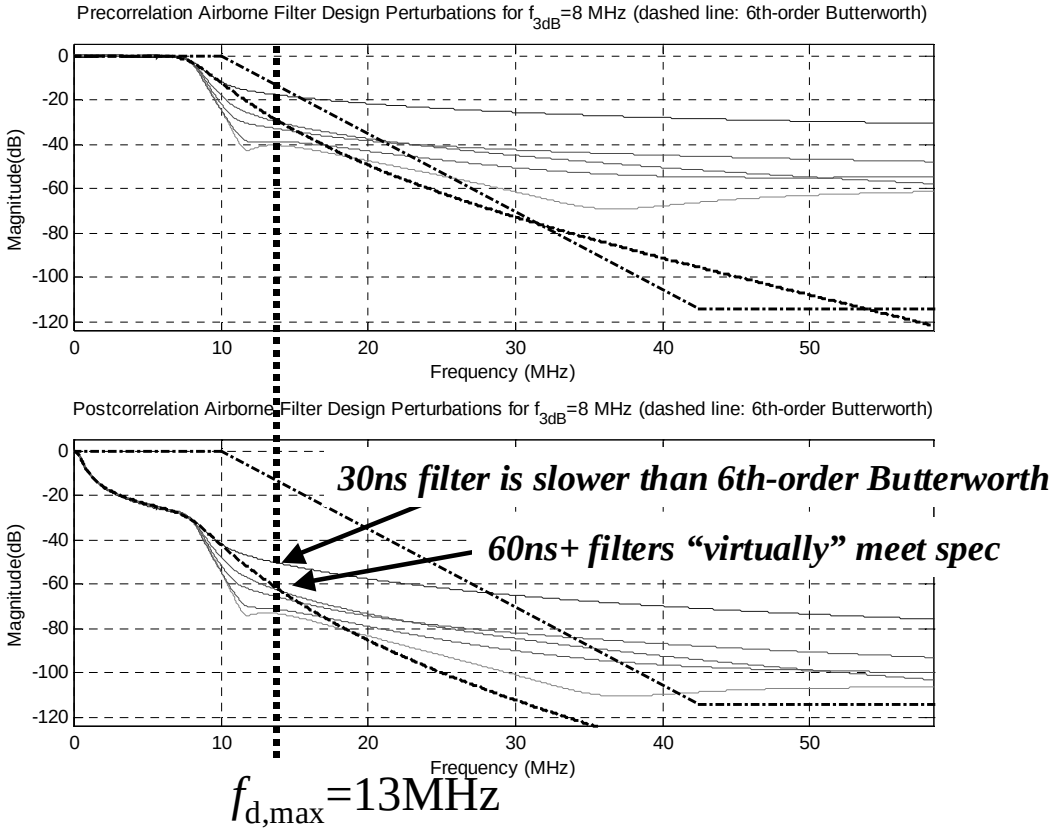

Figure 5-146 User Filter Perturbations (PCBw=16MHz) vs. LAAS Interference Requirement

As shown from the group delay analysis for the ΔΔ Region 2 notch in the previous section, IIR filters with small passband $d\mathrm{T}_{\mathrm{Gd}}$'s tend to have extremely wide transition bandwidths. The unacceptable (30ns $d\mathrm{T}_{\mathrm{Gd}}$) filter from that analysis, however, violated the LAAS interference requirement. The previous section concluded that such wide transition

bandwidths may result in unacceptably large PREs for the very narrow ΔΔ receiver configurations.

To analyze the effects of wide transition band magnitude responses on the resulting PREs, this section analyzes four interference-compliant, low-dT$_{Gd}$ (3rd, 4th, 5th, and 6th-order) Butterworth filters. The magnitude and dT$_{Gd}$ responses of these filters are show in Figure 5-147. (Note that the maximum dT$_{Gd}$'s for all four filters are approximately 35ns.) As in the previous dT$_{Gd}$ analyses, the simulated ground monitor (and reference) implemented an FIR (zero-dT$_{Gd}$) filter.

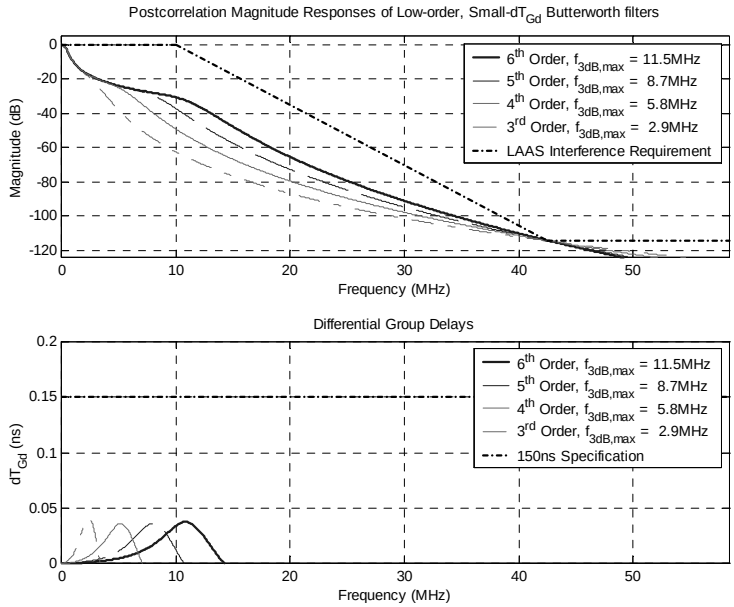

Figure 5-147 Maximum Transition Bandwidth (maximum PCBw) Filters

The following figures plot maximum PRE contours *only for the airborne receiver bandwidths where the filters meet the interference requirement*. This analysis examines only Threat Model C PRE contours corresponding to a given elevation angle (30°). Contour plots for both the E-L correlators and the ΔΔ receivers are shown (again using 100% SU MDEs) in Figure 5-148 through Figure 5-155. On each plot, the thick, shaded contours indicate the corresponding (30°) MERR threshold.

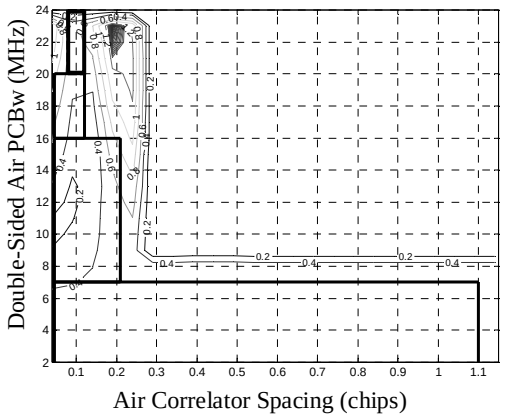

Figure 5-148 E-L – 6th-order Butterworth

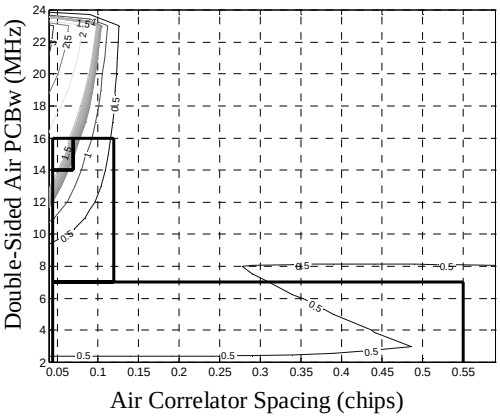

Figure 5-151 ΔΔ – 6th-order Butterworth

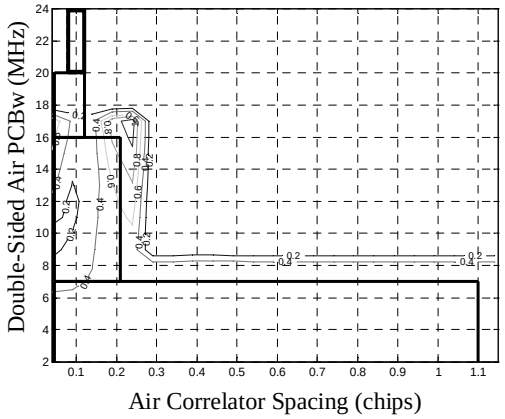

Figure 5-149 E-L – 5th-order Butterworth

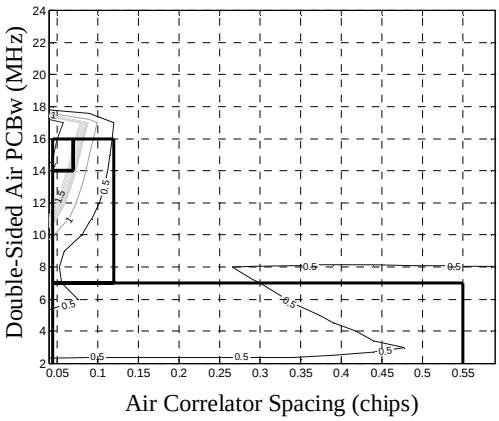

Figure 5-152 ΔΔ – 5th-order Butterworth

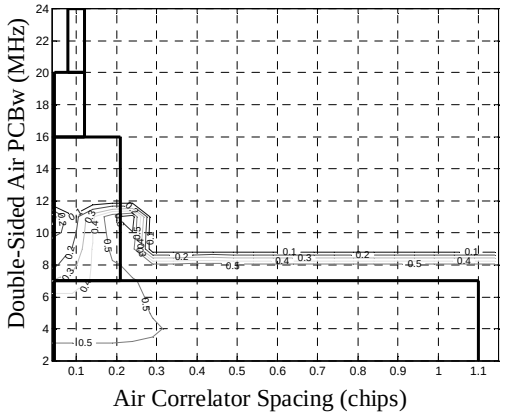

Figure 5-150 E-L – 4th-order Butterworth

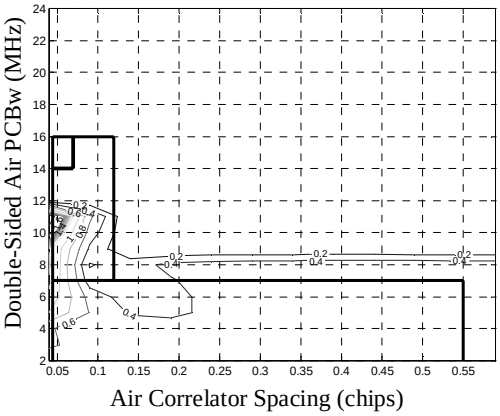

Figure 5-153 ΔΔ – 4th-order Butterworth

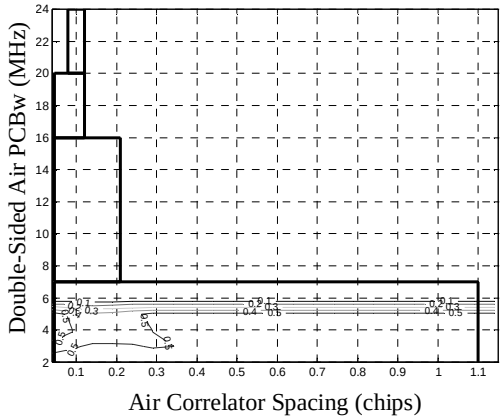

Figure 5-154 E-L – 3rd-order Butterworth

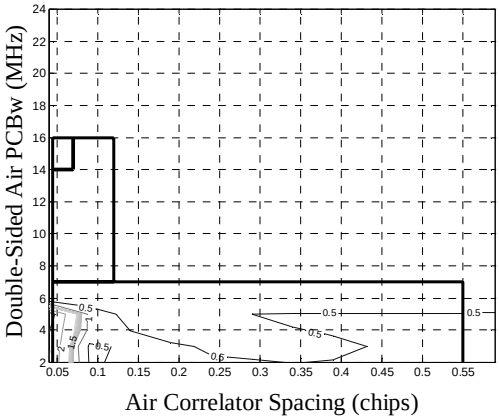

Figure 5-155 ΔΔ – 3rd-order Butterworth

While the E-L receiver configurations are relatively insensitive to such magnitude response variations, these analysis results indicate the need to specify a maximum transition bandwidth for the airborne user filters in addition to the notch requirement in order to protect both the ΔΔ regions. *The maximum transition bandwidth should be upper-bounded by that of the 6th-order Butterworth.*

5.8 Transient SQM Analysis

The previous SQM verified the existence of a practical multicorrelator implementation (SQM2b) capable of protecting user integrity against hazardously misleading information induced by evil waveforms. This analysis implicitly assumed, however, that the EWF failure had reached steady state. In other words, it assumed the EWF detection metrics measured by the monitor receiver and the tracking errors measured by the receivers had reached their final, steady state values. Filtering of both these observables, however, implies the transient values will, in general, differ from their steady state (i.e., maximum) values. To determine whether the hazardous EWFs cause HMI for airborne users, it is necessary to first make assumptions for how the satellite failure occurs. Also, the filter transient responses to that EWF failure must be modeled. If it is discovered that some EWFs cause transient SQM problems, it may become necessary to add even more sensitive detection metrics to mitigate this threat.

5.8.1 Analysis Assumptions

The transient SQM analysis assumes that any EWF failure will occur instantaneously (and persist for a long time relative to the transient responses of any measurement filters such as carrier smoothing), and the instantaneous error it causes in the receiver can be approximated by a step function that occurs at time $t=t_{EWF}$. The amplitude of this (step) error, A_{tss}, is dependent on the observable measured by the receiver. For SQM, there are three such observables. These configuration-dependent variables include the following:

1. Reference station tracking error (i.e., differential error correction)
2. Monitor receiver SQM detection metrics (i.e., correlator value measurements)
3. Airborne receiver tracking errors

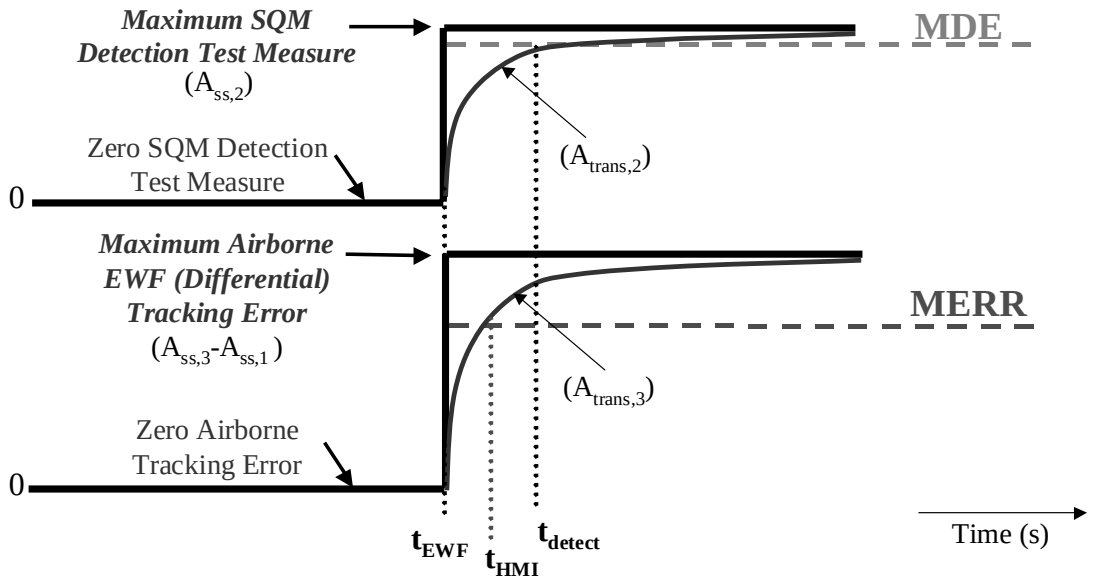

Figure 5-156 Transient SQM Problem with 1st-Order Filter Responses

At the onset of a satellite failure, the tracking errors for the reference station and the user will asymptotically approach their (different) steady-state values, $A_{tss,1}(t)$ and $A_{tss,3}(t)$, respectively. (Refer to Figure 5-156.) Simultaneously, each of the monitor receiver detection metrics will also approach their respective steady-state values. Assuming the

same filter is applied to all detection metrics, the maximum, $A_{tss,2}(t)$, will correspond to the most sensitive detection test. (Recall that only a single metric needs to exceed its corresponding MDE for detection of an EWF.)

The transient airborne error responses of hazardous EWFs will exceed their corresponding MERRs at $t = t_{HMI}$. If the EWF is detectable, this (most sensitive) test will ideally detect it at time, $t = t_{detect} \leq t_{HMI}$. Less conservatively, however, to meet the LAAS Cat I time-to-alarm requirement, t_{detect} can exceed t_{HMI} by no more than 3 seconds—one-half of the total 6-second time-to alarm requirement. (Refer to Section 1.3.2 of Chapter 1.) This analysis assumes the LAAS Ground Facility takes a maximum of 3 seconds to detect and alert the user, and the user requires 3 seconds to receive and process the alarm message. Hence we define TTA = 6 and TTA_{LGF} = TTA/2 = 3s.

5.8.2 Filter Response Models

Hatch Filter: 1st-Order Response

Recall that the Hatch filter, used to carrier-smooth pseudorange measurements, has a first-order filter response. Accordingly, the time domain response of Equation (2.16) (from Chapter 2, Section 2.3.2) is given by

$$A_{trans}(t) = A_{ss}\left(1 - e^{-t/\tau_c}\right) \quad t \geq 0 \tag{5.12}$$

where

$A_{trans}(t)$ is the transient response of the EWF-induced variation,

$A_{tss}(t)$ is the maximum (i.e., steady-state) amplitude of the variation, and

τ_c is time constant of the filter (τ_c = 100s for LAAS receivers).

Figure 5-156 illustrates the transient SQM problem for a first-order smoothing of the detection tests (and user differential PREs). The figure shows the (fastest) transient

responses of the monitor receiver for one example user receiver configuration. Note that as shown, $A_{trans,2}(t - t_{EWF})$ is the transient response resulting from a first-order filter applied to the detection metrics measurements. The maximum transient differential airborne receiver PREs, $A_{trans,3}$, are given by

$$A_{trans,3}(t - t_{EWF}) = (A_{ss,3} - A_{ss,1})\left(1 - e^{-(t-t_{EWF})/\tau_c}\right) \tag{5.13}$$

where $t > t_{EWF}$. It follows that the basic transient SQM problem (with TTA=0 seconds) reduces to a simple comparison of the normalized steady state errors according to

$$\begin{cases} \dfrac{A_{ss,3} - A_{ss,1}}{MERR(\theta)} > \dfrac{A_{ss,2}}{MDE(\theta)}, & t_{detect} > t_{HMI} \\ \text{otherwise}, & t_{detect} \le t_{HMI} \end{cases} \tag{5.14}$$

where θ is the satellite elevation angle.

Moving Average (FIR) Filter: Linear Response

Although LAAS requires that a Hatch filter be used for carrier smoothing of the airborne and reference receiver tracking errors, the SQM metrics may be smoothed with a different filter. For these, the most desirable transient response is one that has as fast a rise time as possible. This implies, however, that the filter has a smaller time constant, or rather that it has a wide bandwidth. In fact, no filtering at all would essentially provide the SQM with a response virtually as fast as the (instantaneous) EWF failure itself.

Wide-bandwidth filtering in general is not practical, since the MDEs presume a filter will adequately smooth the metrics. Recall that this smoothing is required to reduce the nominal variations due to multipath and thermal noise. A faster filter implementation would necessarily require computation of new MDEs, which would, of course, become larger. One simple compromise is to leverage the fact that the SQM-accepted SU MDEs already assume a more conservative (i.e., faster) smoothing filter than a first-order filter.

(Refer to Chapter 3, Section 3.8.3) The MDEs are computed using a 100-tap FIR rectangular window, or a 100-second "moving average" filter. (Each tap of this filter corresponds to one second.)

A comparison of the transient responses of the Hatch filter and the moving average is provided below in Figure 5-157 for $A_{trans,3}$ = 3.5m and τ_c = 100s. For this example, t_{EWF}=200s. Observe that while the Hatch filter (for $t<\infty$) never actually reaches the 3.5-meter steady state value, the moving average reaches 3.5 meters in 100 seconds. Intuitively, a 100-second moving average of the SQM detection metrics will provide better transient SQM performance. Again, use of this type of smoothing does not impact steady state performance, since the SU MDEs already assume this filter implementation.

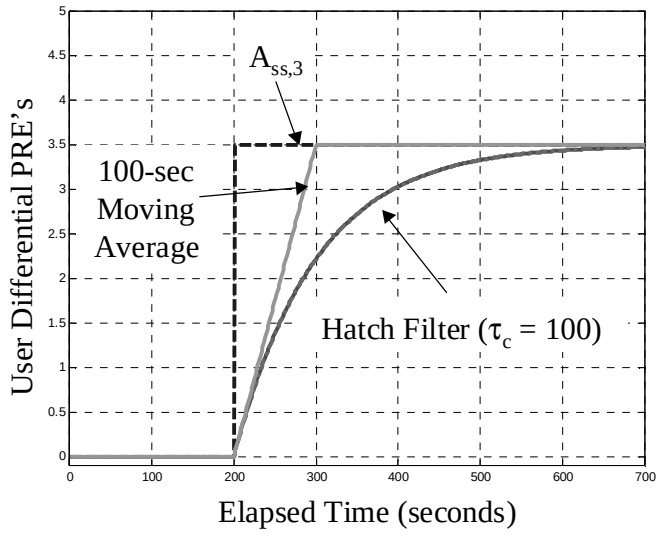

Figure 5-157 Comparison of 1st-Order (Hatch) and Moving Average (100-tap FIR) Filter Transient Responses

5.8.3 Improved Detection Sensitivity

To further assist in the early detection of EWFs (without modifying the SQM2b correlator design), it is also desirable to make the detection metrics as sensitive as possible. It may not be sufficient to merely have (normalized) metrics greater than unity. The maximum SQM test must be sufficiently large to detect the EWF before it breaches the MERR

threshold for any of the airborne users. A simple power operation performed on a sensitive detection metric may significantly increase this sensitivity even in the presence of noise and multipath.

Accordingly, the following detection "squared Δ-test" (Δ^2) was defined:

$$\frac{\left[\left(\Delta_{a,(\pm 0.075)} - \Delta_{a,ref}\right) - \left(\Delta_{nom,(\pm 0.075)} - \Delta_{nom,ref}\right)\right]^2}{MDE\left(\Delta^2_{(\pm 0.075),ref}\right)} \tag{5.15}$$

where $\left(\Delta_{a,(\pm 0.075)} - \Delta_{a,ref}\right)$ is the original (non-MDE-normalized) Δ-test of SQM2b without the nominal bias removed using correlator spacing, d=0.15T_c. $MDE\left(\Delta^2_{(\pm 0.075),ref}\right)$ is the MDE associated with performing this squaring operation., under nominal noise and multipath conditions. It was computed using the SU MDE data. In the above expression, *a* and *nom* represent the anomalous and nominal (filtered) waveforms, respectively. For LAAS, the reference correlator spacing, *ref* = 0.1T_c.

Δ^2-test MDEs

The MDEs for the Δ^2-test are computed as in Section 5.7.1. Table 5-13 lists the 3rd-order polynomial coefficients for the two (standard) Δ-tests and the Δ^2-test. The MDEs for the Δ^2-test are plotted below in Figure 5-158.

	a_3	a_2	a_1	a_0
$\Delta_{\pm 0.075, \pm 0.05}$	-5.5345e-009	1.6638e-006	-1.6604e-004	6.3401e-003
$\Delta_{\pm 0.1, \pm 0.05}$	-1.5115e-008	5.0539e-006	-3.7768e-004	1.3769e-002
$\Delta^2_{\pm 0.1, \pm 0.075}$	1.4044e-013	6.0462e-010	-9.3481e-008	3.6755e-006

Table 5-13 Polynomial Fit Coefficients for SQM2b Δ-tests and Δ^2-test

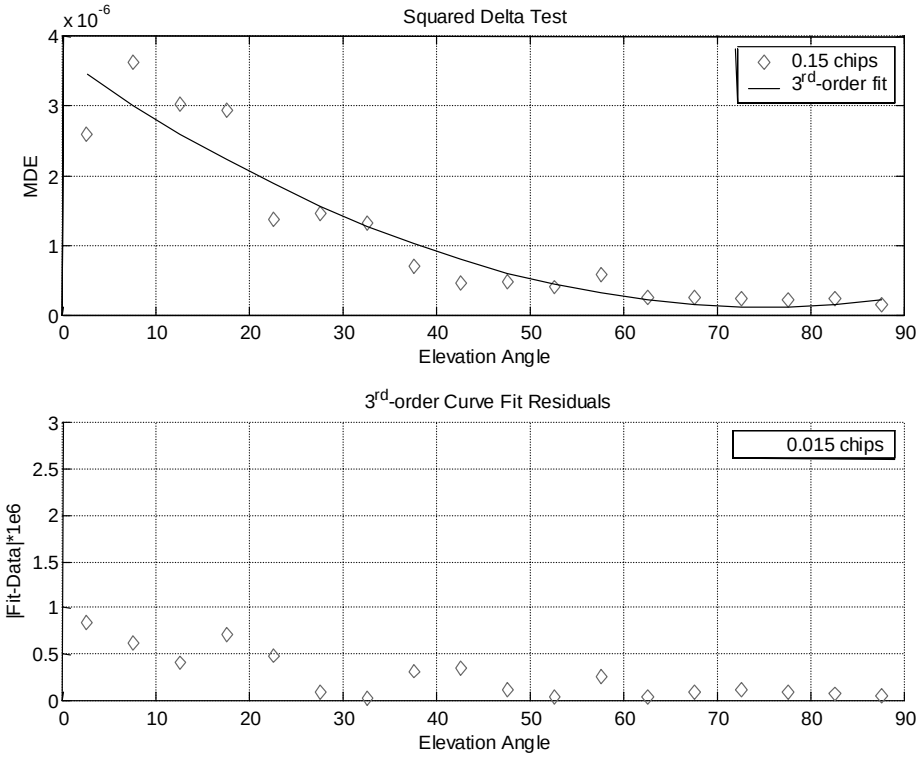

Figure 5-158 Curve fit and residuals for SQM2b Δ^2-tests

Recall that MDEs for the standard Δ-tests and ratio tests are computed according to

$$\mathrm{MDE} = \left(\mathrm{K}_{ffd} + \mathrm{K}_{md}\right) \cdot \sigma_{test} \tag{5.16}$$

where $\mathrm{K}_{ffd} = 5.26$ yields a fault-free alarm probability less than or equal to $1.5\text{x}10^{-7}$, and $\mathrm{K}_{md} = 3.09$ guarantees a missed-detection probability no greater than 10^{-3}. σ_{test} represents the experimentally-measured standard deviation of the peak due to multipath and thermal noise. Accordingly, σ_{test} assumes the distribution of those measurements is gaussian.

The Δ^2-test measurements, however, have a 1-degree of freedom chi-squared distribution. Equation (5.16) can still compute the MDEs (using Δ^2-test measurements with the mean removed) provided a multiplication factor is applied to them, to account for the difference in distribution assumptions. The MDE multiplier, *y*, is simply

$$y = 0.0516\theta + 0.3251 \tag{5.17}$$

where θ is the satellite elevation angle under consideration [Pullen01 (private communication)]. Figure 5-159 plots this factor as a function of elevation angle. Note that although Equation (5.17) above produces a multiplier less than unity for small elevation angles, the factor used in analysis was never less than 1.

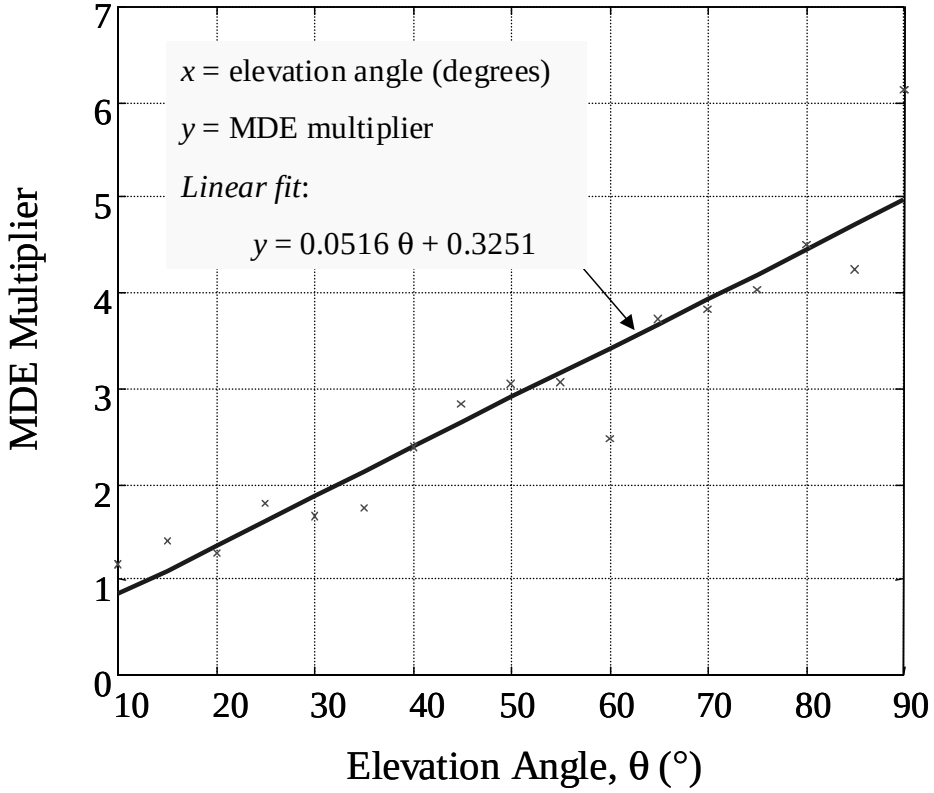

Figure 5-159 MDE Multiplier for Squared SQM Test

Error Sensitivity Issues

The Δ^2-test and higher-order power law tests (including exponential tests) *applied prior to any filtering operation* may improve transient SQM performance. Additionally, other tests (e.g., ratio tests) may prove viable candidates for these adaptations as well. It should be noted, however, that some sensitivity issues could arise with their actual implementation. These tests could become more sensitive to measurements errors—particularly those present in the nominal means, which must be pre-measured and stored offline for all the

metrics. (Refer to Section 4.2.2 of Chapter 4 for a detailed discussion of the bias removal process.)

This can be seen using the following simple model of a Δ^2-test metric:

$$\left[\left(\chi+\varepsilon_{\chi}\right)-\left(\bar{\chi}+\varepsilon_{\bar{\chi}}\right)\right]^2 \tag{5.18}$$

where

χ is the difference of a delta-test at correlator spacing, d_{χ}, and reference spacing, d_{ref}

ε_{χ} is the (instantaneous) error in that detection measurement due to noise and multipath,

$\bar{\chi}$ is the nominal mean of χ, and

$\varepsilon_{\bar{\chi}}$ is the error in $\bar{\chi}$.

Manipulation of this equation and normalization of it by the appropriate MDE yields the following detection metric:

$$\frac{\left(\chi-\bar{\chi}\right)^2+\left(\varepsilon_{\chi}-\varepsilon_{\bar{\chi}}\right)^2}{MDE_{\chi^2}} \tag{5.19}$$

Note that all the previous (steady-state) EWF analyses (i.e., simulations), assumed ε_{χ} and $\varepsilon_{\bar{\chi}}$ were zero. In that case the squared metric only increases the detectability margin of the (detectable) EWFs. In practice, however, the error terms may not be negligible. If they are not small, they may cause this detection metric to false alarm too frequently. Further experimentation and analysis using the real-time SQM monitor will be needed to more fully explore this issue.

5.8.4 SQM2b: Transient Performance

Steady state SQM analysis requires investigating the impact of all undetected points; however, the transient SQM analysis focuses on the detected points of SQM2b. Recall that the steady state analysis already showed that the undetected points (UDPs) corresponding to each respective elevation angle cause no hazardous errors at any time. Transient SQM analysis must verify that the detected points never introduce unacceptably large user PREs (before the monitor receiver detects them (minus 3 seconds)). In other words, it is necessary to analyze the effectiveness of SQM2b at detecting hazardous EWFs before $t = t_{HMI}+3s$.

To this end, this analysis produced standard maximum PRE contour plots using both the 1st-order filter and the moving average filter to smooth the SQM metrics. (Only if unacceptable errors were found within any of the regions, would it become necessary to implement the Δ^2-test.) The contour plots assumed a satellite elevation angle of 90° and three available monitor receivers for both E-L and $\Delta\Delta$ correlators. This implies that they utilized the smallest MDEs for the detection of the EWFs from TM A, TM B, and TM C. Accordingly this analysis examines the maximum number of *detected points* in the EWF threat spaces.

The plots for each case are given below. Here, the maximum PREs correspond to the maximum differential (EWF) tracking errors experienced by the airborne users at time, $t=t_{detect}$, whenever SQM2b did not detect the EWF within the allotted TTA. Otherwise, no transient EWF error would occur, hence no error contour appears. (As was true for the steady state contour plots, a thick, heavily shaded contour is plotted wherever the 90°-MERR threshold is crossed.) For TTA_{lgf}=3s, Figure 5-160 through 5-165 plot the 1st-order filter cases and Figure 5-166 through 5-171 plot the moving average filters. For comparison, Figure 5-172 through 5-183 plot the same cases for TTA_{lgf}=0s.

1st-Order Filter Results: (TTA_{lgf} = 3s)

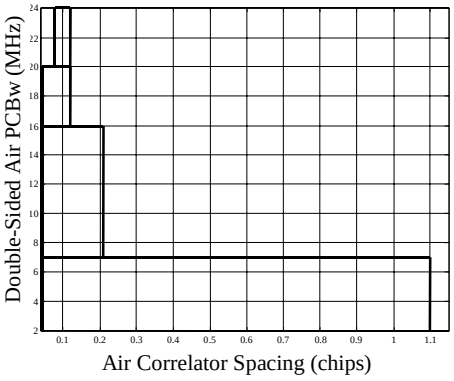

Figure 5-160 ΔΔ - TM A

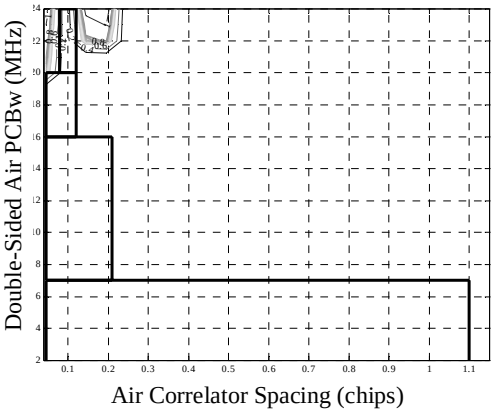

Figure 5-161 E-L - TM B

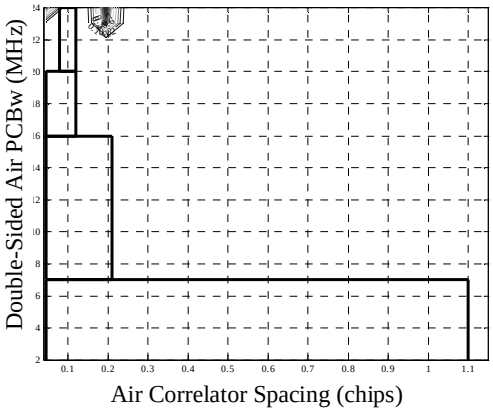

Figure 5-162 E-L – TM C

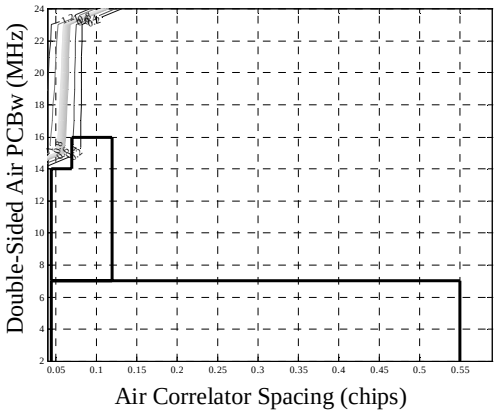

Figure 5-163 ΔΔ - TM A

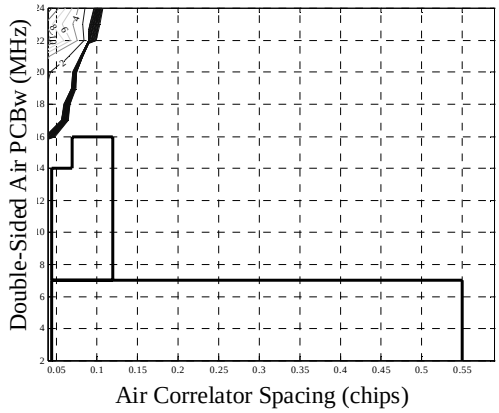

Figure 5-164 ΔΔ - TM B

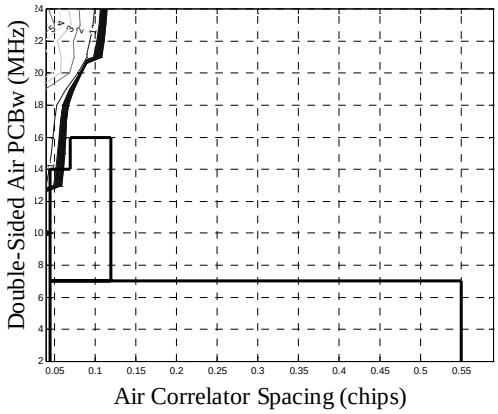

Figure 5-165 ΔΔ - TM C

Moving Average Filter Results: (TTA_{lgf} = 3s)

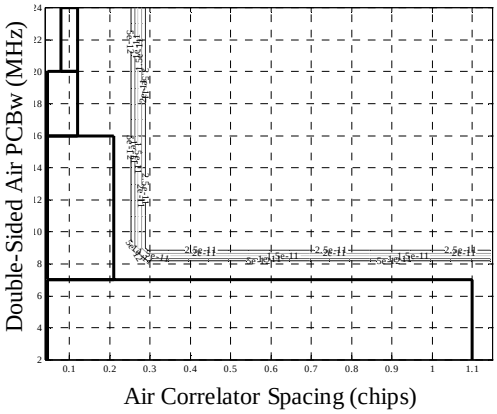

Figure 5-166 E-L - TM A

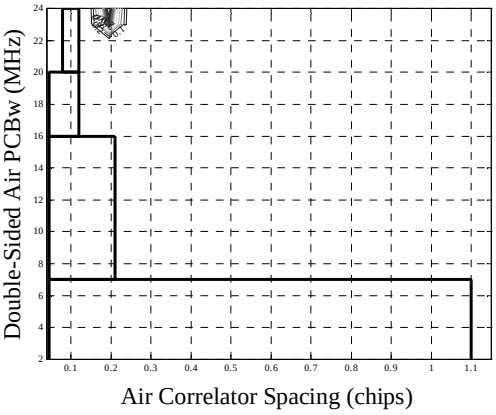

Figure 5-167 E-L - TM B

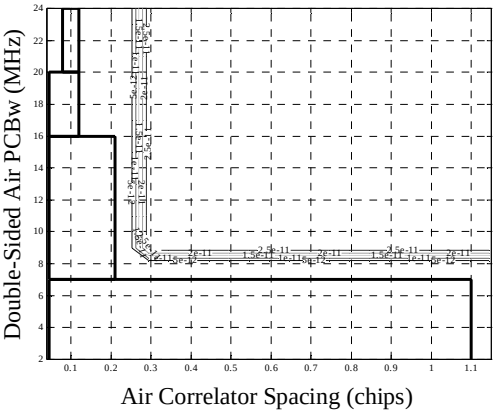

Figure 5-168 E-L - TM C

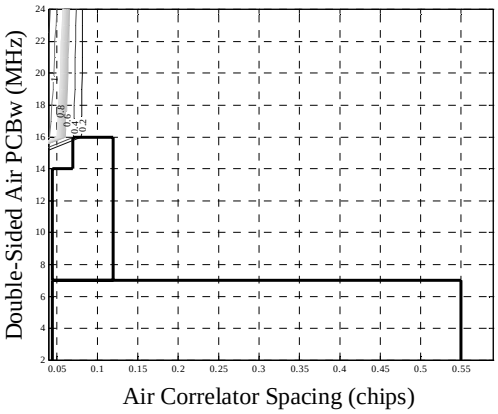

Figure 5-169 ΔΔ - TM A

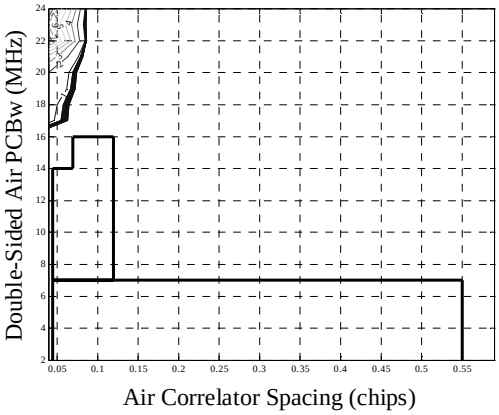

Figure 5-170 ΔΔ - TM B

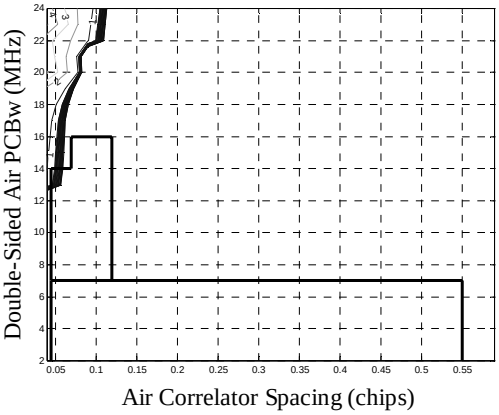

Figure 5-171 ΔΔ - TM C

1st-Order Filter Results: (TTA_{lgf} = 0s)

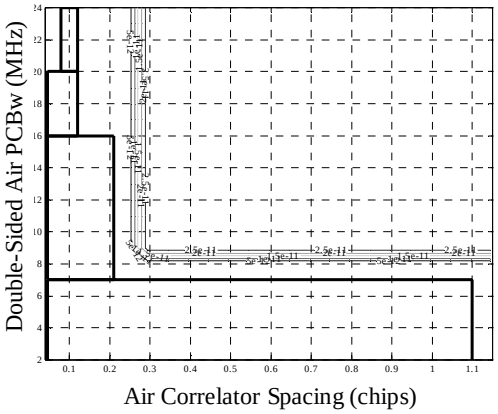

Figure 5-172 E-L – TM A

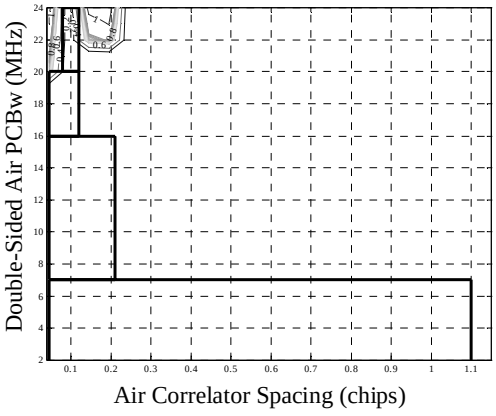

Figure 5-173 E-L – TM B

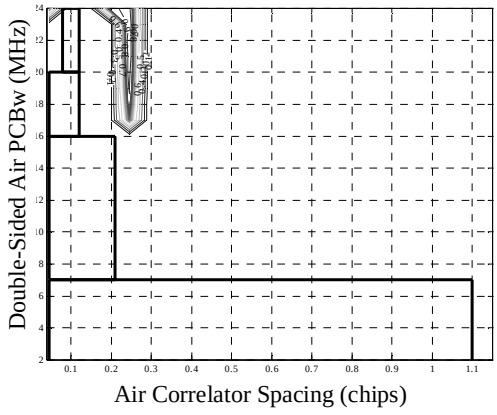

Figure 5-174 ΔΔ – TM C

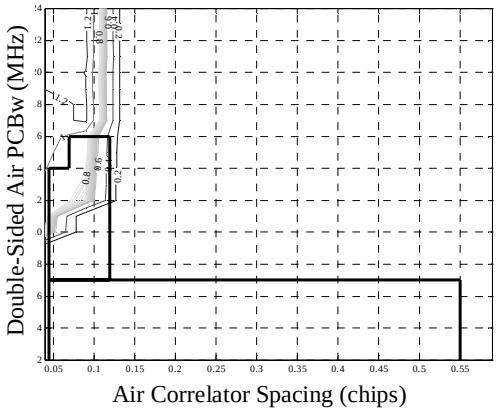

Figure 5-175 ΔΔ – TM A

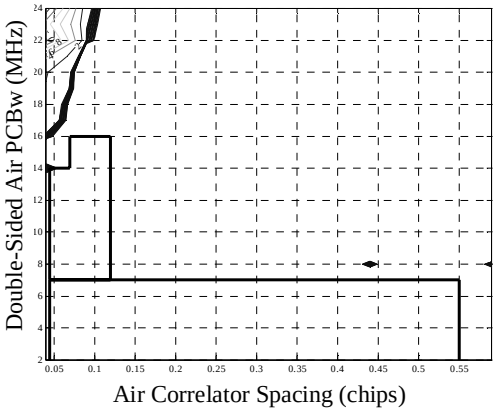

Figure 5-176 ΔΔ – TM B

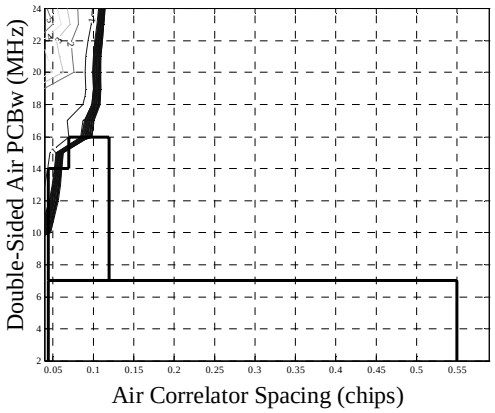

Figure 5-177 ΔΔ – TM C

Moving Average Filter Results: (TTA_{lgf} = 0s)

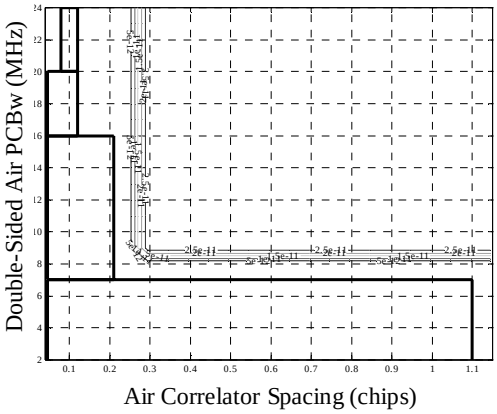

Figure 5-178 E-L – TM A

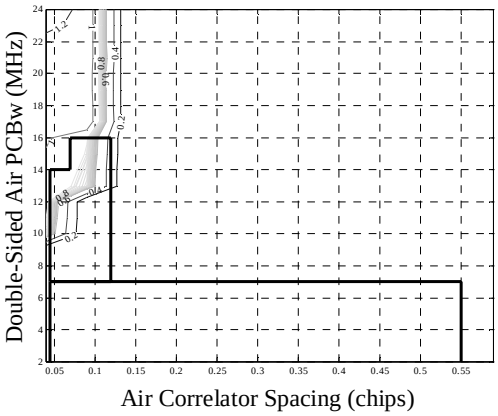

Figure 5-181 ΔΔ – TM A

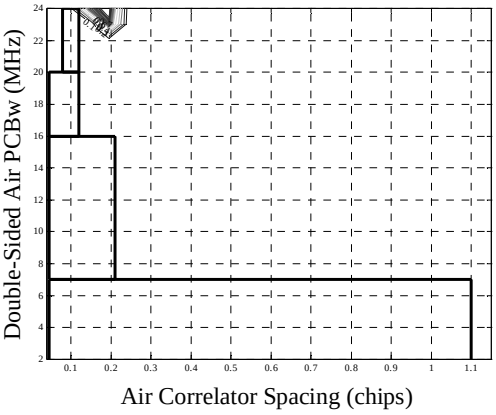

Figure 5-179 E-L – TM B

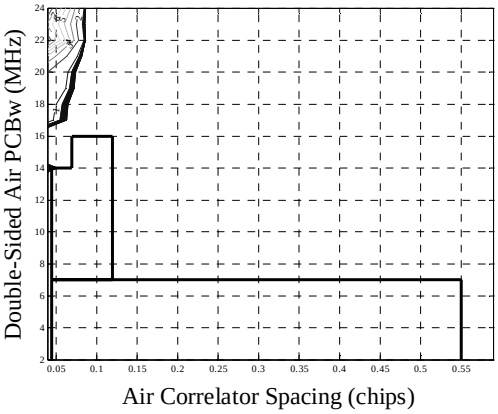

Figure 5-182 ΔΔ – TM B

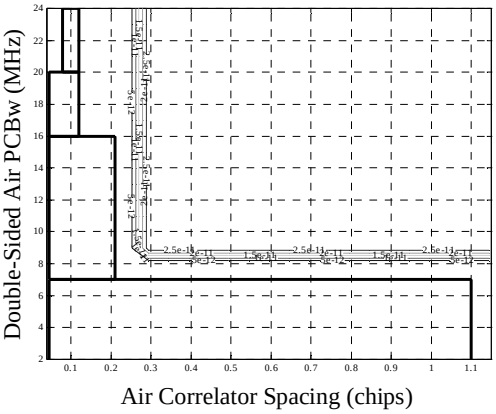

Figure 5-180 E-L – TM C

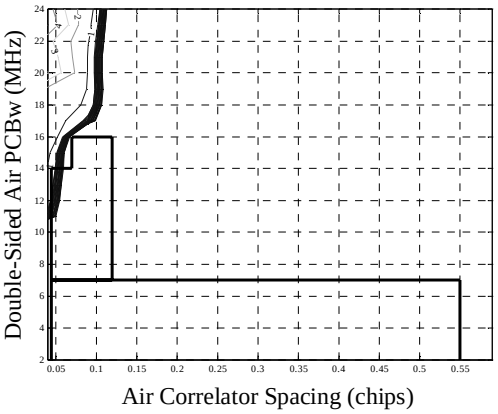

Figure 5-183 ΔΔ – TM C

Observe that for almost all cases, no contours within any of the regions for both E-L and ΔΔ users are above the (most conservative) 90°-MERR. In fact, for TTA_{lgf} = 3s, only the ΔΔ receivers suffered any unacceptably large transient EWF PREs. Even for the TTA_{lgf} = 0s cases, only TM A and TM C were of any concern (to only a few ΔΔ receivers in the 0.045Tc and 14MHz corner only). TM C, however, is the only case for which there were unacceptable transient PREs—for some ΔΔ configurations—with TTA_{lgf} = 3s. This implies that the Δ^2-test may be required to protect these users under transient TM C EWF conditions.

Using the Δ^2-test, a single maximum PRE contour plot for the ΔΔ-receiver users subjected to TM C EWFs was generated and is provided in Figure 5-185 and 5-185. The nominal MDEs for the Δ^2-test were computed from the SU MDE data for all elevation angles as detailed in Section 5.8.3. (Including the inflation factor, the nominal 90˚ elevation angle MDE(Δ^2) for this test was computed as 7.5171e-7.) The analysis used the nominal MDE, a moving average filter assumption, and a TTA_{lgf} = 3s. The results indicate that this single test more adequately protects these users against the hazardous transient TM C EWFs. The plot summarizes the maximum differential PRE results for all elevation angles between 0˚ and 90˚'; it shows only the "notch" region of the ΔΔ Region 2 user configuration space.

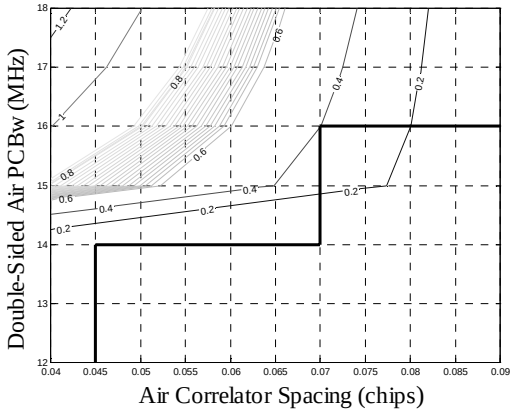

Figure 5-184 ΔΔ - Correlators – TM C MDE (Δ^2-test) – Hatch Filter, Notch Region Shown Only (All Other PREs in Design Space are Smaller.)

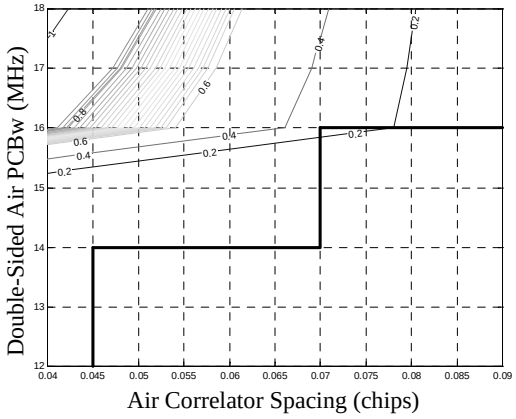

Figure 5-185 ΔΔ - Correlators – TM C MDE (Δ^2-test) – Moving Average Filter, Notch Region Shown Only (All Other PREs in Design Space are Smaller.)

Chapter 6:

Multipath Invariance and the Tracking Error Compensator

Multipath impairs GPS signal quality in very predictable ways. Completely mitigating this threat by conventional means is a difficult if not impossible task even theoretically for current MP mitigation techniques. Indeed even current multicorrelator techniques have great difficulty correcting for short-delay multipath. For less-costly, narrowband receivers, good multipath mitigation techniques are few or nonexistent. By understanding the ways in which multipath distorts the correlation function and sampling the function in so-called multipath invariant locations, however, it becomes theoretically possible to almost completely mitigate these effects on the user position solution. Sections 6.1 and 6.2 discuss the multipath parameters and current receiver MP mitigation performance. Sections 6.3 and 6.4 introduce and present the theoretical analysis for the Multipath Invariance (MPI) concept. Sections 6.5, 6.6, and 6.7 describe the Tracking Error Compensator (TrEC) technique for multipath mitigation. Sections 6.8 and 6.9 detail TrEC error sources and practical limitations resulting from limited receiver hardware capabilities. Finally, Section 6.10 provides theoretical performance bounds for TrEC applied to arbitrary receiver configurations.

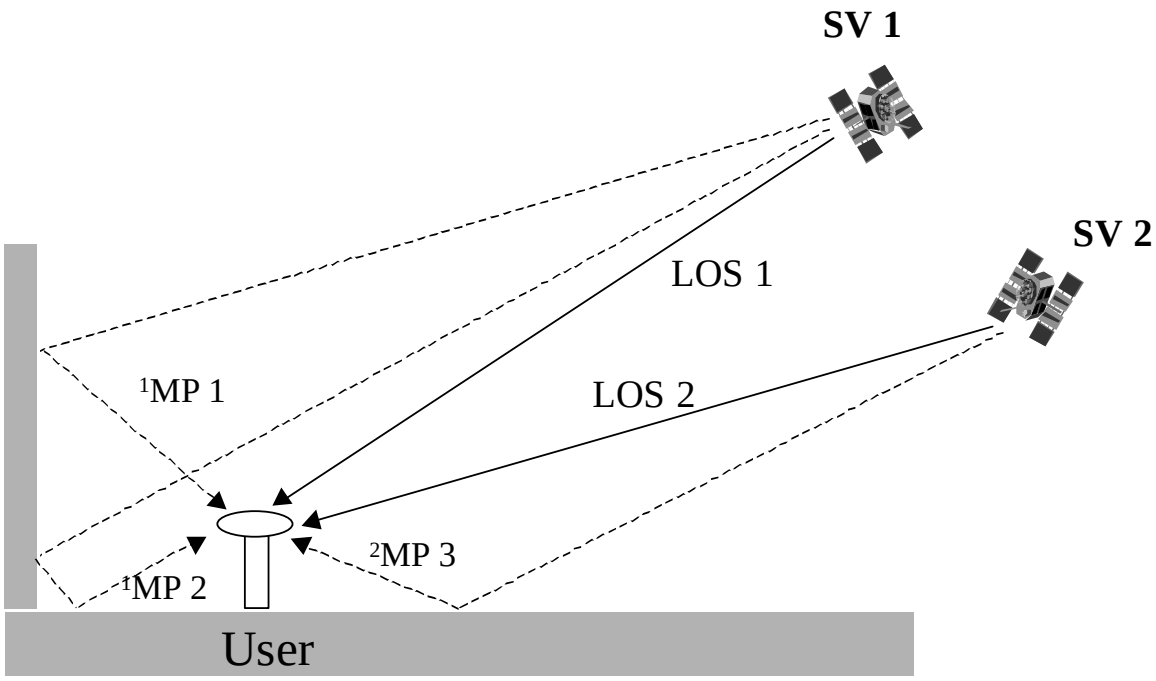

Figure 6-1 Line-of-Sight (LOS) signals and Undesired Multipath (MP) Reflections

6.1 Multipath Parameters

Multipath (MP) signals are (generally undesired) signal reflections from the ground or other nearby obstacles. (See Figure 6-1.) For specular reflections, they are amplitude-scaled (reduced) and time-delayed replicas of the nominal incoming signal or line-of sight (LOS). In the presence of a single MP reflection, the combined signal becomes

$$s_{0m}(t) = Ap(t)\sin(\omega_0 t) + \alpha Ap(t+\delta)\sin(\omega_0 t + \theta_m) \tag{6.1}$$

where α, δ, and θ_m are the relative multipath amplitude, delay, and phase respectively.

In general there are two types of multipath: specular and diffuse. Specular multipath are reflections from highly-reflective surfaces (e.g. metals, glass, calm water, etc.). These reflections usually have the strongest amplitudes. Practically speaking, there are usually relatively few (i.e., ≤3) specular multipath signals in a given composite signal. Diffuse

multipath is made up of many small, closely-separated (spatially) specular reflections. These multipath signals may be numerous and usually have progressively smaller amplitudes that tend to decrease exponentially as the distance to the reflector increases.

6.1.1 Amplitude

The amplitudes of multipath signals are frequently (but not always) less than or equal to the LOS signal. In general, this is due to three things. First, the reflector (or reflectors) attenuates the MP signal relative to the LOS. The amount of this attenuation strongly depends on the properties of the reflecting surface. Second, the antenna polarization may further reduce the MP signal amplitudes. GPS antennas (and the nominal, LOS GPS signal) are right-hand circularly polarized (RHCP). Since a reflected (MP) signal becomes essentially left-hand circularly polarized (LHCP), it may be attenuated by anywhere from 3-10dB [Braasch95], [Clark95], [van Nee92a]. Third, the antenna gain pattern may attenuate MP signals. GPS antennas typically attenuate signals incident from low elevation angles—the direction from which multipath most frequently arrives.

6.1.2 Delay

The time-of-arrival difference between the LOS and the reflected signal characterizes the MP relative delay. This delay is not simply the distance of a given reflector from the antenna. Instead it is the total path length difference between the two received signals. As illustrated in Figure 6-1, this path length difference is strongly dependent on the geometry between the satellite, the user receiver antenna, and the reflector (or reflectors) causing the multipath. Note that there may be several reflectors along the path of the MP signal.

6.1.3 Phase

The relative phase of the multipath ultimately determines the degree to which a multipath signal with a certain amplitude and delay will affect the code tracking loop of the receiver. The phase of the composite depends on the phase, θ_0, of the nominal incoming signal and that of the MP reflection(s), θ_m. Note that the phase (and phase rate) and relative MP delay,

δ_m, parameters are actually coupled. As described previously, the incoming signal is actually a code-modulated carrier wave. Accordingly, a change in the effective MP delay by a fraction of carrier cycle translates to a change in MP phase by an equivalent fraction of 2π radians. In fact, a static geometry between the satellite, user, and reflector(s) implies constant δ_m, θ_m, and θ_0. Holding these terms constant approximates the case for stationary user positioning using a pseudolite or a geostationary satellite [Fuller].

From Equation (6.1) above, it is clear that the multipath phase may result in either a minimum, a maximum or a complete negation of the multipath component of the combined signal. An illustration of the multipath condition is shown for four separate phase conditions and a fixed delay of 100 meters in Figure 6-2 through 6-6. Plotted are the effects of a single strong (Signal-to-Multipath Ratio = 3dB) MP signal at four different relative phases on the received signal, the discriminator and correlation functions of both conventional E-L and $\Delta\Delta$ correlator receivers [Garin97]. (For more about $\Delta\Delta$ correlators refer to Chapter 5, Section 5.3).

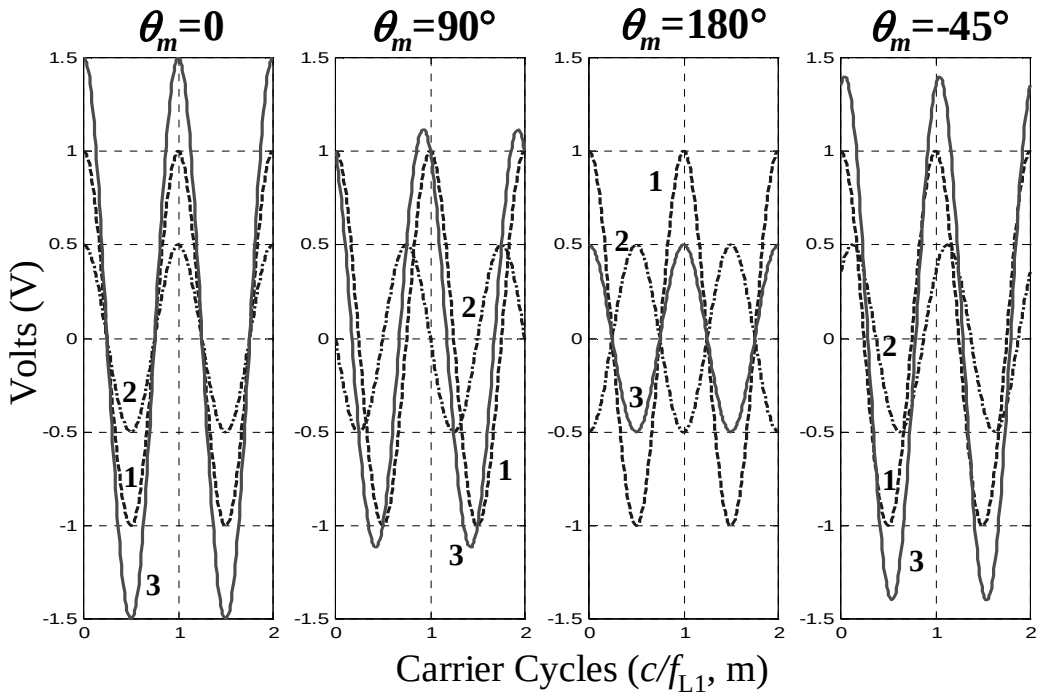

Figure 6-2 Carrier Phase Cycles for θ_m = 0, $\pi/2$, π, and $7\pi/4$. (SMR = 3dB; δ_m=100meters; $d_{E\text{-}L}$=1T_c.) 1) LOS, 2) MP, 3) LOS+MP

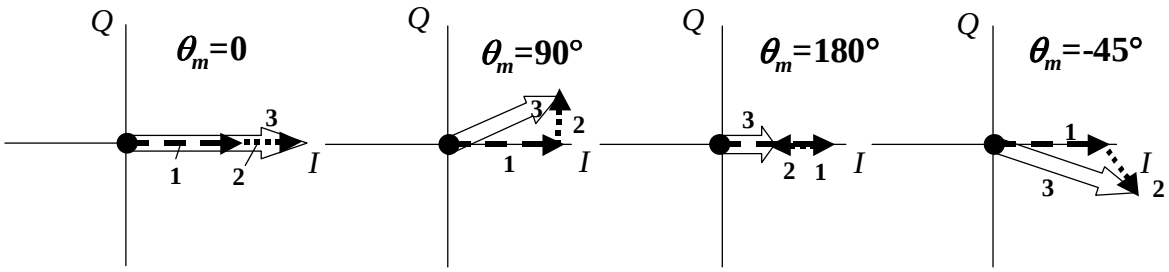

Figure 6-3 In-phase and Quadrature Phasor Diagrams for θ_m = 0, π/2, π, and 7π/4. (SMR = 3dB; δ_m=100meters; $d_{E\text{-}L}$=1T_c.). 1) LOS, 2) MP, 3) LOS+MP

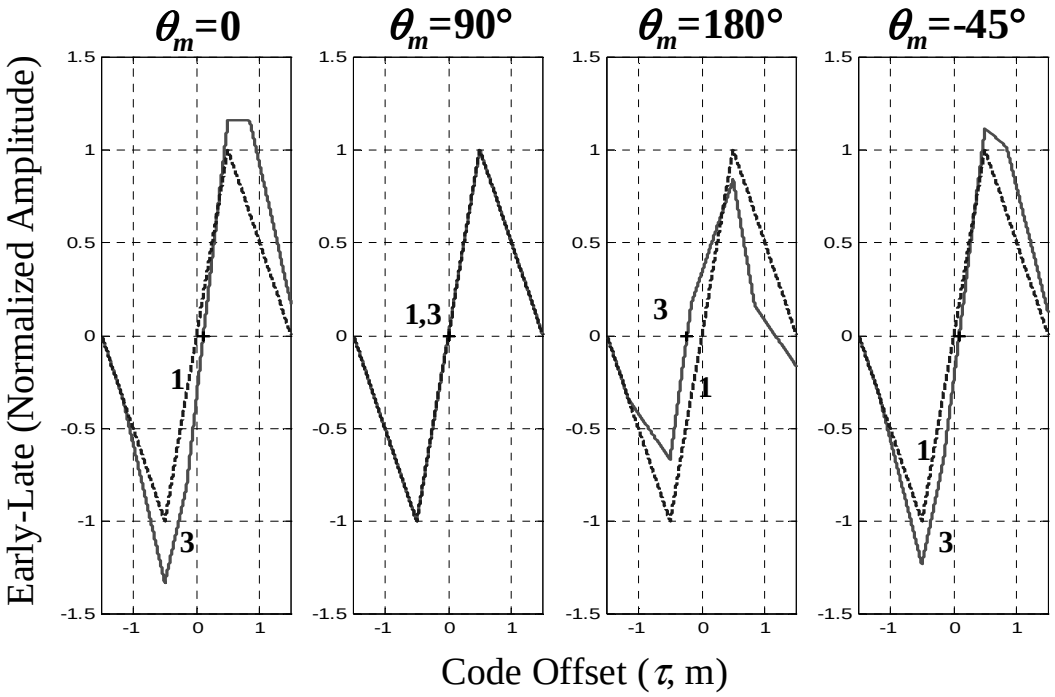

Figure 6-4 Discriminator Functions for E-L Correlators with θ_m = 0, π/2, π, and 7π/4. (SMR = 3dB; δ_m=100meters; $d_{E\text{-}L}$=1T_c.) 1) LOS, 2) MP, 3) LOS+MP

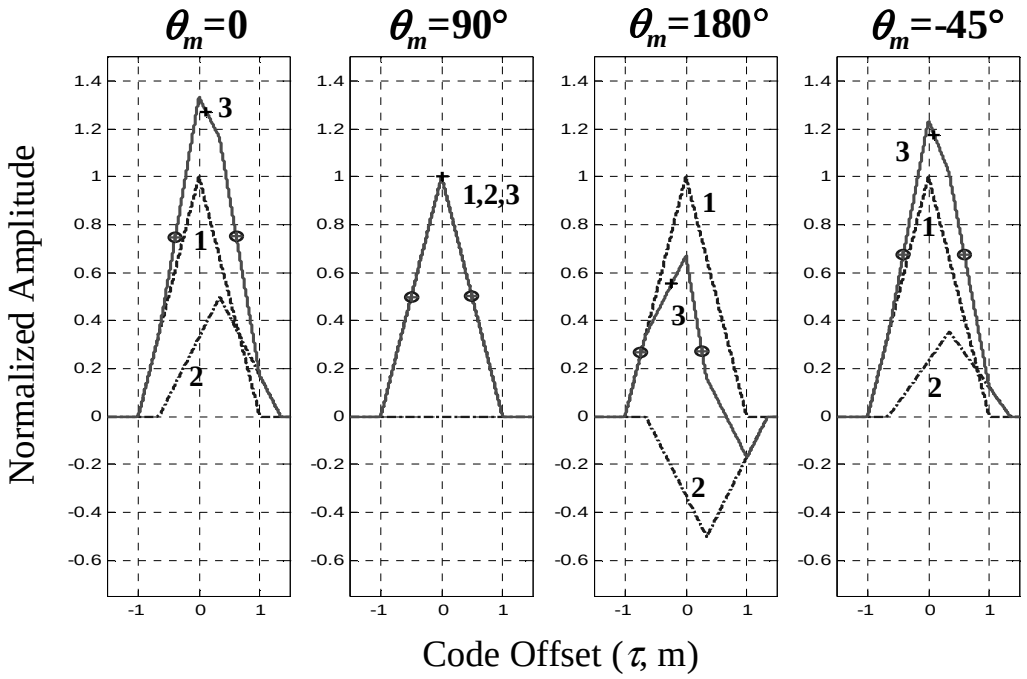

Figure 6-5 Correlation Peaks for E-L Correlators with θ_m = 0, π/2, π, and 7π/4. (SMR = 3dB; δ_m=100meters; $d_{E\text{-}L}$=1T_c.) 1) LOS, 2) MP, 3) LOS+MP

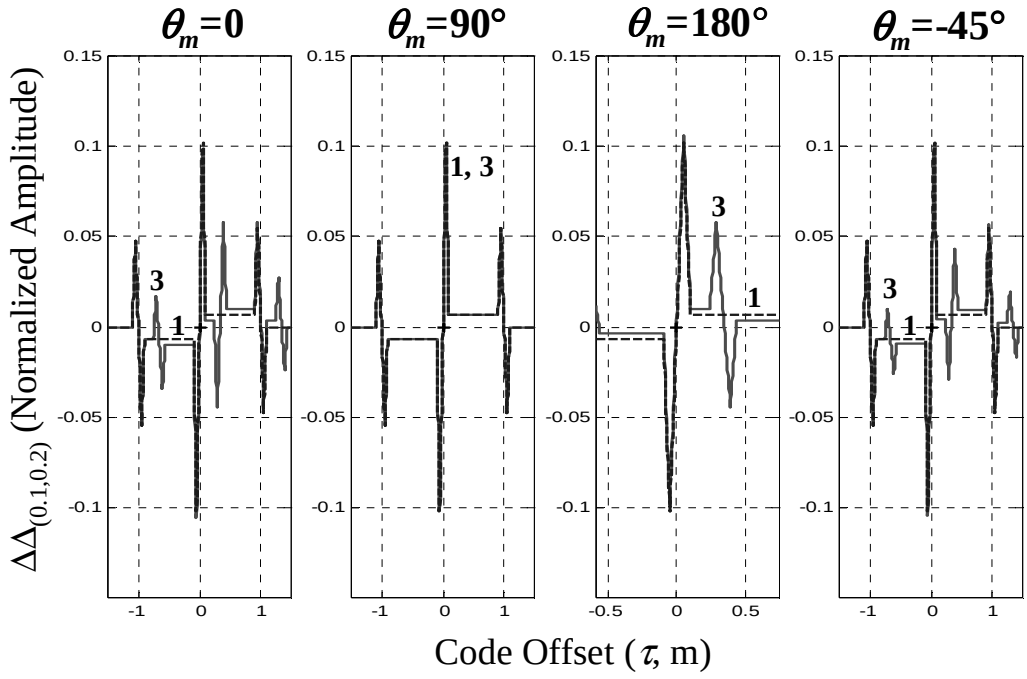

Figure 6-6 Discriminator functions for ΔΔ correlators θ_m = 0, π/2, π, and 7π/4. (SMR = 3dB; δ_m=100meters; d_{narrow}=0.1T_c and d_{wide}=0.2T_c.) 1) LOS, 2) MP, 3) LOS+MP

6.1.4 Phase Rate and MP Fading

Fading results from time-varying changes in the relative phases of the LOS and MP signals. In general, the phase differences between these signals are not constant. Satellite motion causes the phases (or more precisely the Doppler difference between the user and the reflector) to vary even for a stationary user. The composite signal essentially contains the Doppler variations from two different locations—that of user and reflector(s). The effect is geometry-dependent. The maximum Doppler difference for a static user (where the reflector is r meters away) occurs for a satellite at zenith. For a stationary user, this maximum "fading" frequency, f_{fad} (Hz), is $f_{fad} = 1.38r\text{x}10^{-3}$Hz [van Nee92a]. (See Figure 6-7.)

If the user and/or reflectors are in motion, the geometry between the user, reflector, and satellite are continuously changing. In this case, the fading frequency can become significantly larger and may be expressed (for a single reflector) as

$$f_{fad} = (vf_{L1}/c)\left[\cos(\alpha_r)\cos(\beta_r) - \cos(\alpha_s)\cos(\beta_s)\right] \tag{6.2}$$

In the above expression, α_r, β_r, α_s, β_s are the elevation and azimuth angle differences between the user and the reflector and between the user and the satellite, respectively [van Nee92a]. (See Figure 6-8.)

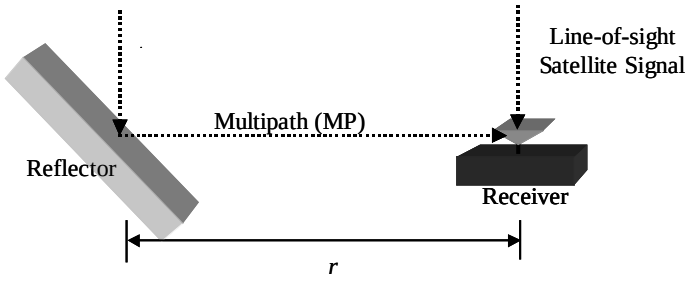

Figure 6-7 Single-Satellite Maximum Doppler Geometry for a Stationary User

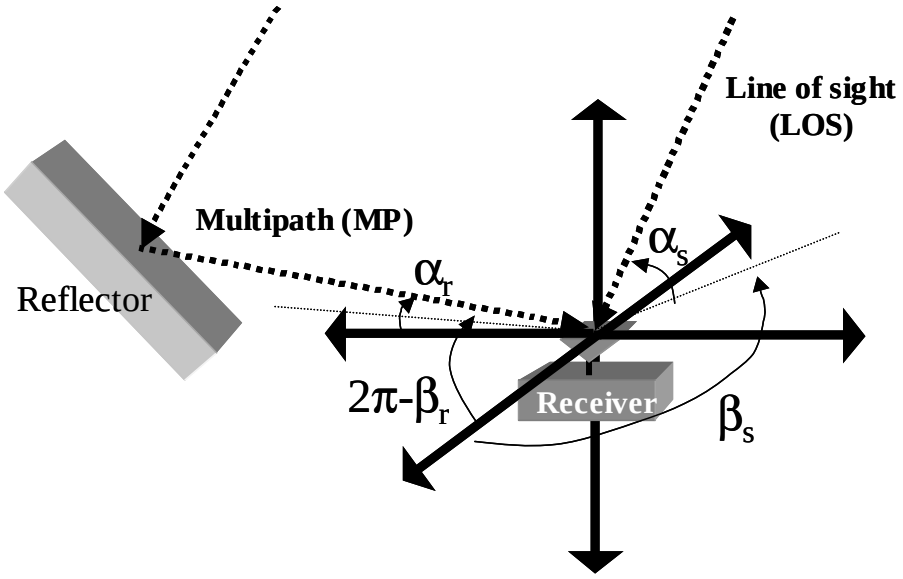

Figure 6-8 Geometry Factors for Fading Caused by a Single MP Reflection (Axes Centered at Receiver Antenna)

When the fading frequency is greater than the code tracking loop bandwidth some averaging of the signal occurs inside the receiver. In general, this is a very favorable condition. High receiver dynamics tend to "whiten" the code tracking errors due to multipath. The more thermal noise-like these tracking errors appear, the more effective the tracking loop is at reducing these errors by filtering (or smoothing) them.

6.2 MP Code Tracking Errors

Perhaps the most common method to measure the code MP (mitigation) performance of a GPS receiver is to plot the maximum code tracking error due to a single MP reflection as a function of relative MP delay, δ [Van Dierendonck95], [Braasch95], [Braasch96], [van Nee92a]. This models the case of a receiver tracking a single satellite located a distance, δ, from a stationary reflector. (See Figure 6-9 and Figure 6-10 below.) In this scenario, the signal-to-multipath ratio (SMR) is assumed to be 3dB. The relative delay is normally plotted (for standard DLLs with a 1-chip correlator spacing) to relative delay distances as large as 1.5Tc.

Figure 6-11 shows these "error envelope" plots for a standard DLL with correlator spacings, d=0.1Tc, d=0.5Tc, and d=1.0Tc for a 16MHz (wideband) receiver. The performance curves for a 2MHz (narrowband) receiver are shown in Figure 6-12.

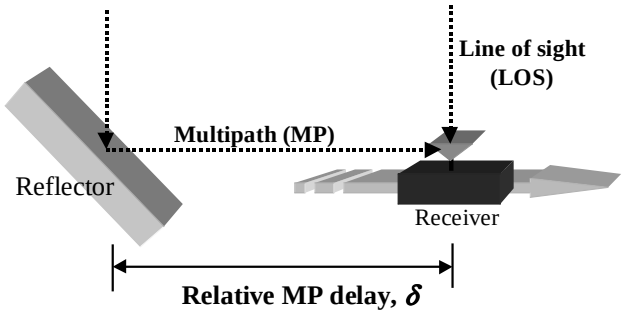

Figure 6-9 Illustration of Standard MP Mitigation Performance Scenario

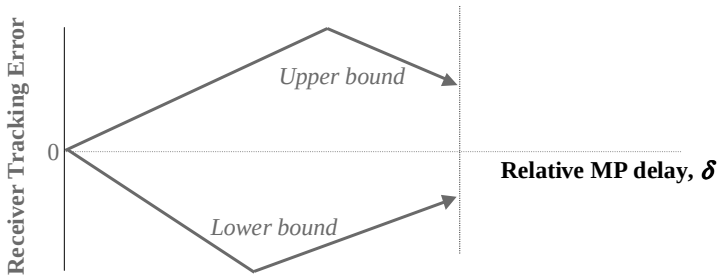

Figure 6-10 Generation of Receiver Multipath Performance Plots ("Error Envelopes")

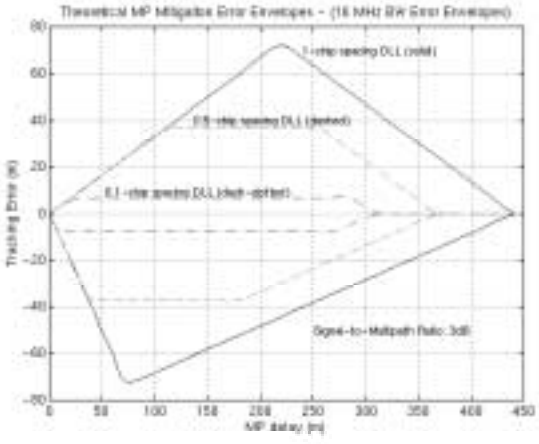

Figure 6-11 DLL Tracking Errors vs. MP Relative Delay for a Wideband (16MHz) Receiver

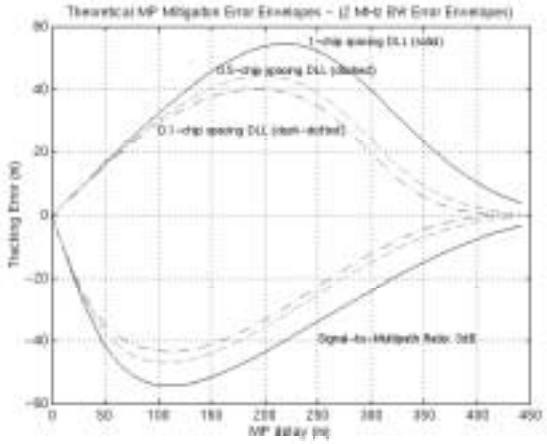

Figure 6-12 DLL Tracking Errors vs. MP Relative Delay for a Narrowband (2MHz) bandwidth Receiver

Observe that for wideband receivers, narrow correlator spacings significantly reduce the maximum MP tracking errors. However, since many narrowband receivers use a 0.5-chip correlator spacing for code tracking, and their correlation peaks are rounded, there is relatively little advantage to using a narrow correlator (with d=0.1T_c) in these receivers.

Any wideband, narrow correlator-based WAAS (Wide Area Augmentation System) receivers tracking the 2.2MHz PCBw, bandlimited geostationary (GEO) satellite will effectively have this poor multipath performance. Since for many users the GEO is at extremely low elevation angles and is essentially stationary, the multipath problem could be even more significant. This is especially true for static GEO users.

6.3 Multipath Invariance: Concept

The concept of multipath invariance (MPI) recognizes that there exist locations on the autocorrelation functions of spread spectrum signals that remain virtually invariant (or independent and constant) as a function of the multipath parameters. Intuitively, one such invariant location can be found at the plateaus of the (nominal, ideal) correlation functions of each PRN code. The combined (LOS+MP) correlation peak becomes distorted because the slopes of the MP are unknown and nonzero. At the plateaus, however, the slopes for all the GPS signals are zero. Provided the plateaus are much longer than the delays of any incident multipath signals, the *slopes of the plateaus remain zero and do not become distorted*.

Since discriminators require a non-zero correlation slope to function, the specific points within the MPI plateaus (i.e., the multipath invariant portions of the correlation function plateaus) must be found to leverage for multipath mitigation. Recalling that MP signals always arrive later than the LOS, multipath invariant points (MPI points) may be defined as those *locations on the correlation functions that are at the far edges (on the late-most side) of the correlation plateaus*. In most cases, these points also lie immediately adjacent to (on the early side of) the main peak and/or sidelobes of the correlation function. This is not always the case, however, as some plateaus may reside atop correlation sidelobes.

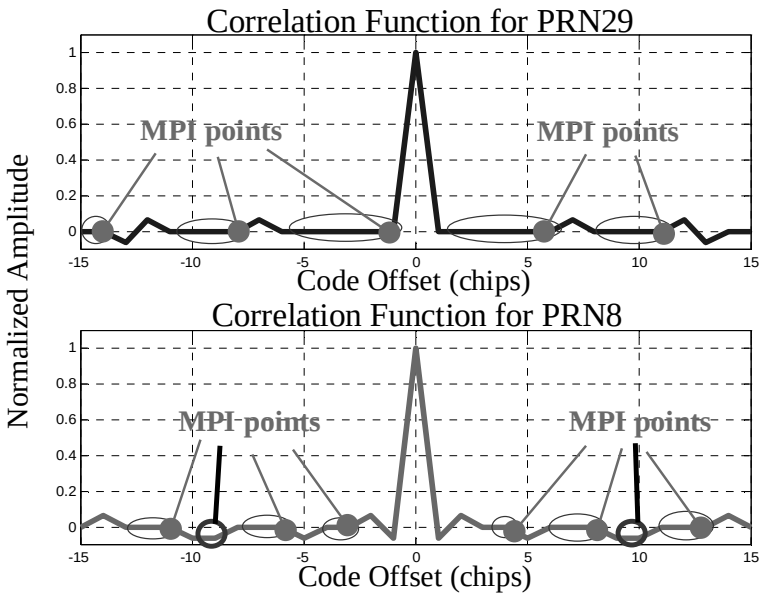

Figure 6-13 Comparison of Actual Ideal Autocorrelation Functions for PRN29 and PRN8 (Ovals Encircle the MPI Plateaus.)

Figure 6-13 shows several MPI locations near the main peak for the correlation functions of PRN8 and PRN29. The MPI plateaus (and points) are different for each PRN. The plateaus may have a minimum length of 1 chip, and they may or may not lie adjacent to the main peak. In fact, of 32 possible GPS (Gold Code) PRNs, only 17 have MPI plateaus adjacent to the main peak. (See Appendix D.) In most cases they occur at the (ideal) normalized plateau height of –1/1023, but they may also occur atop trapezoidal sidelobes. A 1-chip wide (negative) trapezoidal sidelobe occurs for PRN8 at code offsets of ±10 chips. This MPI region is shown highlighted (with thick lines) in the bottom plot of Figure 6-13.

6.3.1 Assumptions

Given that multipath distorts the correlation function, there are only two primary assumptions required to achieving the MPI condition. The first is simply that the MPI plateau length is much greater than the maximum relative MP delay. Accordingly, for each PRN, the best MPI point is the one that terminates the largest plateau. (Actually, since the

correlation function is symmetric, there are two "optimal" MPI points for each code epoch.) Table 6-1 lists the best MPI point locations relative to the main peak along with the corresponding widths of the MPI plateaus. Observe that the minimum of these maximal MPI plateau widths is 10 chips wide and occurs for PRN20.

PRN	Code Offset of MPI Point from Main Peak (±,chips)	Max. MPI Plateau Width (chips)	PRN	Code Offset of MPI Point from Main Peak (±,chips)	Max. MPI Plateau Width (chips)
1	326	23	17	137	22
2	396	16	18	57	19
3	316	21	19	233	11
4	79	14	20	476	10
5	469	14	21	66	13
6	416	12	22	450	11
7	369	19	23	107	15
8	373	15	24	139	13
9	253	12	25	162	17
10	45	19	26	454	11
11	218	21	27	329	13
12	445	11	28	312	15
13	227	27	29	134	11
14	338	14	30	263	15
15	407	18	31	299	11
16	395	26	32	33	23

Table 6-1 Optimal MPI Point Locations and Corresponding Maximum Plateau Widths for all Current GPS PRNs

Note that finite precorrelation bandwidth (PCBw), however, may decrease the effective plateau width. More specifically, distortions introduced by precorrelation filtering may extend from the trailing edge of a correlation peak or sidelobe well into the MPI region. If sizeable distortions extend to the (desired) MPI point, the correlation amplitude bias will render the MPI location unreliable. In fact, even if the oscillations die out, but do so too close to the MPI point, multipath signals could still cause these effects to distort the plateau around the MPI point. Figure 6-14 and 6-15 plot several filtered correlation peaks to illustrate the effects that finite PCBw and variable filter order have on the distortions of the

correlation peak plateaus. Observe that for low-order, narrowband receivers, sizeable distortions may extend as far as 5 chips into the plateau.

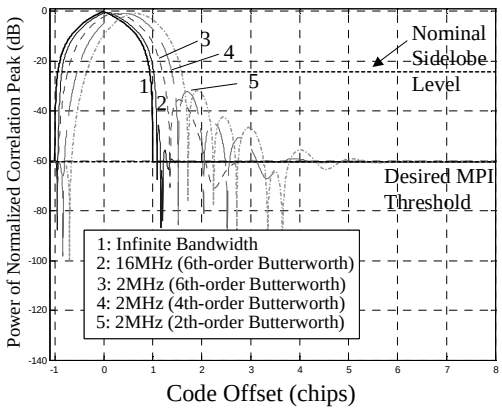

Figure 6-14 Effects of Finite PCBw and Precorrelation Filter Order on Correlation Plateau Distortion (Ideal Main Peak Shown for 6th-Order Butterworth Filter PCBw (MHz) = 16, 2, 2; 4th-Order Butterworth Filter PCBw (MHz) = 2; 2nd-Order Butterworth Filter PCBw (MHz) = 2)

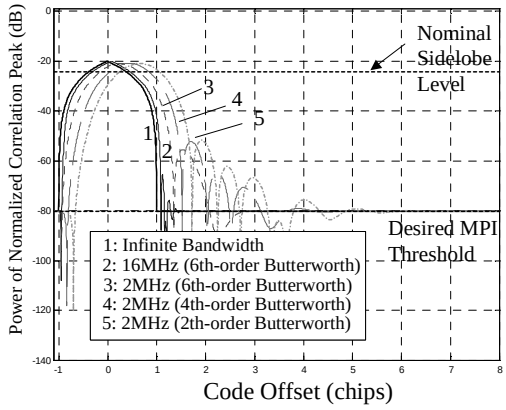

Figure 6-15 Effects of Finite PCBw and Precorrelation Filter Order on Correlation Plateau Distortion (Ideal, Nominal Sidelobe Shown for 6th-Order Butterworth Filter PCBw (MHz) = 16, 2, 2; 4th-Order Butterworth Filter PCBw (MHz) = 2; 2nd-Order Butterworth Filter PCBw (MHz) = 2)

The MPI concept also assumes that multipath having relative delays of two chips (approximately 600 meters) or more are unlikely and/or have extremely low powers compared to the LOS autocorrelation peak and sidelobes. This low signal power assumption is most appropriate in the case of rapidly changing receiver-reflector geometry. As a result, the fading frequency will tend to be higher at greater distances between the reflector and the receiver [van Nee92a]. Recall that the combination of low multipath signal power and high fading frequencies tends to "whiten" any spurious MP interference making them more easily mitigated through time averaging (e.g., carrier aiding and carrier smoothing). (Refer to Section 6.14.)

Finally, the concept of MP invariance assumes that the correlation function itself is not distorted from other effects such as continuous wave (CW) interference. If this occurs, the fundamental code correlation function—the peaks and plateaus—may become distorted in

an unknown (i.e., unmodeled) way [Van Dierendonck99b]. (Recall from Chapter 3 that EWFs—although extremely rare—may also induce distortion of the correlation plateau. Still, only "lead" EWF failure modes affect the *leading edges* of the correlation lobes. As a result, only one-half of TM A and, accordingly, one-half of TM C EWFs violate the MPI assumptions.)

6.3.2 Analysis of MPI Discriminator

Using even a single correlator pair (in addition to a pair used to track the main correlation peak), it is possible to make effective multipath invariant measurements of the correlation function. The correlation equation for *M* multipath signals in a single receiver channel is expressed as

$$\overline{s_1(t)s_2(t)} = R(\tau)\cos(\omega_0 t + \theta_0) + \sum_{m=1}^{M} \alpha_m R(\tau - \delta_m)\cos\left[(\omega_0 - \omega_m)t + \theta_m\right] \qquad (6.3)$$

where

$R(\tau)$ is the correlation function of the nominal signal

θ_0 is the phase of the nominal LOS signal

ω_0 is the frequency of the nominal LOS signal

τ_0 is the nominal tracking error (offset)

α_m is the relative amplitude (i.e., attenuation factor) of the *m*-th MP signal

δ_m is the relative delay of the *m*-th MP signal

ω_m is the relative frequency (differential Doppler) of the *m*-th MP signal

M is the total number of incident MP signals

Assuming perfect PLL tracking, such that $\theta_0 = \omega_0 = 0$, Equation (6.3) above becomes

$$\overline{s_1(t)s_2(t)} = R(\tau) + \sum_{m=1}^{M} \alpha_m R(\tau - \delta_m)\cos(\omega_m t + \theta_m) \qquad (6.4)$$

Conceptually, a receiver may achieve multipath invariance by sampling at the (late most) edge of an MPI plateau as illustrated below in Figure 6-16. For a correlator pair placed in

the vicinity of the MPI point, the late correlator output becomes $R(\tau-(\varepsilon-\mathrm{T_c}))$, where ε is a small code offset of the Late correlator from the MPI point. (The following section discusses how to select ε.)

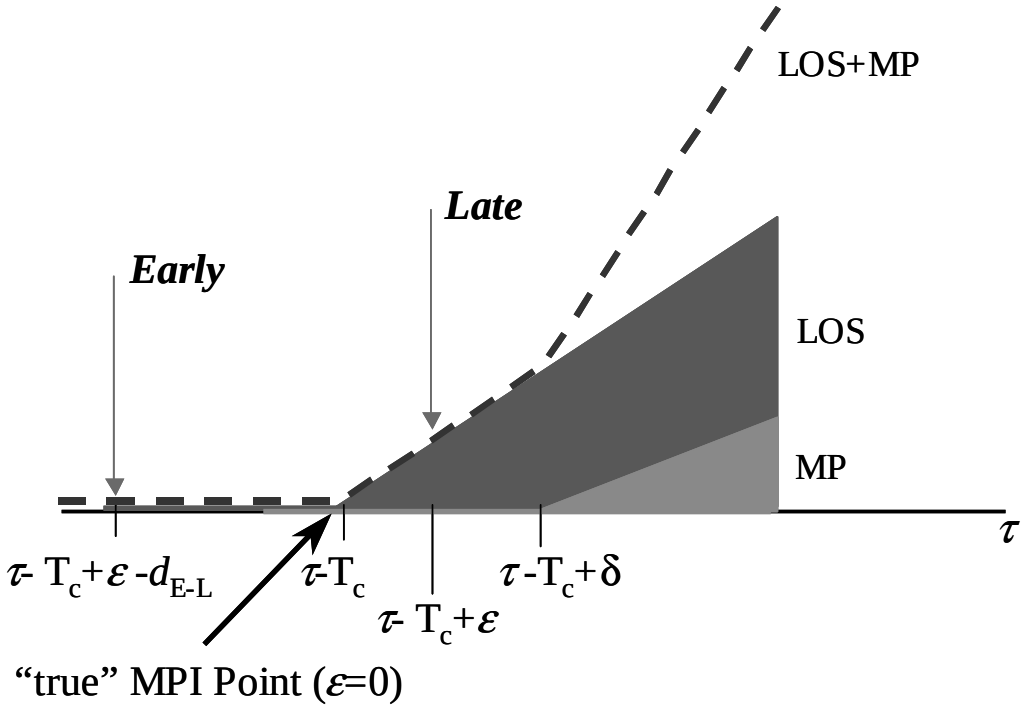

Figure 6-16 Sampling for Multipath Invariance Using a Single (MPI) Correlator Pair (MPI Region of Correlation Peak or Sidelobe Shown)

Accordingly, if ε is small relative to δ, the early correlator measures the MPI plateau according to

$$\overline{s_1(t)s_2(t)} = R(\tau-(\varepsilon-\mathrm{T_c})+d_{\mathrm{E\text{-}L}})+\beta(\alpha_m,\theta_m,\omega_m) \tag{6.5}$$

where $\beta(\alpha_m,\theta_m,\omega_m)$ is the correlation plateau height (correlation power) corresponding to the sum of the M multipath plateaus, and $d_{\mathrm{E\text{-}L}}$ is the correlator spacing for the MPI correlator pair. Note that this quantity varies as a function of the multipath parameters α_m, θ_m, and ω_m, but not the relative delays, δ_m. This is due to the assumption that

$$\varepsilon \le \delta_m < \mathrm{d}^{k}{}_{\text{plateau}} - d_{\text{E-L}}, \forall m \tag{6.6}$$

where $\mathrm{d}^{k}{}_{\text{plateau}}$ is the selected MPI plateau width for a given PRN, *k*. In other words, the late correlator must sample ahead of (i.e., earlier than) the MP correlation peaks. A more detailed illustration of the MPI-correlators and their corresponding output equations are illustrated in Figure 6-17 below.

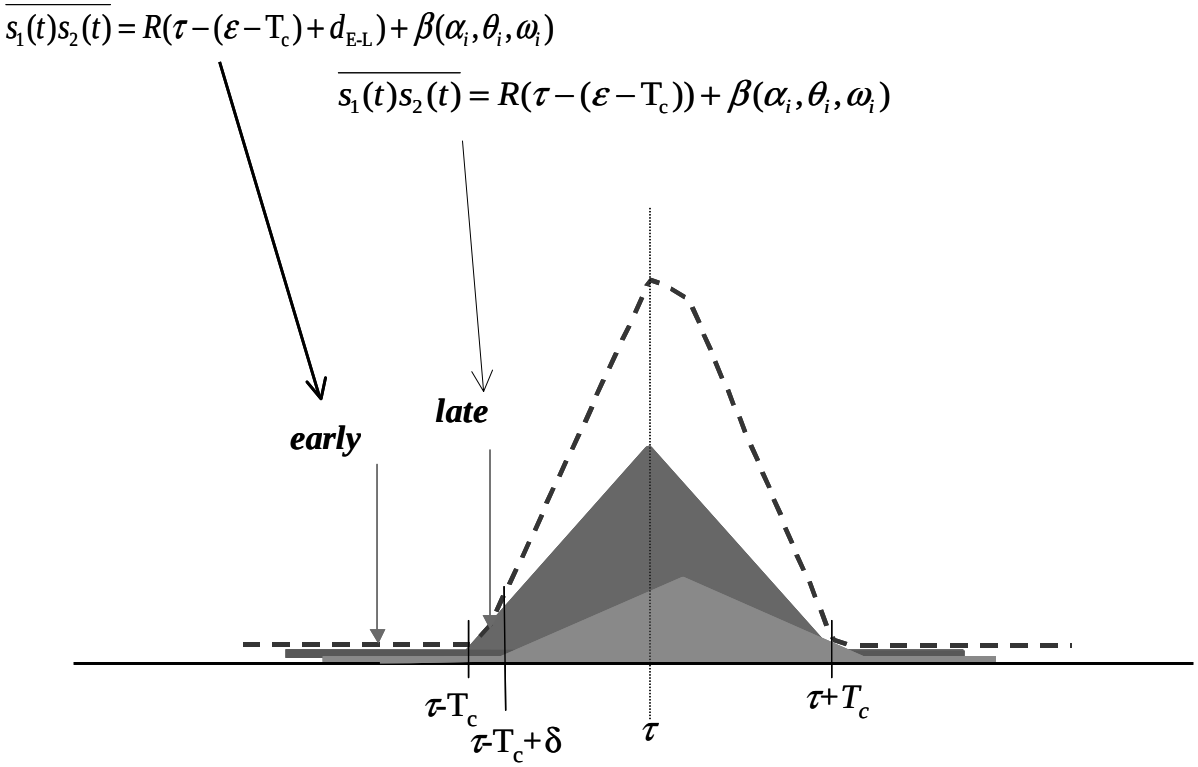

Figure 6-17 Correlation Samples in the MPI Region

Subtracting the early correlator output from the late for this correlator pair forms an *L-E* discriminator, $D(\tau_{mpi})$. Provided the minimum MP delay, $\delta_{m,min}$, is less than ε, then

$$D(\tau_{mpi}) = R(\tau - (\varepsilon - \mathrm{T_c})) - R(\tau - (\varepsilon - \mathrm{T_c}) + d_{\text{E-L}}) \tag{6.7}$$

and the discriminator measurements are multipath invariant. This is the desired MPI condition. Figure 6-18 below illustrates this case for a (fictitious) MPI discriminator function in the MPI region of a bandlimited correlation peak (or sidelobe). Observe that

MP-induced variations do not affect the measurements made at ε. Conversely, if $\varepsilon > \delta_{m,min}$, the MPI discriminator measurements will depend on the MP parameters according to

$$D(\tau_{mpi}) = R(\tau - (\varepsilon - \mathrm{T_c})) + \sum_{i=1}^{N} \alpha_i \left(R(\tau - \tau_i - \delta_i) + b_0 \right) \cos(\omega_i t + \theta_i) - \beta(\alpha_i, \theta_i, \omega_i) \quad (6.8)$$

Figure 6-19 depicts this case. Here, it is clear that MP variations cause the discriminator at ε to be MP-dependent.

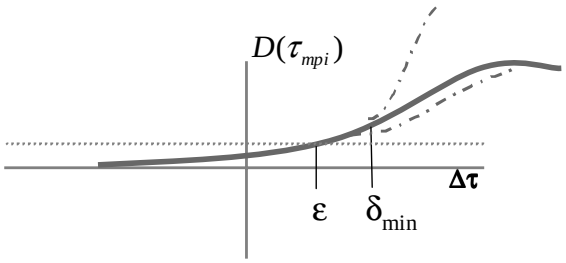

Figure 6-18 Sample desired MPI Discriminator with $\varepsilon > \delta_{m,min}$.

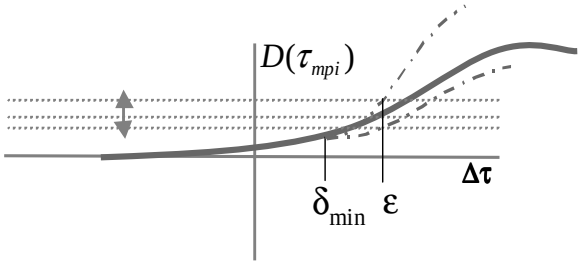

Figure 6-19 Sample Desired MPI Discriminator with $\varepsilon < \delta_{m,min}$.

It should be noted that the MPI condition is not dependent on the bandwidth of the precorrelation filter. Indeed finite PCBw does alter the shape of the correlation peak as discussed in Section 2.1.3 of Chapter 2. This, however, affects only the slope of the MPI discriminator—shallower for narrow bandwidths, steeper for wide bandwidths. The MPI point, remains the same, and is defined as

$$\max_{\tau} \left\{ \arg \left[D(\tau_{mpi}) = 0 \right] \right\} \quad (6.9)$$

Note that for Equation (6.9) above, there is an implicit assumption that τ_{mpi} is valid only in the vicinity (e.g., within $\pm \mathrm{T_c}/2$) of the desired MPI point.

6.3.3 Selection of Desired MPI Point Location

The ideal MPI point within a given MPI region is actually a design parameter. There is a tradeoff between the observability of the MPI point and the multipath invariance of this

location. The plateaus produce a zero discriminator value at more than a single offset, $\varepsilon < \delta_{\min}$. Practically speaking, however, in order to most easily differentiate an MPI point from the plateau, $D(\tau_{mpi})$ should be as large as possible. This implies a larger ε, which is undesirable since the MPI condition might more easily be violated for short-delay (small δ_{min}) MP signals.

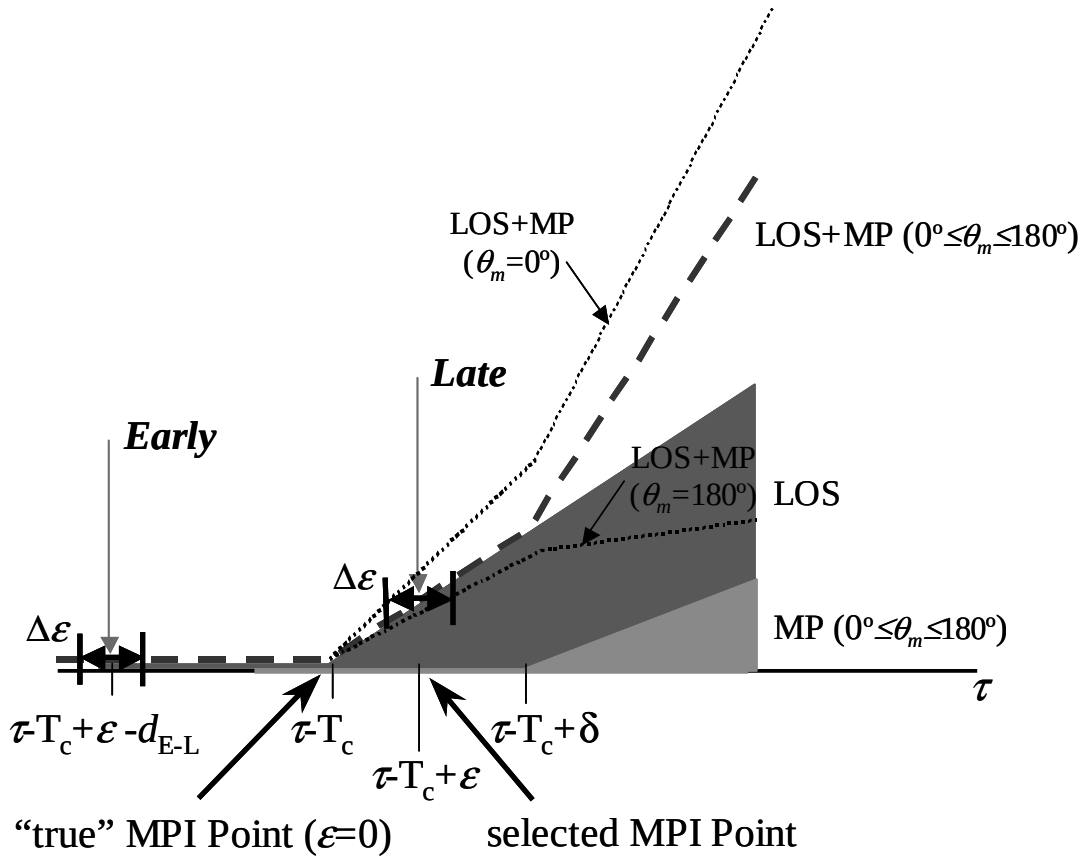

Figure 6-20 MPI Region of Correlation Peak or Sidelobe Showing Maximum MP Error Bounds at Desired MPI Point

It is possible to define an exact "target" MPI point to guarantee minimal MP variation for arbitrarily close MP signals. Assuming that any MP variation in $D(\tau_{mpi})$ induces a tracking error in an equivalent DLL, a maximum variation, $\Delta\varepsilon$, due to multipath can be defined. Assuming a single (strong) MP signal with SMR=3dB, the minimum and maximum variations in ε are governed by the maximum in-phase (θ_m=0°) and out-of-phase

(θ_m=180°) errors, respectively. (See Figure 6-20.) From these bounds, new MPI "double-discriminator" curves—the difference of two MPI discriminator curves—can be found and used to compute Δε corresponding to an arbitrary MPI (design) point, ε. The double-discriminator, ${}^2D(\tau_{mpi})$ is expressed as

$$ {}^2D(\tau_{mpi}) = D(\tau_{mpi} + \varepsilon/2) - D(\tau_{mpi} - \varepsilon/2) \tag{6.10} $$

Figure 6-21 through 6-26 below show the case for the nominal (ideal, infinite bandwidth) signal, a 16MHz, and a 2MHz PCBw, respectively. The analysis evaluated a correlator spacing of 0.5Tc and an MP relative delay of 0.25m. The correlator spacing selection has negligible effect on this analysis. To design for MP delays greater than 1 meter, the analysis placed the MP relative delay (arbitrarily) at a small nominal offsets of 0.25 meters. A total of eight curves are shown for each case and the discriminator curves are $\left[D(\tau_{mpi})\right]_{\max}$, $\left[D(\tau_{mpi})\right]_{\min}$, and $\left[D(\tau_{mpi})\right]_{\text{nom}}$ corresponding to the (main peak-adjacent) MPI-region discriminator curves for the nominal signal, the in-phase sum of the nominal and the MP signal, and the out-of-phase MP and nominal sum, respectively. The ideal MPI point offset corresponds to $\varepsilon = 0\text{m}$. By definition, the MPI variation, $\Delta\varepsilon_{\max}$, at this point is zero. (Recall that any offset where ε is less than 0 is effectively an invalid point, since its magnitude is not unique and cannot be distinguished from the MPI plateau.) In each figure, five separate ${}^2D(\tau_{mpi})$ curves are given corresponding to variations $\Delta\varepsilon_{\max}$=1m, $\Delta\varepsilon_{\max}$=2m, $\Delta\varepsilon_{\max}$=3m, $\Delta\varepsilon_{\max}$=4m, and $\Delta\varepsilon_{\max}$=5m. The vertical dashed lines indicate the values of ε that produce these maximum MPI-point errors. The plots indicate that although there are significant amplitude differences, the MPI point exists for both narrowband and wideband receivers. However, there is a tradeoff between maximum MP error and the selected MPI point. The work that follows uses $\varepsilon = 7\text{m}$ such that $\Delta\varepsilon_{\max}$ is less than 1.5 meters for receivers of all PCBws greater than or equal to 2MHz.

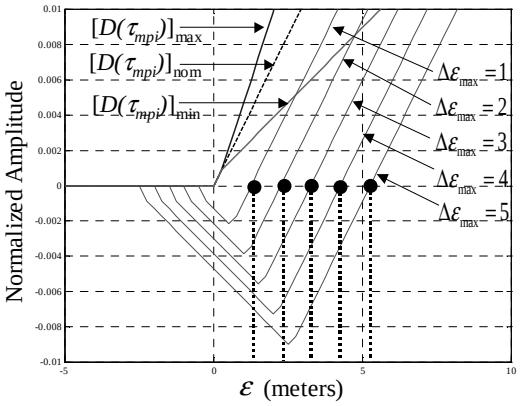

Figure 6-21 MPI-Point Designs for Infinite PCBw, Main Peak-Adjacent MPI Plateau

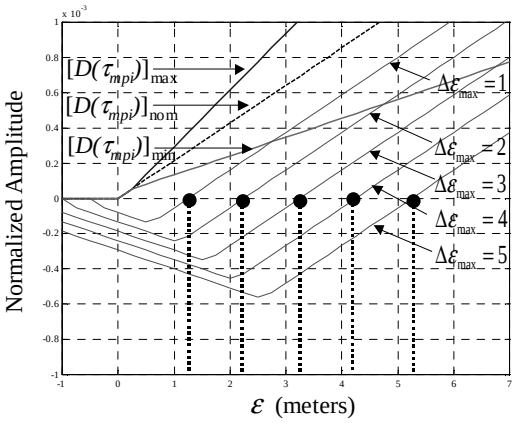

Figure 6-24 MPI-Point Designs for Infinite PCBw, Sidelobe-Adjacent MPI Plateau

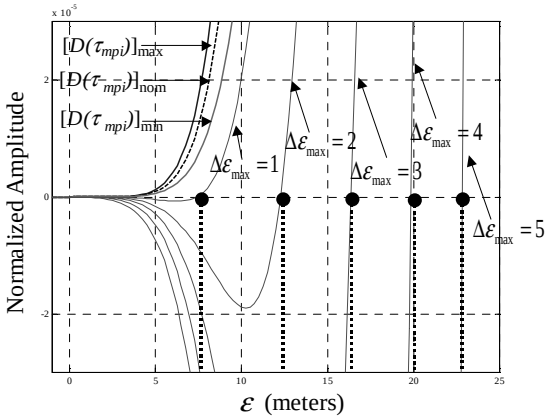

Figure 6-22 MPI-point Designs for 16MHz, Main Peak-Adjacent MPI Plateau

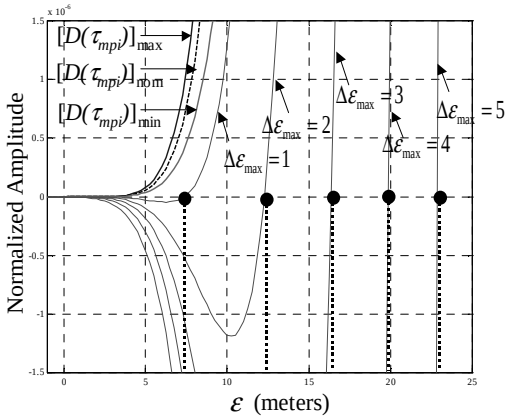

Figure 6-25 MPI-Point Designs for 16MHz, Sidelobe-Adjacent MPI Plateau

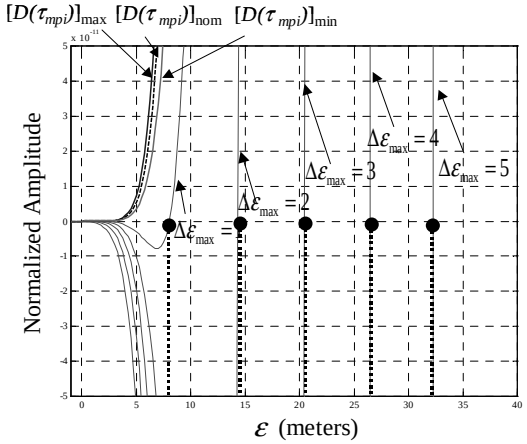

Figure 6-23 MPI-Point Designs for 2MHz, Main Peak MPI-Plateau

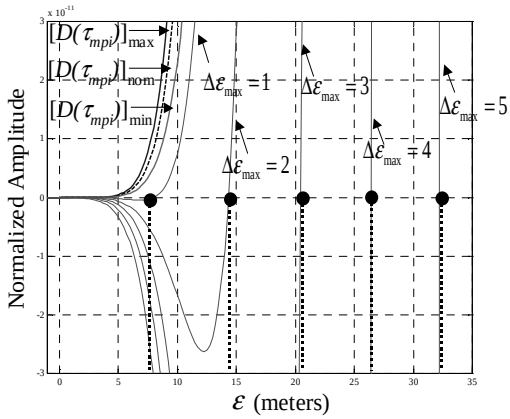

Figure 6-26 MPI-Point Designs for 2MHz, Sidelobe-Adjacent MPI-Plateau

6.4 Multipath Invariance: Practical Considerations

The discriminator of the single-correlator pair (MPI pair) MPI point is simply L-E. Although it samples at the MPI location, it has comparable noise and multipath characteristics to a conventional E-L DLL discriminator. As mentioned previously in Section 2.2.2, the worst noise performance is obtained from non-coherent code tracking. Conversely the best noise performance is achieved by coherent DLLs. Coherent DLLs, however, tend not to be as robust, in low signal power conditions [Van Dierendonck95].

The MPI discriminator relies on sampling at low correlation power signals with fidelity. Signal power variations of the LOS signal (i.e., from rising or setting satellites) only exacerbate noise performance issues associated with this task. In practice it is necessary to remove LOS signal power variations that may adversely affect the location of the desired MPI point. In addition, relatively MP-free and noise-free measurements should be made by decoupling the MPI discriminator dynamics from the MP-corrupted primary code tracking loop and instead linking them to the relatively clean carrier phase measurements. The following sections provide derivations for these processes.

6.4.1 Removal of LOS Amplitude Variations

A receiver must locate the MPI point using signal power measurements. An appropriate threshold can be chosen based on ε and the desired maximum $\Delta\varepsilon_{\max}$. However, changes to the satellite signal power can change the estimate. These variations do not impact the MPI condition. Instead they may cause the filter bias, $b_{u,mpi}$, to differ for each satellite. Specifically, since the received satellite signal powers frequently vary as a function of elevation angle, a non-normalized correlation peak will be elevation-angle dependent. Two methods, provided they remain independent of any MP parameters, may remove the effects of such signal power variations: normalization and calibration. The normalization method works in real-time and may be implemented in the same manner on any receiver and antenna configuration. Calibration requires that hardware-specific measurement data be taken, processed, and stored offline. Once obtained, the calibration data may remove the

signal amplitude variation dynamics more effectively than normalization alone. The following two subsections discuss each of these methods in detail.

Normalization

Recall that the previous analysis utilized the normalized correlation function, $R(\tau)$. More precisely, this presumed a perfect PLL tracking such that all the quadrature samples, Q, were zero. Accordingly, the MP-free correlation function samples, $I_{x,norm}$, were normalized according to

$$I_{x,norm} = \frac{I_x}{I_{\max}} \tag{6.11}$$

where I_x is in-phase samples of the correlation peak for an arbitrary code offset, x. I_{max} is the maximum correlation (peak) value.

In an actual receiver, however, only the Early and Late (and, sometimes, Prompt) correlator outputs are available to normalize the measurements. The equations for a conventional, normalized (noncoherent or coherent) DLL are given from [Kaplan96: Ward] as

$$\bar{E}_{norm} = \frac{\sum_{T_I} \sqrt{\left(I_e^{\,2} + Q_e^{\,2}\right)}}{\sum_{T_I} \sqrt{\left(I_e^{\,2} + Q_e^{\,2}\right)} + \sum_{T_I} \sqrt{\left(I_l^{\,2} + Q_l^{\,2}\right)}} \tag{6.12}$$

and

$$\bar{L}_{norm} = \frac{\sum_{T_I} \sqrt{\left(I_l^{\,2} + Q_l^{\,2}\right)}}{\sum_{T_I} \sqrt{\left(I_e^{\,2} + Q_e^{\,2}\right)} + \sum_{T_I} \sqrt{\left(I_l^{\,2} + Q_l^{\,2}\right)}} \tag{6.13}$$

$\bar{E}_{norm}$ and $\bar{L}_{norm}$ refer to the normalized Early and Late correlator measurement regions integrated over a period of T_I seconds. These equations reduce the SNR sensitivity. However they rely on MP-varying measurements at the main peak.

For the MPI concept we have implicitly assumed that carrier tracking was relatively invariant to code multipath. This assumption generally holds since the carrier phase multipath is always at most on the order of a few centimeters [Braasch95]. Recall (from Equation 2.11) that phase tracking uses a ratio of the I_P and Q_P measurements according to

$$\delta\phi = \text{atan}\left(\frac{\tilde{Q}_P}{\tilde{I}_P}\right) \tag{6.14}$$

where for the *k*th satellite,

$$\tilde{I}_P = A^k \cos(\theta_o) + \sum_{i=1}^{M} \alpha_i A^k \cos(\theta_i) \tag{6.15}$$

and

$$\tilde{Q}_P = A^k \sin(\theta_o) + \sum_{i=1}^{M} \alpha_i A^k \sin(\theta_i) \tag{6.16}$$

In the above equations, A^k is elevation angle dependent such that $A^k = A^k(\theta_{elev})$. In addition, the summed MP terms in the above expressions may be combined and considered a single, MP signal with a resultant phase, θ_{MP} and amplitude, $\alpha_r A^k$ as follows:

$$\alpha_r A^k{}_{MP} \cos(\theta_{MP}) = \sum_{i=1}^{M} \alpha_i A^k \cos(\theta_i) \tag{6.17}$$

$$\alpha_r A^k{}_{MP} \sin(\theta_{MP}) = \sum_{i=1}^{M} \alpha_i A^k \sin(\theta_i) \tag{6.18}$$

(for the in-phase and quadrature samples, respectively).

Letting $A^k{}_{I,MP} = \alpha_r A^k{}_{MP} \cos(\theta_{MP})$ and $A^k{}_{Q,MP} = \alpha_r A^k{}_{MP} \sin(\theta_{MP})$, allows Equations (6.17) and (6.18) to be given in terms of the MP and LOS amplitude scale factors:

$$\begin{aligned} \tilde{I}_p &= A^k A^k{}_{I,MP} I_p \\ \tilde{Q}_p &= A^k A^k{}_{I,MP} Q_p \end{aligned} \tag{6.19}$$

Multipath and LOS signal attenuation effects, however, scale the entire correlation function. It follows that the in-phase and quadrature correlation peak samples are given (more generally) for an arbitrary code offset, *x*, as

$$\begin{aligned} \tilde{I}_x &= A^k A^k{}_{I,MP} I_x \\ \tilde{Q}_x &= A^k A^k{}_{Q,MP} Q_x \end{aligned} \tag{6.20}$$

For MPI sampling, MP-invariant normalization is achievable using combinations of the in-phase and quadrature measurements taken in the vicinity of the MPI point. Note that the desired (in-phase) L-E measurements in the MPI region report the desired slope threshold, $D(\varepsilon)$, and are given by

$$A^k A^k{}_{I,MP} \sum_{\mathrm{T_I}} \left(I_{l,mpi} - I_{e,mpi} \right) = D(\varepsilon) \tag{6.21}$$

where $\sum_{\mathrm{T_I}} \left(I_{l,mpi} - I_{e,mpi} \right)$ is the integrated (mean) difference of the late and early in-phase samples in the MPI. $D(\varepsilon)$ is the amplitude-varying MPI discriminator evaluated at ε. Although this implicitly assumes PLL tracking for MPI sampling, in general the quadrature samples are nonzero and have a nonzero mean. Accordingly, a modified normalized MPI discriminator, $D'(\varepsilon)$, may be found using

$$\frac{\dfrac{\sum_{\mathrm{T_I}}\left(I_{l,mpi}-I_{e,mpi}\right)}{\frac{1}{2}\sum_{\mathrm{T_I}}\left|Q_{l,mpi}+Q_{e,mpi}\right|}}{\dfrac{\sum_{\mathrm{T_I}}\tilde{I}_P}{\sum_{\mathrm{T_I}}\left|\tilde{Q}_P\right|}} \approx D'(\varepsilon) \tag{6.22}$$

where the scale factors have cancelled and are not shown. Equation (6.22) provides effective MP invariant normalization with respect to signal power variations to the extent the following two statements are true:

- The factors A^k, $A^k{}_{Q,MP}$, and $A^k{}_{I,MP}$ model the amplitude scaling of the signal described in Equations (6.17) and (6.18).

- The accumulated quadrature samples, $\sum_{\mathrm{T_I}}\left|\tilde{Q}_P\right|$ and $\frac{1}{2}\sum_{\mathrm{T_I}}\left|Q_{l,mpi}+Q_{e,mpi}\right|$, are correlated, nonzero quantities.

Calibration

For many users, signal power calibration may also be used to remove some of the effects of signal power variations caused by rising and setting satellites. Due to beam shaping of the transmitted GPS signal, the minimal LOS signal powers vary only 2-3dB as a function of elevation angle [Aparicio]. Ignoring attenuation from signal-scattering objects (e.g., foliage), the dominant factor in the received signal power variation is the receiving antenna gain pattern. These patterns may vary widely for different antenna types [Clark95], [Akos00c]. Once known, however, one way to remove the elevation-angle dependence effect is to adjust the tracking threshold as a function of satellite elevation angle (and azimuth if the pattern is not symmetric).

This calibration is simply an experimental determination of the scale factor, $a\left(\theta_{elev}\right)$, such that

$$a\left(\theta_{elev}\right) = A^k \tag{6.23}$$

for all tracked satellites, *k*. Once obtained, the calibration-normalized discriminator, $D_c'(\varepsilon)$ is simply

$$D_c'(\varepsilon) = a\left(\theta_{elev}\right) D(\varepsilon) \tag{6.24}$$

and Equation (6.21) becomes

$$A^k A^k{}_{I,MP} \sum \left(I_{l,mpi} - I_{e,mpi} \right) \approx D_c'\left(\varepsilon\right) \tag{6.25}$$

Equation (6.25) above adjusts the MPI discriminator threshold as a function of elevation angle such that A^k is canceled. $A^k{}_{I,MP}$ is the MP-varying residual that should be small for properly selected $\varepsilon \approx 0$.

6.4.2 Dynamic Decoupling

As mentioned previously, TrEC assumes that code tracking (of the main peak) is continuously enabled and occurs independently of the MPI point sampling. Under these conditions, the MP invariant dynamics of the satellite are known through the carrier phase tracking loop. Carrier aiding provides the mechanism to decouple the MP-varying code dynamics from the MPI sampling pair. Recall from Section 2.3.1 of Chapter 2 that when the code dynamics are ignored, the code phase updates are given by

$$\Delta\tau_i = \left(\Phi_i - \Phi_{i-1}\right) \tag{6.26}$$

Although this (complete) decoupling cannot be used for primary tracking, the MPI correlator pair can use this for station keeping. In other words, the MPI correlator pair can *maintain* any code offset relative to the main peak using only carrier phase-dependent measurements, which are, accordingly, independent of the DLL. The updates account for virtually all signal dynamics—including Doppler and user platform motion—and are governed completely by Equation (6.26) above.

Note that these "carrier aiding-based" updates, however, diverge with time because of code-carrier divergence (due to the ionosphere). The divergence (primarily) varies as a function of satellite azimuth and elevation angles and time of day. Although estimates of the pseudorange error can be made using ionospheric models, the rate of divergence is difficult to quantify for single frequency receivers. (Conversely, dual-frequency receivers may effectively remove these ionospheric effects.) In general, the maximum code-carrier divergence rate occurs for low-elevation angle satellites and is 1.6cm/sec [Klobuchar96]. Without differential corrections, this becomes a (bias) error source for single-frequency users. Otherwise, these users may use carrier-propagated solutions almost indefinitely.

6.5 Tracking Error Compensator (TrEC)

Using (at least) one additional correlator pair per channel in a receiver, the MPI sampling concept can readily be used to obtain virtually multipath error-free code phase measurements. Assuming the code-tracking loop is tracking, an additional, or "free" correlator may independently locate the MPI point relative to the tracking pair. The ideal, noiseless and infinite bandwidth offset of the MPI point from the main peak, $\Delta c^{k}_{mpi,ideal}$, is known for all PRNs; its ideal distance from the MP-free main peak is also known. The tracking error due to multipath (and thermal noise) is then simply a pseudorange error correction (to the *k*th satellite) given by

$$\Delta\hat{\rho}^{k}(t) = \hat{\tau}^{k}{}_{mpi}(t) - \hat{\tau}^{k}(t) + \Delta c^{k}_{mpi,ideal} + b_{PCBw} \tag{6.27}$$

where $\hat{\tau}^{k}{}_{mpi}(t)$ is the time-varying code phase estimate of the peak based on the measured MPI point, and b_{PCBw} is the bias in that estimate due to finite bandwidth. Figure 6-27 below illustrates this operation for a fictitious (infinite bandwidth) autocorrelation function.

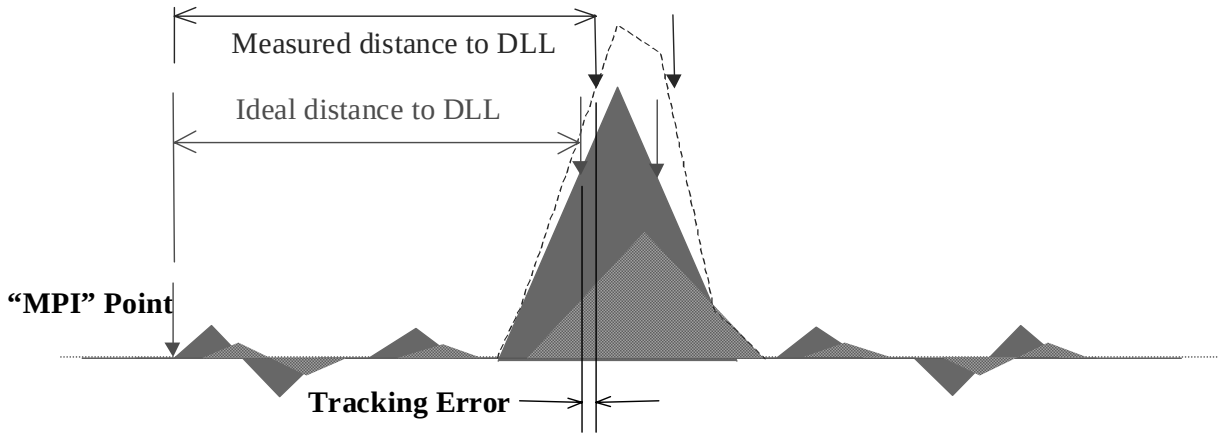

Figure 6-27 Measurement of DLL Tracking Errors by the Tracking Error Compensator

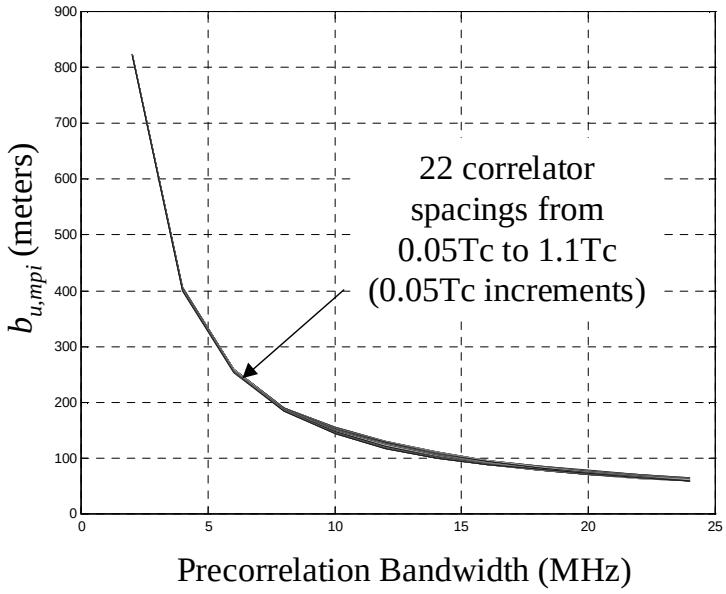

Figure 6-28 Variation of TrEC Precorrelation Filter Bias as a Function of PCBw (22 Curves Plotted Corresponding to 22 Correlator Spacings from 0.05Tc to 1.1Tc in 0.05Tc Increments)

In a noiseless analysis, the ideal MPI point is easily found for both wide and narrow PCBws. For an infinite PCBw, the MPI point is exactly the ideal (known) distance away from the main peak. For finite PCBws, however, this MPI point is actually an additional distance, $b_{u,mpi}$, away. Note that this bias is common to all satellites. It varies most significantly as a function of PCBw, but to a lesser extent DLL correlator spacing as well.

Figure 6-28 plots $b_{u,mpi}$ versus PCBw for 22 correlator spacings between $0.05T_c$ and $1.1T_c$ (in $0.05T_c$ increments). The 22 curves—one for each correlator spacing analyzed—are so similar they almost completely lie atop one another.

Figure 6-29 provides an illustration of the performance of the MPI-based tracking error compensator (TrEC). Again, this plot assumes the standard MP performance plot conditions (i.e., a single reflection with SMR = 3dB, 1 MP signal present). For comparison, the theoretical "best of" current wideband and narrowband DLL ($0.1T_c$) performance is also shown [McGraw], [Weill97]. (The $\Delta\Delta$ correlators described in Section 4.1 of Chapter 4 and also in Section 6.1.4 above achieve this performance.) Note that the analysis behind this plot assumes the ideal MPI point ($\hat{\varepsilon} = \varepsilon = 0\text{m}$) is being tracked. Under these conditions, the characteristic is not an envelope but a straight line. Since these are maximum tracking errors, this indicates that the TrEC tracking errors do not vary as a function of the MP parameters. (Although only one MP signal is assumed for this plot, recall from Equations (6.4) and (6.7) that the MPI condition makes no assumption on the number of MP signals present.)

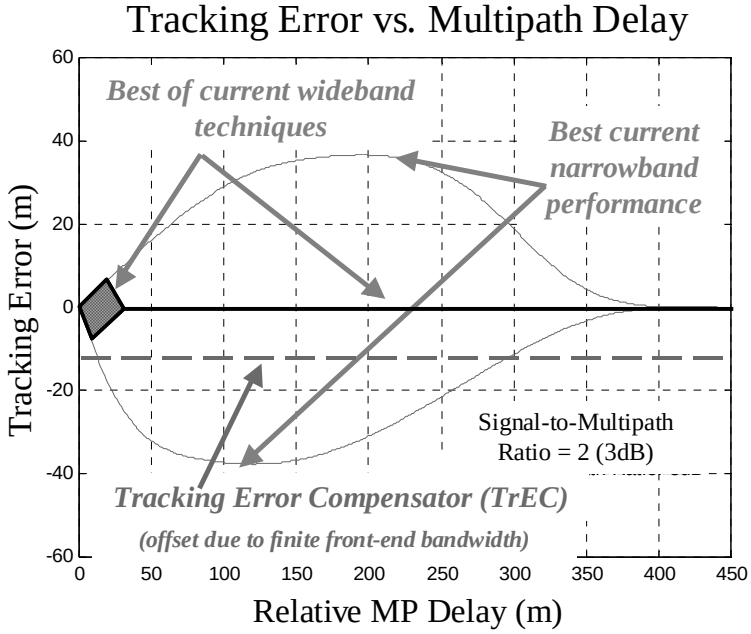

Figure 6-29 Comparison of TrEC MP Mitigation Performance on a Narrowband (PCBw=2MHz) Receiver to Best of Conventional Wideband (PCBw≥8MHz) Techniques

In an actual receiver, TrEC corrects for the nominal code tracking errors using a combination of code phase-based and carrier phase-based information. The TrEC algorithm(s) themselves (discussed in detail in this and in subsequent sections of this chapter) are fairly self-contained and reside inside the receiver microprocessor. The block diagram in Figure 6-30 illustrates the location of the TrEC algorithms relative to normal receiver operations. The MPI-sample (integration) filtering ($H_{d,mpi}$), FS optimization, and TrEC loop filter (H_{Φ}) occur within the TrEC module. (See Figure 6-35.) Each of these processes is described in Sections 6.5 and 6.7. These ultimately generate smoothed, MPI point code phase estimates as described in Section 6.7.3.

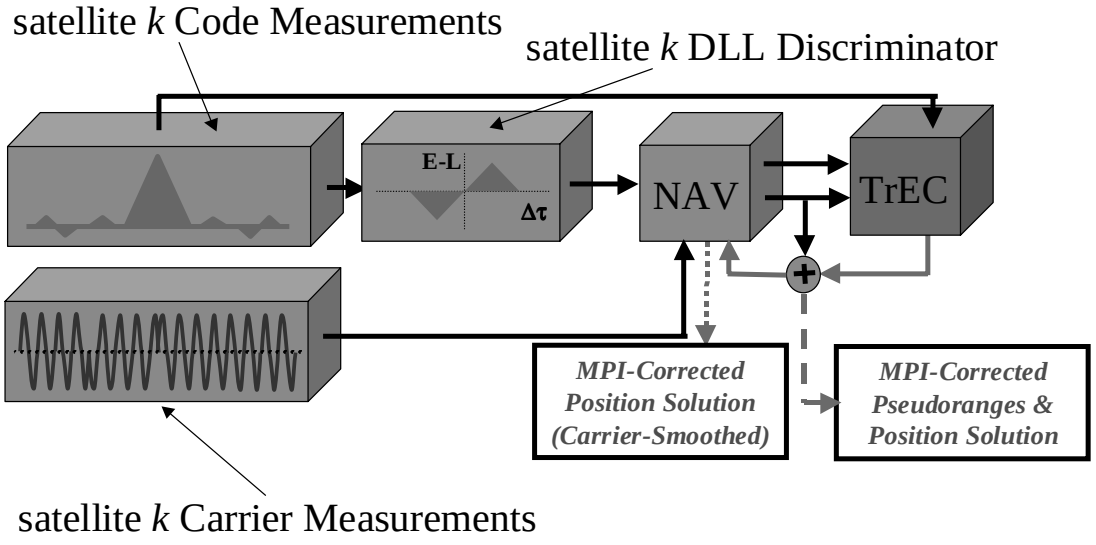

Figure 6-30 Block Diagram of a TrEC-enabled Receiver Channel

6.6 MPI Point Acquisition

Use of only a single (additional) correlator pair in a given receiver channel affords the fewest number of observables at the MPI region. (Multiple MPI correlator pair optimization schemes are discussed in Section 6.9.2.) There are numerous ways to locate the MPI point using only the discrete samples output by one or more correlator pairs. Decisions must be made on where to place that pair in order to precisely locate the MPI point relative to the DLL. The logic that governs those decisions must trade-off estimation accuracy, with convergence (or initialization) time.

Gradient-based searches (GS) are the most straightforward and are likely the simplest to implement. They require only a single (L-E) difference already output by the MPI discriminator. A tracking loop relying on a GS would use such differences (scaled by the appropriate loop gain for the MPI region) to shift the MPI correlators appropriately. For the MPI correlator pair, however, the (slope) difference is very small. Consequently, they need long integration times in order to obtain a reliable slope estimate. Further, the MPI discriminator characteristic is a strong function of PCBw and is nonlinear. As a result, the estimate of the (desired) MPI discriminator output at the MPI location may require (somewhat detailed) knowledge of the front-end filter characteristics of a particular receiver. Recall from Section 6.3.3 that this filter may have a significant impact on the obtainable MPI point offset, ε.

The gradient search method implies using simple L-E differences to locate the MPI point. However, it relies on good knowledge of those differences to update the search. A reasonable compromise is to minimize a function of L-E differences, using (magnitude) comparisons of those differences measured at different locations in the region. To update such an optimization, an efficient single-point search algorithm must be adapted.

The Fibonacci Search (FS) method was chosen as the basis for a better MPI point optimization method for the following reasons:

- It is a binary, decision-based search used in non-linear computer-aided design optimization problems.
- It uses efficient, non-gradient based search updates given large initial uncertainty.
- It is well suited for constrained (bounded) intervals of uncertainty.
- It is readily adaptable for single-point observable functions, where the evaluations are costly.

[Onwubiko] more completely describes the conventional FS algorithm. Put simply, it makes an initial guess, or evaluation of the function at a specific offset. Then, it decides

whether the minimum of that function lies to the right or to the left of that initial guess based on a simple magnitude or amplitude comparison. The routine then adjusts the guess (offset) by a predetermined amount based on the Fibonacci series and repeats the decision process until the estimate converges on the function minimum. Figure 6-31 summarizes the FS algorithm and illustrates it for a general (fictitious) cost function.

The FS method first requires a cost function be defined. For MPI point optimization, the cost function is simply $(L-E)-D(\varepsilon)=0$, where $D(\varepsilon)>0$ to ensure the MPI point is unique. Second, FS requires selection of an initial interval of uncertainty, **I**, which brackets the minimum (optimum) point. The number of evaluations is predetermined based on the Fibonacci numbers, F_n, and the desired convergence tolerance according to

$$\delta\hat{\varepsilon} \le \frac{\mathrm{I}}{F_n} \tag{6.28}$$

where for MPI point optimization, $\delta\hat{\varepsilon}$ is the maximum error in the estimate of the MPI point location, $\hat{\varepsilon}$, given as a fraction of **I**. $\hat{\varepsilon}$ is the FS-based estimate of the desired MPI point location, ε. This tolerance is a design parameter. Subsequently, the minimum F_n can be computed (one time only) from

$$\begin{aligned} F_0 &= 1 \\ F_1 &= 1 \\ F_n &= F_{n-2} + F_{n-1} \quad \kappa \ge 2 \end{aligned} \tag{6.29}$$

In the noise-free case, convergence to the minimum is guaranteed in n evaluations to within a resolution of I/ F_n.

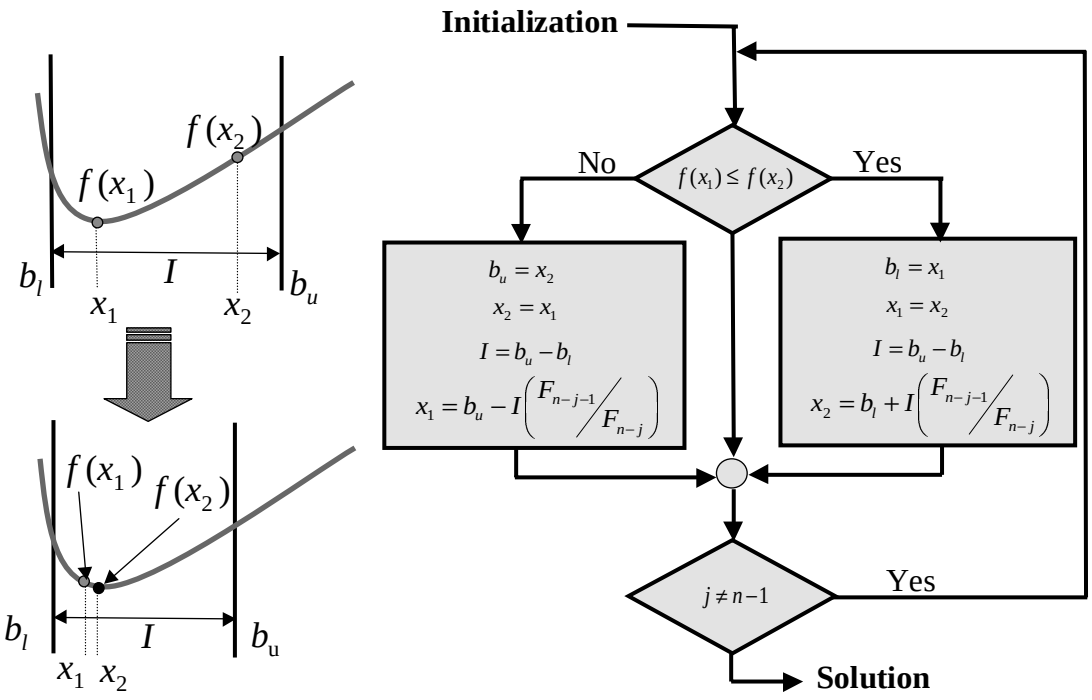

Figure 6-31 Fibonacci Search (FS) Optimization Method [Onwubiko]

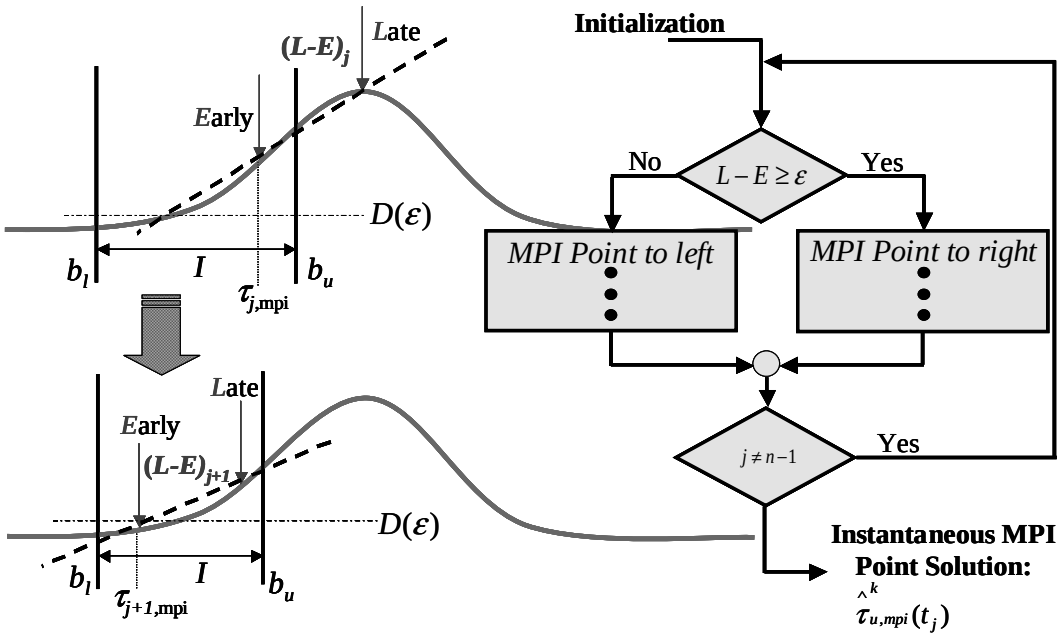

Figure 6-32 Modified Fibonacci Search for MPI Optimization

Figure 6-32 illustrates the optimization algorithm for the MPI point. Note that the MPI region is not nominally a convex function. Also, the "single-point" observable available is the (L-E) difference of the two MPI correlators. More significantly, recall that the correlation function is dynamic. These dynamics are removed using the carrier phase as described in Section 6.4.2. As the receiver accumulators (correlators) integrate (average) evaluations for this optimization for some period of time, the correlator pair maintains a fixed code offset using dynamic decoupling described by Equation (6.30). Accordingly for satellite *k*, each nominal code offset, **x** (and upper and lower bounds, b_u and b_l), gets carrier-propagated in time according to

$$\begin{aligned} x^k &= \mathrm{x}^k + \Delta\tau^k(t) \\ b^k{}_u &= \mathrm{b}^k{}_u + \Delta\tau^k(t) \\ b^k{}_l &= \mathrm{b}^k{}_l + \Delta\tau^k(t) \end{aligned} \tag{6.30}$$

where the subscripts *l* and *u* correspond to the lower and upper bounds, respectively. Note that the uncertainty interval (and the update step size) decreases with each successive evaluation decision.

For most integration times, the initial interval of uncertainty, **I**, may derive from *a priori* knowledge of the typical multipath environment in which a particular receiver must operate. In the absence of this knowledge, the MP error envelopes provide a conservative estimate for **I**. (For a narrowband receiver having a $0.5T_c$, **I**=±60m and, from Equation (6.29), $F_{\kappa,\max}$=144, this translates to 11 evaluations and $\delta\hat{\varepsilon} \le 1$m.) Of course, a large **I** corresponds to a longer initialization time since this interval requires more evaluations for convergence. The number of evaluations and the integration time required for each dictate the performance of TrEC (using only a single MPI correlator pair).

6.7 TrEC Noise Performance

This section separates the analysis of the noise performance into three parts. First it compares the correlation loss (i.e., signal power loss) of samples in the MPI region compared to those on the main correlation peak. Second, it analyzes the discriminator

noise performance in order to determine the necessary integration time for MPI point sampling. Third, it assesses the closed loop noise performance of TrEC. This implies the institution of an MPI point-locating loop filter—the analog of a receiver's code tracking loop filter.

6.7.1 Correlation Loss

At the level of the MPI correlation plateaus, the SNR of the signal of interest is considerably lower than that of the peak used for conventional tracking. Using formulas given in [GEC], the equations below compute the relative attenuation of the signal measured at the MPI point. For a conventional DLL, the correlation loss (i.e., signal power reduction) at a code offset, Δc relative to the main peak is

$$CorLoss_{\Delta code} = 20\log(1-\Delta c), \quad 0 \le \Delta c \le 1 \tag{6.31}$$

where the effects of finite PCBw have been ignored. (The nominal SNR of the LOS has an assumed maximum of 20dB or a C/N_0 of 50dB-Hz.) The correlation loss (attenuation) due to phase tracking errors is negligible.

The code correlation loss is significant, however. In steady state, this loss occurs due to the offset, $\hat{\varepsilon}$, of the target MPI point from the correlation peak. Nominal positive and negative sidelobes have amplitudes attenuated by 24.07dB (64/1023) and 23.94dB (65/1023), respectively. The ideal (noiseless, infinite bandwidth) plateau has its amplitude reduced by 60.20dB (-1/1023).

The factors for samples in the MPI region are found similarly. For ε=1m—a maximum MP-variation error, $\Delta\varepsilon$, of 1 to 2 meters—the noise and MP-free, infinite bandwidth attenuation factors for MPI points adjacent to the main peak and for positive and negative sidelobes, respectively, would be 52.27dB (2.5/1023), 62.34dB (0.8/1023), and 58.46dB (1.2/1023). (Figure 6-33 shows the desired MPI point and the MPI location error bounds for a primary correlation peak or positive sidelobe.) At low elevation angles, however, the received signal power may be attenuated as much as 20dB from its maximum. In other

words, the attenuation factor for the SNR of the MPI point samples is at most (approximately) 82.4dB.

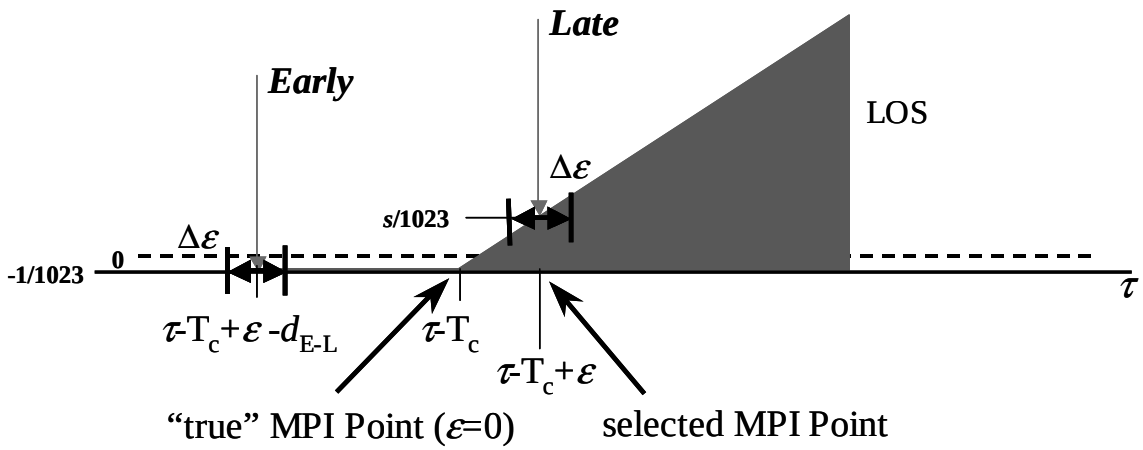

Figure 6-33 MPI Region Showing Correlation Amplitudes at Selected MPI Point; s=2.5 for a Peak-Adjacent MPI Region, s=0.8 for a Positive Sidelobe-Adjacent MPI Region, and s=1.2 for a Negative Sidelobe-Adjacent MPI Region (Not Shown).

Nominal channel noise (including satellite cross-correlation effects) models as a zero-mean AWGN process having a variance, σ_n^2. A reduction in signal power is tantamount to an amplification of this variance by the same factor. A sufficiently long integration time, T_I aims to reduce the noise variance in the MPI region, $\left(\sigma_{n,mpi}\right)^2$. Since the minimum T_I = 1ms (one code accumulation time), the increase in variance may be expressed as

$$\left(\sigma_{n,mpi}\right)^2 = \frac{\sigma_n^2}{N} \cdot 10^{\left(82.4/20\right)} \tag{6.32}$$

where N is the number of samples, and $T_I = N$e-3 seconds assuming one sample per millisecond. 13183 samples are required at a given MPI evaluation to produce an SNR equivalent to that of a correlator sampling the top of the main peak of a correlation function and using a single 1ms sample (code integration). For an FS search using only a single (e.g., L or E) correlator sample to locate the MPI point, this would imply a minimum of 13.2 seconds per evaluation required to complete a full FS optimization—as opposed to

one 1ms per evaluation for a sample taken atop the correlation peak. For the conservative case of **I**=120m (as mentioned in the previous section), this would translate to an (initial) FS convergence time of 143 seconds.

6.7.2 MPI Discriminator Noise Analysis

As discussed in Section 2.2.2 of Chapter 2, conventional discriminator functions translate amplitude measurements of the correlation peak to code delay offset or timing measurements. The fidelity of the resulting code delay estimate, however, depends on two things: 1) the variance on the noise of the difference measurements, and 2) the actual discriminator gain or slope. The variance in delay estimate for a conventional DLL discriminator having a variance, σ_{disc}^2, is given in [Misra] as

$$\sigma_\tau^2 \approx \frac{\sigma_{disc}^2}{slope} = \frac{T_c \sigma_{E-L}^2}{2} \tag{6.33}$$

The noise variance and slope for the MPI discriminator are described below.

Discriminator Variance

The L-E samples of the MPI discriminator have the same noise statistics of the E-L discriminator. The analysis of [Van Dierendonck92] derives the discriminator statistics for non-coherent, coherent and dot-product discriminators. Note that these relationships assume infinite receiver PCBw. They do not assume, however, that the tracking pair is located at the peak. Moreover, since the MPI discriminator samples have no dynamics (apart from code-carrier divergence over long integration times as discussed in Section 6.4.2), the noise performance is expected to be comparable to that of a coherent DLL discriminator—the least noisy of the three.

The normalized noise variance for a coherent E-L discriminator (σ_{E-L}^2 from Equation (6.33)) for infinite PCBw is given by [Van Dierendonck92] as

$$\sigma_{E-L}^2 = 2 \cdot d_{E-L} \tag{6.34}$$

The variance is a linear function of the correlator spacing. To verify this theory, using the implementation techniques described in Section 7.1 of Chapter 7, measurements were taken in the MPI region at a correlation function sidelobe of an actual live satellite (PRN2). A narrowband (2MHz PCBw) receiver was used, and multiple correlator pairs were used to sample the entire MPI region of the received correlation function. E-L, (1-σ) standard deviations were computed for various correlator spacings ranging form $0.2T_c$ to over $1.1T_c$ and compared to the theoretical E-L 1-sigma performance. Pairwise L-E differences were taken using several redundant spacings at several different locations within the MPI region. The differences, normalized by the (conventional DLL) prompt measurement, are given by

$$\frac{\sum_{T_I}\left(I^2{}_{l,mpi} + Q^2{}_{l,mpi}\right) - \sum_{T_I}\left(I^2{}_{e,mpi} + Q^2{}_{e,mpi}\right)}{\sum_{T_I}\left(I_l{}^2 + Q_l{}^2\right) + \sum_{T_I}\left(I_e{}^2 + Q_e{}^2\right)} \tag{6.35}$$

where $\sum_{T_I}\left(I^2{}_{l,mpi} + Q^2{}_{l,mpi}\right) - \sum_{T_I}\left(I^2{}_{e,mpi} + Q^2{}_{e,mpi}\right)$ is the (arbitrary-time, T_I) integrated L-E code correlation samples made in the MPI region. $\sum_{T_I}\left(I_l{}^2 + Q_l{}^2\right) + \sum_{T_I}\left(I_e{}^2 + Q_e{}^2\right)$ is the integrated "virtual" prompt measurement. Note that Equation (6.35) is akin to an "Early-Late Power" discriminator, and not a coherent one. However, as previously stated, once the dynamics are removed, even this more-noisy discriminator may be modeled by the simpler, coherent discriminator theory.

The normalized sigmas for the experiment are plotted below in Figure 6-34. A 100-second integration time, T_I was used to reduce the dispersion of the samples. The results indicate that the coherent discriminator noise performance, in general, upper bounds the MPI discriminator for a narrowband receiver. This is especially true for correlator spacings above $0.5T_c$. As previously stated, Equation (6.34) assumed an infinite receiver PCBw. Although no comparative results are shown here for a wideband receiver, it is expected the theory will even more closely correspond to the measured data in the wideband case.

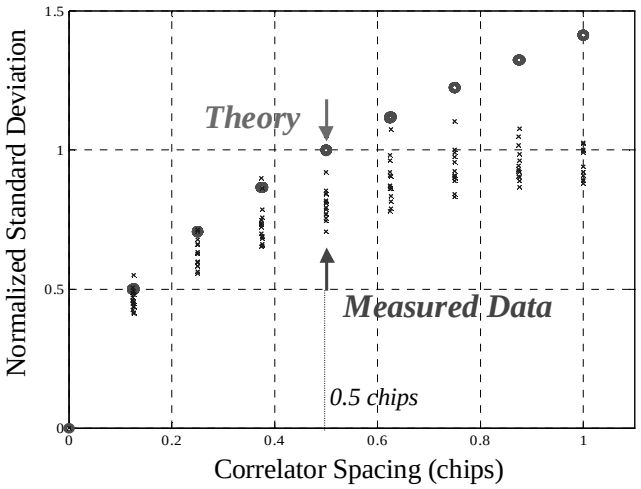

Figure 6-34 L-E Normalized Noise Statistics of MPI Samples as a Function of Correlator Spacing

It follows that the coherent DLL discriminator may somewhat-conservatively estimate the noise performance of the MPI discriminator at arbitrary correlator spacings, *d*, independent of receiver PCBw.

Discriminator Slope

The nominal slope of the MPI discriminator is, unlike that of a conventional DLL, nonlinear. As derived in Section 6.3.2, this slope equals $D(\tau_{mpi})$ (formed by L-E measurements) in general, and, at the desired MPI point it equals $D(\varepsilon)$. Without proper normalization (or calibration) of the measurements as described previously in Section 6.4.1, the tracking point also varies as a function of received signal power.

Conventional code tracking error variance (or MPI point estimation error variance) in the MPI region follows from Equation (6.33) and is given by

$$\sigma_\tau^2 \approx \frac{\sigma_{disc}^2}{slope} = \frac{\sigma_{mpi}^2}{D(\tau_{mpi})} \tag{6.36}$$

The slope, $D(\tau_{mpi}) = D(\varepsilon)$, at the desired MPI point must be non-zero. However, a smaller $D(\varepsilon)$ leads to a better approximation of the true MPI point. This implies a large inherent sensitivity to errors in the measurement of $D(\varepsilon)$ if conventional tracking were used in this region. Recall from Section 6.6, however, that the FS optimization overcomes much of this sensitivity by bracketing the true MPI point and using pre-determined incremental code offsets ($\Delta\tau$) towards that point. Only the individual ("move left" or "move right") decisions are then slope dependent, and the magnitude of the maximum error in the MPI point estimate at the end of one FS optimization is approximately the initial interval of uncertainty, **I**.

6.7.3 TrEC Loop Filter

A finite integration time is required for each L-E measurement. However, the FS will not make the correct ("move right" or "move left") decisions at each evaluation point. Consequently, the final (converged) estimate will contain some error. For TrEC to provide practical and useful corrections for multipath tracking errors, a loop filter must filter these errors over time.

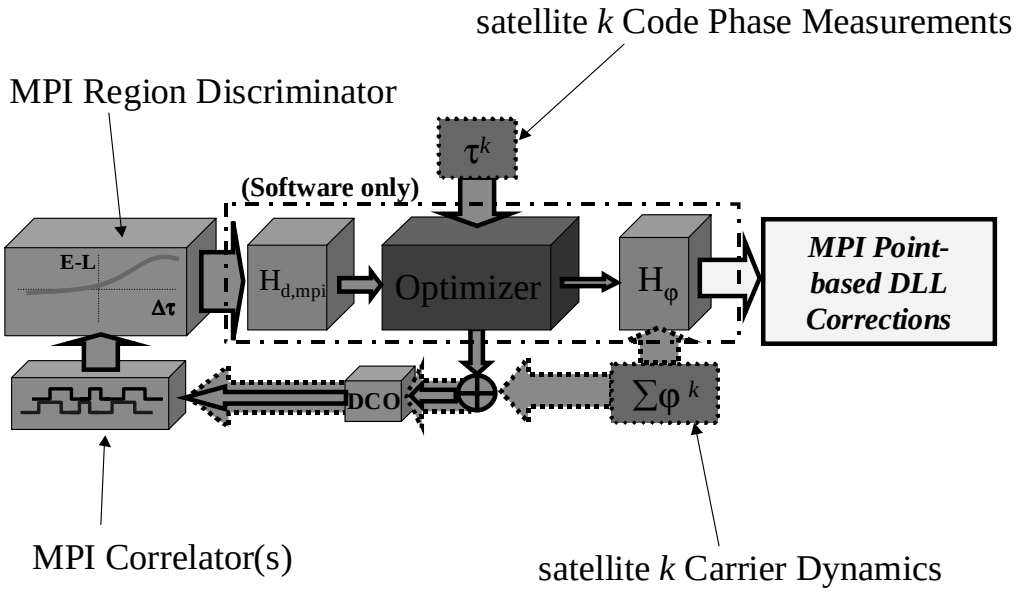

Figure 6-35 TrEC Loop Filter Implementation Overview (Note: Wider arrows indicate higher update rates)

A closed loop estimation filter can adapt to refine the MPI estimates made at time updates, t_j and t_{j+1}, separated by hundreds of seconds. It accomplishes this using integrated carrier phase (ICP) propagation of the estimates at one time step to the estimate made at the next. Recall that there is no latency associated with this dynamic decoupling; hence, the solutions can immediately and continuously compensate for DLL tracking errors. As illustrated in Figure 6-35, the TrEC loop filter blends so-called "slow-updates" (e.g., FS evaluations and MPI point acquisition), which occur at frequencies well below 1Hz, with "fast updates" (e.g,, 1kHz sampling of the correlation function, or 10Hz ICP propagation), which occur at frequencies up to 1kHz.

The instantaneous code phase MPI solution (slow update) for the *k*th satellite signal at time t_j is given by

$$\hat{\tau}^k_{mpi}(t_j) = \hat{\tau}^k_{mpi}(t_{j-1}) + \Delta\tau_{FS}(t_j) \tag{6.37}$$

where $\Delta\tau_{FS}$ is the update governed by the FS algorithm. This update is a function of MPI correlator pair spacing, d_{mpi}, the actual code phase of the MPI correlator, τ^k_{mpi}, and the time, t_j. The ICP-propagated solution (fast update) is then

$$\hat{\tau}^k_{mpi}(t_{j+1}) = \hat{\tau}^k_{mpi}(t_j) + \left(\Phi^k(t_{j+1}) - \Phi^k(t_j)\right) \tag{6.38}$$

The Hatch filter can subsequently average the next estimate of the MPI point with the ICP-propagated one as follows:

$$\hat{\tau}^k_{mpi}(t_{j+2}) = \frac{1}{L_{MPI}}\hat{\tau}^k_{mpi}(t_{j+2}) + \frac{L_{MPI}-1}{L_{MPI}}\left[\hat{\tau}^k_{mpi}(t_{j+1}) + \left(\Phi^k(t_{j+2}) - \Phi^k(t_{j+1})\right)\right] \tag{6.39}$$

In the above equation, L_{MPI} is the TrEC filter constant selected to determine the filter response (time constant). Finally, the TrEC (MPI point-based) DLL corrections (fast updates) are given as:

$$\Delta\hat{\rho}^k(t_j) = \hat{\tau}^k_{mpi}(t_j) - \hat{\tau}^k(t_j) + b^k_{u,mpi} \tag{6.40}$$

where

$$b^k_{u,mpi} = \Delta c^k_{mpi,ideal} + b_{PCBw} \tag{6.41}$$

The updates in Equation (6.41) can occur in real-time. Only the first FS need have a (relatively) large interval of uncertainty, **I**. Subsequent iterations can and should use a smaller **I**. Accordingly, such updates may be made more frequently. (Note that these will still be (relatively) slow updates.) Repeated FS optimizations, combined with the TrEC filter, continue to improve the bias in the TrEC corrections over time.

6.8 TrEC Error Sources

Noiseless, bandlimited TrEC performance without biases approaches that of complete removal of code multipath. Thermal noise alone degrades that ideal performance by making the desired MPI point more difficult to estimate. Time is required to average the estimates and reduce the random errors—the variance of the MPI point estimate. In addition, several bias errors may also appear in the TrEC solution. These errors may persist despite TrEC loop filter averaging.

Errors in TrEC corrections may result from a combination of the following five error sources:

1. MPI Point Acquisition Tolerance ($\delta\hat{\varepsilon}_{FS}$): The FS optimization (or another search-based function minimization scheme) only converges on an MPI code phase estimate to within this uncertainty. In the absence of noise, this error can be made arbitrarily small. The need for long MPI sample integration times makes it necessary to relax the requirements on this tolerance. As a result, this bias may be designed to reduce the initialization time required.

2. Thermal Noise ($\delta\hat{\varepsilon}_n$): These errors result from sampling the correlation function at the low-signal powers associated with the MPI region. These biases are higher for low-elevation satellites and low signal powers. They also tend to be greater when **I** and/or $\delta\hat{\varepsilon}_{FS}$ are large and when T_I is small. Accordingly, these bias errors require longer integration times (more MPI-point smoothing) to reduce them.

3. Multipath ($\delta\hat{\varepsilon}_{MP}$): MP-induced TrEC errors mainly occur due to extremely short-delay MP signals. These biases are greater for low-SNR signals and are generally larger for smaller MPI integration times. Increased ICP-propagation smoothing (i.e., larger smoothing constant, L_{MPI}) and larger integration time, T_I, act to reduce the influence of this error source.

4. Amplitude Variations ($\delta\hat{\varepsilon}_A, \delta\hat{\varepsilon}_{\dot{A}}$): The magnitude of this effect varies for each satellite as a function of elevation angle. MPI normalization (or antenna-gain calibration) may remove some of these effects. Neither integration time nor ICP-smoothing can reduce residual biases from these errors.

5. Ionospheric (Code-Carrier) Divergence Rate ($\delta\hat{\varepsilon}_I$): Assuming nominal ionospheric conditions, these errors are largest for low-elevation satellites. Long integration times and long-term ICP-smoothing worsen their effects. It follows that the divergence effects become smaller when both L_{MPI} and T_I are small. Dual-frequency receivers or others (e.g., WAAS receivers), where an estimate of the rate of ionospheric divergence is available, virtually eliminate these effects after the satellite has been in view for some time.

The following two subsections further discuss these TrEC random and bias errors.

6.8.1 Random Errors

TrEC random errors result from random variations in the estimate of the MPI point caused by thermal noise (or noise-like, ultra-short delay MP variations) on each of the

measurements made in the MPI region. Assuming the variance of the TrEC estimate within **I** is inversely proportional to N (as is $\sigma^2_{n,mpi}$ in Equation (6.32) above), and assuming steady state "locating" of the desired MPI point having slope, $D(\varepsilon)$, the closed loop noise variance becomes

$$\sigma^2_{n,TrEC} \approx \sigma^2_{ICP} + \frac{\min\left\{\left(\frac{\mathrm{I}^2}{12N} + \frac{\left(\delta\hat{\varepsilon}\right)^2}{12}\right), \frac{\mathrm{I}^2}{12}\right\}}{\max\left(D(\varepsilon)\cdot\Delta t_{j-1,j}\cdot L_{MPI}, 1\right)} \tag{6.42}$$

where

σ^2_{ICP} is the variance of the ICP propagated code phase updates,

$\frac{\left(\delta\hat{\varepsilon}\right)^2}{12}$ is the (uniform) variance of the FS estimate about ε,

$\frac{\mathrm{I}^2}{12N}$ is the (uniform) variance of the FS estimate within **I** ($N \geq 1$ evaluations),

and

$\Delta t_{j-1,j}$ is the time between slow updates and may also be expressed as

$$\Delta t_{j-1,j} = \left(N\cdot\kappa_{\max}\right)\times 10^{-3}\,\mathrm{sec} \tag{6.43}$$

Observe that the slope, $D(\varepsilon)$, is tantamount to the "signal" which, when sufficiently large, reduces the noise (variance) significantly. Even for a large nominal SNR, if $D(\varepsilon)$ equals zero, it implies the MPI correlators are measuring the plateau only. Since the MPI discriminator gain at the plateau is zero, the closed loop MPI point-locating variance is maximized. This maximum variance is (approximately) the variance of the uniform random variable of width I chips, and is captured in the numerator of Equation (6.42).

For large L_{MPI} (L_{MPI} >> 1), in steady state, the TrEC-corrected tracking error variance approaches the centimeter levels of the carrier phase, since the (slow) updates are weighted less as time increases. (Refer to Section 2.2.3 of Chapter 2 for a discussion on carrier phase

errors.) This implies old, potentially biased MPI point estimates may corrupt the TrEC estimates for long periods of time before the filter reduces them. In addition, by relying too heavily on the carrier phase, the TrEC corrections may become adversely affected by the code-carrier divergence induced by the ionosphere. For small L_{MPI} ($L_{MPI} \geq 1$), the mean of the estimates will vary uniformly about the desired offset, ε. Integration time is accounted for by the appearance of N in Equations (6.42) and (6.43). When N=1 the code phase estimates are essentially random and are uniformly distributed within I. As stated previously, infinite MPI integration time is required to ensure the FS converges to $\varepsilon \pm \delta\hat{\varepsilon}/2$.

Equation (6.42) provides a means for approximating the closed-loop TrEC-enabled DLL performance. Since it is expressed as a variance, however, it does not necessarily provide insights into the residual mean biases—the most difficult component to remove—from multipath and implementation effects. For the sake of discussion, assume the TrEC residual errors on a given pseudorange are normal with a mean, μ_{TrEC}, and standard deviation, σ_{TrEC}. In steady state, where **I** and $\delta\hat{\varepsilon}$ are small, σ_{TrEC} is also small. These variations (due to ICP propagation and smoothing) will be on the order of carrier-phase tracking errors. The mean errors, however, are more difficult to predict and may be much more significant.

Note that in many cases, it is more useful to provide performance bounds for MP mitigation approaches such as TrEC. These may provide "worst case" assessments of the MP and noise tracking error mitigation properties. Further these assessments may be used to design a receiver system to meet specific requirements on initialization time and code tracking accuracy. Section 6.10 derives such performance bounds.

6.8.2 Bias Errors

With the exception of thermal noise, all of the error sources listed at the beginning of Section 6.8 contribute to TrEC bias errors. Receiver processing can only remove these errors directly using two methods. The primary approach smoothes the (slow) FS optimization estimates over time. Another option involves using multiple MPI correlators

on the same receiver channel. (This option is discussed in more detail in Section 6.9.2 below.) Note that since GPS position solutions depend on satellite geometry, even small pseudorange biases can introduce significant position errors.

6.9 TrEC Performance Enhancements

There are several ways to improve actual TrEC performance beyond what the previous sections discuss (e.g., increased time averaging). In particular, the single-correlator pair implementation described in the previous sections, although practical for low-end receivers, alone may not yield the best MP mitigation performance. This section details two practical alternatives for improving TrEC performance. The first still requires only a single MPI correlator pair and proposes to mitigate the TrEC error biases by averaging them across all receiver channels. The second suggests possible hardware additions or improvements and ways to improve TrEC performance when multiple MPI correlators are available.

6.9.1 Cross-Channel Smoothing (CCS)

Independently, the TrEC error biases may be difficult to remove. Additional hardware, (i.e., wider PCBw, more correlators per channel, dual-frequency tracking, etc.) can reduce or eliminate some of these errors. A more practical way to account for them, however, is to attempt to make them the same for all pseudoranges. Recall that common mode biases do not affect the final GPS position solution since such biases fall into the user clock estimate. (Refer to Chapter 1, Section 1.3.)

Cross-channel smoothing (CCS) reduces all the aforementioned bias errors (listed in Section 6.8.2) on each individual TrEC correction by averaging the (raw) TrEC corrections made on all *K*, TrEC-enabled channels. CCS then creates new, reduced-error TrEC corrections, weights them, and applies them to each respective pseudorange measurement.

Recall from Equation (6.27) that the error-free TrEC pseudorange corrections are simply

$$\Delta\hat{\rho}^k(t) = \hat{\tau}^k{}_{mpi}(t) - \hat{\tau}^k(t) + \Delta c^k_{mpi,ideal} + b_{PCBw}$$

Including all the errors described above, the *k*th TrEC correction, $\Psi^k(t_j)$ at time t_j is given as

$$\Psi^k(t_j) = \hat{\tau}^k_{mpi}(t_j) - \hat{\tau}^k(t_j) + b^k_{u,mpi} + \delta\hat{\varepsilon}^k_A(t_j) + \delta\hat{\varepsilon}^k_{\dot{A}}(t_j) + \delta\hat{\varepsilon}^k_{\dot{I}}(t_j) + \delta\hat{\varepsilon}^k_{FS}(t_j) + \delta\hat{\varepsilon}^k_n(t_j) + \delta\hat{\varepsilon}^k_{MP}(t_j) \tag{6.44}$$

or

$$\Psi^k(t_j) = b_{PCBw} - \left(\varepsilon^k_{MP}(t_j) + \varepsilon^k_n(t_j)\right) + \delta\hat{\varepsilon}^k_A(t_j) + \delta\hat{\varepsilon}^k_{\dot{A}}(t_j) + \delta\hat{\varepsilon}^k_{\dot{I}}(t_j) + \delta\hat{\varepsilon}^k_{MPI}(t_j) \tag{6.45}$$

where ε^k_{MP} and ε^k_n are the desired (error-free) TrEC corrections for the DLL code multipath tracking errors. In Equation (6.45) above, the MP, thermal noise, and FS errors have combined into a single filtered error term, $\delta\hat{\varepsilon}_{MPI}$. $\delta\hat{\varepsilon}_{MPI}$ is defined as

$$\delta\hat{\varepsilon}_{MPI} = \left(\delta\hat{\varepsilon}_{FS} + \delta\hat{\varepsilon}_n + \delta\hat{\varepsilon}_{MP}\right) * h_{MPI} \tag{6.46}$$

where h_{MPI} is a first-order smoothing filter similar to that described in Section 2.3.3 of Chapter 2. This filter weights new code-based MPI point measurements with the constant, $\frac{1}{L_{MPI}}$ and old, carrier-propagated measurements with $\frac{L_{MPI}-1}{L_{MPI}}$. Figure 6-36 below illustrates how the errors and the desired TrEC MP and thermal noise corrections combine inside a (*K*-channel) receiver system.

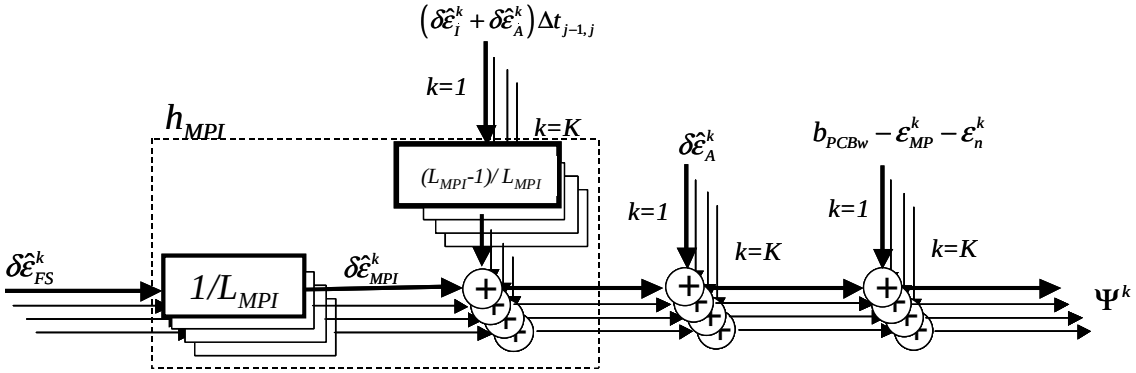

Figure 6-36 TrEC Error Terms in the GPS Receiver (*K*=4 Channels as Depicted)

Note that in general, ${}^{b}h_{MPI} \approx 1$ and the ionosphere rate and amplitude variation rate terms pass essentially unattenuated by h_{MPI}. As a result, over time they may grow large and introduce biases into the TrEC corrections.

The modified, CCS TrEC correction is simply

$$\tilde{\Psi}^{k}_{xc}(t_j) = \Psi^{k}(t_j) + \left(\bar{\Psi}(t_j) - \hat{\Psi}^{k}(t_j)\right) \tag{6.47}$$

where

$$\bar{\Psi}(t_j) = \frac{1}{K}\sum_{k=1}^{K} \hat{\Psi}^{k}(t_j) \tag{6.48}$$

and

$$\hat{\Psi}^{k}(t_j) = \frac{1}{L_{xc}}\Psi^{k}(t_j) + \frac{L_{xc}-1}{L_{xc}}\hat{\Psi}^{k}(t_{j-1}) \tag{6.49}$$

and L_{xc} is the design constant for determining the response of the CCS smoothing filter. A block diagram of these equations is shown below in Figure 6-37.

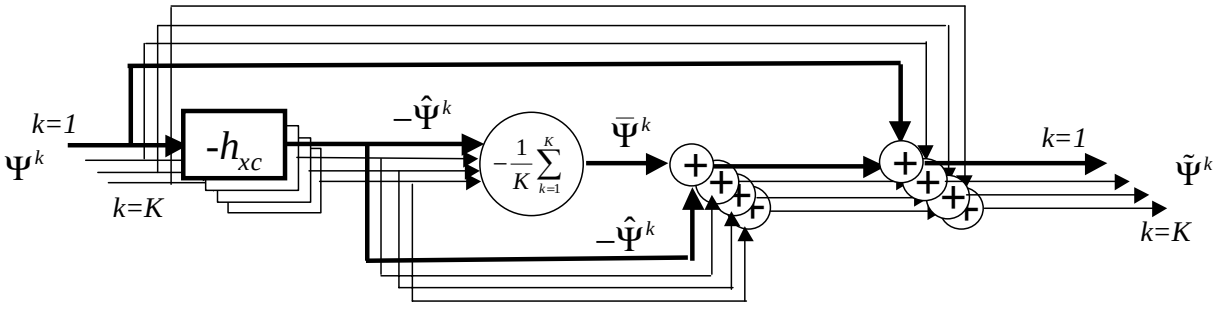

Figure 6-37 Cross-Channel Smoothing (CCS) Block Diagram

For arbitrary, constant biases on *K* pseudoranges, the modified TrEC correction in Equation (6.47) above results in the same bias applied to each pseudorange. For real signals, however, the biases change with time. To the extent these biases are slowly varying

relative to the desired TrEC correction components of Equation (6.45), they may be made to appear common mode. The penalty, however, is the validity of the (generally high-frequency) TrEC corrections, $\Delta\hat{\rho}^k(t)$. The parameter, L_{xc}, trades off the effectiveness of the TrEC bias removal with the nominal TrEC performance reduction.

A large value for L_{xc} reduces the bandwidth of the filter for the nominal corrections. It updates very slowly and heavily weights old correction information. In general, this results in a better estimate of the mean TrEC correction on each pseudorange, and greater reliance on the nominal TrEC corrections, $\Delta\hat{\rho}^k(t)$. If L_{xc} is too large, however, the filter will respond too slowly. If this occurs, the corrections, $\bar{\Psi}(t_j)$, will not occur quickly enough. In other words, they will essentially only rely on information obtained at time, t_{j-1}. Since such a filter will "remember" old bias information, this may exacerbate biases in the system.

Conversely, a small value for L_{xc} widens the bandwidth of the TrEC correction filter. The wider this filter bandwidth, the more easily the filter removes relatively rapidly changing error components (e.g., possibly $\delta\hat{\varepsilon}_A$ and $\delta\hat{\varepsilon}_I$). If L_{xc} is too small, the valid (MP and thermal noise) components of the corrections are estimated as bias errors. In this case, they subtract from each pseudorange and become ineffective. Under these conditions, the TrEC biases errors get removed in addition to the valid corrections.

It should be noted that the TrEC corrections contain the MP and thermal noise DLL tracking error corrections for each pseudorange. As a result, $\tilde{\Psi}^k_{xc}(t_j)$ will contain additional MP and thermal noise errors that are not valid for satellite, *k*. Assuming the multipath and thermal noise tracking errors are independent between channels, the combined MP (and the TrEC biases) will have maximum value reduced by 1/*K*. The combined thermal nose will have a variance reduced by 1/K. This implies that the reduction in mean TrEC biases through CCS will also see an increase in standard deviation of the errors. Indeed the re-introduction of MP-varying components to each pseudorange measurement makes each slightly less MP invariant. If, however, more hardware (e.g.,

more MPI correlators or a wider PCBw) is available in a given channel, then CCS (and this compromise) may not be necessary.

6.9.2 Multicorrelator Implementations

The above equations apply only to receivers using a single MPI correlator pair per satellite signal. If more MPI correlators are available, they may offer several ways to obtain better performance. This subsection describes a few of these techniques.

MPI Region Estimation

Three or more MPI correlators (or three or more samples of the MPI region) would better estimate the shape of the entire region. The simplest estimations take the form of a curve (e.g., polynomial or exponential) fit of the sampled data. The sample points of each of the correlators or pairwise (L-E) differences may constitute the observables for this. A depiction of this implementation is provided below in Figure 6-38.

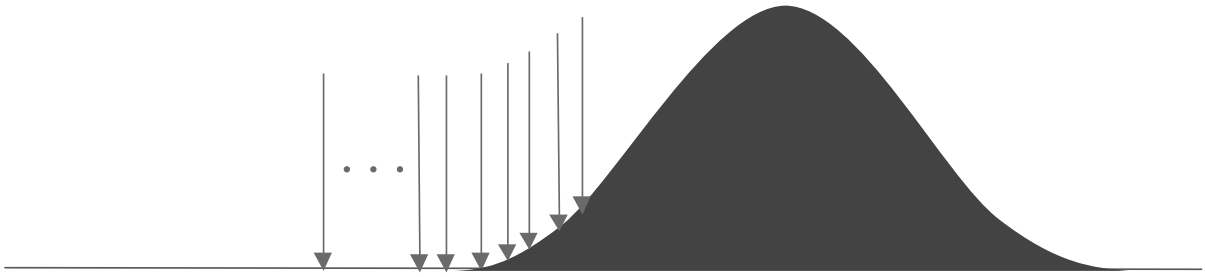

Figure 6-38 Multicorrelator Sampling of a Single MPI Region for Improved TrEC Performance

The mechanics of this estimation process itself is straightforward and well known. For *W*/2 correlator pairs (or *W* pairwise differences), the general equations for a polynomial fit are given as

$$\begin{aligned} Y_1 &= h_0 + h_1 x + h_2 x^2 + \cdots + h_W x^W \\ Y_2 &= h_0 + h_1 x + h_2 x^2 + \cdots + h_W x^W \\ &\vdots \\ Y_W &= h_0 + h_1 x + h_2 x^2 + \cdots + h_W x^W \end{aligned} \tag{6.50}$$

where Y_w is the wth observable output and x_w is the wth (deterministic) correlator spacing code offset. These equations are easily inverted and solved for the coefficients, h_w. Once obtained, a threshold must be set which distinguishes the MPI point from the plateau. This may be any function such that it extracts an estimate, $\hat{\varepsilon}$, for the MPI point. For the example in Equation (6.50), where the observables, Y_w, are L-E differences, an improved estimate of $D(\varepsilon)$ is simple to acquire since the curve fit provides smoothing as a function of code delay as well as integration time. Note that this fit should afford a significant reduction in initialization time as well. In fact, with sufficient numbers of MPI correlators, no search should be required if the curve fit spans the MPI region. In this case, continuous (fast) updates to the MPI point estimate may be made and smoothed over time.

Multiple-MPI Points

A second possible implementation that utilizes multiple MPI correlator pairs involves locating several MPI points on a given correlation function. An illustration of this concept is shown in Figure 6-39 below. Two primary improvements to performance may be made using this method. First, this approach may improve the MPI estimate though averaging. Assuming the optimization errors, $\delta\hat{\varepsilon}_{opt}$, are uniformly distributed and random, they may be reduced by a factor of the number of MPI correlator pairs per channel, $C_{p,mpi}$.

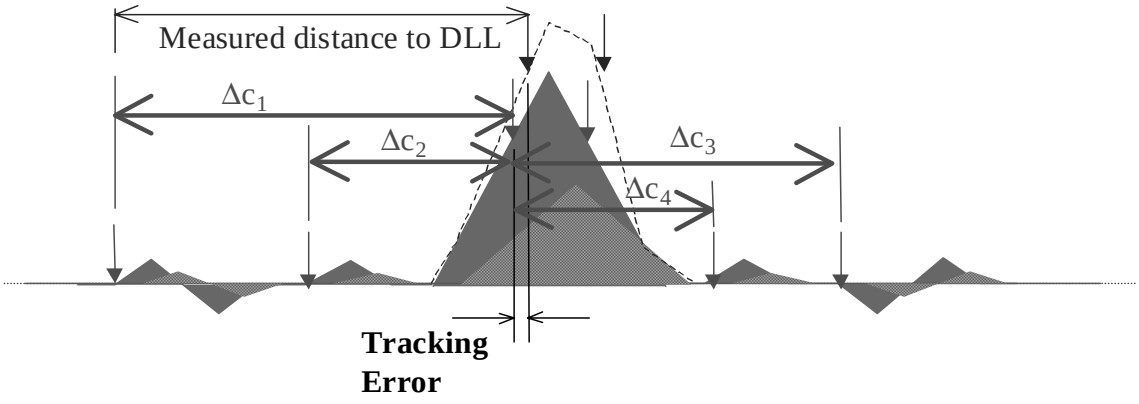

Figure 6-39 Sampling Multiple MPI Points for Improved TrEC performance

Second, this implementation can confirm and improve the individual MPI estimates by using code phase differences between MPI correlators. Noise and multipath corrupt the code phase difference between an MPI correlator pair and the tracking pair (DLL). The differences between MPI correlator pairs, however, are only affected by TrEC-implementation biases (e.g., carrier phase MP, estimation errors, etc.) Note the number of potential (unique) differences that may be compared is found from

$$\textit{Number of differences} = \frac{C_{p,mpi}}{2}\left(C_{p,mpi}-1\right) \tag{6.51}$$

By comparing the expected MPI code phase offsets in this manner, this approach may discover outliers (i.e., failures of an individual FS solution). In addition, it may increase confidence in the integrity of the TrEC corrections being applied to the DLL. (Note that multiple correlators may sample at each MPI location as well for even better TrEC performance.)

6.10 TrEC Theoretical Performance Bounds

This section derives conservative theoretical bounds on TrEC performance obtained by making assumptions on the magnitude of the bias and noise errors. Further, it includes assumptions for the maximum DLL MP tracking errors and the minimum nominal incoming signal strength. Use of these bounds and assumptions, in conjunction with the CCS and multicorrelator techniques discussed in Section 6.9, may lead to TrEC implementation designs for various receiver configurations that meet or exceed current code tracking performance expectations. Sections 6.10.4 and 6.10.5 present analysis results that substantiate this claim.

6.10.1 Minimum Probability of Convergence Assumptions

The integration time (T_I), the interval of uncertainty (**I**), and the desired convergence tolerance ($\delta\hat{\varepsilon}$), may combine to predict the worst-case performance for the TrEC-corrected DLL. To parameterize initialization time, code tracking accuracy and receiver

configuration, the MPI point acquisition must converge in all cases. In other words, for any set of (worst case) assumptions, the designated MPI point tolerance is presumably obtainable within a prescribed number of evaluations, Λ, with a certain probability.

Intuitively, the lowest probability of convergence to the MPI point occurs when the most evaluations (decisions) are made from samples on the MPI plateau—below the threshold slope, $D(\varepsilon)$. Since $D(\varepsilon)$ is (usually) very close to zero, probability of any decision (i.e., "shift MPI correlator left" or "shift MPI correlator right") is (nearly) 0.5. Also, by definition, the probability of making either decision equals 0.5 at the desired MPI offset, ε. It follows that the worst-case convergence sequence for the FS optimization begins with an initial evaluation at ε and a subsequent decision to "move left" (shift early) and sample at the MPI plateau. Slowest convergence then occurs if all subsequent decisions are "move right" (shift late) decisions. This scenario is illustrated below in Figure 6-40 for Λ evaluations. (Note that this example assumes that the initial evaluation, λ=0, is available without a distinct evaluation. This follows from the assumption that the initial evaluation results in a "move left" decision.)

The initial interval of uncertainty, I_0, determines Λ for a given (trial) FS-based MPI point acquisition. As mentioned previously, the largest I for a narrowband receiver having a $0.5T_c$ correlator spacing is approximately 120m. This implies Λ=11 FS evaluations for a final $\delta\hat{\varepsilon}$ of less than 1 meter. Accordingly, this is the theoretical maximum uncertainty error in the MPI point estimate for TrEC. (Note that once the initial estimate is made, subsequent optimizations—made to refine the mean correction over time—can occur in only a few (i.e., 3 or fewer) evaluations. This acquisition process only requires that the final convergence tolerance, s, is bounded for optimization, s+1, such that $\mathbf{I}_{s+1} \le \mathbf{I}_s \le \mathbf{I}_0$ for all $t>0$.)

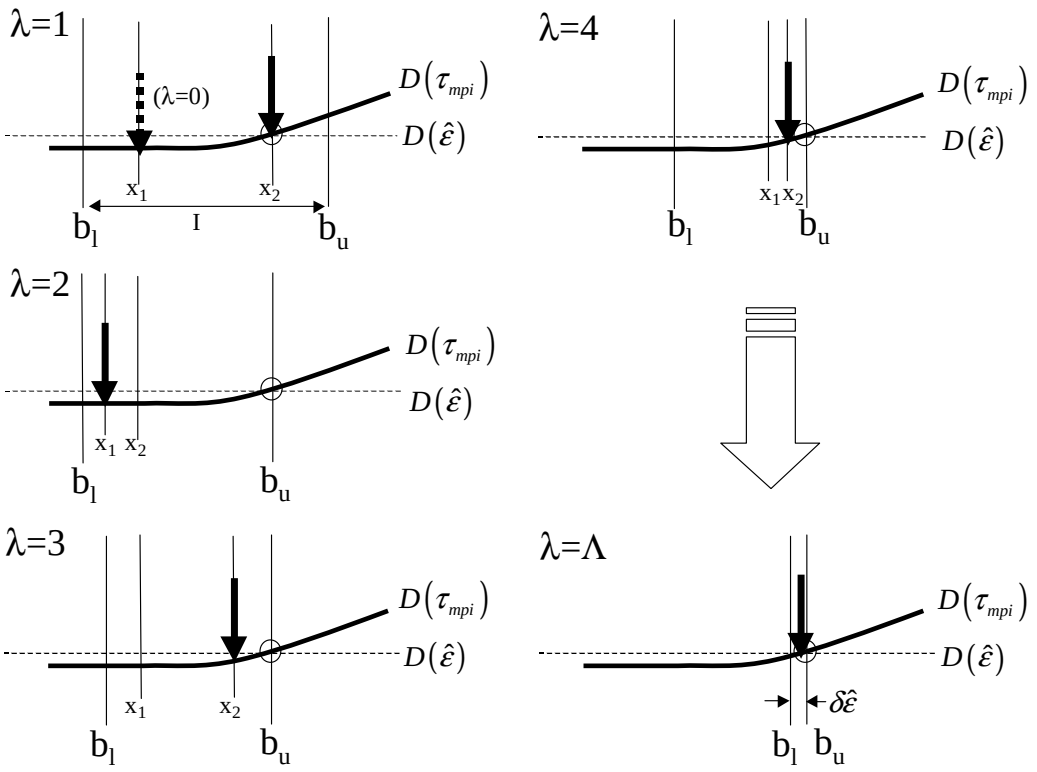

Figure 6-40 Worst-Case Convergence of Fibonacci Search to Desired MPI Point

Using these assumptions, a conservative probability of convergence can be found from the probabilities of each successive evaluation (decision). Since each decision, Ω_λ, is predetermined, the probability of not converging to the MPI point within the prescribed tolerance is described by

$$\Pr(\mathrm{X}) = 1 - \left(\Pr(\Omega_1^c) + \Pr(\Omega_1^c) \cdot \Pr(\Omega_2^c) + \cdots + \prod_{\lambda=1}^{\Lambda} \Pr(\Omega_\lambda^c) \right) \tag{6.52}$$

where $\Pr(\Omega_\lambda^c)$ is the probability of a correct decision at evaluation λ.

The probability density functions (PDF) needed to compute the probabilities in Equation (6.52) above result from first recognizing that the FS optimization problem is analogous to that of signal acquisition. The signal acquisition PDFs equations were introduced in Section 2.2.1 of Chapter 2, and the relevant equation is shown in Figure 6-41. The PDF for FS (MPI point optimization) evaluations is simply

$$p_{fd} = \frac{z}{\sigma^2_{n,e-l}} e^{-\left(\frac{z^2}{2\sigma^2_{n,mpi}}\right)} \tag{6.53}$$

where $z = D(\tau_{mpi})$ and, for this analysis, $\sigma^2_{n,mpi} = 2d_{mpi}$. Here, d_{mpi} is the correlator spacing of the MPI correlator pair used. (Section 6.10.2 discusses this in more detail.) This formulation will be used to compute the noise component of the TrEC performance bounds computed in Sections 6.10.4 and 6.10.5. (Figure 6-42 illustrates the probabilistic FS evaluation problem.)

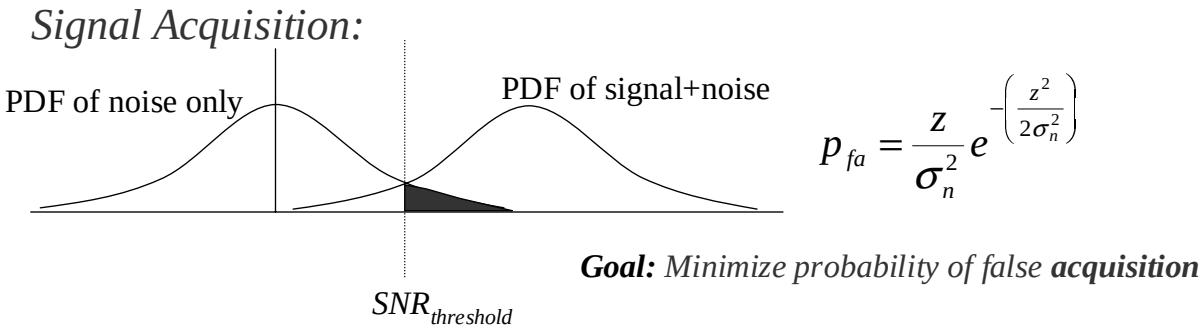

Figure 6-41 Signal Acquisition Problem

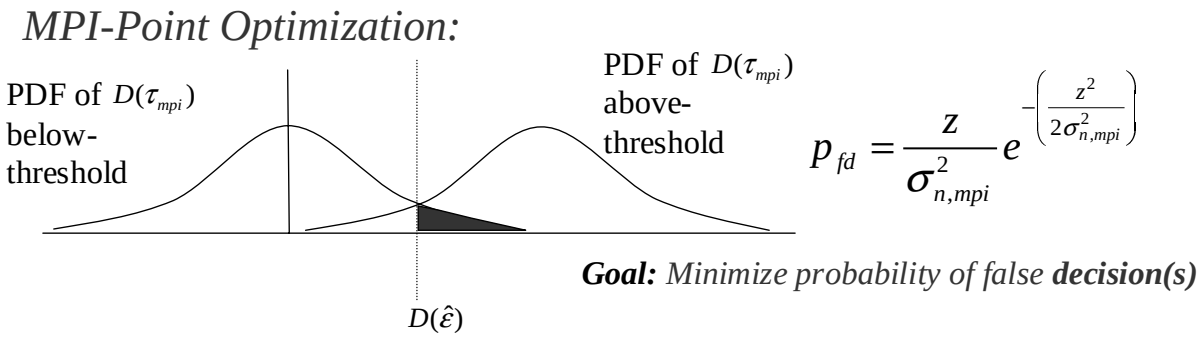

Figure 6-42 The MPI-Point Optimization Problem

6.10.2 Minimum Performance Assumptions

A conservative application of multiple MPI correlators places them all at a single MPI point and uses them only for reduction of the FS initialization time. This implies that the

MPI correlators are distributed to achieve a minimum correlator spacing, d_{mpi}. Figure 6-43 illustrates this case for two, three, and four correlator pairs. For simplicity, an effective correlator spacing, $d_{mpi,eff}$ may be modeled (conservatively) as

$$d_{mpi,eff} = 2 * \max\left(0.05\mathrm{T_c}, \left[\frac{1}{\mathrm{PCBw\ (MHz)}}\right]\mathrm{T_c}\right) \tag{6.54}$$

where it is implicitly assumed the nominal correlator spacing for a DLL (in a conventional receiver) to be the inverse of the PCBw (in units of MHz). Note that although this analysis assumes that the FS optimization is still performed, the reduction in correlator spacing does yield a significant reduction in thermal noise on the MPI L-E differences.

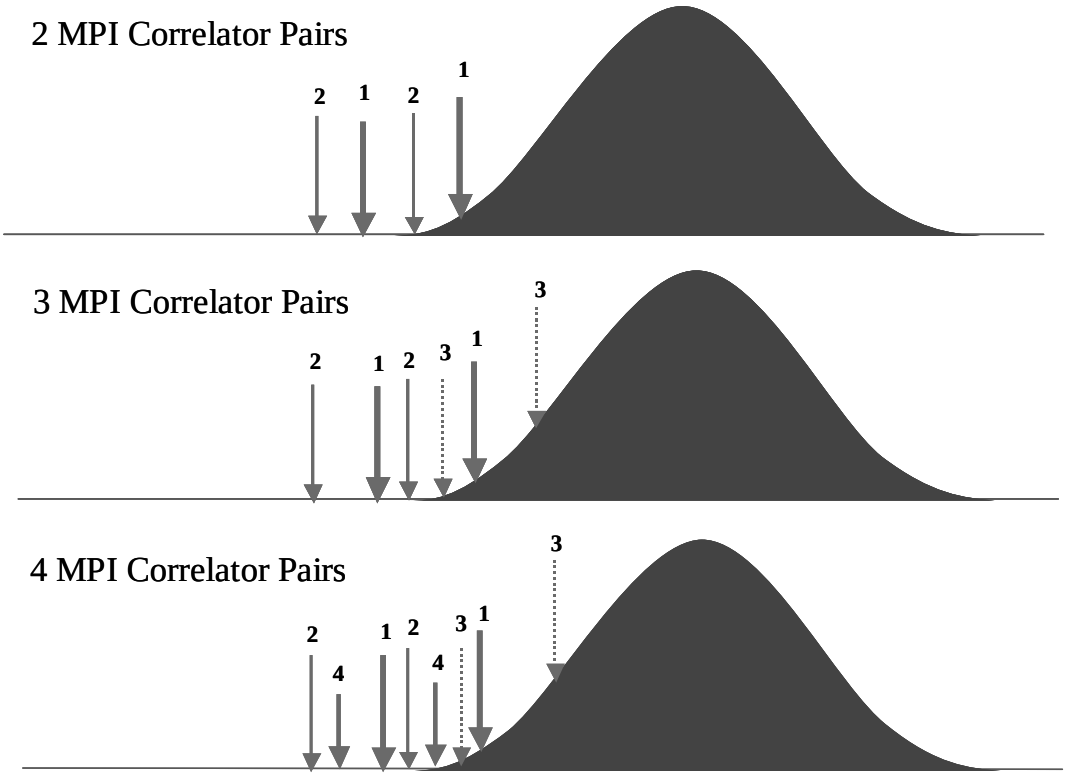

Figure 6-43 Conservative Model for Application of Multiple MPI Correlator Pairs for Improved TrEC Performance

The bound analysis further assumes that the number of independent MPI correlator pair differences effectively increases the number of independent code-phase estimates (i.e.,

TrEC corrections). Using mean-square estimation or curve fitting of these differences may further reduce the variance of the L-E MPI samples. Assuming each difference is independent (so the noise from each is uncorrelated), the number of pairwise differences that may be taken given $C_{p,mpi}$ MPI correlator pairs constitutes a variance reduction factor, r_{var}, given by

$$r_{\text{var}} = C_{p,mpi}\left(2C_{p,mpi} - 1\right) \tag{6.55}$$

For the conservative performance analysis performed in Sections 6.10.4 and 6.10.5, however, a modified (smaller) reduction factor, $\hat{r}_{\text{var}}$, was used, where $\hat{r}_{\text{var}} = \frac{r_{\text{var}}}{2}$. This ensured that the assumed noise variance reductions for any presumed multicorrelator implementations would be minimal—only one-half that predicted assuming uncorrelated AWGN on the discriminator measurements.

6.10.3 Maximum Signal Error Assumptions

Nominal Signal Power

The previous sections (e.g., Section 6.7) implied that due to low signal power (hence, small MPI discriminator slope) considerations, the most difficult MPI point to locate corresponds to a sidelobe on a correlation function produced from a low-elevation satellite. Recall from Section 6.7.1 that this is tantamount to a signal attenuated by 20dB. This low signal power assumption may significantly impact the integration time (and, hence, the initialization time) required to locate the MPI point.

The integration time employed by TrEC largely determines the pseudorange accuracy bound. Increasing this time may reduce the thermal noise on the L-E MPI differences; however, this also increases the errors induced by code-carrier divergence. In addition, long integration times only worsen the effects of changing amplitude (SNR) of the received signal. A conservative analysis of TrEC code-tracking accuracy must take both of these factors into account.

Ionospheric Divergence Rate and Amplitude Rate

Recall that the largest ionospheric errors occur for low-elevation satellites. [Klobuchar] cites this maximum code-carrier divergence rate of range error as 1.6cm/s. For the highly conservative accuracy bound in this analysis, however, twice this rate (3.2cm/s) was assumed.

The amplitude of the signal also changes at its fastest rate at low elevation angles. Sharp rolloffs in antenna gain patterns frequently occur for elevation angles below the horizon [Clark]. (Assuming a conservative, ideal mask angle of 0°, these effects do not appear, since the satellite would instantaneously disappear below this mask.) The FS updates (i.e., move-left or move-right decisions), utilize samples of the amplitude-varying MPI region that are averaged over time. This provides some reduction in the impact of signal amplitude variation effects. In addition, normalization (or calibration) as discussed in Section 6.4.1 removes some of these effects. Considering these measures, the analysis of Sections 6.10.4 and 6.10.5 assumed these errors were (at most) equal to the final MPI point acquisition tolerance, $\delta\hat{\varepsilon}_{FS}$ (or, in general, simply $\delta\hat{\varepsilon}$). Note that this assumption implies an incentive to make $\delta\hat{\varepsilon}_{FS}$ as small as possible. However, such a design decision could cause the MPI point acquisition time to become unacceptably long.

Multipath and Thermal Noise

The maximum MP tracking error on each pseudorange can be taken from the maximum error envelopes for a DLL of spacing d_{eff}, where $d_{eff} = \frac{d_{mpi,eff}}{2}$. For thermal noise errors, Equation (2.10) from Chapter 2, Section 2.2.2, computed a maximum (2-σ) noncoherent DLL code tracking error for each correlator spacing, d_{eff}. CCS attenuates this maximum tracking error (for each channel) by a factor of $1/K$. Recall that CCS also trades off the maximum error for a reduced mean error. (Refer to Section 6.9.1.) As a result, the maximum MP errors must be more conservative when implementing CCS.

6.10.4 Maximum (2-σ) Initialization Times

Using Equation (5.55) and the assumptions in Sections 6.10.1, 6.10.2, and 6.10.3, it becomes possible to predict the largest initialization time required to locate the desired MPI point at an offset approximately 7 (or $\varepsilon = 7\text{m}$) meters from the ideal on this "worst case" correlation function. This translates to less than 1.5 (or $\Delta\varepsilon = 1.5\text{m}$) meters of maximum MP tracking errors for all receivers modeled. The independent variables for this analysis are simply receiver PCBw, number of available MPI correlator pairs (C_p) per channel, and integration time (T_I). Figure 6-44 below shows 2-σ (95%) maximum integration times for receivers having PCBws from 2-20MHz and having 1-10 additional MPI correlator pairs.

By far the largest initialization times are required for narrowband (e.g., low-end) receivers with $C_{p,mpi}$=1. For these receivers, the initialization times can reach as high as 7.5 minutes. Observe that this time requirement decreases rapidly as $C_{p,mpi}$ is increased. This is particularly true for large PCBws. For a (wideband) receiver equipped with 16MHz PCBw and 3 MPI correlators—a practical configuration for high-end receivers—this maximum initialization time is less than 50 seconds.

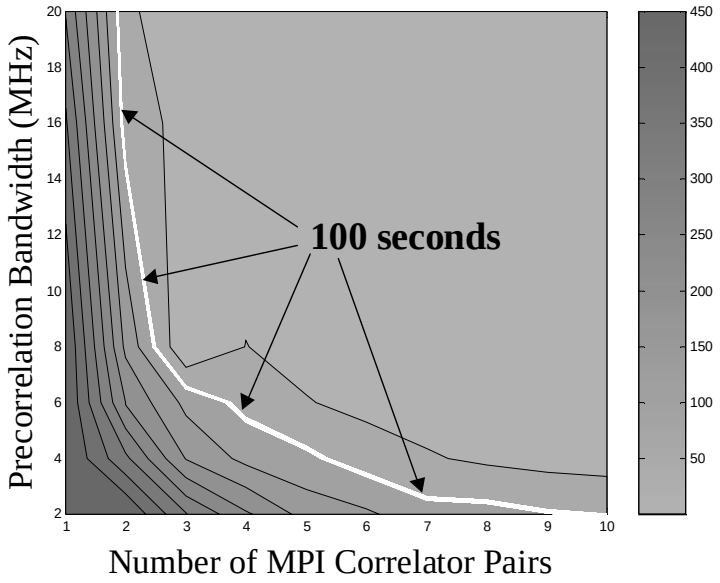

Figure 6-44 Maximum (2-σ) Initialization Time Bounds in Seconds (MPI Point Acquisition Time)

6.10.5 Maximum (2-σ) Code Tracking Errors

Using the assumptions and results from the preceding sections, Figure 6-45 though 6-48 below plot the maximum errors for 6, 8, 10, and 12 satellites tracked. (Recall from Section 6.9.1 that implementing CCS causes the results to become dependent on the number of satellites tracked.) Again, the worst performance is predicted for a narrowband receiver with only a single MPI correlator pair. This accuracy bound decreases most rapidly as the PCBw increases.

These error bounds may seem large in comparison to the theoretical performance predicted by the error envelopes for the "best" current wideband techniques. Those predictions, however, depend on the MP parameters and number of MP reflections. Here, only assumptions on maximum DLL tracking error are made. In addition, these TrEC performance bounds also take into account other implementation concerns. Initialization time, low elevation angle effects, and thermal noise errors are also taken into account for these results. Still, tracking only 8 satellites, tracking errors for a practical wideband receiver should be less than 1 meter 95% of the time.

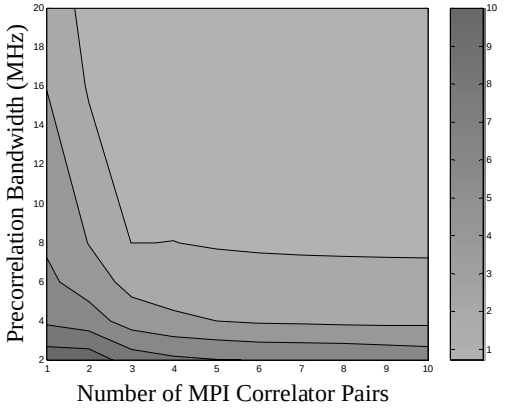

Figure 6-45 TrEC 2-σ Maximum Tracking Errors – 6 Satellites

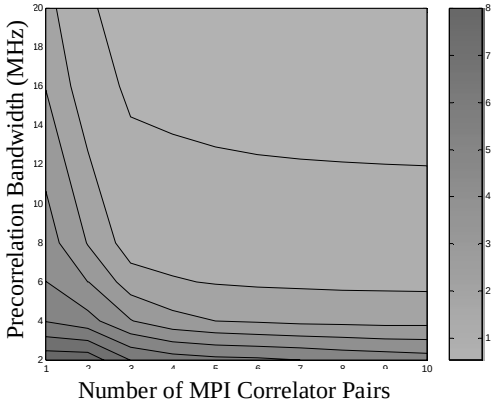

Figure 6-46 TrEC 2-σ Maximum Tracking Errors – 8 Satellites

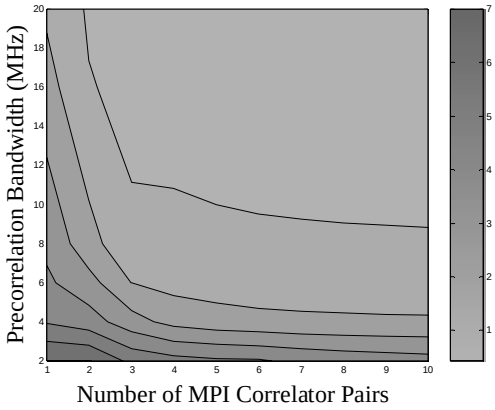

Figure 6-47 TrEC 2-σ Maximum Tracking Errors – 10 Satellites

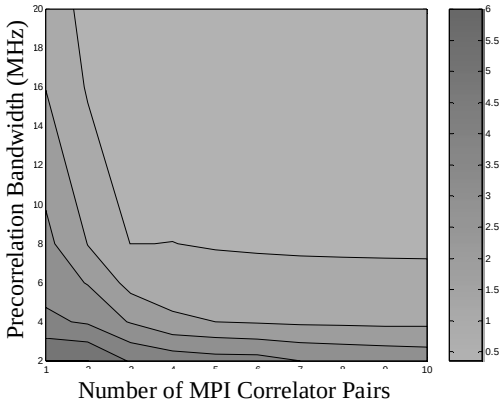

Figure 6-48 TrEC 2-σ Maximum Tracking Errors – 12 Satellites

For narrowband receivers, TrEC predicts the most significant payoff. The maximum (2-σ) tracking error for these receivers is approximately 10 meters for 6 satellites. This falls to only 7 meters for a receiver tracking 10 satellites. In all cases, however, the predicted *bounds for TrEC-enabled narrowband receivers are significantly smaller than those bounds for current conventional narrowband receivers.*

Chapter 7:

TrEC Performance Validation

Theory and analysis alone cannot substantiate the claims of improved multipath performance using TrEC. Well-designed experiments are required to assess the true impact of initialization time, finite PCBw, and thermal noise on TrEC performance. This chapter describes the experimental validation of the MPI concept and of TrEC performance. Sections 7.1 and 7.2 detail the specifics of modifying a conventional 12-channel narrowband receiver with only a single correlator pair per channel to act as a multicorrelator receiver having 2 correlator pairs per channel. Section 7.3 utilizes these implementation techniques to verify that receiver correlation functions can be reliably sampled at low correlation levels. Section 7.4 extends these techniques and uses TrEC to verify that MPI points can be found. Sections 7.5 and 7.6 validate theoretical TrEC performance in the pseudorange and position domains, respectively, using a GPS signal generator. Section 7.7 describes the (position domain) validation of TrEC performance on live GPS satellites under various MP conditions. Lastly, Section 7.7 discusses the validation of the TrEC performance bounds—for the narrowband receiver under test conditions—predicted by the analysis in the previous chapter.

7.1 Hardware Setup and Description

The GPS receiver chipset manufactured by Mitel Semiconductor, Inc. (formerly GEC Plessey) used to test the TrEC algorithm came embedded on a (ISA) PC card. It resided in a Pentium 166MHz PC and was capable of real-time, simultaneous tracking on 12 channels, and it had a 2MHz front-end bandwidth. Each channel possessed a single (E-L) correlator pair; only a virtual prompt measurement was available. Note that this narrowband receiver (NBR) normally reports the signal power in terms of SNR. For this receiver, the relation of SNR to C/N_0 is as follows:

$$SNR = C / N_0 + 10\log(\mathrm{T_{CA}}) \tag{7.1}$$

where $\mathrm{T_{CA}}$ equals the integration time for one code period (1e-3s).

The NBR's code tracking loop was a carrier-aided DLL. Its carrier loop was an FLL. [Ndili] describes the tracking configuration and the accompanying parameters for this receiver in more detail. Most conventional receivers use a form of carrier aiding for smoothing their DLL dynamics so this configuration setting was left unchanged. Most receivers with precise phase tracking, however, utilize a PLL. A (FLL-aided) 3rd-order PLL was designed and implemented according to the specifications provided in [Kaplan].

Nominally, the code-tracking loop and carrier tracking operated using the highest interrupt rate (1/505μs or approximately 2kHz). The navigation routines—including the integrated carrier phase measurements—were configured to operate at 10Hz. Also the code correlators had a code phase (delay) resolution of $1/2048\mathrm{T_c}$ (0.14m). The phase resolution of the NBR was $2\pi/1024$rad (0.3516°).

The primary reason for selecting this receiver was that it was almost entirely software-configurable. The manufacturer made available the complete source code. This was necessary since the ability to access all signal samples (*I* and *Q*), modify carrier and code tracking loops, and also refine the final navigation/position solution algorithms was necessary to implement TrEC.

7.2 Multicorrelator Implementation

Using receiver-specific commands, it was possible to program the correlators to track the satellites in different ways. For example, software commands could assign any given correlator pair (of a given receiver channel) to be a "master" tracking pair, and another a "slave" pair. Master channels would operate as normal. The slave channel(s) would receive exactly the same signal information as its corresponding master.

Without additional modifications, the slave correlators output the same *I* and *Q* samples as the master channel correlators. The signal tracking and processing are identical. This effectively reduces the number of valid receiver channels to the number of master channels. However, software instructions can command the correlators of slave channels to move, or "slew," relative to their respective master channel correlators using the receiver DCOs. This permits multicorrelator sampling of the correlation peak, using a conventional single-correlator pair NBR. Using this technique, the correlators may sample the correlation function to the full (0.14m) resolution of the NBR.

7.3 Measurements

7.3.1 Correlation Function

The first step towards validating the existence of MPI regions and points was to verify the shape of the correlation function. To verify the modeled NBR correlation peak, the NBR used all 12 channels to track a single satellite. Channel 1 was the "master" or primary channel and the others were "slave" channels placed relative to it. The DCOs of the 11 slave channels commanded the respective correlators to approximately equally spaced ($0.0417T_c$) offsets later than (to the right of) the Early correlator of the primary channel.

12800 *I* and *Q* samples were taken at 1kHz updates then averaged and stored at a 10Hz rate. The mean (I^2+Q^2) measurement values were subsequently compared against a computed (theoretical) peak. Figure 7-1 below illustrates the comparison. A (2MHz PCBw) 2^{nd}-order Butterworth filtered the theoretical peak. Simulation placed the peak of

this function at a code offset of $0T_c$ and scaled it to have the same peak amplitude (SNR) as the measured data. Post-processing centered the measured data, however, (at $0T_c$) using only the midpoint of the master (E-L) correlator pair. Although the two data sets used different approaches to predict the trend of this correlation peak, it can be seen that the measured data closely corresponds to the theoretical correlation peak.

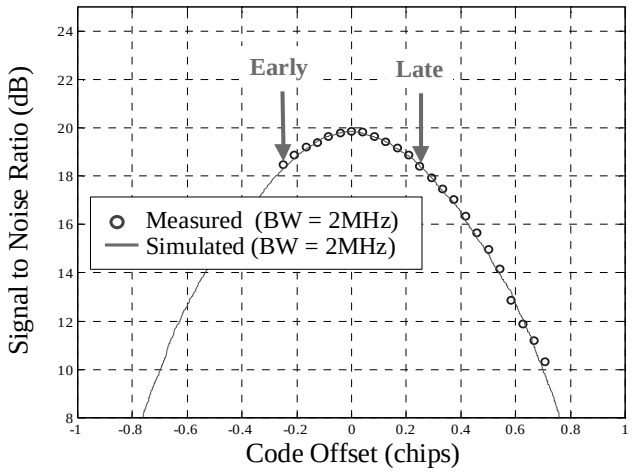

Figure 7-1 Comparison of Simulated and Measured Correlation Peaks

Next, several experiments used the NBR to demonstrate the ability to sample and resolve an actual received correlation function down to the relatively low-SNR levels of the correlation plateau and sidelobes. Using the same master-slave correlator technique described above, the NBR first tracked SV25 and then SV7. SV25 had an SNR of 18.24dB and SV7 had an SNR of 18.87dB. For each signal, the NBR recorded 10300 samples and 16100 samples, respectively. Post processing analysis then averaged and normalized them using the virtual prompt measurement. Figure 7-2 and Figure 7-3 below compare the measured correlation functions to their ideal (normalized) counterparts.

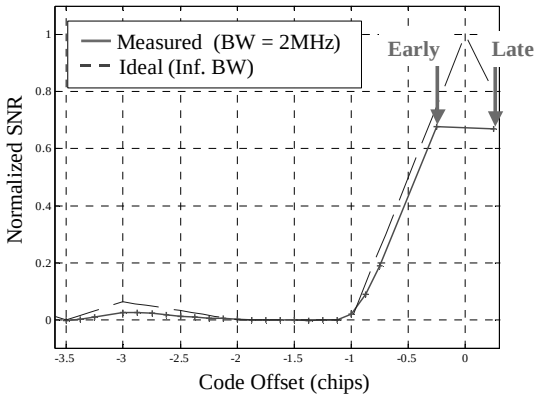

Figure 7-2 Comparison of Ideal and Measured Autocorrelation Peak and a Near-Peak Sidelobe for PRN 25

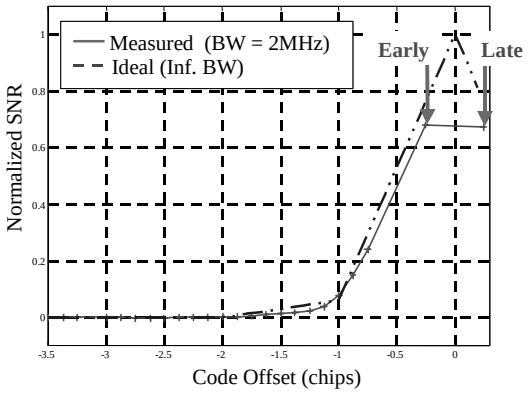

Figure 7-3 Comparison of Ideal and Measured Autocorrelation Peak and an Adjacent Sidelobe for PRN 7

7.3.2 MPI Region

To further validate the ability to sample the MPI plateaus of correlation functions of actual GPS signals, the software-modified NBR sampled an MPI region of SV2. 100,000 samples were averaged. The results are shown in Figure 7-4 below and are compared against the ideal correlation sidelobe. The SNR for the measured signal was 12.7dB. The rounding effects of the finite PCBw are evident from the plot.

Figure 7-5 illustrates the effect varying integration time has on the MPI region. 100,000 samples (approximately 100 seconds) produced the smooth trend shown in Figure 7-4. The characteristic of the MPI region degrades considerably, however, as the integration time is decreased. 1e4-sample evaluations (10 seconds) and 1e3-sample evaluations (1 second) are more desirable for evaluations since they permit more-rapid estimations of the MPI point. These estimations, of course, will be significantly less reliable for extremely short integration times.

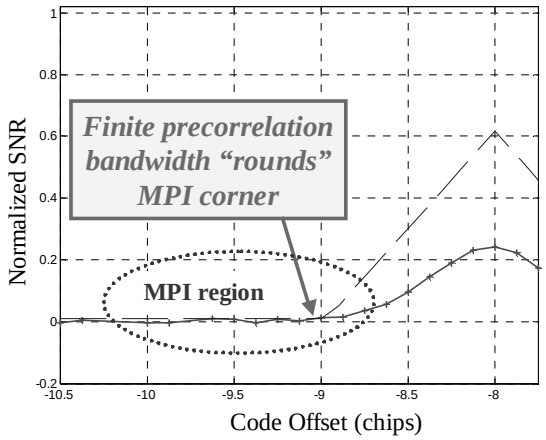

Figure 7-4 Ideal and Measured Autocorrelation Sidelobe of PRN2 (T_I=100s, or 1e5 samples averaged)

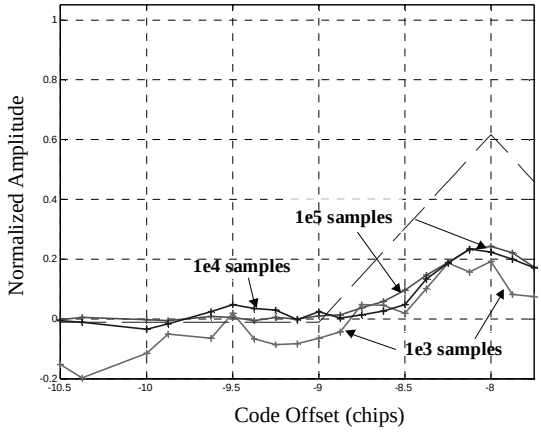

Figure 7-5 Ideal and Measured Autocorrelation Sidelobe of PRN2: 1e5 samples (T_I=100s), 1e4 samples T_I=10s) 1e3 samples (T_I=1s)

7.4 Demonstration of MP Invariance

An actual bias estimate (for one particular TrEC implementation) was made using a GPS Signal Generator (SigGen) and is shown in Figure 7-6. As stated previously, the bias is independent of relative MPI point location and PRN number. Note, however, that the convergence time for this TrEC was approximately 5 minutes. This convergence time translates directly to the initialization time required by the TrEC algorithm prior to making valid, real-time corrections to the DLL. Recall, however, that this time can be shortened (or lengthened) depending on the actual implementation assumptions (i.e., *a priori* knowledge of MP conditions) and/or requirements of TrEC.

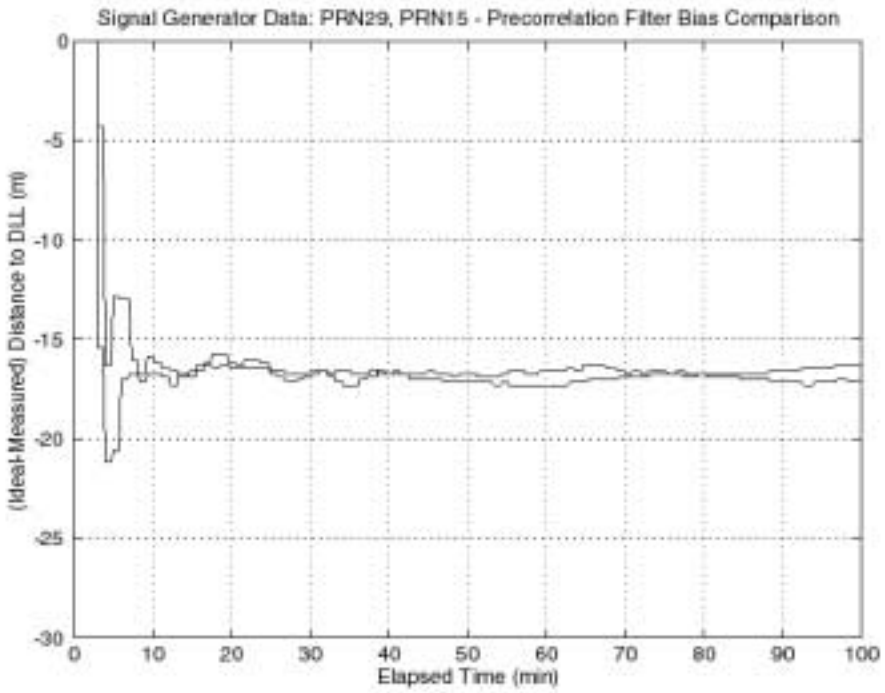

Figure 7-6 PCB Filter Bias Comparison for PRN25 and PRN29 (Signal Generator Data)

7.5 TrEC Pseudorange Domain Performance: GPS Signal Generator Data

Assuming the multipath has a short or medium delay—the most difficult multipath to remove—the SigGen provided the required RF signals to evaluate standard MP tracking error performance curves. The SigGen was capable of simulating the entire GPS satellite constellation. It could also generate multipath (with known parameters) on a given pseudorange. This latter feature served to experimentally verify the multipath performance of the NBR implementing TrEC.

Figure 7-7 illustrates the experimental setup. The signal generator was set to output the GPS satellite signals at a (relatively high) C/N_0 of approximately 50-53dB-Hz to ensure the receiver could maintain lock even when a strong, out-of-phase multipath signal was added. A single pseudorange (PRN25) was given multipath appropriate for generating the performance curves. The NBR obtained the measured pseudoranges. Post-processing

subtracted the "true" pseudoranges (retrieved from the signal generator truth file) from the measured ranges. A single subsequent inter-channel difference removed the receiver clock bias. Only variations due to thermal noise and the bias due to multipath remained.

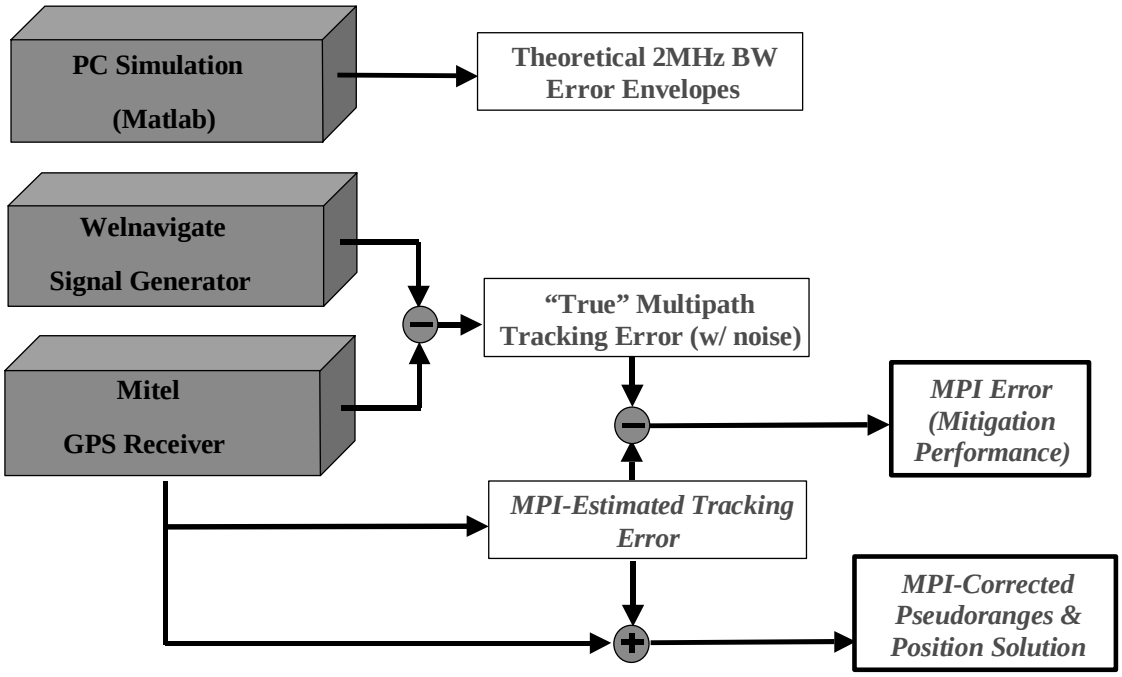

Figure 7-7 Setup for TrEC MP Performance Validation Experiment

The SigGen multipath was set to slew at a rate of 3.6 meters/min starting from a relative delay of 0 meters. The signal-to-multipath ratio (SMR) was 3dB. The effect of these specifications on the received signal power is shown in Figure 7-8. Observe how the high signal power of the MP signal induced correlation peak amplitude (fading) swings of approximately 9dB at a relative MP delay of 0 meters. Also note that the data is shown subsampled for clarity. The actual fading frequency (as described in Chapter 5.1.4) of the combined multipath-plus-direct signal is higher than that depicted.

Figure 7-9 plots the resulting DLL tracking errors for this scenario for the cases with and without carrier aiding. In addition, the carrier smoothed (unaided) results are plotted. As expected, with no carrier aiding the envelopes bound the tracking errors quite well. Carrier aiding filtered the high frequency (out-of-phase MP) tracking errors and caused the DLL to integrate the multipath errors. As previously stated, however, nominally many GPS

receivers' code-tracking loops are carrier-aided. For this reason, subsequent error envelope performance evaluations implemented the TrEC algorithm with carrier aiding enabled. Note that this is not a requirement for TrEC. Section 7.7 of this chapter, in fact, provides compelling position domain TrEC results with the conventional DLL carrier aiding disabled.

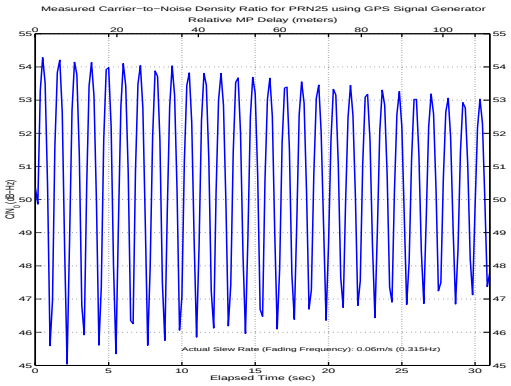

Figure 7-8 C/N_0 for PRN25 During Programmed Multipath Slew (Fading Frequency Shown Aliased)

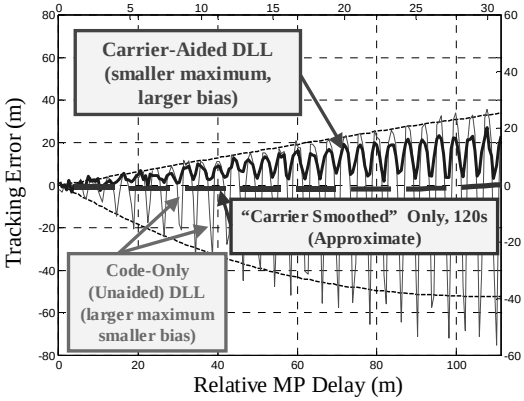

Figure 7-9 Nominal and Measured 2MHz Multipath Error Envelopes

The top plot in Figure 7-10 shows the true multipath tracking errors compared to the MPI-measured tracking errors. Using the NBR receiver, the TrEC algorithm measured the tracking error in real-time. Note that at approximately t=10 minutes, however, the tracking loop temporarily lost lock on SV25. A momentary fault in the generated signal caused this outage. It occurred at the same time for each trial and forced the MPI routine to reinitialize. (Note that the outages partially affected the resulting performance curve, since about 5 minutes were required for the routine to re-converge to the proper MPI point and resume making valid pseudorange corrections.) The second plot shows both the raw and carrier-smoothed (128-sec time constant) differences between the actual and measured tracking errors. The carrier-smoothed curve is the performance curve for the MPI approach for this particular trial. (See bottom plot of Figure 7-10.) The mean of this curve is 1.18 meters and its standard deviation is 2.45 meters.

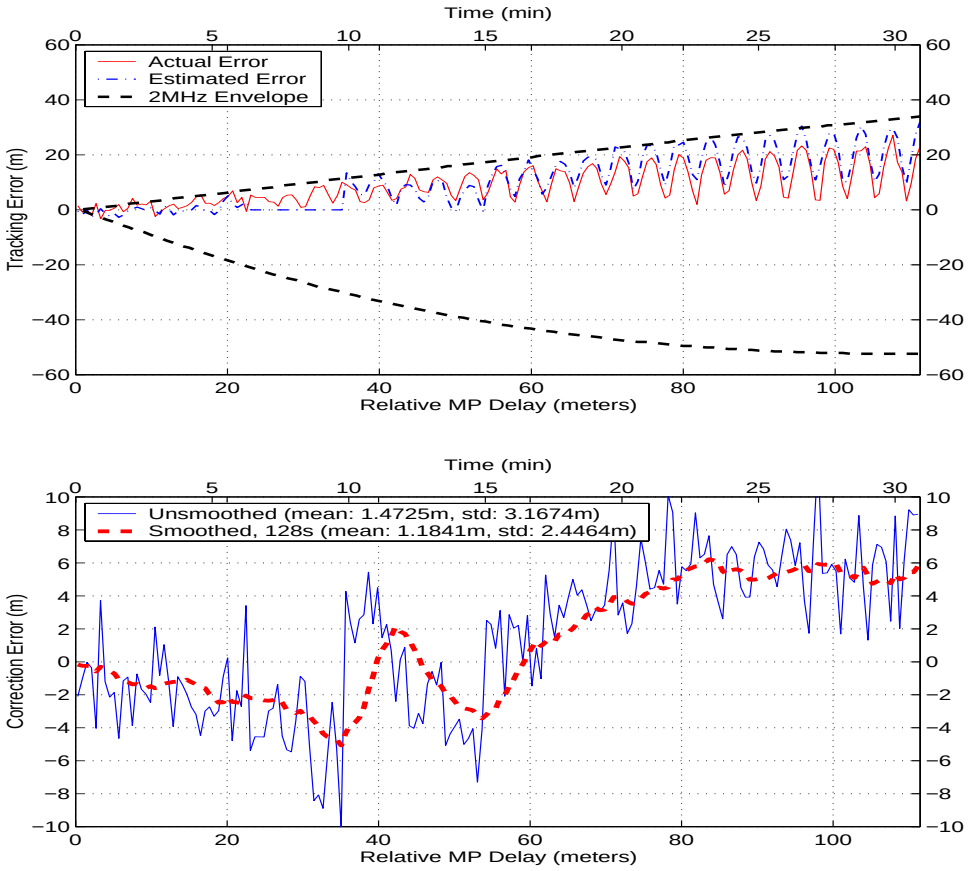

Figure 7-10 TrEC-Measured and Actual DLL Tracking Error

In order to validate the theoretical performance curve (the straight horizontal line) of Figure 6-29 in Chapter 6, data was taken from 10 trials. The results are shown in Figure 7-11 and the corresponding statistics can be seen in Figure 7-12. The mean bias (for this TrEC implementation) is approximately -2.5m. Accounting for the increased variance due to the single-difference, the average smoothed and unsmoothed standard deviations are 1.4m and 3.2m, respectively. Significant perturbations occurred, however, because of the temporary signal outage on SV25, so the true (undisturbed) standard deviation of the performance curves is actually smaller than that reported here.

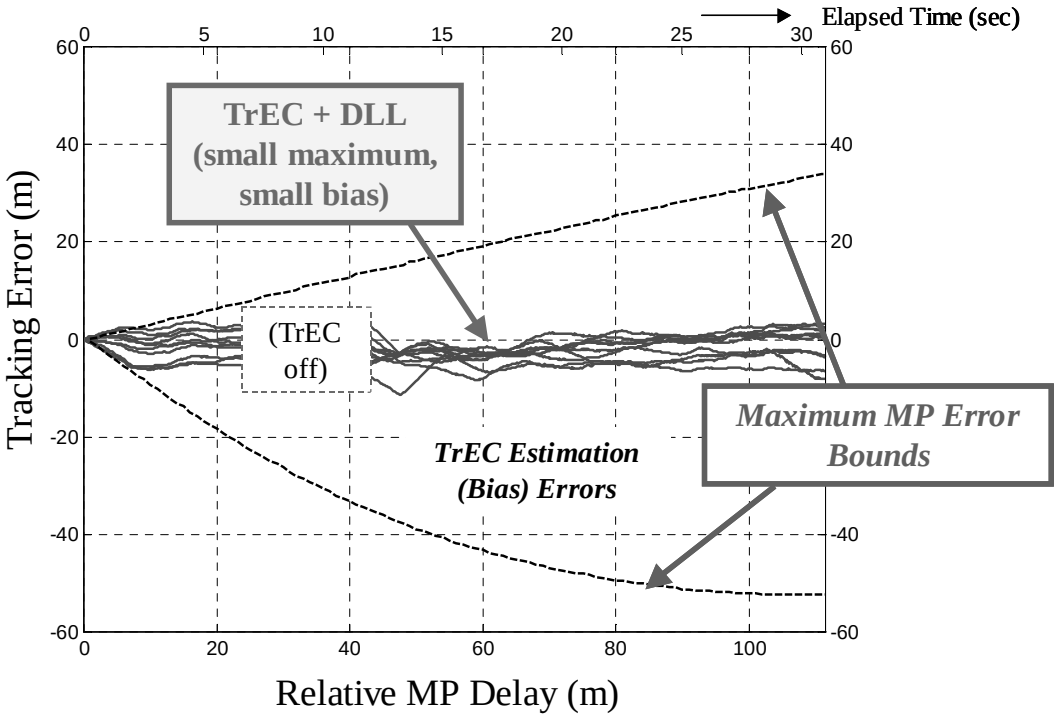

Figure 7-11 Short-Delay TrEC Performance Curves (10 trials, 1-Hz data)

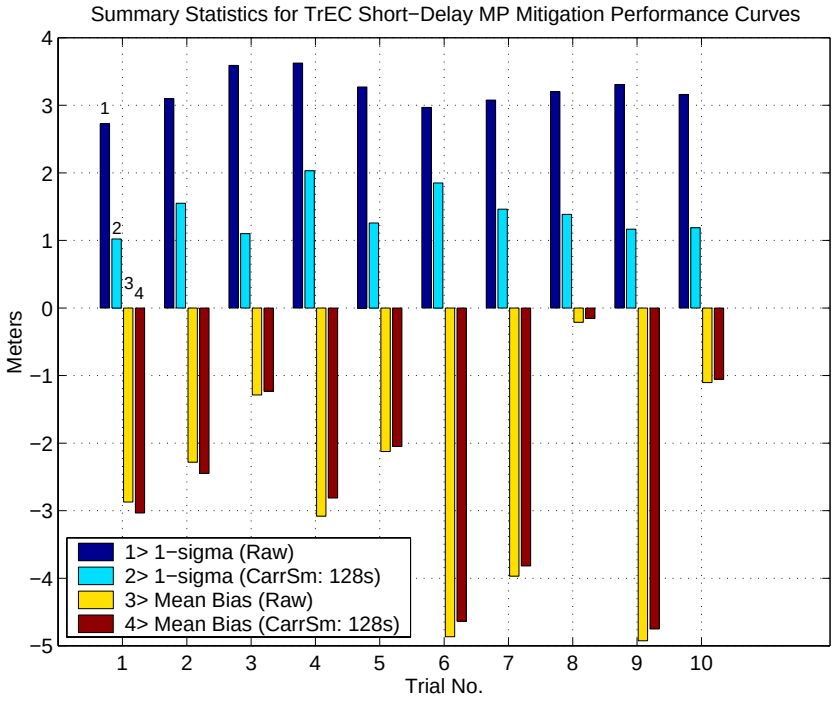

Figure 7-12 Short-Delay TrEC Performance Statistics (10 trials, 1Hz data)

The averaged results from the 10 trials—as performed by [Braasch96] for a conventional DLL—are shown in Figure 7-13. The top plot again compares the curves for the 0.5-chip spacing DLL and a conventional receiver implementing the TrEC. The bottom plot compares the true and measured tracking error curves at ultra-short relative MP-delays. Note that where all widely used current mitigation techniques (including wideband) have performance curves little better than a conventional DLL, the nearly identical upward slopes indicate that TrEC is still compensating for the tracking errors in this range. (Recall that the C/N_0 for this signal is quite high (50-53dBHz). This means that even at small relative MP delays the multipath errors still dominate over thermal noise errors.) In other words, this *TrEC is able to provide useful tracking corrections even for nearly zero-delay multipath.*

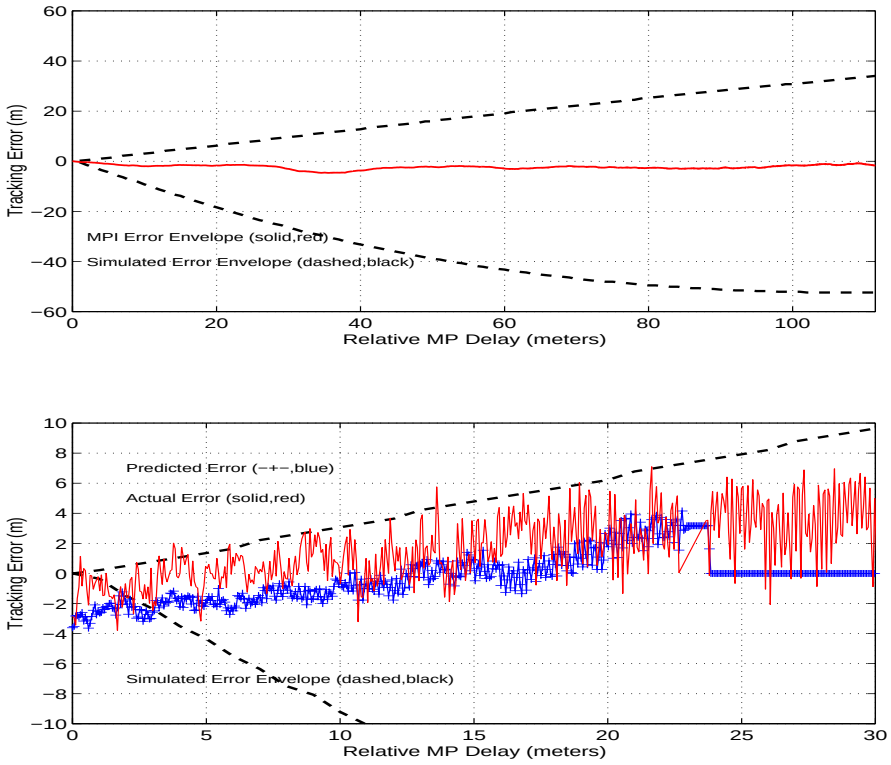

Figure 7-13 Top: TrEC Mean MP Performance Curve; Bottom: Ultra-Short Delay MP TrEC Mean Measurements (10 trials, 1-Hz data)

7.6 TrEC Position Domain Performance: GPS Signal Generator Data

In addition to thermal noise errors, the pseudoranges generated by the SigGen contained only a small, slowly varying ionospheric error that ranged from 3-5 meters. No Selective Availability (SA) or troposphere errors were added. By applying the TrEC corrections to the multipath-corrupted pseudoranges to be used in the navigation solution, the position-domain performance of the TrEC was examined.

The top and bottom plots of Figure 7-14 show the (nominal, zero-multipath) horizontal and vertical position errors, respectively, for the NBR receiver for a single trial. Each plot shows both the nominal errors for a small smoothing time constant (12.8s time constant—nominal for the NBR) and a large one (128.0s time constant) as a function of time. Also seen are the position dilution of precision (PDOP) and vertical dilution of precision (VDOP) values. (These provide an estimate of the purely geometry-dependent, root mean square position errors for the given satellite constellation, assuming identically distrubuted, zero-mean gaussian errors on each pseudorange.) Note that there are other small signal "glitches" that occurred during the trial (at t≈11min and t≈25min). These originated from the SigGen. Although they resulted in brief jumps in the horizontal and vertical position errors, the faults did not occur on PRN25, hence, the TrEC performance was not impacted.

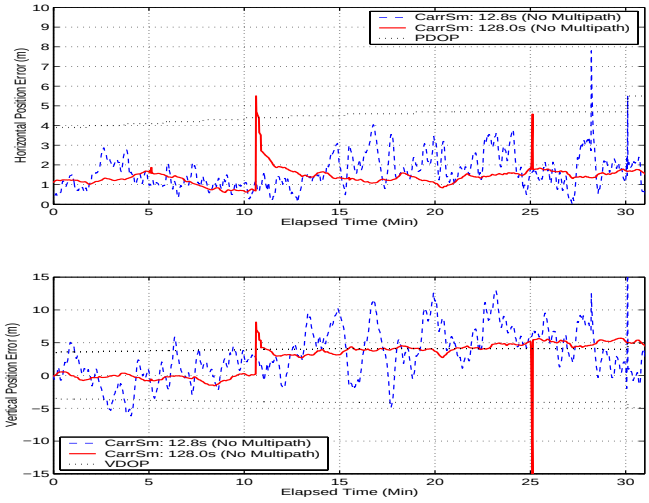

Figure 7-14 Nominal NBR Postion Errors (No Multipath, No TrEC)

Figure 7-15 shows the same NBR position errors for the case where multipath has been added as described in the previous section. Here, however, the carrier smoothed-only errors contrast against those of the TrEC-corrected position solution. (The nominal smoothing time of 12.8 seconds applied for the TrEC-corrected pseudoranges.) For the horizontal position errors, the TrEC was capable of removing the large bias, where the carrier smoothing alone was not. In fact, TrEC suffered its worse position errors between t≈5min and t≈15 min. The first large excursion occurred due to the reinitialization previously discussed. This lasted for approximately 4-5 minutes as the TrEC was reinitialized. The second excursion occurred shortly thereafter—while the TrEC was converging/refining its estimate of the MPI location. Neglecting the SigGen-induced discontinuity at t≈25min, the vertical position errors remain relatively small and consistent for all of the implementations in this entire range of MP delays.

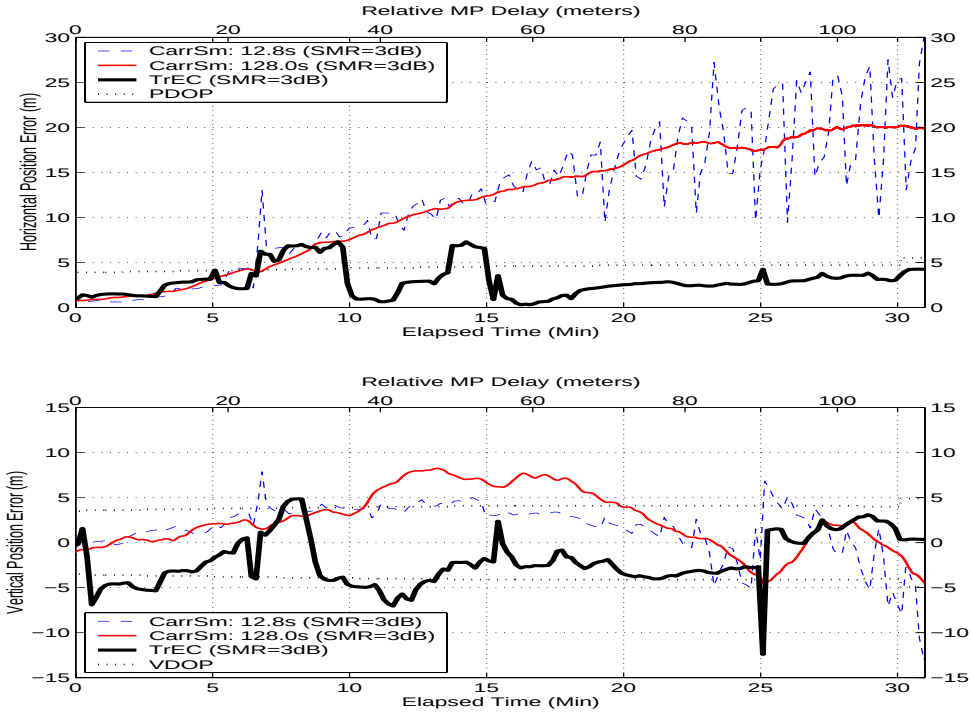

Figure 7-15 NBR Postion Errors With and Without TrEC (Multipath Added, SMR=3dB; No Cross-Channel Smoothing Used with TrEC)

7.7 TrEC Position Domain Performance: Live Satellite Data

Pseudorange performance plots may not reveal the multipath mitigation performance of a given technique. Though validation of these plots is possible, it may sometimes be challenging to completely remove the effects of other pseudorange errors (e.g., atmospheric effects). Consequently, in many cases, a signal generator or variable-length delay-line serves to validate the tracking error envelopes [Braasch96]. This action, however, may call into question the capability of a particular method to mitigate multipath on actual satellites in real-time.

The theoretical performance plots for TrEC contain biases that may not manifest themselves as errors in the position domain. This may be the case for many other techniques as well. Examining position error results from live satellites can enable a better assessment of the capabilities of many MP mitigation approaches.

Position error (reduction) comparisons permit a "bottom-line" assessment of the relative performance of various MP mitigation techniques. Unlike pseudorange error analyses, position "truth" measurements can be relatively easily found unambiguously to sub-centimeter accuracy. In addition, by using results from live GPS satellites, real-time tracking, low signal power performance, and initialization time issues may be become more apparent.

7.7.1 Experimental Setup

As in the previous section, to evaluate the TrEC position domain performance, six (slave) NBR channels simultaneously tracked a total of six GPS satellites. The other available correlator pairs (from the remaining six channels) located the MPI points of each of those satellites. The TrEC-enabled NBR subsequently computed real-time tracking error estimates for each pseudorange.

For the live satellite tests, code phase double-differences were made for the measurements taken at two (surveyed) antennas spaced 154.08 meters apart. ([Kaplan, Chapter 8]

describes this well-known and straightforward procedure.) Because the two antennas had a relatively small spatial separation, any residual atmospheric errors (along with the satellite and receiver clock biases) were negligibly small. The only significant position errors that remained in the three-dimensional double-difference position solutions were due to multipath and thermal noise.

The evaluation compared the following four different "modes" of receiver multipath mitigation performance:

- "Code Only" – nominal DLL code tracking performance, 0.5-chip spacing
- "Carrier Smoothing Only" – carrier smoothed (120-second time constant), "Code-Only" measurements
- "TrEC Only" – TrEC corrections applied to nominal "Code Only" pseudoranges
- "TrEC Smoothed" – Carrier smoothing (120-second time constant) applied to TrEC-corrected pseudoranges

Note that bias is frequently the most difficult multipath error component to remove. Time averaging methods (e.g., carrier smoothing operations) tend to have little effect on this error component. To make the carrier smoothing process more effective against the error variations, the evaluation disabled carrier aiding of the NBR code tracking loops for all experiments. This permitted the nominal (unsmoothed) code tracking errors to remain as close to zero-mean as possible. (Refer to Figure 7-9.)

The four MP mitigation modes were evaluated under the following three different multipath scenarios (cases):

- *Case 1*: Small amplitude, short relative delay (0~20m) "nominal" multipath
- *Case 2:* Large amplitude, short relative delay (0~20m) multipath
- *Case 3:* Large amplitude, medium-long relative delay (0~120m) multipath

Each of these cases is described in more detail below.

Case 1: Small amplitude, short relative delay (0~20m) "nominal" multipath

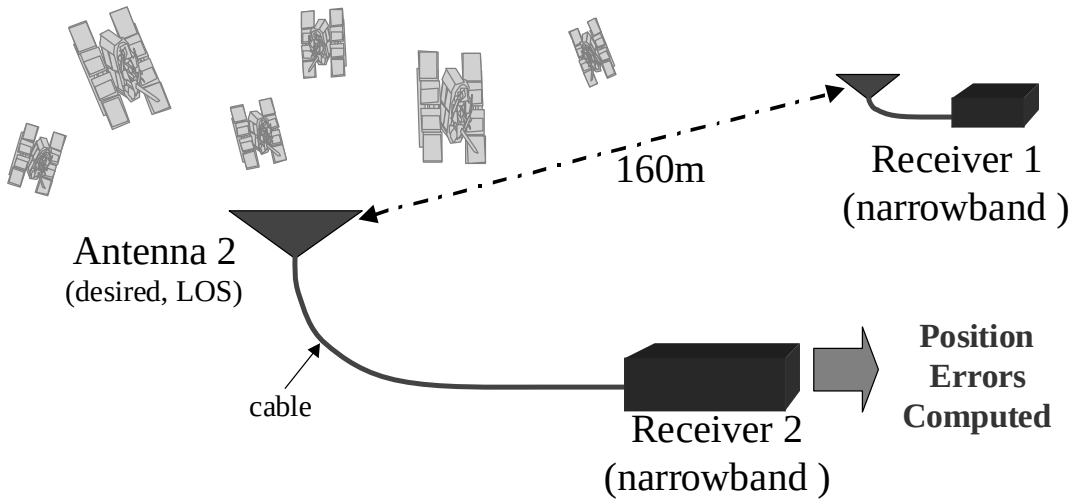

Figure 7-16 Experimental Setup for Case 1

The first scenario involved so-called "nominal" multipath that was normally incident on two rooftop antennas atop two different buildings on the campus of Stanford University. (See Figure 7-16.) It was impossible to completely characterize the multipath at both of these locations under nominal conditions. Still, given the locations of most of the rooftop reflectors relative to each antenna, the majority of the incident multipath signals presumably had relatively short delay (less than 20 meters). The amplitudes of these reflections were also small.

These characterizations are consistent with the care taken during the siting of both of these antennas. The antenna connected to Receiver 1 also serves as the Stanford National Satellite Testbed (NSTB, or WAAS–testbed) reference station antenna. Antenna 2 (or 2a and 2b illustrated in Figure 7-17 and 7-18) normally serves as the LAAS testbed reference station antenna at Stanford. In addition, the SU MDEs use data from this antenna. (Refer to Section 4.2.3 of Chapter 4.) Accordingly, for SQM investigations, [Akos00c]

characterized the distortion of the received correlation peak due to nominal multipath and thermal noise at both of these sites.

Case 2: Large amplitude, short relative delay (0~20m) multipath

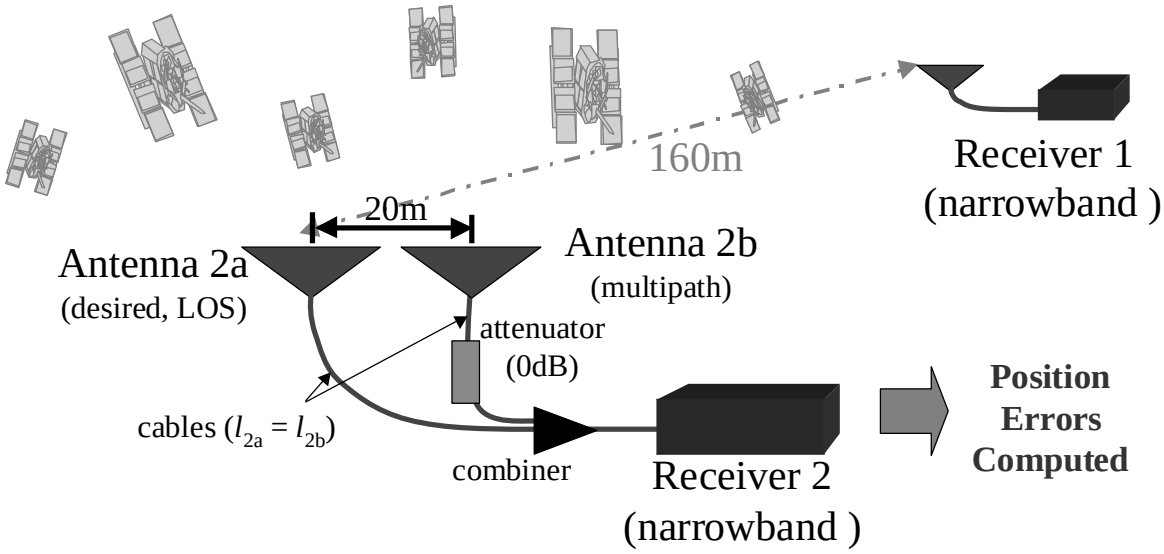

Figure 7-17 Experimental Setup for Case 2

To ensure the multipath had short delay relative to the line-of-sight (LOS), this experiment combined signals from two nearby (LAAS testbed) antennas. (See Figure 7-17.) The antennas were 20 meters apart, and the cables had approximately equal length. The "multipath" signal (Antenna 2b in Figure 7-17) had negligible attenuation with respect to the line-of-sight signal.

For a satellite at 90° elevation and/or in the vertical plane equidistant from each antenna, the code tracking loops of the receiver perceived the received signal as a LOS signal combined with an equivalent reflection at a relative delay of approximately 0 meters. The effective relative delay (magnitude) could reach as large as 20 meters (for a satellite both in the plane of and along the co-linear azimuth direction of both antennas). The fading

frequencies of each of the combined signals varied for each of the satellites as they traversed the sky.

Note that the "nominal" multipath—characteristic of Scenario 1—was also present for this case (and for Case 3). Since the multipath between Antenna 2a and Antenna 2b (as well as Antenna 1) was independent, there was effectively *more than one multipath reflection* on each pseudorange. Of course, the dominant multipath source was still the single "multipath" signal entering Antenna 2b.

Case 3: Large amplitude, Medium-long relative delay (0~120m) multipath

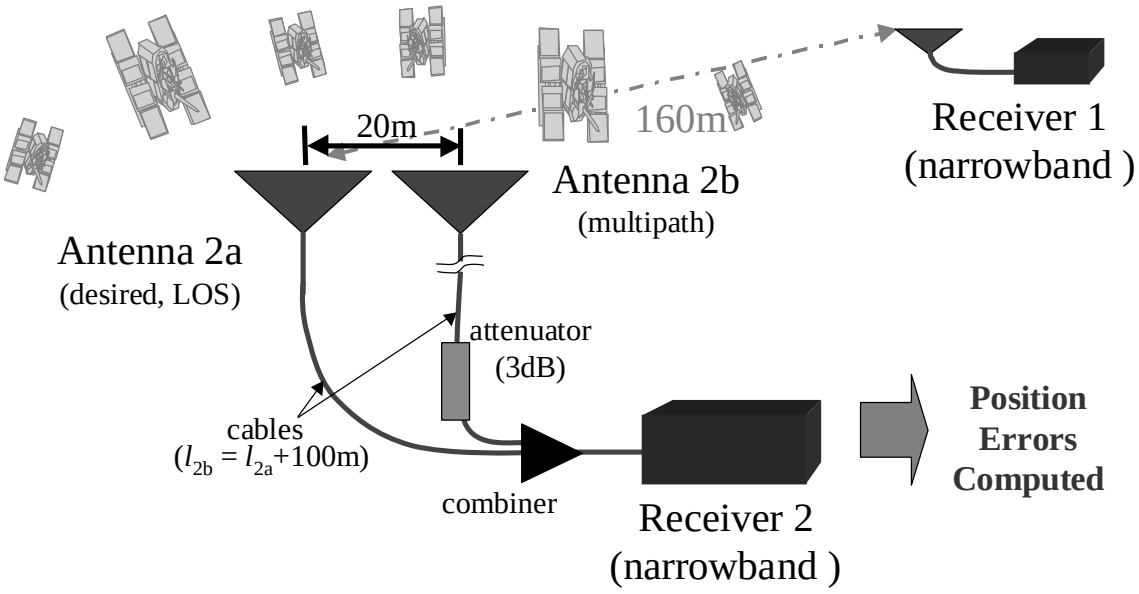

Figure 7-18 Experimental setup for Case 3

To evaluate the ability of the TrEC algorithm to compensate for extremely large tracking errors, this experiment added a 100-meter length of cable to the Antenna 2b signal path. (See Figure 7-18.) As in Case 2, the fading frequencies and elevation angles of each of the satellite signals varied independently over time. To prevent frequent loss of lock, the signal-to-multipath ratio for this case was set to 3dB. All other setup parameters remained the same as in Case 2.

An additional receiver "mode" comparison was made for Case 3. A pair of wideband, narrow correlator receivers was evaluated in parallel with the TrEC-enabled narrowband ones. (This will henceforth be referred to as the "Narrow Correlator" mode.) These wideband receivers were identical; each had 12 available channels. Although all 12 channels were active, for comparison, the code double-difference position errors for these receivers used only the same six satellites tracked simultaneously by their narrowband counterparts. Also, although it was impossible to completely disable carrier aiding for these receivers, the carrier aiding time constant for these receivers was minimized.

Figure 7-19 illustrates the "best" tracking errors to be expected for a conventional (0.1-chip correlator spacing) code DLL subjected to half-power multipath at the maximum relative delays evaluated by all three cases. For Case 3, the maximum MP tracking error bounds for each pseudorange were effectively at a maximum for the out-of-phase multipath (with carrier aiding disabled).

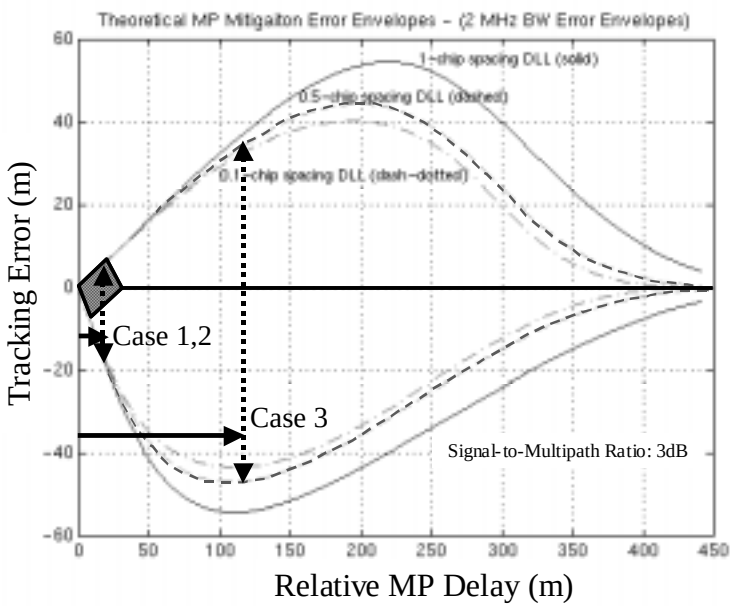

Figure 7-19 Theoretical Maximum Tracking Error Bounds for Cases 1, 2 and 3

Note that for Cases 2 and 3 the conventional DLL theoretical bounds were likely somewhat worse than those predicted by Figure 7-19. For Case 2, the signal-to-multipath ratio (SMR)

was approximately 0dB. Consequently, the maximum tracking error for that case likely exceeded the bounds of Figure 7-19.

7.7.2 Experimental Results

For each of the three multipath scenarios, the following (six) plots were generated:

- Signal Power (C/N_0, dB-Hz) vs. Time (minutes) for all six satellites tracked
- Elevation Angle (degrees) vs. Time (minutes) for all six satellites tracked
- TrEC-estimated DLL Corrections (meters)—applied to all six pseudoranges for both Receivers 1 and 2—vs. Time (minutes)
- Position Error (Magnitude, meters) vs. Time (minutes) for the Carrier Smoothed Only, TrEC Only, and TrEC Smoothed receiver modes only
- Error Statistics: Mean, Standard Deviation (1-σ), and Root-Mean-Square (RMS) for Code Only, Carrier Smoothed Only, TrEC Only, and TrEC Smoothed receiver modes

Since code-double differences were taken using only six satellites (or five effective measurements), the position error computation was fairly sensitive to satellite dropouts. Consequently a few brief outages in the data can be seen where one of the receivers lost lock on a satellite. In all cases, loss of lock occurred due to low satellite elevation angle and/or excessive signal power variations caused by multipath. No changes were made to affect the normal tracking performance of the receivers.

The error traces are shown only for the most continuous set of data. Statistics correspond, however, to the length of the entire steady-state data set. Accordingly, the error statistics presented may include some position error data that are not shown in the respective preceding plots.

Case 1: Small amplitude, short relative delay (0~20m) "nominal" multipath

The plots of the signal powers and respective elevation angles of the six satellites tracked are given below in Figure 7-20. Two satellites dropped out of view during the time period shown. Two other satellites were reacquired shortly thereafter. The increase in C/N_0 variations for the descending (and rising) satellites illustrates the increased multipath on these signals at the lower elevation angles.

The TrEC-estimated DLL corrections for each pseudorange as measured by both receivers are shown in Figure 7-21. The individual traces are less important than the (approximate) magnitudes of the corrections, so all six curves are shown on the same plots. Their peak-to-peak magnitudes range from about 3-20 meters (for high and low-elevation satellites, repectively). The offset of the six traces corresponds to the TrEC common-mode filter (i.e., finite PCBw) bias on each pseudorange. (Refer to Figure 6-29 of Chapter 6.)

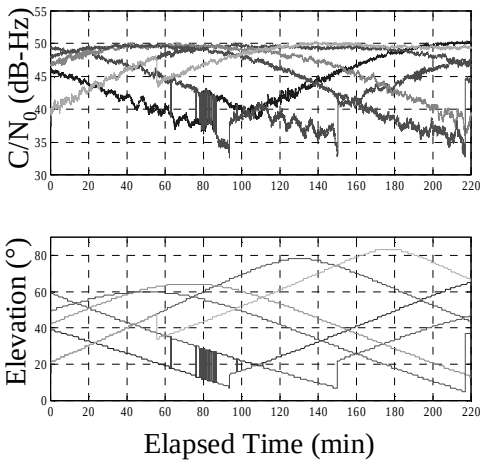

Figure 7-20 Satellite Signal Powers and Elevation Angles for Case 1

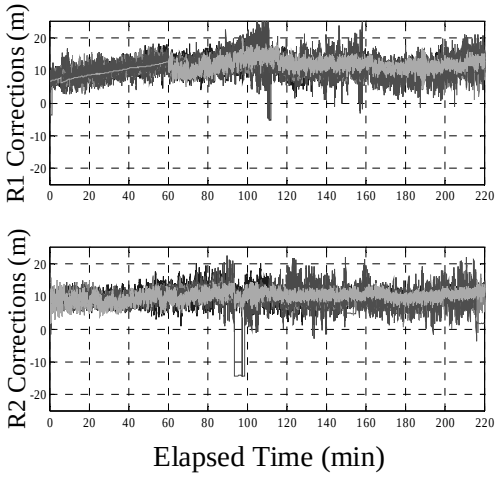

Figure 7-21 TrEC-Estimated DLL Corrections for Case 1

The position error results for the Carrier Smoothing Only, TrEC Only, and TrEC Smoothed modes are shown below in Figure 7-22. (The Code Only position errors were not shown since they would have obscured the other error traces.) The plot reveals that the TrEC Only and TrEC Smoothed traces had a maximum error greater than that for the Carrier

Smoothed Only mode. This occured as TrEC reinitialized after a new satellite came into view and was acquired by the two receivers.

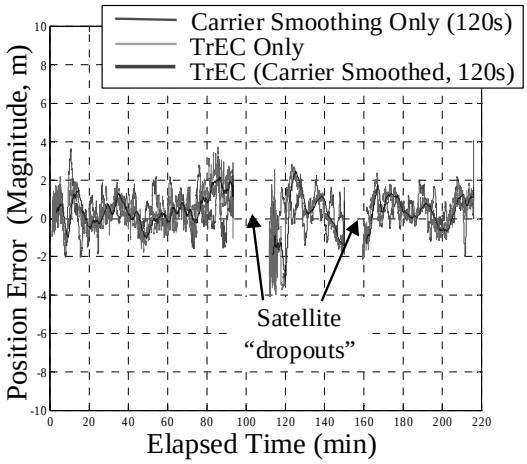

Figure 7-22 Position Error Comparison for Case 1

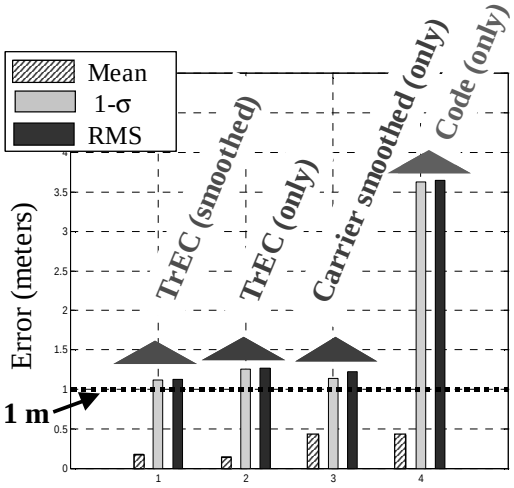

Figure 7-23 Position Error Statistics for Case 1

The Case 1 summary statistics are given in Figure 7-23. Clearly the Code Only receiver mode resulted in the worst 1-σ and RMS errors. Carrier smoothing dramatically reduced these two error statistics, but did little to reduce the mean bias. The two TrEC modes did not significantly change the 1-σ and RMS errors from the Carrier Smoothing Only results. The TrEC corrections—even without carrier smothing—did, however, *significantly reduce the mean position errors* due to multipath by more than a factor of two. Also note that since TrEC was actually correcting for code noise and multipath, the TrEC Smoothed statistics are comparable to those for the TrEC Only mode.

Case 2: Large amplitude, short relative delay (0~20m) multipath

Figure 7-24 plots the signal powers (for Receiver 2) and corresponding elevation angles of the tracked satellites. The large-amplitude "multipath" signals combined to produce 3-4dB oscillations in the received C/N_0 of each signal. (Figure 7-25 illustrates the corresponding

increased activity of the TrEC corrections for Receiver 2.) The frequencies of these oscillations varied as a function of the satellite trajectories through the sky. One satellite dropped from view of both receivers—due to low elevation angle and high multipath amplitude variations—at the end of the (approximately) 100-minute time interval shown.

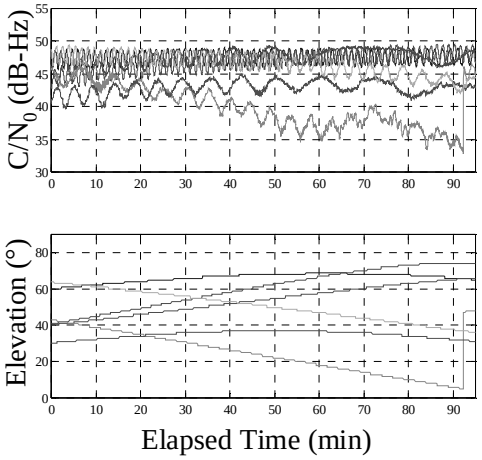

Figure 7-24 Satellite Signal Powers and Elevation Angles for Case 2

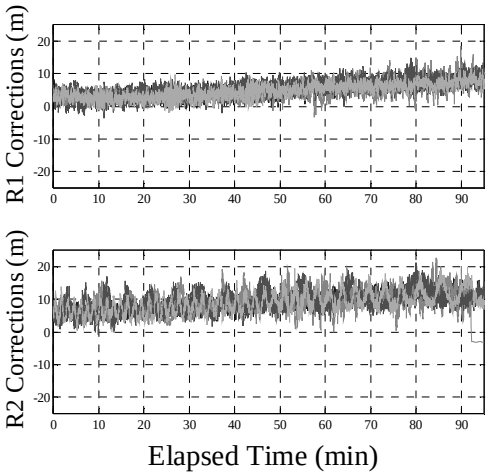

Figure 7-25 TrEC-Estimated DLL Corrections for Case 2

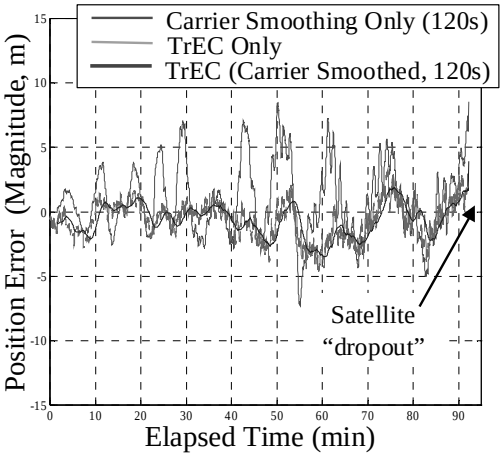

Figure 7-26 Position Error Comparison for Case 2

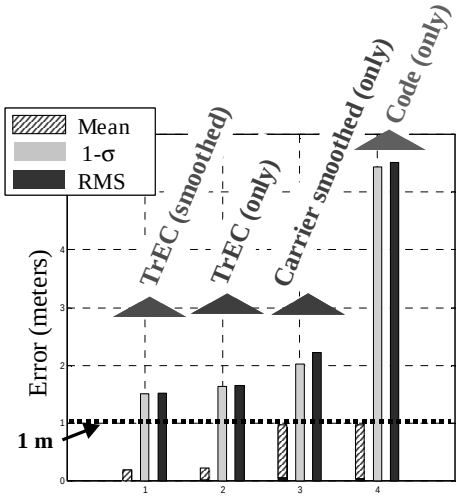

Figure 7-27 Position Error Statistics for Case 2

The position errors shown in Figure 7-26 illustrate that carrier smoothing alone was incapable of mitigating the low-frequency multipath tracking errors. The maximum errors for the Carrier Smoothing Only mode reached as high as 7-8 meters.

Again, the Code Only mode resulted in the worst position errors. (See Figure 7-27.) Carrier Smoothing Only reduced those 1-σ and RMS errors from over 4.5 meters to approximately 2 meters, but it did little to affect the mean error. The TrEC Only implementation reduced the 1-σ and RMS slightly more than did the Carrier Smoothing Only mode. More significantly, the TrEC reduced the mean bias by almost a factor of 5 (as compared to the Code Only or Carrier Smoothing Only modes). In fact, the TrEC mean errors for this case are comparable to those from Case 1.

Case 3: Large amplitude, medium-long relative delay (0~120m) multipath

As shown in Figure 7-28, the long-delay multipath signal caused signal power variations ranging as large as 7-8dB on every received signal. Wide fading frequency variations were also present on every channel. One satellite dropped from view (and another was subsequently reacquired) during the time period shown. The TrEC-estimated corrections (shown in Figure 7-29) for every pseudorange varied between 60-80 meters for Receiver 2.

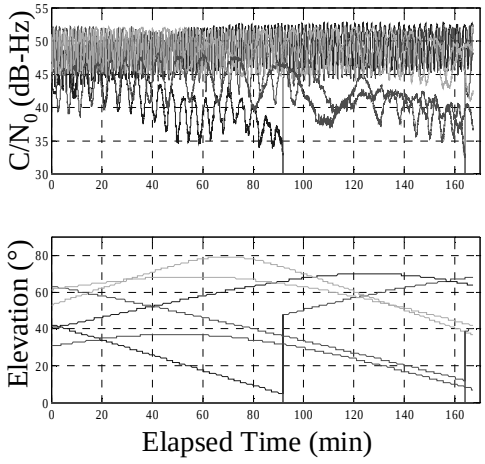

Figure 7-28 Satellite Signal Powers and Elevation Angles for Case 3

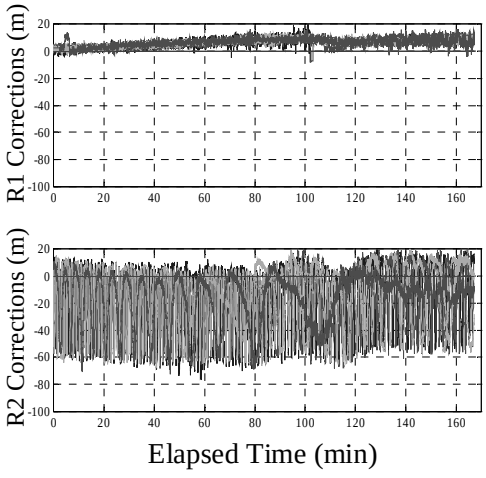

Figure 7-29 TrEC-Estimated DLL Corrections for Case 3

The position errors for the Carrirer Smoothing Only mode became as large as 250 meters. (See Figure 7-30.) That maximum error declined to less than 30 meters for the TrEC modes. Even the maximum position errors for the Narrow Correlator mode—which contained a significant negative bias—were noticeably larger than for either of the TrEC modes.

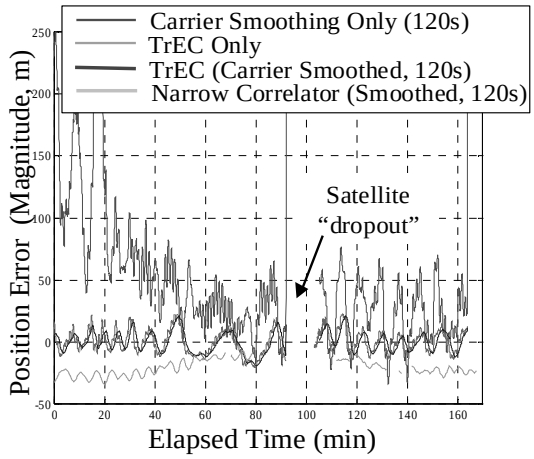

Figure 7-30 Position Error Comparison for Case 3 (Narrow Correlator Results Also Shown)

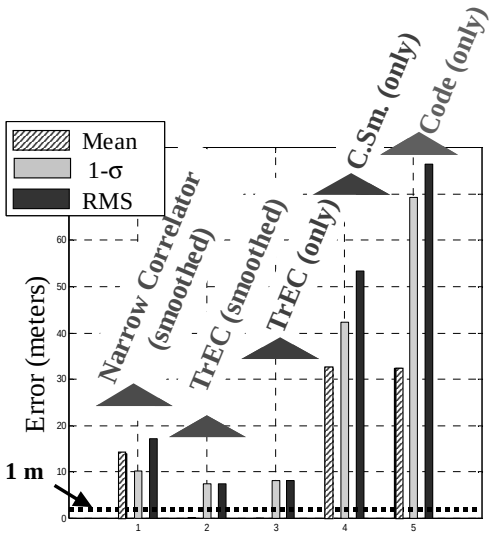

Figure 7-31 Position Error Statistics for Case 3 (Narrow Correlator Results Also Shown.)

The statistical error diffferences (shown in Figure 7-31) were even more pronounced. Code Only 1-σ and RMS errors were as large as 70-80 meters. Carrier Smoothing Only 1-σ and RMS errors, although somewhat smaller, still ranged between 40-55 meters. Once again, carrier smoothing did little to affect the mean positon error.

The TrEC Only and TrEC Smoothed modes both had 1-σ and RMS errors less than 10 meters and had a mean well below the 1 meter reference line. (Note that this extremely small mean is at least partly due to the sinusoidal nature of the position errors for this case. Still, the relative advantages of TrEC are clear.) The Narrow Correlator receivers easily outperformed the Code Only and Carrier Smoothing Only modes of the narrowband

receiver. Still, this wideband technique had significantly larger errors for all statistics than either of the TrEC modes.

Summary Statistics

The statistical error reduction factors for all modes evaluated (as compared to the Code Only mode) are given in Figure 7-32 for all three cases. The smallest multipath error reduction factor achieved by the TrEC implementations occurred for Case 1. (This is intuitive since the least multipath was present to mitigate in that case.) For that scenario, TrEC reduced the uncorrected error mean by a factor of 2.4. The narrow correlator achieved a comparable mean error reduction factor for Case 3—under significantly more severe (large amplitude and delay) multipath conditions. In that case, however, the TrEC Only and TrEC Smoothed reduction factors were many times larger.

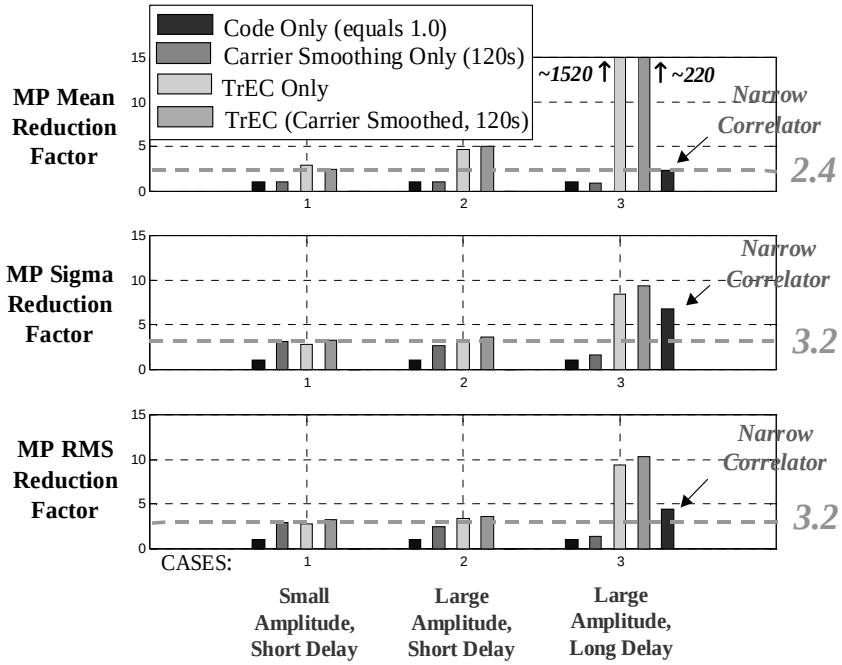

Figure 7-32 Summary Error Statistics: Multipath Error Reduction Factors

The minimum TrEC reductions in 1-σ and RMS errors also occurred for Case 1. They were each reduced by a factor of 3.2. However, unlike mean error performance, significant reductions in these error statistics are relatively easy to achieve in any receiver. TrEC 1-σ

and RMS error reductions were comparable to the Carrier Smoothing Only mode for the first two cases. Also, for Case 3, the Narrow Correlator achieved as much as 70-80% of the 1-σ reduction factor of the TrEC modes.

7.8 TrEC Performance Bounds: Experimental Verification

The Case 3 multipath conditions provide a useful method for validating the predicted maximum MP tracking error bounds. Because the actual receiver tracking errors were so large (on all pseudoranges), Case 3 represents a "worst case" multipath scenario. The (2-σ) maximum error that was predicted for the narrowband receiver used here was 10 meters. Position domain analysis offers the most straightforward and insightful way to examine the conservativeness of this error bound.

Note that since position errors may also include satellite geometry sensitivities, position domain error bounds will vary as a function of satellite geometry. Indeed small errors on a "critical" satellite—a satellite very sensitive to errors (e.g., one of only a few being tracked with poor geometry, or sky distribution)—could induce sizeable errors. Conversely, large errors on a less critical satellite might induce negligible position errors.

To examine the TrEC error bounds in the position domain, the pseudorange bounds derived in Section 6.10.5 of Chapter 6 must be translated into position error bounds. Recall that the position error results in this chapter come from code phase double-differences. The double-differenced code position errors are given by

$$\Delta\bar{x}(t) = \left[G(t)\right]^{\dagger} \cdot \Delta\bar{\rho}(t) \tag{7.2}$$

where $\Delta\bar{x}(t)$ is the 3x1 position error vector resulting from the product of the (Kx1) vector of pseudorange errors, $\Delta\bar{\rho}(t)$, and the pseudoinverse of the (3xK) satellite geometry matrix, $\left[G(t)\right]^{\dagger}$. Each column of $\left[G(t)\right]^{\dagger}$ captures the sensitivity of the position vector to a single unit (1-meter) change in each respective pseudorange error. For example, the position error that results from a 1-meter pseudorange error in (only) Pseudorange 2 is

simply Column 2 of $\left[G(t)\right]^{\dagger}$. Similarly, a 10-meter error only in Pseudorange 3 of *K* Pseudoranges causes an error described by Column 3 of $\left[G(t)\right]^{\dagger}$ multiplied by 10.

Accordingly, the (1xK) vector magnitudes of the position error individually subjected to a 1-meter error is simply

$$\left[\left|\Delta\bar{x}(t)\right|\right] = \left\{\left|g^{\dagger}(1)\right|, \left|g^{\dagger}(2)\right|, \left|g^{\dagger}(3)\right|, ..., \left|g^{\dagger}(K)\right|\right\} \tag{7.3}$$

where $\left|g^{\dagger}(k)\right|$ represents the *k*th column of $\left[G(t)\right]^{\dagger}$. The squared norm of this vector computes a mean-square position error (MSE) bound. The MSE bound assumes that the MP errors are distributed across all the satellites in a mean-square sense. This is a reasonable assumption since, in general, even optimally TrEC-corrected pseudoranges will have non-zero residual errors. Computing the minimum of this vector (for all time, *t*) yields a minimum MSE bound. This more aggressive bound assumes the worst case MP errors occur only on the most critical (i.e., most sensitive) satellite. (Note that a maximum MSE bound would maximize the vector of Equation (7.3) for all time, *t*.) The minimum MSE bound only assigns the 10-meter pseudorange error to the satellite that induces the largest position error.

Figure 7-33 below plots MSE and minimum MSE bounds for Case 3 MP conditions. The figure compares the TrEC-smoothed trace to these bounds as well. Observe how the bounds vary as a function of changing satellite geometry (and time). The variations indicate that the receiver is actually more sensitive to position errors towards the beginning of the run, and that sensitivity decreases as time progresses. (Recall from Figure 7-30 that the Carrier Smoothing Only position errors responded to this sensitivity.). One or more rising satellites likely cause this trend.

The MSE bounds—the more design-practical bounds—conservatively over-estimate the receiver performance. The MSE bounds are conservative by a factor of 2 or more. The minimum MSE bounds, as expected, are much less conservative. The actual TrEC-smoothed position errors exceed these bounds in several places. Significantly, the

minimum MSE still bounds more than 1-σ (82%) of these worst-case position errors. These results further substantiate the claim that the TrEC effective pseudorange errors are substantially lower than those predicted by the analysis of Section 6.10.5 of Chapter 6. Also, although the MSE bound should be used for design purposes, the minimum MSE bound may more accurately predict the true TrEC position domain performance.

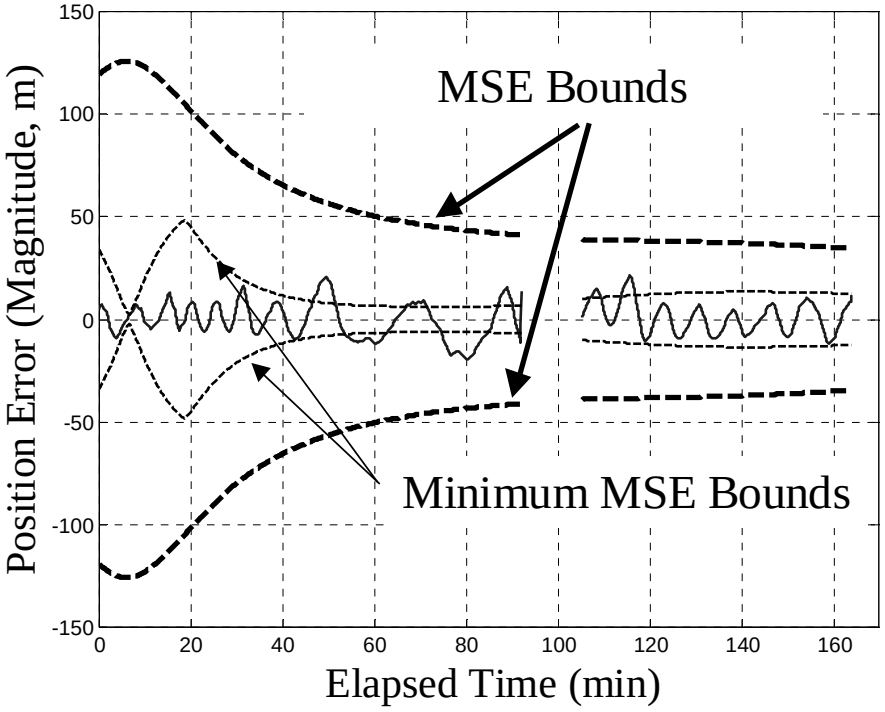

Figure 7-33 Residual Case 3 (Post-TrEC) Position Errors with MSE and Minimum MSE Bounds

Chapter 8:

Conclusions and Recommendations for Future Research

Robust mitigation of two threats to GPS signal quality—evil waveforms and multipath—was shown possible by developing techniques utilizing multiple correlators per receiver channel. For the signal quality monitoring and evil waveform detection problems, conclusions are drawn in Section 8.1. Section 8.2 lists several suggestions for future research in these areas. Sections 8.3 and 8.4, respectively, provide conclusions and future research recommendations in the field of multipath mitigation.

8.1 Signal Quality Monitoring Conclusions

The SQM research in this thesis may be categorized into the following three primary areas: Evil Waveform Threat Models, Minimum Detectable Errors, and SQM Design and Analysis. The conclusions corresponding to each of these subgroups are listed below.

8.1.1 Evil Waveform Threat Models

An "evil waveform" is an anomalous GPS signal caused by a failure of the signal generating hardware onboard the GPS satellites. The only known occurrence of an EWF

occurred on SV19 sometime in 1993. The Second-Order Step (2OS) Threat Model is best suited for modeling evil waveforms (EWFs) since it can generate deadzones, distortions, and false peaks on the correlation peak. At the same time it explains the actual SV19 failure spectrum data.

The 2OS Threat Model developed herein consists of a digital failure mode (Threat Model A, or TM A), an analog failure mode (Threat Model B, or TM B), and a combined analog and digital failure mode (Threat Model C, or TM C). The digital failure mode causes the correlation peak deadzones. The analog failure mode induces oscillations (distortions) and, sometimes, false peaks. Analytical equations derived in this thesis can compute a 2OS EWF correlation function directly and very efficiently.

8.1.2 Minimum Detectable Errors (MDEs)

Minimum detectable errors (MDEs) represent the smallest correlation peak distortions that any specific signal quality monitoring (SQM) technique can distinguish (with high integrity and low false-alarm probability) from nominal peak distortions caused by multipath and thermal noise. MDEs are based on experimentally-determined standard deviations of the correlation peak. A smaller MDE for a given detection test implies a more sensitive (and effective) detection test. Note that the MDE computation removes any means or biases that may accompany the measurements, and assumes that those biases are not present (i.e., calibrated out) when the multicorrelator SQM receiver attempts to measure true EWF distortions.

The sensitivities of multicorrelator SQM techniques directly depend on the MDEs and, hence, strongly depend on the nominal biases present on the correlation peak. As described herein, peak-flush sidelobes (PFSLs) and the receiver front-end filtering process may introduce significant biases into EWF detection tests and need to be accounted for (removed) for best SQM performance. Unlike filtering biases, PSFL biases are satellite-specific, so this thesis analyzes these on a satellite-by-satellite basis. More specifically, using this information, it derives the MDE thresholds based on a specific PRN code of a given satellite.

Experimental MDE data was taken at Stanford University (SU). The SU MDEs (now accepted as standard by the International Civil Aviation Organization, or ICAO) were tabulated for SQM2b—a practical three-correlator pair SQM design—for elevation angles from 0° to 90°. The data was fit using a 3rd-order polynomial, so the MDEs could be found for any elevation angle.

8.1.3 SQM Design and Analysis

LAAS SQM: Steady State

This thesis examined several candidate multicorrelator SQM implementations to determine the most practical and effective means of detecting EWFs which may cause hazardously misleading information (HMI) for airborne users of the Local Area Augmentation System (LAAS). Each implementation provided several samples of the correlation peak at various locations and permitted the monitor to perform two types of simple EWF detection tests—ratio tests and Δ tests. Ratio tests measure the relative "flatness" of the peak and delta tests measure the degree of asymmetry relative to the nominal, filtered peak.

It was found that closely-spaced correlator pairs located nearest to the peak of the correlation function produce smaller MDEs and, hence, are most effective at detecting EWFs. The practical monitor design of choice consisted of three correlator pairs (on a 16MHz PCBw receiver) and placed these correlators at spacings of 0.1Tc, 0.15Tc and 0.2Tc, respectively. This implementation—SQM2b—used a total of nine ratio tests plus two delta tests and, ignoring the 6-seond time-to-alarm (TTA) requirement, was proven capable of satisfying the current LAAS requirements for Category I landings for both Early-minus-Late (E-L) and so-called ΔΔ correlator receivers.

The ΔΔ correlators characterize receiver tracking loop implementations that are less sensitive to multipath errors. In contrast to conventional E-L receiver configurations, ΔΔ receivers are in general the most difficult to protect for any SQM. For LAAS, these discriminator implementations are not duplicated on the ground, so they are not used to

form the differential corrections. Consequently, the corrections frequently add EWF errors where they may not have existed before instead of wholly or partially canceling them out.

The primary 11 SQM2b detection tests were unable to protect a small section of the original, ΔΔ receiver configuration design space. In fact, 36 additional EWF detection tests developed in this thesis were shown to improve the performance of SQM2b. However, they did not remove the need to exclude certain ΔΔ receivers. More specifically, this "notch" region excluded ΔΔ receivers with correlator spacings less than $0.07T_c$ and PCBws greater than 14MHz.

This thesis also found that modification of the precorrelation filter could increase the performance of multicorrelator SQM's. For SQM2b, decreased transition band attenuation in conjunction with linear phase (zero differential group delay) led to improved detection capability for satellites at high elevation angles. This modification does not aid performance on satellites at low elevation angle, however. These may require additional (external) multipath mitigating hardware or equipment to improve SQM detection capability.

The Multipath Limiting Antenna (MLA), for example, is specially designed to reduce the effects of multipath on the received signal. It may provide the needed reductions in MDEs at low elevation angles. Combined with the proper precorrelation filter design, the MLA may permit SQM2b to satisfy the more stringent Category II and Category III requirements for LAAS.

LAAS SQM: Transient

The transient SQM problem analyzes the ability of a multicorrelator SQM implementation to detect hazardous EWFs *before* they cause HMI for the (E-L or ΔΔ) airborne users. In other words, the transient analysis ensures that the steady-state SQM implementation detects the EWFs within the Category I 6-second time-to-alarm requirement.

It was found that even including the secondary detection tests (Appendix A), SQM2b is generally incapable of detecting all hazardous EWFs within the 6-second time to alarm. The time required to detect EWFs may be reduced without penalty by using a 100-second moving average (100 tap, rectangular window FIR) filter instead of a first-order (Hatch filter model, IIR) one. This alone, however, does not completely mitigate the problem.

A single nonlinear detection test—the square of the most sensitive steady-state test, or the Δ^2-test—was found to produce increased sensitivity for the transient detection problem. For SQM2b, the transient analysis indicated the first Δ test ($\Delta_{0.15,0.1}$) was best suited for this operation. It showed that this single Δ^2-test was able to promptly detect the hazardous EWFs. This completed the validation that SQM2b could effectively protect airborne users for Category I landings.

WAAS SQM: Steady State (*See Appendix D.*)

For the Wide Area Augmentation System (WAAS), this thesis analyzed two cases of EWFs: the original 2OS Threat Model and a *most likely* subset of these EWFs. The analysis of the full 2OS Threat Model, also called the full ICAO model, was identical to that performed for LAAS. WAAS reference station receivers, however, monitor using the equivalent of a single, pre-normalized Δ-test. The MDEs for WAAS may be substantially smaller, however, than those of their LAAS counterparts since averaging may be performed over a larger number of monitor receivers—two at each WAAS reference station. Using the full ICAO model, it was shown that this limited multicorrelator is capable of protecting the integrity of WAAS users against EWF threats.

The most-likely EWF threat model consisted of a reduced version of TM A and TM C. These EWF parameters most closely approximate the SV19 event. For WAAS, it was shown that no monitoring is required to protect $\Delta\Delta$ and E-L correlators for this subset of the full ICAO EWF model because of relaxed error requirements for LNAV/VNAV (the current aircraft landing certification for WAAS) versus Category I landings.

8.2 Signal Quality Monitoring Future Research

The SQM research in this thesis leaves open several possible areas of future work. These areas include performing a calibration error sensitivity analysis, further validating the SQM results presented in this thesis, and analyzing the transient SQM problem for WAAS. Each of these suggestions is detailed below.

Monitor Precorrelation Filter Modification

This thesis showed (in Appendix B) that the detection capability of an SQM implementation is sensitive to the characteristics of the precorrelation filter. Future research should explore this avenue further, by first developing better models for the current SQM receiver precorrelation filters. Second, this work should explore practical, implementable filter design modifications. Once the feasible filter design space is known, this research should model and analyze this set to determine and propose the best design for EWF detection.

Calibration Error Sensitivity

The ultimate goal of the analysis in this thesis is to develop a real-time SQM for installation in LAAS reference stations. The sensitivity of the results presented here to manufacturing tolerances and other implementation-specific variations may be explored. This is particularly true for the nominal bias calibrations. Since these biases must be measured, stored, and used to calibrate each SQM receiver, it may be advantageous to explore their sensitivity to changes in satellite elevation angle and temperature (for the filter biases).

For the analysis, this implies developing bounds for the measurement errors and tolerances on the filter design specifications. Deviations in the expected and actual mean biases may have significant implications when using nonlinear detection metrics like those proposed to meet the transient SQM constraints. Moreover, if these biases are time varying, a real-time calibration technique may need to be devised. The filter design specifications may be

particularly critical for determination of the Category II and III SQM precorrelation filter requirements.

Experimental SQM Validation

The current challenge for SQM research focuses on testing and prototyping a real-time SQM to validate these analysis results. (Mitelman is presently accomplishing much of this SQM work [Mitelman00].) [Akos00b] and [Macabiau00] in part accomplished experimental validation of a modeled EWF correlation function. However, more quantitative exploration of the errors between the measured and the actual data may yield greater insights into the precorrelation filter biases and other (unmodeled) receiver-dependent effects. Further, using the EWF generator, it becomes possible to directly measure the transient SQM responses of the detection metrics. In conjunction with users receivers of various configurations, it is possible to also measure their respective transient PRE responses as well. In this way, the true TTAs resulting from a given SQM may be discovered and, if needed, reduced through SQM design enhancements.

WAAS Transient SQM

The most likely threat model discussed in the previous section (and in Appendix C) works well for a satellite that has failed (transmits an EWF) prior to coming into view of the WAAS reference station network. In that case, both the user and the reference station will experience errors due to the EWF. If, however, the satellite initially fails while at a high elevation angle relative to the WAAS network of reference stations, only the user will experience EWF-induced errors. This is because the dual-frequency WAAS reference receivers will rely only on carrier phase propagated corrections for these satellites. They will virtually ignore the code (correlation) tracking errors, which EWFs affect. As a result, there will be negligible cancellation of the errors due to the WAAS differential corrections, and the resulting user pseudorange errors will be significantly larger. In other words, some form of SQM may be required even for the reduced subset of the full ICAO EWF threat model.

This thesis presented results for the steady state WAAS SQM problem only. From the LAAS transient analysis, it became clear that a steady-state analysis may not guarantee that users will be alerted of HMI within the TTA requirement. (The TTA for WAAS is 6 seconds as well.) To be certain no EWFs cause HMI for WAAS users under the full, ICAO EWF (2OS) model, a transient analysis should be performed for this case as well.

8.3 Multipath Mitigation Conclusions

The novel multicorrelator MP mitigation technique developed in this thesis led to many significant conceptual, theoretical and experimentally based conclusions. These fall under the following: Multipath Invariance Concept, Tracking Error Compensator: Design, Analysis and Optimization, and Tracking Error Compensator: Experimental Validation. The contributions to each of these are described below.

8.3.1 Multipath Invariance Concept

Conventional multipath mitigation techniques focus on the main peak of the correlation function. Multipath distorts this peak. As a result, these techniques all exhibit a characteristic dependence on the parameters (i.e., relative amplitude, delay, phase, and phase rate) of the incident multipath signals.

The concept of multipath invariance asserts that the slope of the correlation function plateaus, however, remains multipath invariant (MPI). Accordingly, this slope does not change as a function of multipath parameters or the number of incident multipath signals. It is approximated by computing L-E—the MPI discriminator—measurements using one or more additional (MPI) correlator pairs inside a given receiver channel.

MPI points can be found at the late-most points of the correlation peak plateaus. There are many MPI points present on every PRN code correlation function. The location of these points relative to the main peak is PRN-dependent. In general, the optimal MPI points are defined as those adjacent to the longest MPI plateau; the minimum width of these maximal-length plateaus for all GPS PRNs is 10 chips. The best MPI point would reside at the base

(1 early) of the main peak of a code correlation function immediately adjacent to an optimal MPI plateau.

8.3.2 Tracking Error Compensator Design, Analysis, and Optimization

The Tracking Error Compensator (TrEC) leverages the MPI concept to directly measure the code-tracking error due to multipath. While the conventional DLL tracks the satellite, TrEC uses an independent correlator pair to locate the MPI point. Since the location of the MPI point relative to the main peak is known, TrEC differences this ideal distance from that reported by the DLL to compute the code tracking error. TrEC subsequently subtracts this error from the pseudorange measurement. In the noiseless, finite bandwidth (and, by extension, infinite bandwidth) scenario, TrEC results in code tracking errors that are multipath invariant.

After applying TrEC, the tracking errors on a given signal have a constant offset due to finite receiver PCBw. The magnitude of this bias varies as a function of receiver PCBw and also as a function of the implementation and/or selection of the MPI point. Still, provided this offset is common to all satellites being tracked (in the noiseless, finite PCBw case), TrEC results in nearly zero position errors due to multipath with arbitrary parameters.

Optimal TrEC performance requires that the MPI correlators locate the true MPI point. This point, however, is not obtainable in practice since it is indistinguishable from the MPI plateau. (On the plateau, the discriminator output, L-E, is zero.) A less-than-ideal MPI point, which trades off some MP mitigation performance, must be found instead. Analysis revealed that maximum TrEC MP tracking errors of less than approximately 1 meter are achievable provided the actual located MPI point is within 5 meters of the true MPI point.

Signal power variations of the (nominal) incoming signal may cause the (constant) TrEC filter bias offsets (from the MPI point locations) to differ between satellites. This may introduce errors into the position solution. MPI normalization can partially remove this variation. Alternatively, the attenuation effects (primarily of the antenna gain pattern) may

be removed through calibration. This implies dynamically modifying the desired MPI point as a function of the elevation angle of a particular satellite. This latter method, of course, would only be valid for a specific antenna or antenna type. A third alternative would be to simply model the precorrelation filter rounding effects and to compute the bias using the model under different signal power assumptions.

The MPI correlators may operate on the direct signal, independent of the primary code tracking loop by using the carrier phase. They leverage the fact that carrier loop dynamics are relatively insensitive to the (code) multipath. These correlators use an adaptation of traditional carrier aiding to provide this direct decoupling. Once performed, they may obtain correlation samples in the MPI region on the correlation function without being influenced by the multipath-varying conventional DLL.

A Fibonacci Search (FS) is an efficient algorithm for locating the MPI point using a limited number of observations (or samples at different locations) of the MPI region. It leverages *a priori* knowledge of the uncertainty bounds and the desired convergence resolution to locate the desired MPI point in a minimum number of observations. Assuming an initial uncertainty in the location of the desired MPI point of 120 meters and a single MPI correlator pair per receiver channel, the FS requires a maximum of 11 observations to locate the desired MPI point within ±0.5 meters.

Correlation samples in the MPI region have low signal power, which places some limitations on how fast the MPI point can be found. These individual samples (i.e., from one of the correlators in an MPI correlator pair) require approximately 13-second integration times required to elevate their SNRs to the same levels as those obtained on the main correlation peak.

The MPI discriminator results from L-E differences of the MPI correlator samples within the MPI region. Its variance is, in general, upper-bounded by twice the corresponding correlator spacing. This implies that its measurements are well modeled by a coherent E-L discriminator. Note that the coherent discriminator has the best noise performance of all the (three) standard DLL discriminators.

Several error sources limit the multipath mitigation performance of TrEC. Random errors result from thermal noise and low signal power considerations. Bias errors may result from a combination of the following four error sources: FS convergence tolerance, multipath, unmodeled signal amplitude variations, and code-carrier divergence due to the ionosphere. Averaging may reduce random errors (caused by thermal noise from low signal power considerations), but the bias errors require more sophisticated reduction methods.

Cross-channel smoothing (CCS) is one technique used to reduce TrEC bias errors. It removes residual biases by averaging them across all tracked satellites. The maximum bias error is reduced by a factor of the number of satellites tracked. As a consequence of this, however, the TrEC corrections become multipath varying, and the maximum expected multipath error increases. This trade-off, however, is acceptable in many instances where small mean errors are most desirable. Cross-channel smoothing may not be necessary if more MPI correlators and/or a wider PCBw is available.

The addition of multiple MPI correlators can also significantly improve TrEC performance by reducing the bias errors. Estimation-based algorithms may better estimate the location of a single MPI point. In addition, redundant MPI correlators may be used to form TrEC corrections at several different MPI points on a single correlation function. These corrections may subsequently be averaged to form a single, improved correction estimate.

Both CCS and multicorrelator implementations may significantly improve TrEC performance. Specifically, even under conservative assumptions for signal power and multipath, these techniques may reduce the time required initially to locate the MPI point and also reduce the maximum expected tracking errors due to multipath. Using TrEC, the maximum (2-σ) initialization time for a narrowband receiver equipped with only one MPI correlator pair per channel (in addition to the code tracking pair) is approximately 7.5 minutes. This bound decreases most rapidly as the number of MPI correlators are increased. The maximum (2-σ) MP pseudorange error for this receiver configuration is 10 meters for a 6-channel receiver (using CCS). This decreases most rapidly with increasing PCBw and number of active GPS (TrEC-enabled) channels. For example, 95% of the time, a 16MHz PCBw receiver, equipped with three MPI correlators per channel would initialize

in less than 50 sec, and have maximum tracking errors of one meter or less when tracking only 6 satellites.

8.3.3 Tracking Error Compensator: Experimental Validation

TrEC was implemented on a conventional 12 channel narrowband receiver. The receiver had a single correlator pair per channel, but was reconfigured to host two pairs per channel. One pair in each channel performed convetional (DLL) code tracking. The other became the MPI correlator pair.

Results from both a GPS signal generator and live GPS satellites validated TrEC's superior performance over a conventional DLL, carrier-smoothed code, and, in the instance of extremely large multipath on actual GPS satellite signals, a (wideband) narrow correlator receiver. The results indicated that TrEC is capable of providing corrections for multipath in any regime—including ultra short-delay multipath. Tracking error comparisons demonstrated TrEC was able to estimate multipath tracking errors at MP relative delays well below 10 meters.

Analysis of the live GPS satellite data results (for Case 3, the most severe multipath conditions) revealed that the initialization time and maximum pseudorange error bounds are quite conservative. It showed that the effect of initialization time had negligible effect on the steady-state performance of TrEC. (In general, this will always be the case since the bounds assume the worst case uncertainty.) Also, the data showed that the mean-square error (MSE) accuracy bound for the narrowband receiver overbounded the actual errors by a minimum factor of (approximately) 2. In addition, it found the significantly less conservative minimum MSE bound could more-accurately predict the true (worst-case) TrEC performance.

8.4 Multipath Mitigation Future Research

Introduction MPI concept and TrEC has opened the door to several interesting possibilities and potential areas of research. This subsection describes six possible areas for future research including:

- New MPI code properties or characteristics
- Additional or improved hardware implementations of TrEC
- Improved filtering and estimation algorithms
- Further experimental validation of TrEC performance and performance bounds
- Active control of signal tracking using the TrEC corrections
- Discovery and application of carrier phase MPI properties

MPI properties

The slope of the correlation plateaus is one multipath invariant property. However, others may exist as well. The discovery of other, perhaps more-easily-obtainable MPI properties may lead to faster initialization times, increased pseudorange, and, hence, position accuracy.

Hardware Improvements

There is significant room for improvements in both initialization time and pseudorange accuracy bounds. Since it is desirable to retain the MPI properties of TrEC as much as possible, improving accuracy may entail curbing the use of cross-channel smoothing. Still, the TrEC (implementation) biases must be kept as small as possible. Moreover, keeping initialization times as short as possible, generally reduces the fidelity of the MPI point (location) estimates, which may lead to degraded accuracy.

Perhaps the most straightforward way to improve TrEC performance is to implement the technique on a (high-end) receiver equipped with more sophisticated hardware. The most ambitious of such receivers include software radio GPS receivers [Akos97]. With these, it becomes possible to utilize arbitrary numbers of MPI region samples (i.e., correlators). Properly implemented, this feature alone could provide the leverage necessary to achieve near carrier phase level multipath performance, and sub-second initialization times. Additionally, high-end receiver attributes might include a wider precorrelation bandwidth and dual (or triple) frequency code/carrier tracking capability.

Improved Estimation Algorithms

Improved (loop-filter) estimation algorithms could assist in achieving faster, more robust convergence to the MPI point. Additionally, using SNR, elevation angle, and other signal observables in an adaptive estimator or Kalman filter may provide even more effective TrEC corrections. This may be particularly useful when hardware is limited and when CCS is necessary.

Experimental Validation

It may be desirable to experimentally validate some of the secondary claims made in this thesis. First, TrEC analysis revealed that the MPI properties held not only for the multipath parameters, but also the number of incident reflected signals. Second, the theoretical accuracy bounds were found to be fairly conservative for the narrowband, single MPI correlator case. Several other receiver configurations need to be examined to substantiate that all these bounds are indeed conservative. Additionally, TrEC performance should be directly compared to the best of the current wideband techniques (e.g., $\Delta\Delta$ discriminators) to substantiate the claim that TrEC is able to outperform those methods when implemented using comparable receiver hardware.

TrEC-Aided DLL

A simple extension to the current TrEC implementation would be to use the TrEC corrections to control the primary code tracking loop. Once performed, the nominal DLL

carrier aiding equation (from Equation (2.14) for satellite, *k*) is simply modified by the TrEC corrections according to

$$\Delta\tau_i^k = \left(\Phi^k(t_i) - \Phi^k(t_{i-1})\right) + \left(\Delta\hat{\rho}^k(t_i) - b_{PCBw}\right) \tag{8.1}$$

In other words, this addition of TrEC corrections, minus the filter bias, may steer the DCO of the primary DLL. This may reduce the maximum tracking excursions of the DLL due to multipath or thermal noise. Accordingly, it may help further reduce the maximum pseudorange errors expected to result from CCS. (Recall that CCS decreases the bias errors on the TrEC-corrected pseudoranges at the expense of increased variances on these ranges.) If properly designed, a "TrEC-assisted DLL" may also be less likely to lose lock in high-multipath or high-interference environments.

Carrier Phase Multipath Invariance

A natural extension to the MPI concept applied to code multipath mitigation would be to find a similar or complimentary property for the carrier phase. Although carrier phase multipath is substantially smaller than code phase multipath, in many high-accuracy, differential applications (e.g., attitude determination) this multipath remains a significant source of error. Note that since the carrier cycles are not pseudorandom in nature, and have an extremely short period, there is not direct analog between the code and carrier MPI concepts.

Appendix A:

Additional Tests Supported by SQM2b Correlators

The 11 standard tests for SQM2b described in Chapter 4, Section 4.6 may be supplemented by additional tests to improve steady state EWF detection performance. To this end, 35 new tests were developed. These include one additional delta test, 15 asymmetric ratio tests, ten linear fit parameter tests, and nine parabolic fit parameter tests. This appendix lists each of these in Section A.1. Section A.2 discusses results obtained from using the tests together to improve the steady state SQM performance of SQM2b discussed in Chapter 4.

A.1 Formulations of New Tests

The EWF detection tests are simple algebraic expressions of the correlator measurements. They propose to detect EWF-induced distortions of the correlation peak in the presence of nominal (ambient) noise and multipath. Recall from Section 4.1.2 of Chapter 4 that Δ-tests are samples of the in-phase measurements of the correlation peak computed according to

$$\Delta_m = \frac{\tilde{I}_{early,m} - \tilde{I}_{late,m}}{2 \cdot \tilde{I}_{prompt}} \tag{A.1}$$

where $\tilde{I}_{early,m}$, $\tilde{I}_{late,m}$, and $\tilde{I}_{prompt}$ correspond to the filtered correlator values for (Early and Late) correlator pair *m*, respectively. Similarly, ratio tests are given for all individual early and late correlator values as

$$\mathrm{R}_{avg,\,P} \equiv \frac{I_{early} + I_{late}}{2 \cdot I_{prompt}} \tag{A.2}$$

The original 11 SQM2b tests for steady state EWF detection include the following tests:

- Two Δ-tests: $\Delta_{\pm 0.075,\,\pm 0.05}$, and $\Delta_{\pm 0.1,\,\pm 0.05}$
- Three average ratio tests (ratio of mean of Early and Late correlator values to prompt): $R_{\pm 0.05av,P}$, $R_{\pm 0.075av,P}$, and $R_{\pm 0.075av,P}$
- Three negative ratio tests (ratio of Early correlator value to Prompt): $R_{-0.05,P}$, $R_{-0.075,P}$, $R_{-0.1,P}$
- Three positive ratio tests (ratio of Late correlator value to Prompt): $R_{+0.05,P}$, $R_{+0.075,P}$, $R_{+0.1,P}$

The SQM2b observables, however, may combine to compute arbitrary EWF detection metrics. Provided the MDEs are computed as described in Section 4.2 of Chapter 4, and those (test-specific) MDEs are sufficiently small relative to their respective EWF detection output, these new tests may be used to improve the detection capability of SQM2b. Using the SQM2b measurements, 35 new tests were created based on the Δ-test and ratio test kernels.

Each of these additional tests are characterized as follows:

- One Δ-test:

- $\Delta_{0.15,0.2}$

- 15 asymmetric ratio tests (Prompt correlator not used)

$$\left\{\begin{array}{ccc} R_{-0.1,-0.05} & R_{-0.1,-0.075} & R_{-0.05,-0.075} \\ R_{+0.1,+0.05} & R_{+0.1,+0.075} & R_{+0.05,+0.075} \\ R_{-0.1,+0.05} & R_{-0.1,+0.075} & R_{-0.1,+0.1} \\ R_{-0.075,+0.075} & R_{-0.075,+0.075} & R_{-0.075,+0.1} \\ R_{-0.05,+0.05} & R_{-0.05,+0.075} & R_{-0.05,+0.1} \end{array}\right\}$$

- 10 linear fit metrics (one linear fit—with five total parameters—on each side)

  - $\xi_1, \xi_2, \xi_3, \xi_4$

  - $\hat{R}_{+0.05,P}, \hat{R}_{+0.075,P}, \hat{R}_{+0.1,P}, \hat{R}_{-0.05,P}, \hat{R}_{-0.075,P}, \hat{R}_{-0.1,P}$

$\xi_1, \xi_2, \xi_3, \xi_4$ are obtained by solving the following relation (using least-squares)

$$\begin{bmatrix} 0.05 & 1 \\ 0.075 & 1 \\ 0.1 & 1 \end{bmatrix} \begin{bmatrix} \xi_1 \\ \xi_0 \end{bmatrix} = \begin{bmatrix} R_{+0.05,P} \\ R_{+0.075,P} \\ R_{+0.1,P} \end{bmatrix} \tag{A.3}$$

and

$$\begin{bmatrix} -0.05 & 1 \\ -0.075 & 1 \\ -0.1 & 1 \end{bmatrix} \begin{bmatrix} \xi_3 \\ \xi_4 \end{bmatrix} = \begin{bmatrix} R_{-0.05,P} \\ R_{-0.075,P} \\ R_{-0.1,P} \end{bmatrix} \tag{A.4}$$

$\hat{R}_{+0.05,P}, \hat{R}_{+0.075,P}, \hat{R}_{+0.1,P}, \hat{R}_{-0.05,P}, \hat{R}_{-0.075,P}$, and $\hat{R}_{-0.1,P}$ are smoothed estimates of the time-averaged, single-side ratios (the right-hand-side vectors in Equations (A.3) and (A.4) above). These are given by

$$\begin{bmatrix} \hat{R}_{+0.05,P} \\ \hat{R}_{+0.075,P} \\ \hat{R}_{+0.1,P} \end{bmatrix} = \begin{bmatrix} 0.05 & 1 \\ 0.075 & 1 \\ 0.1 & 1 \end{bmatrix} \begin{bmatrix} \xi_1 \\ \xi_0 \end{bmatrix} \tag{A.5}$$

and

$$\begin{bmatrix} \hat{R}_{+0.05,P} \\ \hat{R}_{+0.075,P} \\ \hat{R}_{+0.1,P} \end{bmatrix} = \begin{bmatrix} -0.05 & 1 \\ -0.075 & 1 \\ -0.1 & 1 \end{bmatrix} \begin{bmatrix} \xi_3 \\ \xi_4 \end{bmatrix} \tag{A.6}$$

- Nine parabolic fit metrics
  - ξ_5, ξ_6, ξ_7
  - $\breve{R}_{+0.05,P}$, $\breve{R}_{+0.075,P}$, $\breve{R}_{+0.1,P}$, $\breve{R}_{-0.05,P}$, $\breve{R}_{-0.075,P}$, $\breve{R}_{-0.1,P}$

ξ_5, ξ_6, ξ_7 are obtained by solving the following relation (using least-squares)

$$\begin{bmatrix} (0.1)^2 & -0.1 & 1 \\ (0.075)^2 & -0.075 & 1 \\ (0.05)^2 & -0.05 & 1 \\ 0 & 0 & 1 \\ (0.05)^2 & +0.05 & 1 \\ (0.075)^2 & +0.075 & 1 \\ (0.1)^2 & +0.1 & 1 \end{bmatrix} \begin{bmatrix} \xi_5 \\ \xi_6 \\ \xi_7 \end{bmatrix} = \begin{bmatrix} R_{-0.1,P} \\ R_{-0.075,P} \\ R_{-0.05,P} \\ 1 \\ R_{+0.05,P} \\ R_{+0.075,P} \\ R_{+0.1,P} \end{bmatrix} \tag{A.7}$$

$\breve{R}_{+0.05,P}$, $\breve{R}_{+0.075,P}$, $\breve{R}_{+0.1,P}$, $\breve{R}_{-0.05,P}$, $\breve{R}_{-0.075,P}$, and $\breve{R}_{-0.1,P}$ are smoothed estimates of the time-averaged single-side ratios (the right-hand-side vectors in Equation (A.7) above). These are given by

$$\begin{bmatrix} \breve{R}_{-0.1,P} \\ \breve{R}_{-0.075,P} \\ \breve{R}_{-0.05,P} \\ \breve{R}_{+0.05,P} \\ \breve{R}_{+0.075,P} \\ \breve{R}_{+0.1,P} \end{bmatrix} = \begin{bmatrix} (0.1)^2 & -0.1 & 1 \\ (0.075)^2 & -0.075 & 1 \\ (0.05)^2 & -0.05 & 1 \\ (0.05)^2 & +0.05 & 1 \\ (0.075)^2 & +0.075 & 1 \\ (0.1)^2 & +0.1 & 1 \end{bmatrix} \begin{bmatrix} \xi_5 \\ \xi_6 \\ \xi_7 \end{bmatrix} \tag{A.7}$$

A.2 Steady-State SQM Performance of SQM2b Using All Detection Tests

MDEs were found for each of these new tests using the methods defined in Chapter 4 for these tests and the SU MDE data. (Note that these MDEs still presume a gaussian distribution for the test statistics.) The results of applying all of these tests together (in addition to the original 11 SQM2b Δ and ratio tests) are summarized in the figures below. Figure A-1 through A-24 plot the E-L and ΔΔ contour plots for both two and three monitor receivers and elevation angles from 7.5° to 82.5° (in 15°-increments), resulting from TM A, TM B, and TM C.

Figure A-25 through A-30 provide the MERR comparison plots for both receiver types. Evident from these (ΔΔ, TM C) MERR comparison plots is the fact that the additional detection tests significantly improve performance, but still do not eliminate the need for the notch in the ΔΔ Region 2 design space. Note, however, that inspection of the contour plots indicates that a significant reduction in the size of the notch is made possible by these tests.

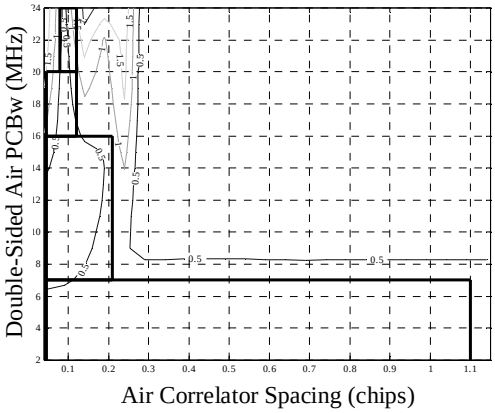

Figure A-1 E-L – TM C - 7.5°- Two Monitors (SQM2b, 11+35 Tests)

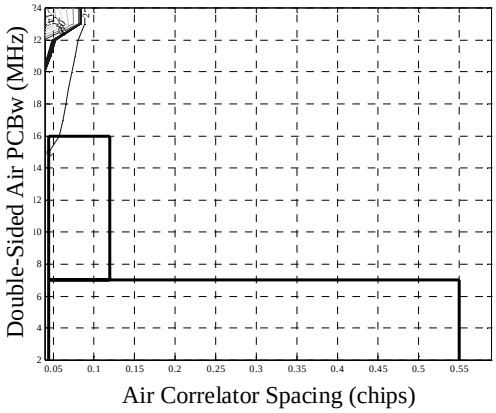

Figure A-4 ΔΔ – TM C - 7.5°- Two Monitors (SQM2b, 11+35 Tests)

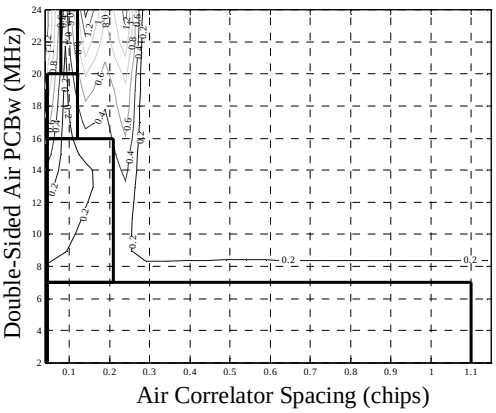

Figure A-2 E-L – TM C - 22.5°- Two Monitors (SQM2b, 11+35 Tests)

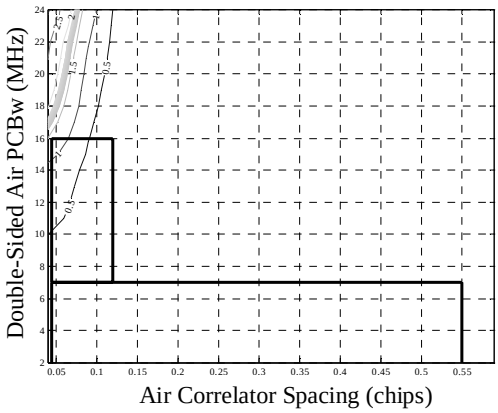

Figure A-5 ΔΔ – TM C - 22.5°- Two Monitors (SQM2b, 11+35 Tests)

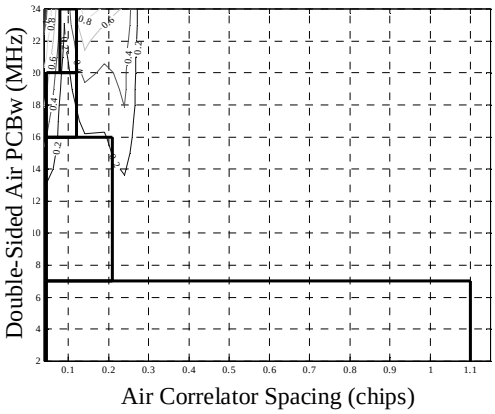

Figure A-3 E-L – TM C - 37.5°- Two Monitors (SQM2b, 11+35 Tests)

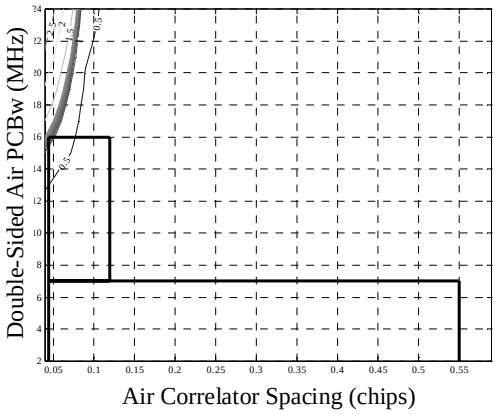

Figure A-6 ΔΔ – TM C - 37.5°- Two Monitors (SQM2b, 11+35 Tests)

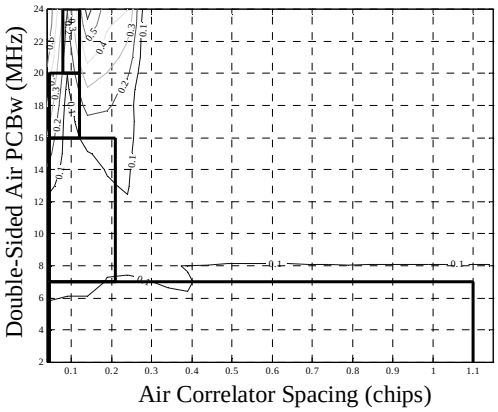

Figure A-7 E-L – TM C - 52.5°- Two Monitors (SQM2b, 11+35 Tests)

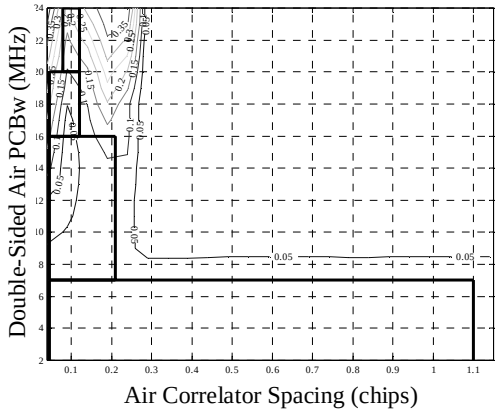

Figure A-8 E-L – TM C - 67.5°- Two Monitors (SQM2b, 11+35 Tests)

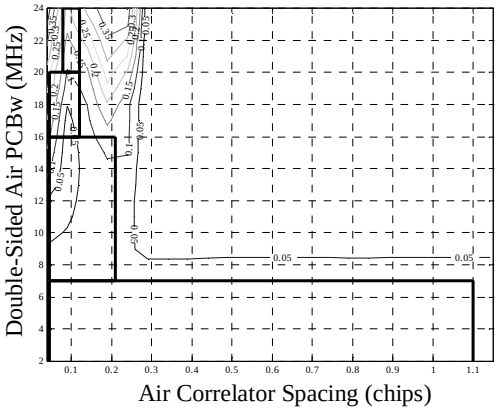

Figure A-9 E-L – TM C - 82.5°- Two Monitors (SQM2b, 11+35 Tests)

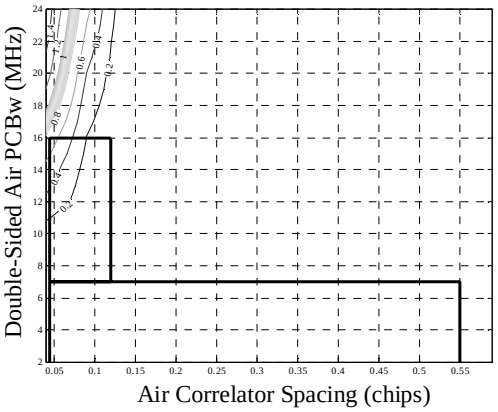

Figure A-10 ΔΔ – TM C - 52.5°- Two Monitors (SQM2b, 11+35 Tests)

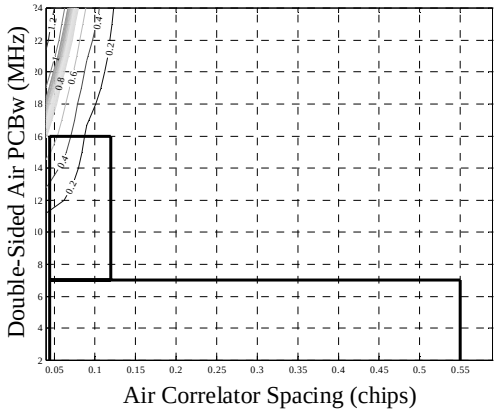

Figure A-11 ΔΔ – TM C - 67.5°- Two Monitors (SQM2b, 11+35 Tests)

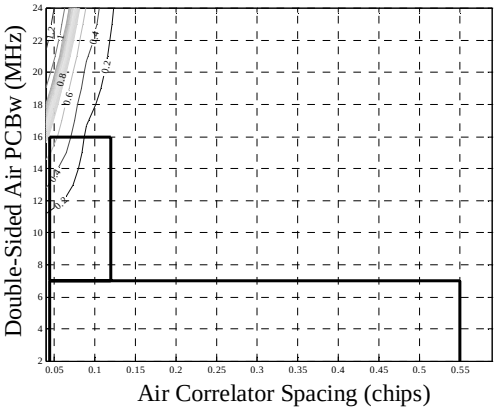

Figure A-12 ΔΔ – TM C - 82.5°- Two Monitors (SQM2b, 11+35 Tests)

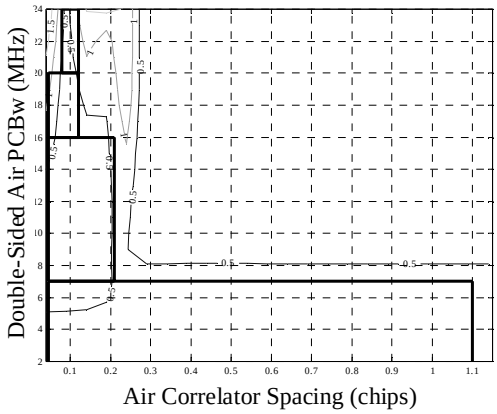

Figure A-13 E-L – TM C - 7.5°- Three Monitors (SQM2b, 11+35 Tests)

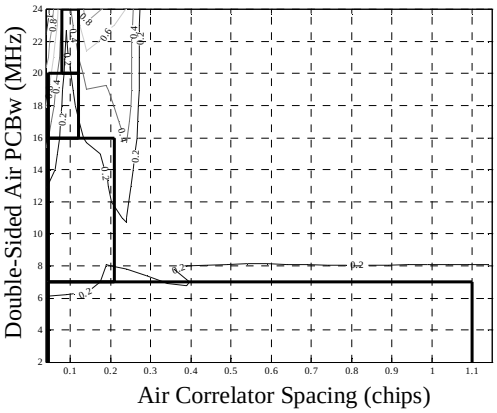

Figure A-14 E-L – TM C - 22.5°- Three Monitors (SQM2b, 11+35 Tests)

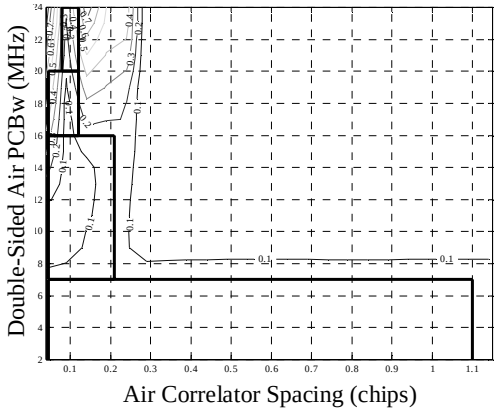

Figure A-15 E-L – TM C - 37.5°- Three Monitors (SQM2b, 11+35 Tests)

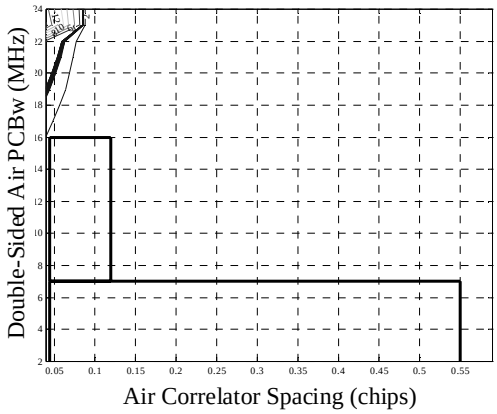

Figure A-16 ΔΔ – TM C - 7.5°- Three Monitors (SQM2b, 11+35 Tests)

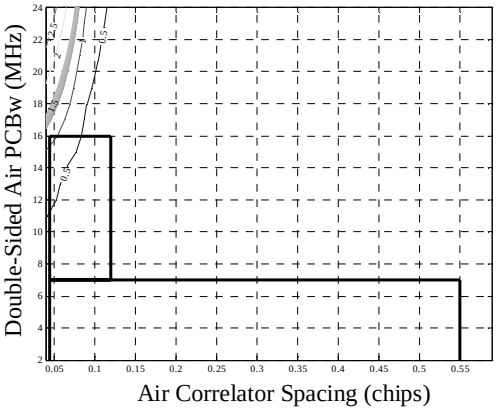

Figure A-17 ΔΔ – TM C - 22.5°- Three Monitors (SQM2b, 11+35 Tests)

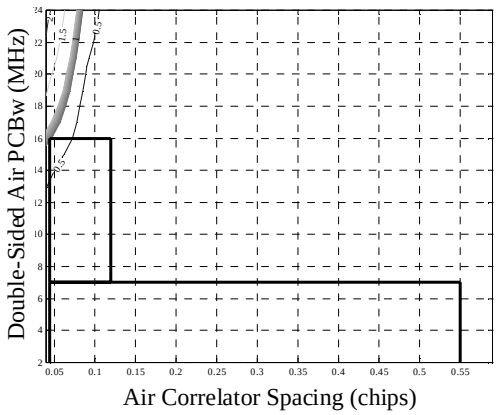

Figure A-18 ΔΔ – TM C - 37.5°- Three Monitors (SQM2b, 11+35 Tests)

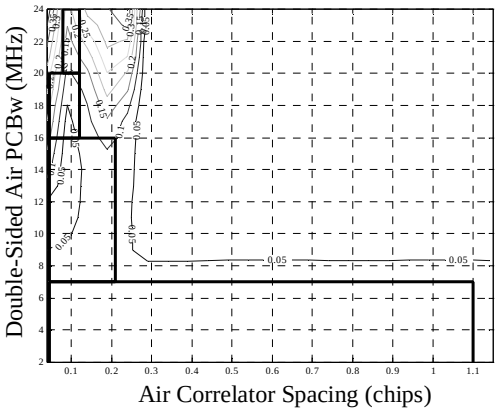

Figure A-19 E-L – TM C - 52.5°- Three Monitors (SQM2b, 11+35 Tests)

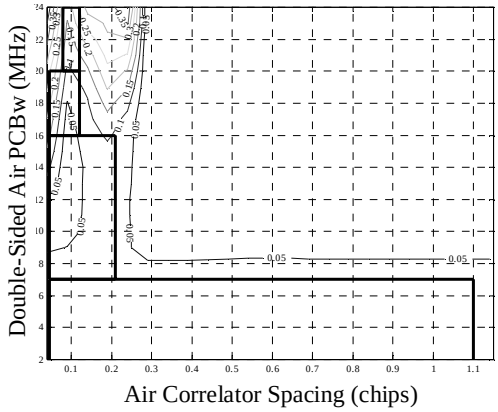

Figure A-20 E-L – TM C - 67.5°- Three Monitors (SQM2b, 11+35 Tests)

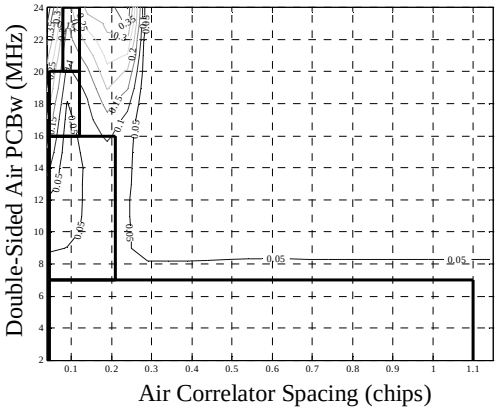

Figure A-21 E-L – TM C - 82.5°- Three Monitors (SQM2b, 11+35 Tests)

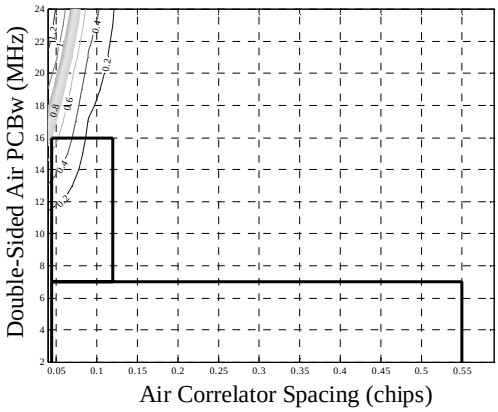

Figure A-22 ΔΔ – TM C - 52.5°- Three Monitors (SQM2b, 11+35 Tests)

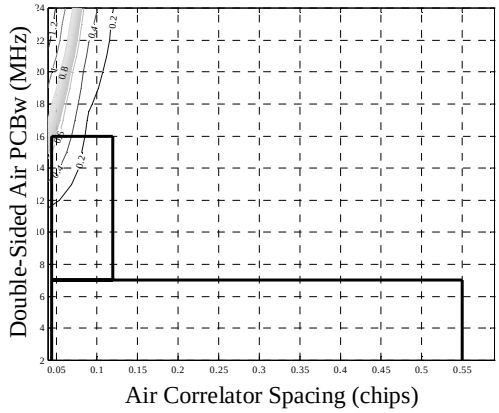

Figure A-23 ΔΔ – TM C - 67.5°- Three Monitors (SQM2b, 11+35 Tests)

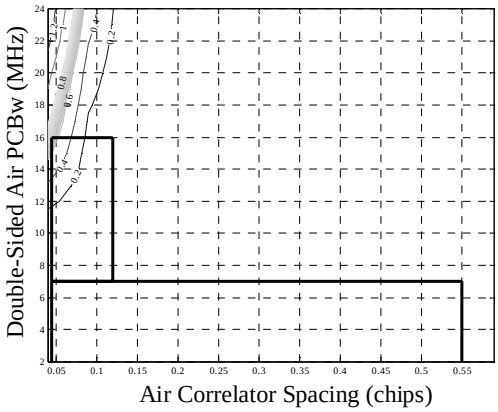

Figure A-24 ΔΔ – TM C - 82.5°- Three Monitors (SQM2b, 11+35 Tests)

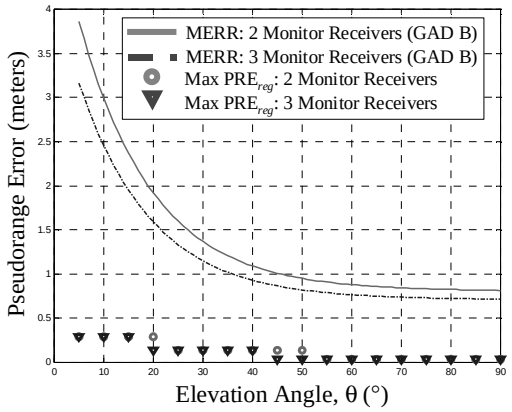

Figure A-25 E-L – TM A (SQM2b, 11+35 Tests)

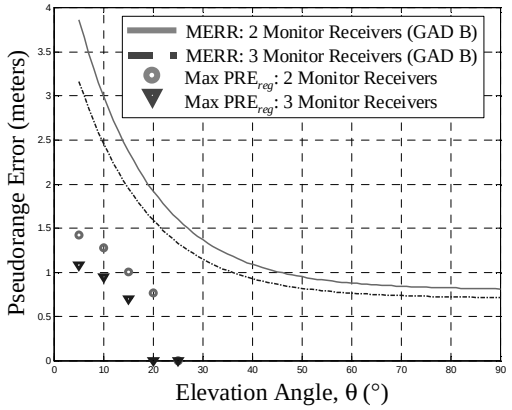

Figure A-26 E-L – TM B (SQM2b, 11+35 Tests)

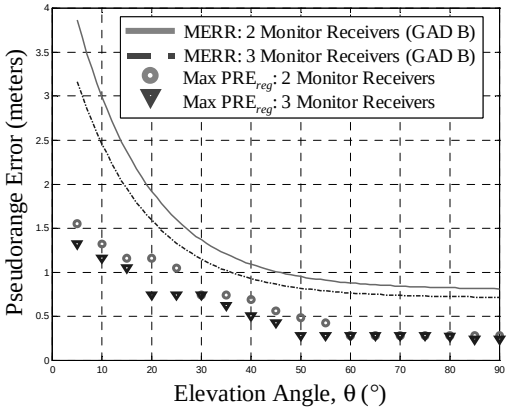

Figure A-27 E-L – TM C (SQM2b, 11+35 Tests)

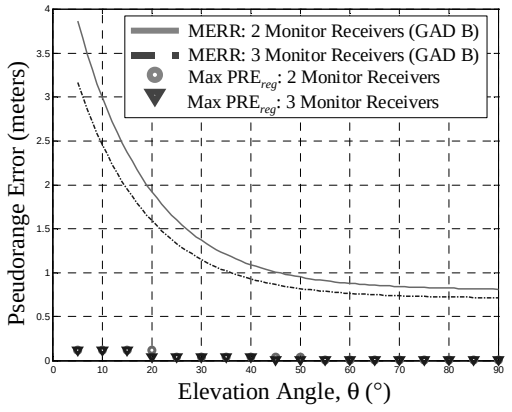

Figure A-28 ΔΔ – TM A (SQM2b, 11+35 Tests)

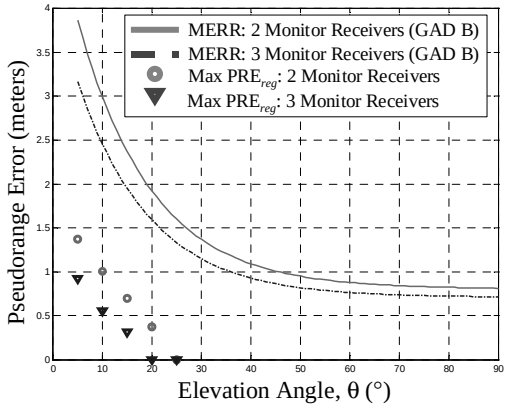

Figure A-29 ΔΔ – TM B (SQM2b, 11+35 Tests)

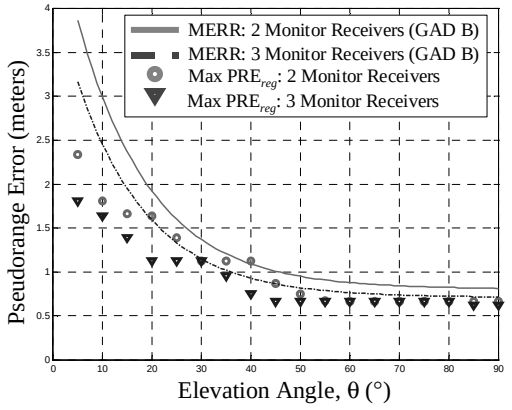

Figure A-30 ΔΔ – TM C (SQM2b, 11+35 Tests)

Appendix B:

Monitor Precorrelation Filter Considerations for Improved SQM Performance

Much of the LAAS SQM analysis assumed a 6^{th}-order Butterworth precorrelation filter for both the ground monitor receiver and the airborne user receiver. The group delay and magnitude response analyses extended these results by including an FIR (zero-dT$_{Gd}$) monitor (ground) filter and a varying magnitude response and group delay for the user (airborne) filter. This implies that SQM2b has been validated for arbitrary airborne E-L and $\Delta\Delta$ configurations and filter implementations with group delay variations less than or equal to 150ns. Accordingly, SQM2b has effectively validated two single ground filter implementations—the 6^{th}-order Butterworth and the 300-tap Hamming Window (FIR).

This appendix examines the effect of modifying the ground monitor filter characteristics to achieve better EWF detection capabilities. This may be the best way to meet the more stringent Category II and Category III precision approach requirements on MERR. Section B.1 describes the filter characteristics of interest. Section B.2 proposes a new design to detect more EWFs. Section B.3 demonstrates that performance of this new design—in

tandem with the expected Multipath Limiting Antenna (MLA) technology—may help meet GAD C MERR requirements.

B.1 Airborne and Monitor Precorrelation Filter Design Considerations

The user differential PREs are sensitive to airborne filter characteristics in the transition band. (The transition band is the "roll-off" region between f_{3dB} and a designated "stopband" frequency where the magnitude response must be below some specified level.) They are somewhat less sensitive to $d\mathrm{T}_{Gd}$ variations of the airborne precorrelation filters. However, a monitor receiver's detection capability may also be sensitive to variations in front-end filter magnitude response and group delay in addition to magnitude response, however. Intuitively, the $d\mathrm{T}_{Gd}$ should be kept as small as possible, so the EWF distortions—normally largest at the correlation peak—do not move away from the monitor correlator pairs. Recall that the monitor pairs (e.g., the SQM2b configuration) generally reside at the peak of the correlation function.

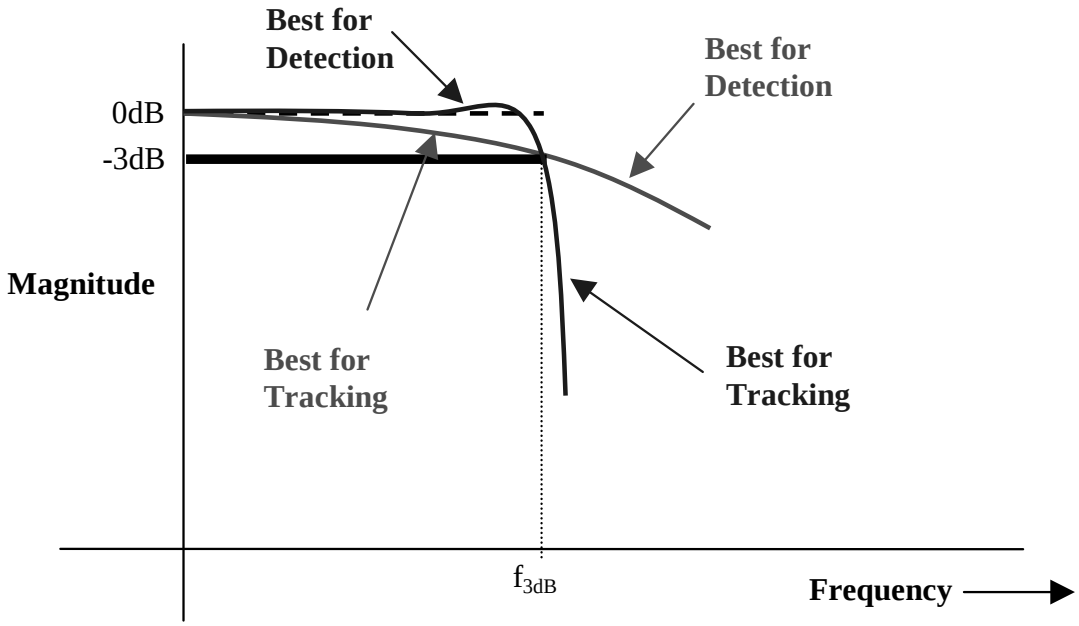

Figure B-1 Best Precorrelation Filter Magnitude Responses for Robust EWF Detection and Mitigation

Figure B-1 qualitatively illustrates a “rule of thumb” for the best SQM monitor (and airborne) filter magnitude responses. The “best” precorrelation filter for the monitor would attenuate the EWF frequencies the least—yet still meet the LAAS interference requirement. This ensures that the correlation peak will be maximally distorted by the EWF, and hence more easily detected. Conversely, the airborne filter that results in the smallest PREs should provide more attenuation of the EWF frequencies.

Note that these are “rules of thumb” only. Magnitude and group delay variations of the monitor filter affect which EWFs the monitor can detect. They also affect the “quality” of the differential pseudorange corrections sent to the airborne users. In order to design a monitor filter more suited for SQM2b, this appendix more rigorously examines these considerations coupled with those for the various airborne receiver configurations. (Note, however, that filter implementation (i.e., manufacturing) tolerances could also become critical in some cases. This section does not examine these sensitivity issues.)

B.2 A Better Monitor Filter Design

Ideally, a monitor filter would have linear phase (zero $d\mathrm{T}_{\mathrm{Gd}}$) and exactly meet the LAAS interference requirement for magnitude response. The following analysis constructs an SQM precorrelation filter with these goals in mind. Figure B-2 shows—in postcorrelation—the suite of filters previously discussed in Section 4.6.3 of Chapter 4. The FIR filter depicted there is the 300-tap Hamming window. Recall that the ground monitor (and the differential correction reference) receiver implemented this filter to analyze user $d\mathrm{T}_{\mathrm{Gd}}$ variations. Beside this figure, Figure B-3 shows a (postcorrelation) 100-tap Hamming window FIR filter response (compared only to the 6^{th}-Order Butterworth response curve).

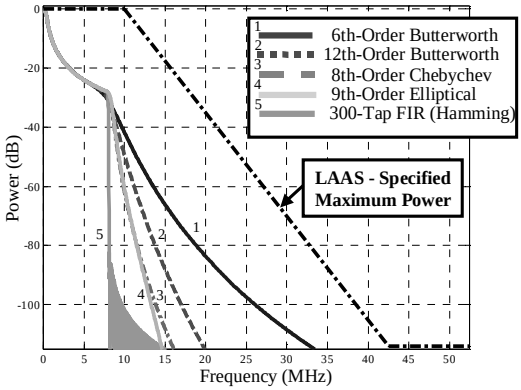

Figure B-2 Various Filter Magnitude Responses (300-tap FIR has Fastest Response)

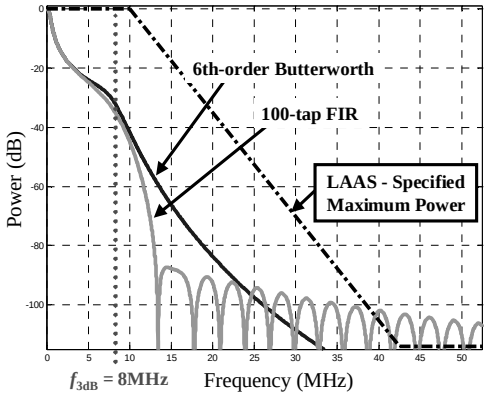

Figure B-3 Various Filter Magnitude Responses (100-tap FIR has Fastest Response)

The transition band magnitude response of this filter is quite different from that of the 300-tap FIR. Below 13MHz—the maximum EWF frequency (f_d) of TM C—it almost becomes as large as the 6th-Order Butterworth curve. Also note that this design actually does violate a small portion of the LAAS magnitude specification at and above 40MHz (below -100dB). This relatively small violation does not affect the present analysis. However, in practice, this filter would require additional design refinements (e.g., additional taps).

B.3 MERR Analysis Results: GAD C

Use of the relaxed-transition bandwidth FIR filter provides noticeable improvements in EWF detection capabilities where it is most needed—at high elevation angles. Below, Figure B-4 shows the result from the 35 additional detection tests (plus the original 11 of Chapter 4) described in Appendix B for a ΔΔ correlator receiver subjected to TM C EWFs. Note that the two and three maximum regional PREs (above approximately 40°) come relatively close to the GAD B MERRs. By contrast, Figure B-5 shows the same plot for the case where the ground monitor (and correction filters) has been replaced with the 100-FIR filter. Observe that in this case the maximum regional PREs (for both two and three monitor receivers) above 35° meet the GAD C MERR requirements.

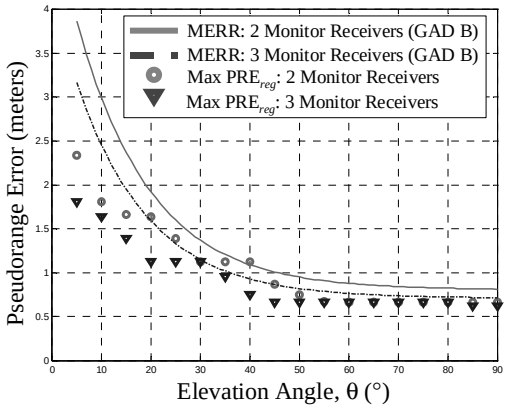

Figure B-4 GAD B – 300-tap FIR – SQM2b (Using Extra Detection Metrics of Appendix A)

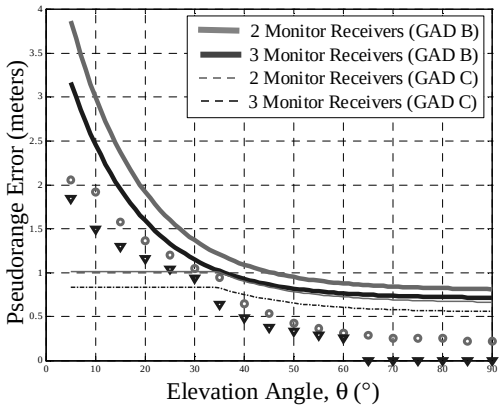

Figure B-5 GAD C – 100-tap FIR – SQM2b (Using Extra Detection Metrics of Appendix A)

Low Elevation Angle MERRs and the Multipath Limiting Antenna (MLA)

The MLA provides effective mitigation for multipath incident from ground reflections. It accomplishes this by utilizing a special high-gain (dipole) antenna directed at the horizon, which has a sharp gain pattern cutoff for signals arriving from angels less than 0°. This antenna is coupled to a second antenna (a helibowl antenna) that is trained on the sky. This antenna provides high-gain for high elevation satellite signals. By knowing the approximate location of the satellites, the receiver transitions between the signals processed by each antenna, between approximately 35°-45°. These angles are, accordingly, the "critical angles" for the MLA.

Assuming the MLA cannot provide any additional mitigation capability above 35°, Figure B-5 indicates that the GAD C MERR requirements at high elevation angles can be met by modifying the precorrelation filter characteristics as described above. Figure B-5 also indirectly reveals the MDE reduction requirements on the MLA. To meet the Category II and III requirements for SQM, in general, *the MLA-improved MDEs must always be less than or equal to the 35° SU MDEs*. This means that the MLA must reduce the 5°-35° MDEs by 70% or more.

Appendix C:

SQM for the Wide Area Augmentation System

C.1 Introduction

Similar to the steady state SQM analysis performed for LAAS in Chapters 3 and 4, the Wide Area Augmentation System (WAAS), too, requires SQM to guarantee user integrity against the threat of EWFs. This appendix addresses the steady-state WAAS problem and analysis methodology.

Section C.2 describes a pair of models that readily explain the observations that were made at the time of the SV19 failure, and are computationally tractable. The first model has been adopted by the International Civil Aviation Organization (ICAO) and is described in the draft Standards and Recommended Practices (SARPS). Chapter 3 discussed this model in detail. We call this first model the *full ICAO model*. The second model is a subset of the first, but encloses the most likely subset or subspace of signal failures. It includes the PRN19 failure and the surrounding neighborhood in the signal space. Consequently, we call it the *most likely model*. Section 3.6 of Chapter 3 developed closed form expressions for the anomalous correlation functions that result from either model. These have been used

to greatly speed the calculations required by Sections C.3 through C.5. All figures are at the end of this appendix.

Section C.3 calculates the worst pseudorange errors suffered by an airborne receiver that conforms to the ICAO SARPS when no signal quality monitor is used by WAAS to detect anomalous signals. This analysis subjects the victim avionics to all of the waveforms in the most likely model. Such a conservative approach is warranted even though WAAS contains a signal quality monitor, because the Phase I SQM is partially housed in Level D software. Consequently, we take no safety credit for its function against the most likely threats.

Section C.3 also plots the worst pseudorange errors against two key design parameters for the avionics. It finds that these errors are acceptably small compared to the maximum errors (MERRs) that an aircraft conducting an LNAV/VNAV approach can tolerate. Specifically, the pseudorange errors that result from the most likely threats are all smaller than 4 meters, and the remainder of the Phase I errors are always greater than 4.8 meters.

Section C.4 studies the performance of the Level D SQM against the full ICAO threat model. This simple SQM compares the range measurements made by reference receivers operating at two different locations on the correlation peak. One reference receiver uses a correlator spacing of 0.1 and the other uses a correlator spacing of 0.15, and so they are called the narrow and wide receivers respectively. Three narrow and three wide receivers are contained in each WAAS reference station (WRS). Both receivers have double sided pre-correlator bandwidths of approximately 16 MHz.

The performance of any SQM is sensitive to the nominal effects of noise, interference and multipath. These ever-present effects will cause the test statistics to vary randomly and the test threshold must be chosen so that the false alarm rate is acceptably small. We make no attempt to derive these limits in this paper. Rather, we use the minimum detectable errors (MDEs) that have been measured by [Akos00a] while analyzing the local area augmentation system (LAAS). For rising satellites, we use a margin of 100% to account for uncertainties in the actual WAAS reference measurements. For high satellites, we use no

margin relative to the measurements of Akos, but we take no credit for the long averaging times enabled by dual frequency carrier smoothing.

Section C.5 computes the aircraft pseudorange error due to the anomalies from the full ICAO model that are not detected by our Level D SQM. The worst case errors are calculated across the acceptable design parameters for the avionics. These errors are tabulated and compared to the confidences dictated by the other error sources. The comparison is favorable. Specifically, the largest pseudorange error due to an undetected signal anomaly on a rising satellite is approximately 8 meters. At the same time, the tolerable error is approximately 28 meters for low satellites, because the confidence placed on the corrections for the ionosphere, satellite clock and satellite ephemeris is quite low. For high elevation satellites, the largest pseudorange error is much smaller than the 4.8 meters minimum due to other Phase I error sources.

Section C.6 summarizes the results and presents several conclusions from this analysis.

The approach is summarized in Figure C-1, which shows the most likely threat model interior to the full ICAO threat model. The avionics errors due to the most likely threats are computed when no SQM is used. The avionics errors due to the full ICAO model are computed with the benefit of the Level D SQM.

C.2 A Pair of Threat Models Based on the ICAO Model

In this section, we introduce our preferred threat models for the WAAS SQM investigation—the *full ICAO model* and the *most likely model*. As described in Section C.1, the full ICAO model is so named, because it has been adopted by the International Civil Aviation Organization (ICAO) and is described in the draft Standards and Recommended Practices (SARPS). The most likely model is a subset of the first, but encloses the most likely subset or subspace of signal failures. It includes the PRN19 failure and the surrounding neighborhood in the signal space.

As described below, the full ICAO model includes the three Threat Models A, B and C as described in Chapter 3. In contrast, the most likely model only includes Threat Models A and C, and the parameter ranges for these are smaller than for the full ICAO model. Table C-1 summarizes the relationships between these pieces.

	Full ICAO Model	Most Likely Model
Threat Model A: Lead/Lag Only	$-0.12 \le \Delta \le 0.12$	$-0.04 \le \Delta \le 0.04$
Threat Model B: Amplitude Modulation Only	$\Delta = 0$ $4 \le f_d \le 17$ $0.8 \le \sigma \le 8.8$	None
Threat Model C: Lead/Lag Plus Amplitude Modulation	$-0.12 \le \Delta \le 0.12$ $7.3 \le f_d \le 13$ $0.8 \le \sigma \le 8.8$	$-0.04 \le \Delta \le 0.04$ $9.0 \le f_d \le 11.0$ $1.8 \le \sigma \le 7.8$

Table C-1 Summary of Threat Models and Parameters

C.2.1 Threat Model A: Lead/Lag Only

The proposed ranges for the TM A parameters are noted in Table C-1. Observe that the most likely Threat Model A truncates the lead/lag parameter at $|\Delta| > 0.04$, because the actual PRN19 failure showed smaller leads and lags. Chapter 3 derives the correlation function for Threat Model A.

C.2.2 Threat Model B: Amplitude Modulation Only

Table C-1 lists the allowable ranges for EWF parameters in Threat Model B. Note that although PRN19 did exhibit amplitude modulation, the most likely threat model does not include Threat Model B, because Threat Model C is a better description of the PRN19 data.

C.2.3 Threat Model C: Lead/Lag and Amplitude Modulation

This model includes all three parameters described above, again shown in Table C-1. The most likely threat model C limits the lead/lag parameter to $|\Delta| \le 0.04$, because the data for PRN19 indicates that the magnitude of this parameter never grew larger than 0.03. It also

limits the range for f_d and σ, because the PRN19 data could be modeled as ringing at f_d=10 MHz with σ in the indicated range.

C.2.4 Threat Model Summary

These proposed Threat Models are fairly simple with only three parameters. Indeed, all of the threat waveforms can be envisaged as points within a cube that we will refer to as the threat space or threat cube. Figure C-2 provides a geometrical summary of the full ICAO threat model and the most likely threat model. Section C.3 computes the pseudorange errors due to waveforms in the most likely threat model when no signal quality monitoring is used. Section C.4 describes the SQM that resides in the Level D software, and shows how to identify the waveforms within the full ICAO threat model that are detected by this SQM. Section C.5 calculates the airborne errors due to the undetected points in the full ICAO threat model.

C.3 Aircraft Pseudorange Errors Due to the Most Likely Threat Model

We now subject the aircraft receiver to the waveforms from our most likely threat subset. We assume that the aircraft does not have the benefit of any signal quality monitoring on the ground. In short, it is exposed to every point in the most likely Threat Model, because the Phase I SQM does include some Level D software and so we should not assume that it will protect against the most likely threats. The points in the most likely threat model A are denoted $\{\Delta_n\}\big|_{n=1}^{N_A}$, where each element unambiguously identifies a signal with anomalous lead or lag. The points in the most likely Threat Model C are denoted $\{(\sigma, f_d, \Delta)_n\}\big|_{n=1}^{N_C}$, where each triplet unambiguously identifies an anomalous signal. The aircraft pseudorange error is computed for each point in these sets as defined in Equations (4.1) and (4.2) in Chapter 4.

As analyzed for the (steady state) LAAS SQM analysis, this study models the pre-correlator filter used by the ground system as a sixth order Butterworth filter with a (double-sided) 3dB bandwidth of 8MHz. This is a close approximation to the filter used by

the WAAS reference receiver. Also identical to the LAAS SQM investigations, the bandwidth of the aircraft filter is allowed to vary within the constraints allowed by the ICAO SARPS. The aircraft filter type is a sixth order Butterworth filter since, as shown in Chapter 4, this aircraft filter is probably the worst case amongst those types that are allowed by the SARPS.

The resulting aircraft pseudorange errors (maximum PRE contour plots) are plotted in Figures C-3 though C-14. Again, the heavy lines are the boundaries on the airborne correlator spacings and bandwidths that are allowed by the ICAO SARPS. Figure C-3 through C-5 are for the most likely Threat Model A when applied to avionics that use an early-minus late discriminator. Figure C-6 through C-8 are for the same threat model applied to avionics that use a double delta discriminator. The ICAO SARPS allow either type of discriminator, but the allowable range of correlator spacings and bandwidths are not the same for the two types. Notice that the heavy lines in Figure C-3 through C-5 are in different places than the heavy lines for Figure C-6 through C-8. Figure C-9 through C-11 are for the E-L discriminator under the influence of the most likely TM C, and Figure C-12 through C-14 are for the double delta discriminator when subjected to the most likely TM C.

Three reference correlator spacings are used in the figures. They are 0.1, 0.2 and 0.3. In fact, the WAAS reference receiver includes a Multipath Estimating Delay Lock Loop (MEDLL) that employs these spacings plus others. Rather than simulate the operation of the MEDLL in the presence of these signal perturbations, we assume that the worst case across spacings of 0.1, 0.2 and 0.3 will bound the true pseudorange error.

The results are summarized in Table C-2. The final column shows the maximum pseudorange error across all the threat waveforms *and* all the allowable correlator spacings and bandwidths. As shown, the pseudorange error never exceeds 4.0 meters when we consider the worst case with respect to:

- all the waveforms in the most likely Threat Model A

- all the waveforms in the most likely Threat Model C
- all the air correlator spacings allowed by the SARPS
- all the airborne bandwidths allowed by the SARPS
- both discriminator types allowed by the SARPS.

Figure	Reference Spacing (All reference bandwidths are 8 MHz)	Most Likely Threat Model A or C	Avionics Discriminator (Early Minus Late or Double Delta)	Maximum Avionics Pseudorange Error (meters)
C-3	0.1	A	E-L	<0.5
C-4	0.2	A	E-L	<0.4
C-5	0.3	A	E-L	<0.6
C-6	0.1	A	ΔΔ	<0.3
C-7	0.2	A	ΔΔ	<0.4
C-8	0.3	A	ΔΔ	<0.6
C-9	0.1	C	E-L	<3.0
C-10	0.2	C	E-L	<3.0
C-11	0.3	C	E-L	<3.5
C-12	0.1	C	ΔΔ	<4.0
C-13	0.2	C	ΔΔ	<4.0
C-14	0.3	C	ΔΔ	<4.0

Table C-2 Summary of Pseudorange Errors When No Signal Quality Monitoring is Used and the Threats are Drawn from the Most Likely Threat Model

The worst case pseudorange error of four meters means that no signal quality monitoring is required to protect Phase I WAAS users from the effects of signal anomalies that distort the correlation peak. The worst error due to signal anomalies will be dominated by other factors. Specifically, the Phase I vertical protection level (VPL) includes the term

$$5.33\sqrt{\sigma_{\mathrm{UDRE}}^2 + \left(F\sigma_{\mathrm{UIVE}}\right)^2} \qquad \text{(C.1)}$$

In this equation, σ^2_{UDRE} is the bounding variance due to errors in the satellite clock and ephemeris corrections. Similarly, σ_{UIVE} is the bounding standard deviation in the user's vertical error due to ionospheric delays after correction. *F* is the obliquity factor that maps the vertical error into the slant error. Finally, the factor 5.33 multiplies this bounding standard deviation out to the 10^{-7} level required for safety.

The quantity specified by (C.1) has been computed for 14 hours of data that was collected from the prototype WAAS on June 7, 2000. The resulting histograms are plotted in Figure C-15 over a coarse four by four grid of longitude and latitude within CONUS. This data set reveals that the quantity (C.1) never drops below 4.8 meters. It should be noted that, the true bound used by the avionics also includes terms due to local multipath, noise and tropospheric effects. Consequently, our results are conservative.

C.4 Level D Signal Quality Monitoring (SQM)

C.4.1 Information Flow for Phase I SQM

Phase I SQM is summarized in Figure C-16. As shown, it utilizes measurements from all three receiver types, i.e., wide (0.15 E-L), narrow (0.1 E-L) and the multipath estimating delay lock loop (MEDLL). Each of these is referred to as WAAS Reference Equipmnent (WRE). This data is used to develop statistics associated with differences in pseudorange observed by each type of receiver. SQM processing is accomplished in two locations within the WAAS architecture. The measurement statistics are computed at the reference receiver while the view across receivers is performed at the WAAS Master Station (WMS) in the WAAS Safety Processor (SP). (The SP is the only DO-178B Level B component in WAAS; there is one SP in the WMS and one in the uplink station for the geostationary satellite.)

WRE processing is conducted on a per satellite basis using pseudorange differences across the different receiver types. MEDLL and wide pseudorange measurements are corrected for inter-receiver/card biases (ICBias algorithm) prior to this processing. The WAAS reference receiver SQM algorithm computes pairwise pseudorange differences (M-N, N-

W, and M-W), edits these differences for outliers, and then processes them with a lag filter with a time constant of 900 seconds. The outputs of this filter are smoothed pairwise differences (WRE SV19 estimates) representing measurement biases across receiver types at this WRE. The WRE SV19 estimates are then sent to the WMS via Rate Group 3 (i.e., every 30 seconds).

WMS receives Rate Group 3 data from all WREs in PID (Level D—in the Corrections Processor (CP)), repackages the WRE SV19 estimates and forwards them to the Safety Processor's SQM. The SQM in the SP contains several processing criteria, such as the two WRS in view rule, valid UDRE, and minimum number of WRE SV19 estimates pre/post edit. If these criteria are satisfied, the monitor computes the mean and standard deviations of all remaining WRE SV19 estimates from both the primary and secondary threads. This mean estimate from each satellite/receiver type is then tested against a fixed threshold to determine whether an anomalous signal exists. If so, the UDRE value is increased.

The SQM performs some fault detection by keeping track of the number of WRE SV19 estimates at a particular WRE that fails a threshold test. If the number of failures exceeds a threshold, a message is sent via PID to fault the WRE. There is also additional SQM logic for carrier phase processing at both the WRE and Safety Processor. For Phase I WAAS, it is suggested that this carrier phase logic be ignored (or removed).

C.4.2 Tests Based on the Maximum Pseudorange Difference

The SQM tests described in this subsection only consider the wide-narrow pseudorange differences. As such, our results are conservative, because the wide-MEDLL and narrow-MEDLL measurements could reveal difficulties that the wide-narrow tests do not detect.

When the signal is nominal, the difference between the pseudorange measured using the 0.1 correlator spacing and the pseudorange from the 0.15 correlator spacing is denoted

$$\begin{aligned} \Delta\tau_{\text{nom}}(d_1 = 0.10, d_2 = 0.15) = \mu_{nm}^{j} = \tau_{\text{nom}}(d_1 = 0.10) - \tau_{\text{nom}}(d_2 = 0.15) \\ \tau_{\text{nom}}(d) = \arg_{\tau}\left\{\tilde{R}_{\text{nom}}(\tau + d/2) - \tilde{R}_{\text{nom}}(\tau - d/2) = 0\right\} \end{aligned} \tag{C.2}$$

In contrast, the $\Delta\tau_a(d_1 = 0.10, d_2 = 0.15)$ are the pseudorange differences measured in real-time while seeking an anomalous waveform. These test statistics are given by

$$\begin{aligned} \Delta\tau_a(d_1, d_2) &= \tau_a(d_1 = 0.10) - \tau_a(d_2 = 0.15) \\ \tau_a(d) &= \arg_{\tau}\left\{\tilde{R}_a(\tau + d/2) - \tilde{R}_a(\tau - d/2) = 0\right\} \end{aligned} \tag{C.3}$$

In these equations, the subscripts *nom* and *a* continue to denote nominal and anomalous correlation functions, respectively.

As described in the last subsection, Phase I SQM algorithms simply compare the pseudorange difference to its nominal value. If this measured difference exceeds a specified threshold, then the *UDRE* for that satellite is increased. In other words, the *UDRE* is increased if

$$\beta = \left|\Delta\tau_a(0.1,0.15) - \Delta\tau_{nom}(0.1,0.15)\right| \geq T_{osp} \tag{C.4}$$

For the analysis described in this report, β is compared to the *minimum detectable error* (MDE), which is not the test threshold itself. Rather, it is the minimum pseudorange error that can be detected with the specified probability of missed detection given that the threshold has been chosen to meet the false alarm rate when no anomalies are present.

The MDEs used in this study are developed in Table C-3 for two cases—a rising satellite and a satellite at 45 degrees elevation. In both cases, the MDEs are small, because both measurements are made on data from a common antenna and the samples are simultaneous. Simultaneous measurements made on signals from a common antenna will cause most of the error due to multipath to cancel. If the measurements used different antennas or were not simultaneous, then the MDEs could be much larger.

	Satellites at 5°-10° elevation (meters)	Satellites at 45° elevation (meters)
σ_{field} of β from ICAO field tests (Akos, Phelts and Enge, 2000)	6.2×10^{-4}	2.1×10^{-4}
σ_{sim} of β from Honeywell simulations (Brenner and Kline, 2000)	4.7×10^{-4}	Not available
$MDE_{field}=(K_{FFD}+K_{MD})\sigma_{field}$	5.2×10^{-3}	$.7\times10^{-3}$
$MDE_{sim}=(K_{FFD}+K_{MD})\sigma_{sim}$	3.9×10^{-3}	Not available
$MDE_{low}=2Max[MDE_{field},MDE_{sim}]$	$.0\times10^{-2}$	Not applicable
$\frac{MDE_{low}}{\sqrt{4}}$	0.5×10^{-2}	Not applicable
$MDE_{high}=Max[MDE_{field},MDE_{sim}]$	Not applicable	$.7\times10^{-3}$
$\frac{MDE_{high}}{\sqrt{20}}$	Not applicable	3.8×10^{-4}

Table C-3 MDE(0.1,0.15) Development

The table gives the standard deviations of the test statistic, β, from actual measurements made at Stanford University. For the rising satellite, it also gives the standard deviation from simulations conducted by Honeywell. As shown, the simulations show similar standard deviations to the real data. Moreover, many other field trials conducted at the time of the ICAO SQM deliberations confirm that these standard deviations are approximately correct.

The table multiplies σ_{field} and σ_{sim} by $K_{FFD}+K_{MD}$. The multiplication by K_{FFD} places the test threshold well above the normal variation of the test statistic, so the false alarm rate will be tolerable in the absence of any signal anomalies. The multiplication by K_{MD} places the minimum detectable error well above the test threshold to ensure that the probability of missed detection is very low.

The minimum detectable error for low elevation satellites, MDE_{low}, is twice the largest of MDE_{field} and MDE_{sim}. We multiply by two to account for the use of two separate receivers by WAAS SQM. The ICAO data was based on a single receiver with multiple correlator spacings per satellite. When one receiver is used, the nominal difference in the pseudorange difference is unlikely to change with environment or age. With two receivers, the threshold may have to be increased to account for such variations. Additionally, the thermal noise on

the wide correlator will not be correlated with the thermal noise on the narrow correlator. Thankfully, the thermal noise from both early correlators is strongly correlated with the thermal noise of both late correlators. Recall that the narrow and wide correlator spacings are 0.10 and 0.15, respectively.

The factor of two also accounts for WAAS reference sites that may be significantly noisier than the sites used during the ICAO validation process. The RMS pseudorange errors from the ICAO validation sites are well approximated by the ground accuracy designators denoted as GAD B1 in Figure C-17. The WAAS pseudorange errors are shown in Figure C-18. As shown, GAD B1 runs through the middle of the WAAS traces. Accordingly, we feel that a factor of two is appropriate for rising satellites.

Finally, the MDE for rising satellites is divided by 2 to account for the averaging gain across the two sets of receivers that must see any satellite used by Phase I WAAS.

The minimum detectable error for satellites at 45 degrees, MDE_{high}, is equal to the maximum of MDE_{field} and MDE_{sim}. In this case, we do not multiply by two, because WAAS measurements of high satellites have approximately the same noise as the measurements used during ICAO validation. The ICAO measurements only used a time constant of 100 seconds, whereas the WAAS measurements are smoothed for the entire time that the satellite is in view. Thus, the analysis leveraged the advantage provided by dual frequency carrier smoothing. Finally, the MDE for high elevation satellites is divided by $\sqrt{20}$ to account for the averaging gain from the 20 receivers that certainly view a GPS satellite at 45 degrees elevation.

All the waveforms in the full ICAO threat model are subject to the test given in Equation (C.4). Those points that result in β>MDE are discarded. Those that result in β<MDE are collected in two sets of undetected points denoted as follows

$$\begin{aligned}
\beta \le \mathrm{MDE}_{\mathrm{high}} \Leftrightarrow \alpha_{\mathrm{high}} &= \left\{ \{\Delta_n\}\Big|_{n=1}^{N_{\mathrm{A,U,high}}}, \{(\sigma, f_d)_n\}\Big|_{n=1}^{N_{\mathrm{B,U,high}}}, \{(\sigma, f_d, \Delta)_n\}\Big|_{n=1}^{N_{\mathrm{C,U,high}}} \right\}_{\mathrm{HIGH}} \\
\beta \le \mathrm{MDE}_{\mathrm{rise}} \Leftrightarrow \alpha_{\mathrm{rise}} &= \left\{ \{\Delta_n\}\Big|_{n=1}^{N_{\mathrm{A,U,rise}}}, \{(\sigma, f_d)_n\}\Big|_{n=1}^{N_{\mathrm{B,U,rise}}}, \{(\sigma, f_d, \Delta)_n\}\Big|_{n=1}^{N_{\mathrm{C,U,rise}}} \right\}_{\mathrm{RISE}}
\end{aligned} \tag{C.5}$$

Needless to say, the second set is larger than the first since it is more difficult to detect anomalous signals on rising satellites. The impact of these two sets of undetected points on the aircraft receiver performance is discussed in Section C.5.

C.5 Aircraft Pseudorange Errors Due to Undetected Threats Within the Full ICAO Threat Model

We now subject the aircraft receiver to the set of undetected points given in Equation (C.5). Like the analysis in Section C.3, these studies have also resulted in many PRE contour plots of $\max_{\sigma, f_d, \Delta} \Delta\tau\left(d_{\text{air}}, BW_{\text{air}}\right)$ where the maximum error over the threat waveform parameters $\left(\sigma, f_d, \Delta\right)$ is plotted versus the correlator spacing and bandwidth used by the avionics.

Rather than replicate all of these plots in this appendix, we summarize the results in Table C-4 for rising satellites.

	Early Minus Late Discriminator			Double Delta Discriminator		
	d_{ref}=0.1	d_{ref}=0.2	d_{ref}=0.3	d_{ref}=0.1	d_{ref}=0.2	d_{ref}=0.3
Threat Model A	2.2	2.5	3.0	8.0	8.0	8.8
Threat Model B	5.0	4.2	5.5	7.0	8.0	9.0
Threat Model C	3.8	3.9	4.1	8.0	8.2	8.3

Table C-4 Summary of Pseudorange Errors (in meters) for Rising Satellites. The data assumes that Level D SQM is used and the waveforms are drawn from α_{rise}.

Phase I SQM is effective in detecting signal anomalies for rising satellites. Even though the largest pseudorange error is larger than for that from the most likely threat model, the other Phase I error sources are much larger. The histogram for Equation (C.1) is plotted in Figure D-19 for the same 14 hour set of data that was used in Figure C-15. However, the data set is limited to those satellites that have been in view for 20 minutes or less. This data set reveals that the quantity (C.1) never drops below 27.1 meters, which certainly compares favorably to the 9.0 meters shown in Table C-4.

Phase I SQM is also effective in detecting signal anomalies for high elevation satellites. In this case, it must protect the avionics from any threat that would cause a user pseudorange error greater than 4.8 meters. The limited search here could not find an undetected waveform that caused an error larger than 2 meters. Even though this search did not cover all the possibilities in Table C-4, it did search the most troublesome cases. Specifically, it analyzed the effect of the full ICAO Threat Models A, B and C on double delta discriminators when the reference receiver was modeled as an early minus late discriminator with a correlator spacing of 0.3 chips.

C.6 WAAS SQM Summary

This section summarizes the signal quality monitoring (SQM) strategy for Phase I of the Wide Area Augmentation System (WAAS). In general, SQM detects anomalies in the signals from the GPS (or GNSS) satellites. These anomalies do not cause the satellite signal to be conspicuously in error, nor do they cause the signal to disappear altogether. Rather, these anomalies are subtle and simply cause the correlation peak formed by the receiver to be distorted.

Such distortion can result in position errors even when differential processing is used to improve accuracy. Differential processing is used in the WAAS, where GPS measurements at fixed reference receivers are used to improve the performance of airborne receivers. If the reference receivers and the airborne receivers are identical, then the errors due to the distorted correlation peak will more nearly cancel. However, if the receivers are dissimilar, then the errors will not necessarily cancel. Specifically, errors will probably result if the airborne receiver uses a different correlator spacing or pre-correlator filter than the reference receiver. In this case, the errors are not completely removed by normal differential processing. Even if the airborne receiver and the reference receivers are identical, the errors due to the distorted signal will not always cancel, because of the different multipath environments.

As mentioned previously, this type of signal anomaly occurred in 1993 on Space Vehicle 19 (SV19), and resulted in vertical positioning errors of 2 to 8 meters for differential GPS

users that used SV19. The problem was alleviated when the GPS operators switched to redundant components on the satellite.

Navigation integrity requires that WAAS provide an accurate estimate of its own performance in real-time. This assessment is called a protection level (PL), and is continuously compared to the alarm limit (AL) required for the operation. If the PL is smaller than the AL, then the operation may proceed. If not, then the operation cannot be initiated or must be aborted. The PL must overbound the true position error with high probability. If the true error is greater than the protection level, then the pilot may attempt an operation that is overly ambitious and unsafe. On the other hand, the PL cannot be too conservative. If so, the intrinsic capability of the system is not being fully utilized and operations may be needlessly aborted or avoided. Phase I WAAS is designed to enable LNAV/VNAV, which has a vertical alarm limit (VAL) of 50 meters. It will also support other modes of flight, but these have less stringent AL requirements.

This appendix developed a threat model from the sparse data that describes the degraded signal from SV19. The threat model defines a set of signal distortions and contains two pieces. As previously discussed, these are: The *most likely threat*, which contains the SV19 failure and its immediate neighborhood, and the *full ICAO model*, which contains a much larger neighborhood around the SV19 failure. The full ICAO model is equal to the threat model that is described in the Standards and Recommended Procedures (SARPS) to be published by the International Civil Aviation Organization (ICAO).

Three main findings result from the development of these two EWF threat models. First, no signal quality monitor (SQM) is required to protect Phase I WAAS users against the most likely threats, because the resulting errors are dominated by other errors in the system. Specifically, the pseudorange errors that result from the most likely threats are all smaller than 4 meters, and the remainder of the Phase I errors are always greater than 4.8 meters.

Second, GLS—a landing type with more stringent requirements than LNAV/VNAV, however less stringent than Category I—will require the Phase I SQM algorithm to be replaced by an algorithm similar to the ones that have been designed for the Local Area

Augmentation System (LAAS). This change is dictated by the reduction in the required VAL from 50 to 20 meters. It will also require changes in the reference receiver hardware.

Third, the existing Phase I SQM algorithm is adequate to protect users against all threats in the full ICAO model. When the satellite is rising, Phase I SQM limits the pseudo-range errors suffered by the avionics to 9 meters. For rising satellites, the remainder of the Phase I error budget always exceeds 27 meters. When the satellite is at high elevation angles, the resulting errors are smaller than the 4.8 meters due to the other Phase I error sources.

The existing Phase I algorithm makes use of some Level D software, but should be retained to provide protection against faults that are very different than any that have been observed. To achieve best performance, the correlator spacing for the *wide* correlator receiver in the WAAS reference receivers should be reduced from a spacing of 1.0 to 0.15.

Phase I SQM may not achieve the above stated performance due too the fact that this our analysis is based on noise statistics from our prototype SQM that drew both wide and narrow correlator spacings from one receiver. The Phase I receiver hardware cannot enable such sampling and the two samples will need to come from two different receivers. Fortunately, both receivers are connected to one antenna. As a result, the thermal noise contribution to the measurement noise will increase, but the multipath contribution will not. We feel that this is an acceptable risk for three reasons:

- Multipath is a much larger error source than noise.
- Our analysis includes margin to account for the larger thermal noise contribution.
- Phase I SQM is not required to protect against the most likely threats. These threats required no SQM whatsoever.
- Phase I SQM will only operate until planned product improvements are incorporated.

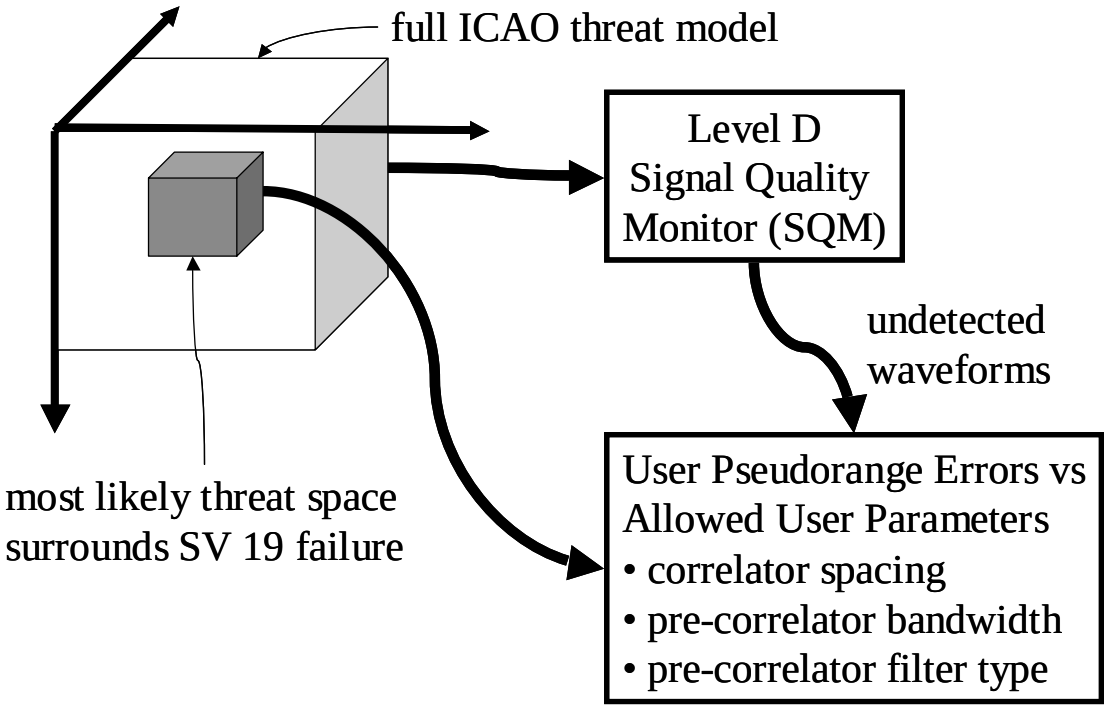

Figure C-1 Summary of SV-19 Threat Analysis

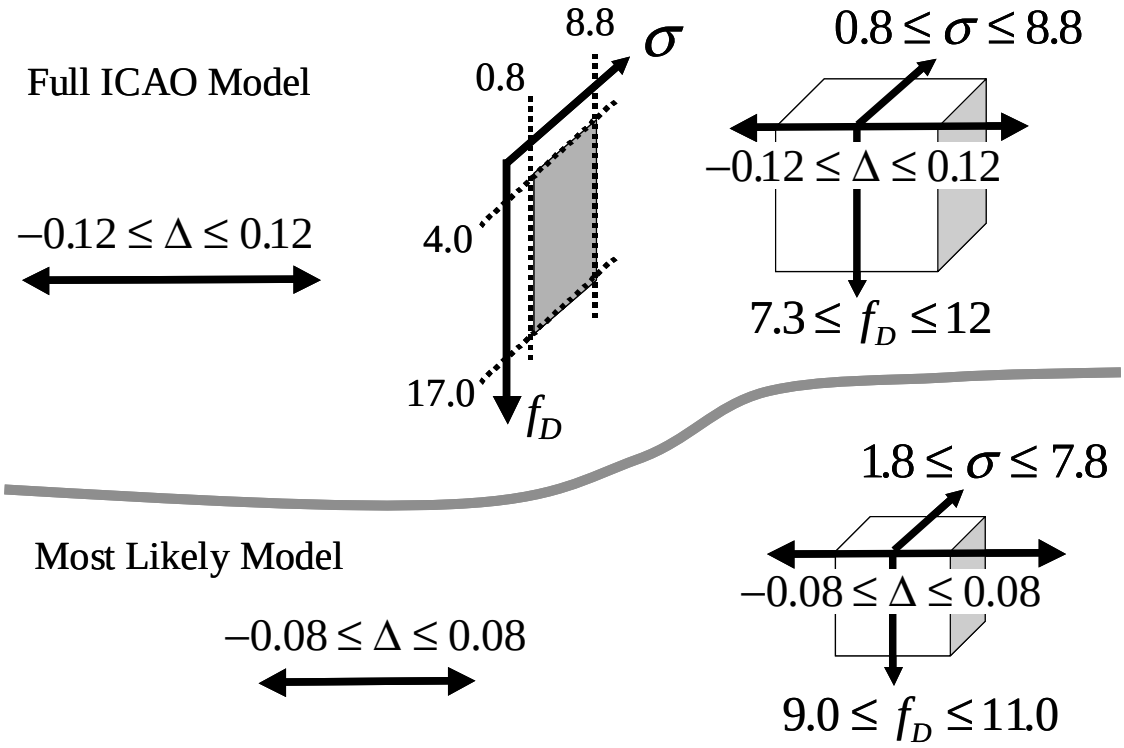

Figure C-2 Full ICAO and Most Likely Threat Models

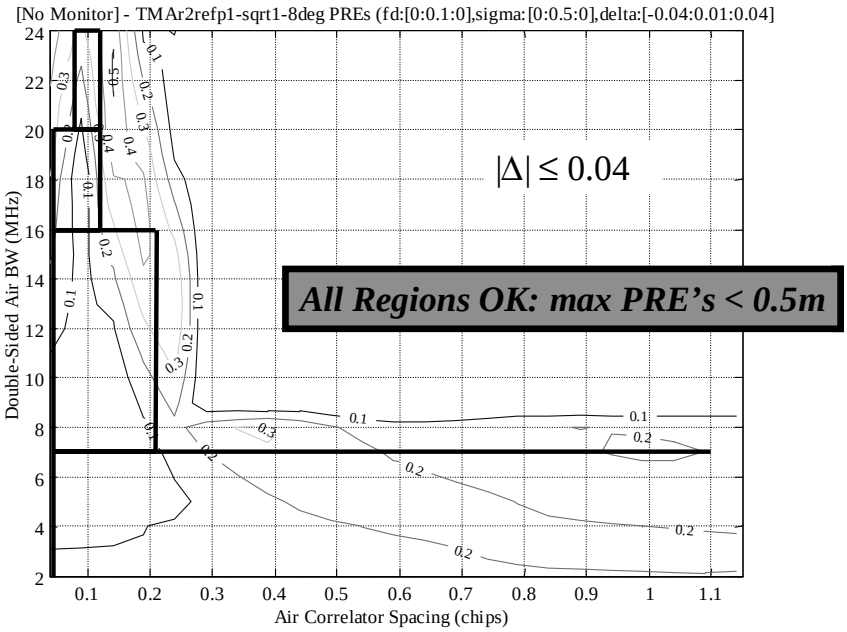

Figure C-3 Maximum Pseudorange Error for the Avionics With an Early Minus Late Discriminator Against Most Likely Threat Model A. No SQM is used and the reference receiver has a correlator spacing of 0.1 chips and a bandwidth of 8 MHz.

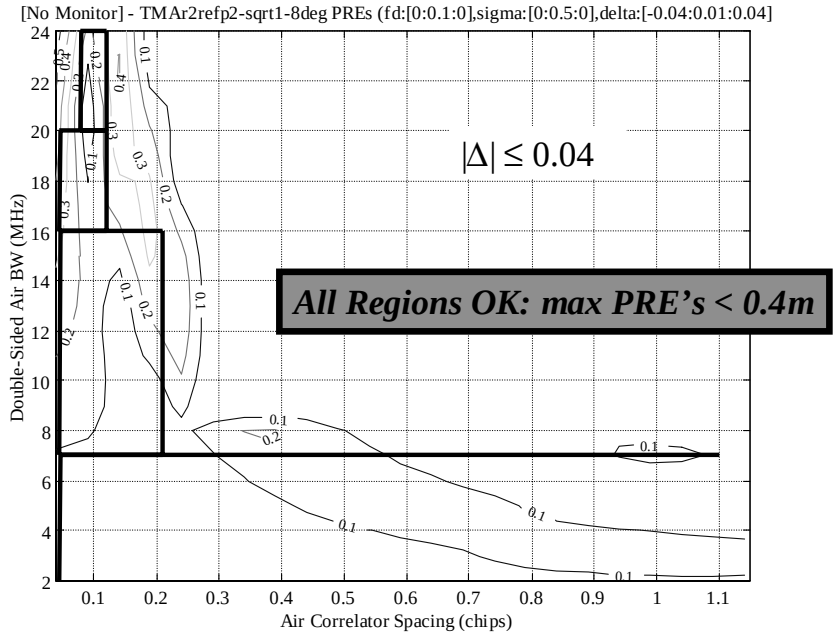

Figure C-4 Maximum Pseudorange Error for the Avionics With an Early Minus Late Discriminator Against Most Likely Threat Model A. No SQM is used and the reference receiver has a correlator spacing of 0.2 chips and a bandwidth of 8 MHz.

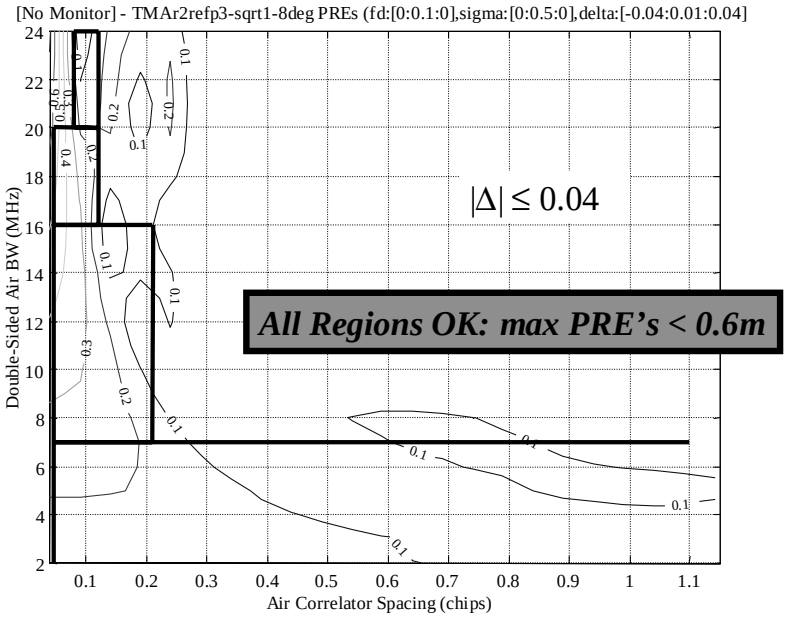

Figure C-5 Maximum Pseudorange Error for the Avionics With an Early Minus Late Discriminator Against Most Likely Threat Model A. No SQM is used and the reference receiver has a correlator spacing of 0.3 chips and a bandwidth of 8 MHz.

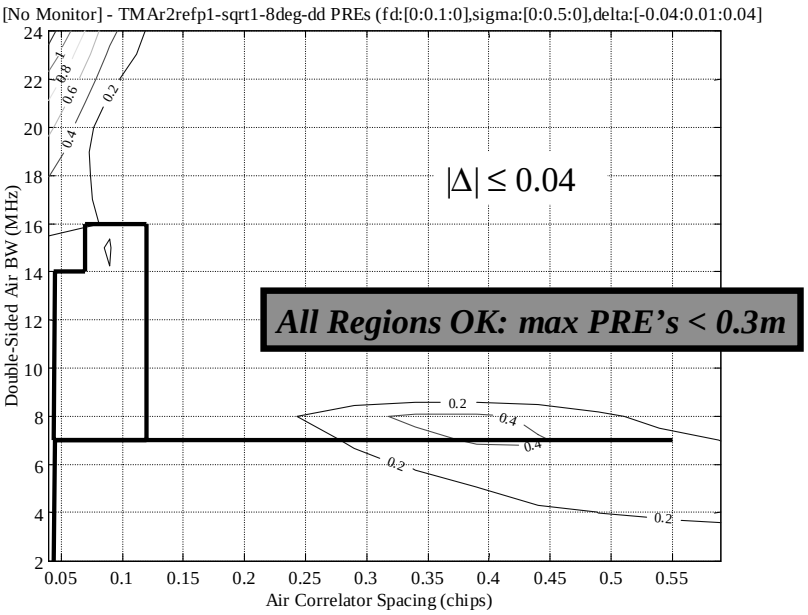

Figure C-6 Maximum Pseudorange Error for the Avionics With a Double Delta Discriminator Against Most Likely Threat Model A. No SQM is used and the reference receiver has a correlator spacing of 0.1 chips and a bandwidth of 8 MHz.

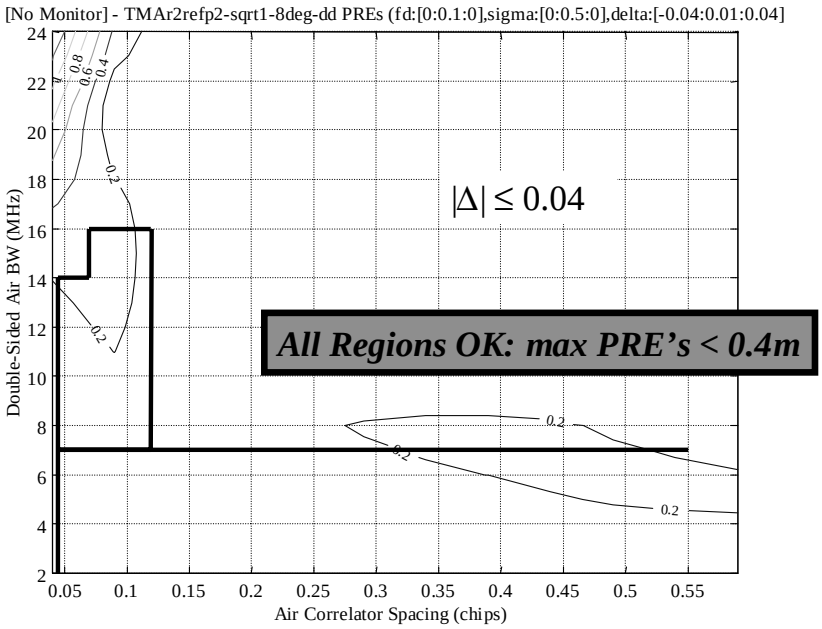

Figure C-7 Maximum Pseudorange Error for the Avionics With a Double Delta Discriminator Against Most Likely Threat Model A. No SQM is used and the reference receiver has a correlator spacing of 0.2 chips and a bandwidth of 8 MHz.

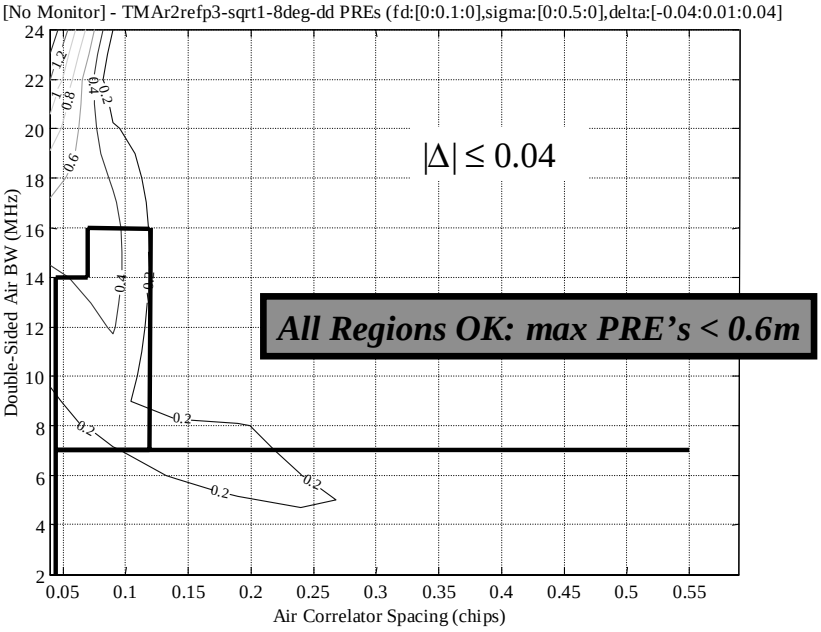

Figure C-8 Maximum Pseudorange Error for the Avionics With a Double Delta Discriminator Against Most Likely Threat Model A. No SQM is used and the reference receiver has a correlator spacing of 0.3 chips and a bandwidth of 8 MHz.

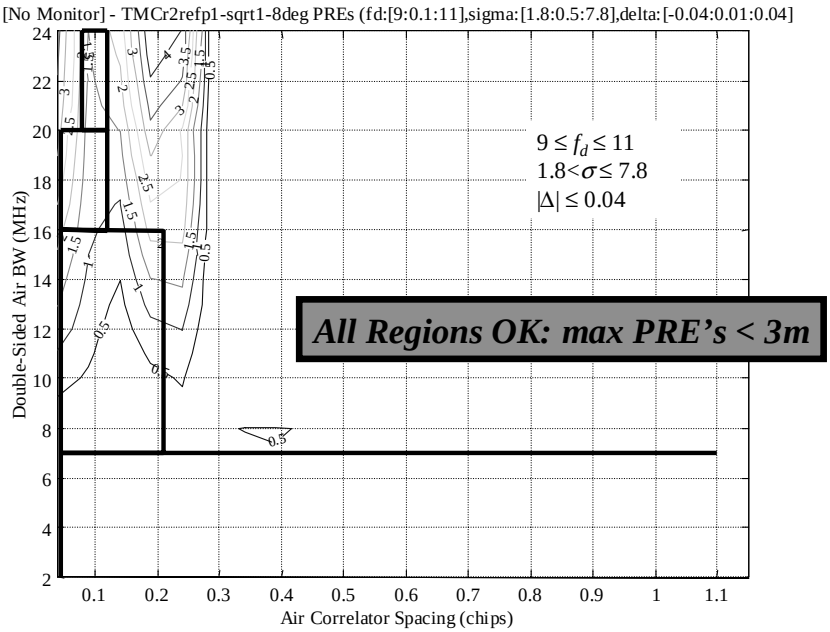

Figure C-9 Maximum Pseudorange Error for the Avionics With an Early Minus Late Discriminator Against Most Likely Threat Model C. No SQM is used and the reference receiver has a correlator spacing of 0.1 chips and a bandwidth of 8 MHz.

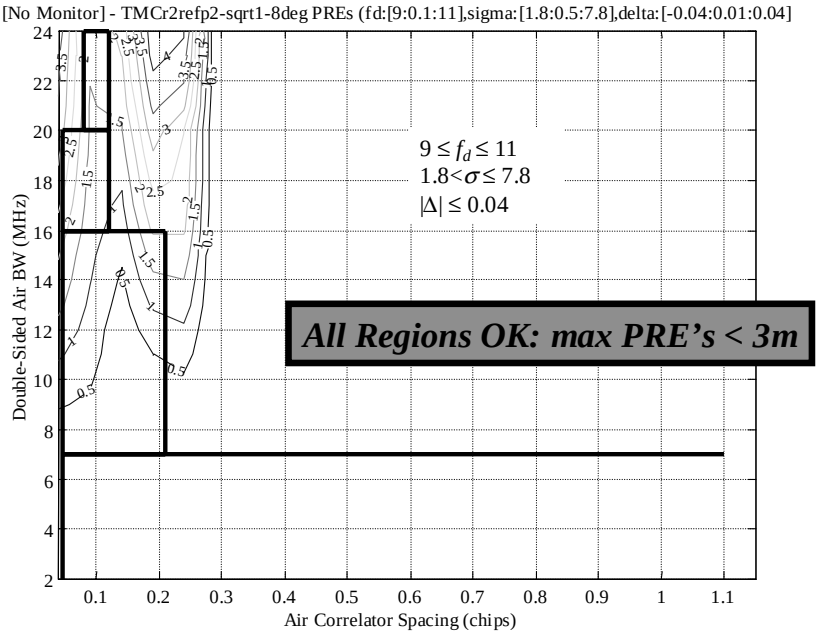

Figure C-10 Maximum Pseudorange Error for the Avionics With an Early Minus Late Discriminator Against Most Likely Threat Model C. No SQM is used and the reference receiver has a correlator spacing of 0.2 chips and a bandwidth of 8 MHz.

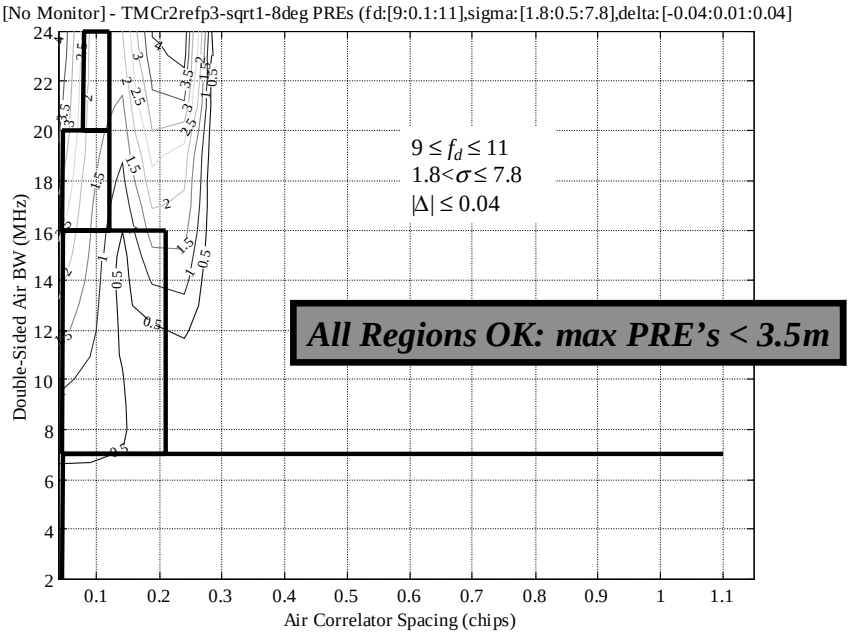

Figure C-11 Maximum Pseudorange Error for the Avionics With an Early Minus Late Discriminator Against Most Likely Threat Model C. No SQM is used and the reference receiver has a correlator spacing of 0.3 chips and a bandwidth of 8 MHz.

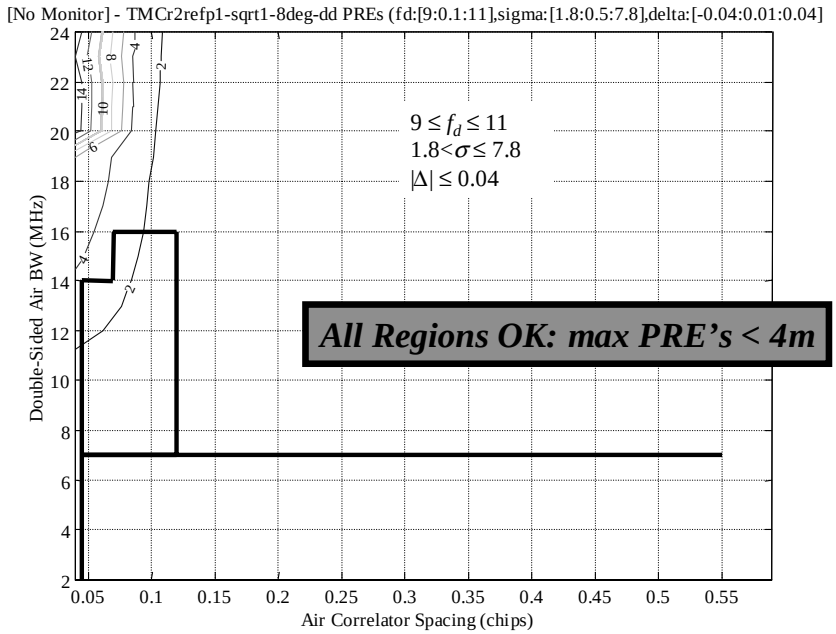

Figure C-12 Maximum Pseudorange Error for the Avionics With a Double Delta Discriminator Against Most Likely Threat Model C. No SQM is used and the reference receiver has a correlator spacing of 0.1 chips and a bandwidth of 8 MHz.

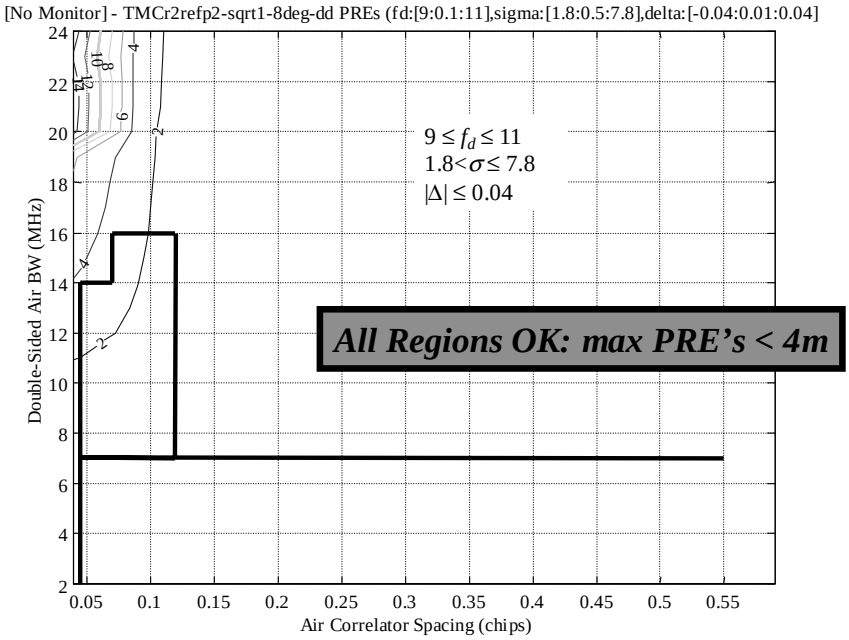

Figure C-13 Maximum Pseudorange Error for the Avionics With an Double Delta Discriminator Against Most Likely Threat Model C. No SQM is used and the reference receiver has a correlator spacing of 0.2 chips and a bandwidth of 8 MHz.

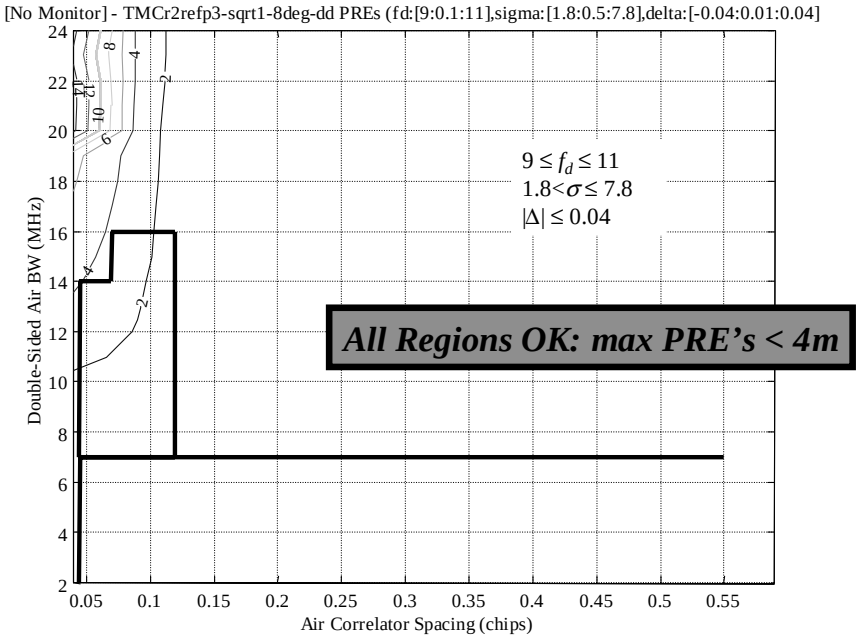

Figure C-14 Maximum Pseudorange Error for the Avionics With an Double Delta Discriminator Against Most Likely Threat Model C. No SQM is used and the reference receiver has a correlator spacing of 0.3 chips and a bandwidth of 8 MHz.

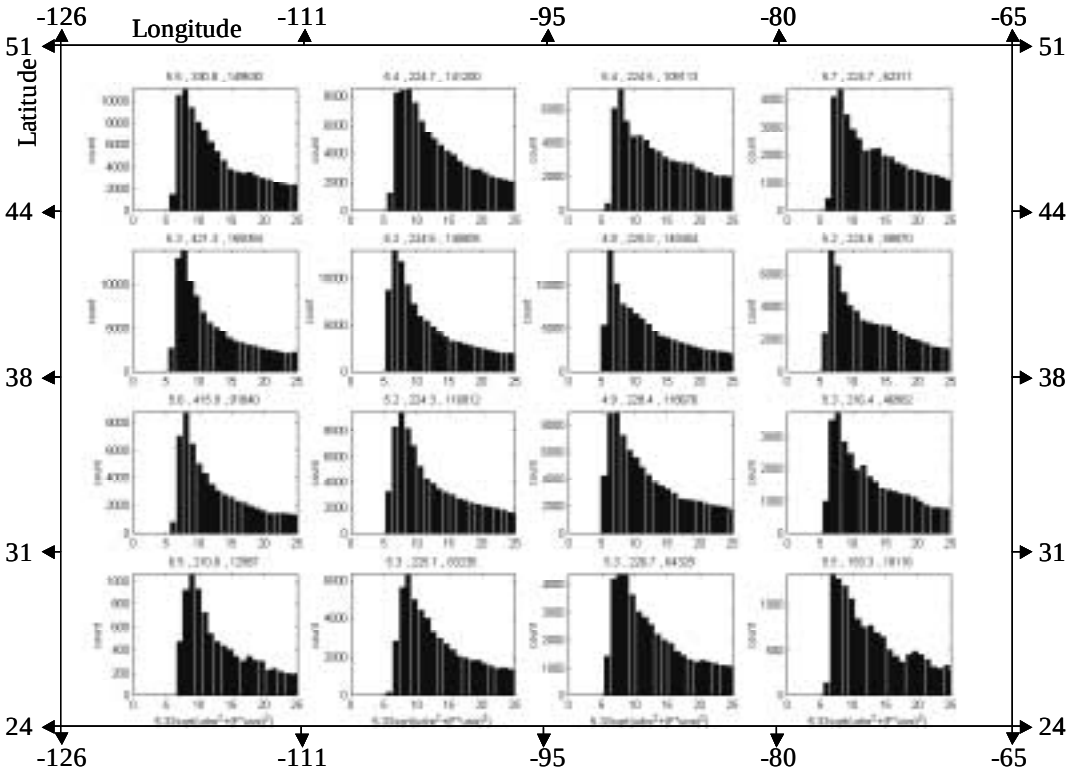

Figure C-15 Histograms of $5.33\sqrt{\sigma_{\text{UDRE}}^2+\left(F\sigma_{\text{UIVE}}\right)^2}$ for users with VPLs < 50m. Over 14 hours of data on June 7, 2000, the minimum value of this metric was 4.8.

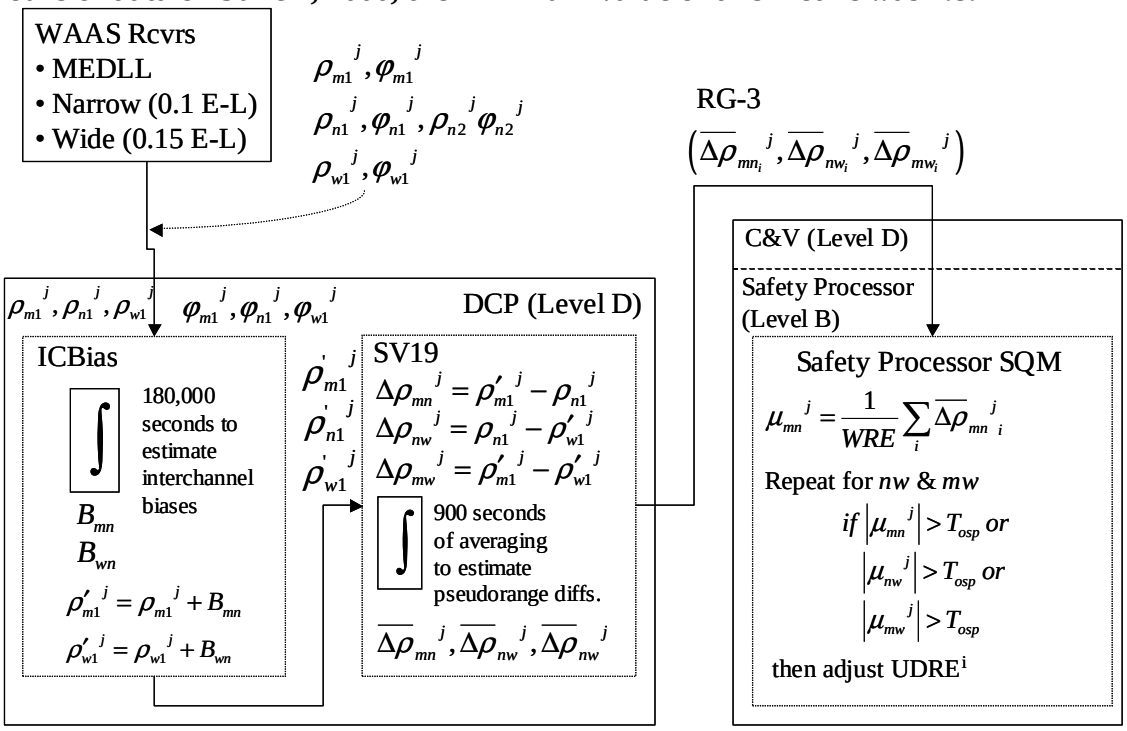

Figure C-16 Level D Signal Quality Monitoring

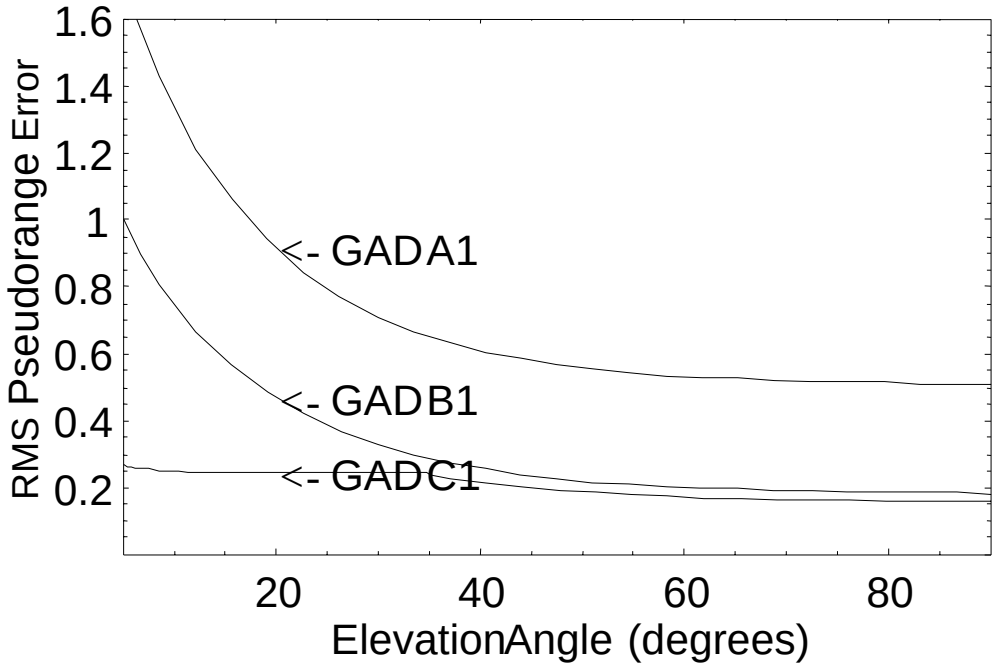

Figure C-17 Ground Accuracy Designators (GADs) from the Minimum Aviation Performance System (MASPS) for the Local Area Augmentation System (LAAS)

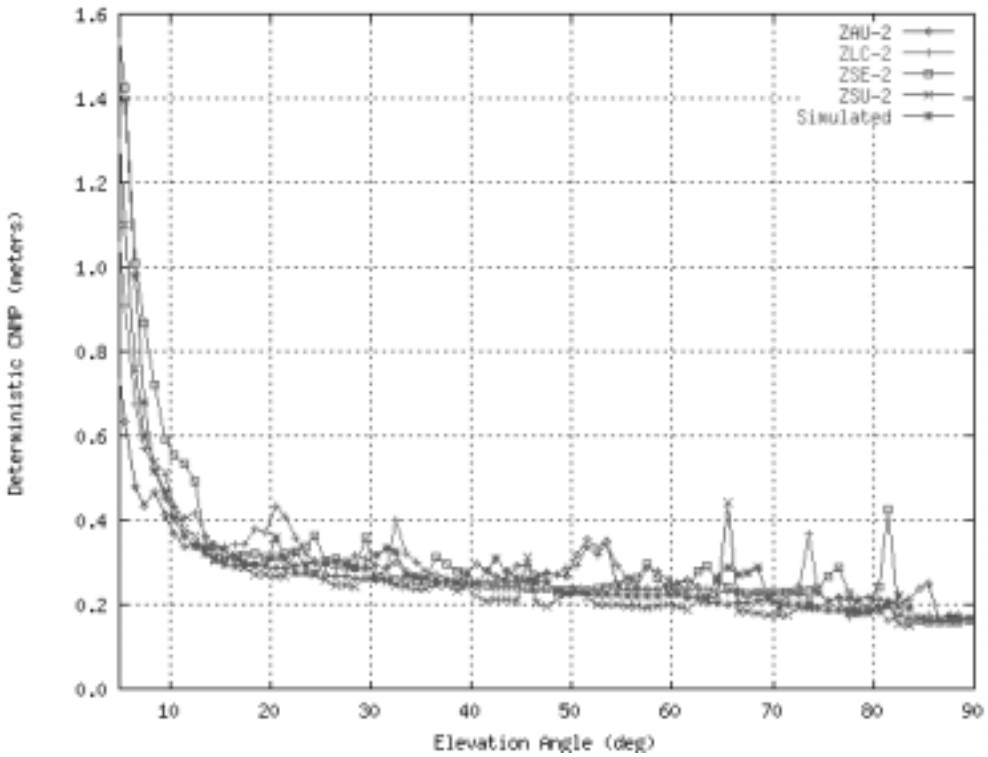

Figure C-18 Deterministic Code Noise and Multipath (CNMP) From the Prototype WAAS

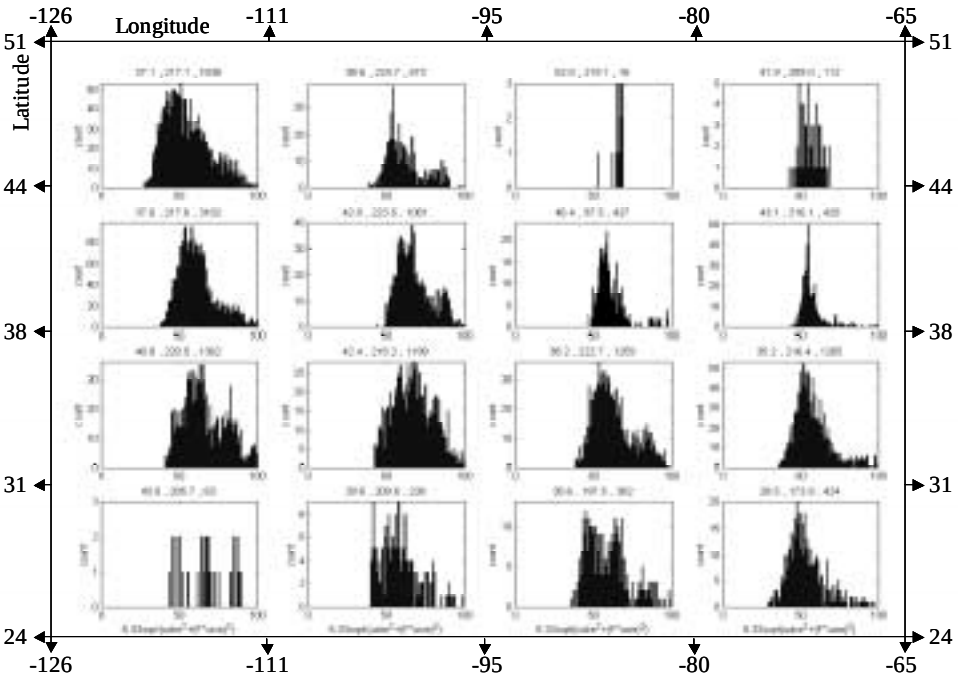

Figure C-19 Histograms of $5.33\sqrt{\sigma_{\text{UDRE}}^2 + \left(F\sigma_{\text{UIVE}}\right)^2}$ for Satellites in View Less Than 1200 Seconds. Over 14 hours on June 7, 2000, the min value of this metric was 27.1.

Appendix D:

GPS Autocorrelations and Near-Peak Sidelobes

Figure D-1 plots the normalized autocorrelation peaks corresponding to each of the 32 current GPS C/A code PRNs. (Note that not all are currently assigned to satellites). Each peak is shown centered at a code offset of zero chips and the functions are plotted to $\pm 4T_c$ on either side of the peak. The following observations may be made about these functions:

- 8 of 32 (e.g., PRN4, PRN6, PRN10, etc.) have peak-adjacent sidelobes (PASLs).
- 7 of 32 (e.g., PRN7, PRN8, PRN15, etc.) have peak-flush sidelobes (PFSLs).
- 4 (PRN3, PRN20, PRN25, PRN27) have only a $1T_c$-wide plateau adjacent to the main peak.
- 5 (e.g., PRN2, PRN9, PRN11, etc.) have only a $2T_c$-wide plateau adjacent to the main peak. (As discussed in Section 5.3.1 of Chapter 5, this is the minimum for traditional MPI assumptions to hold.)
- 8 (e.g., PRN1, PRN5, PRN12, etc.) have peak-adjacent plateau widths $3T_c$ wide or more.
- All 32 have at least two (by symmetry) trapezoidal sidelobes (not shown in Figure D-1).

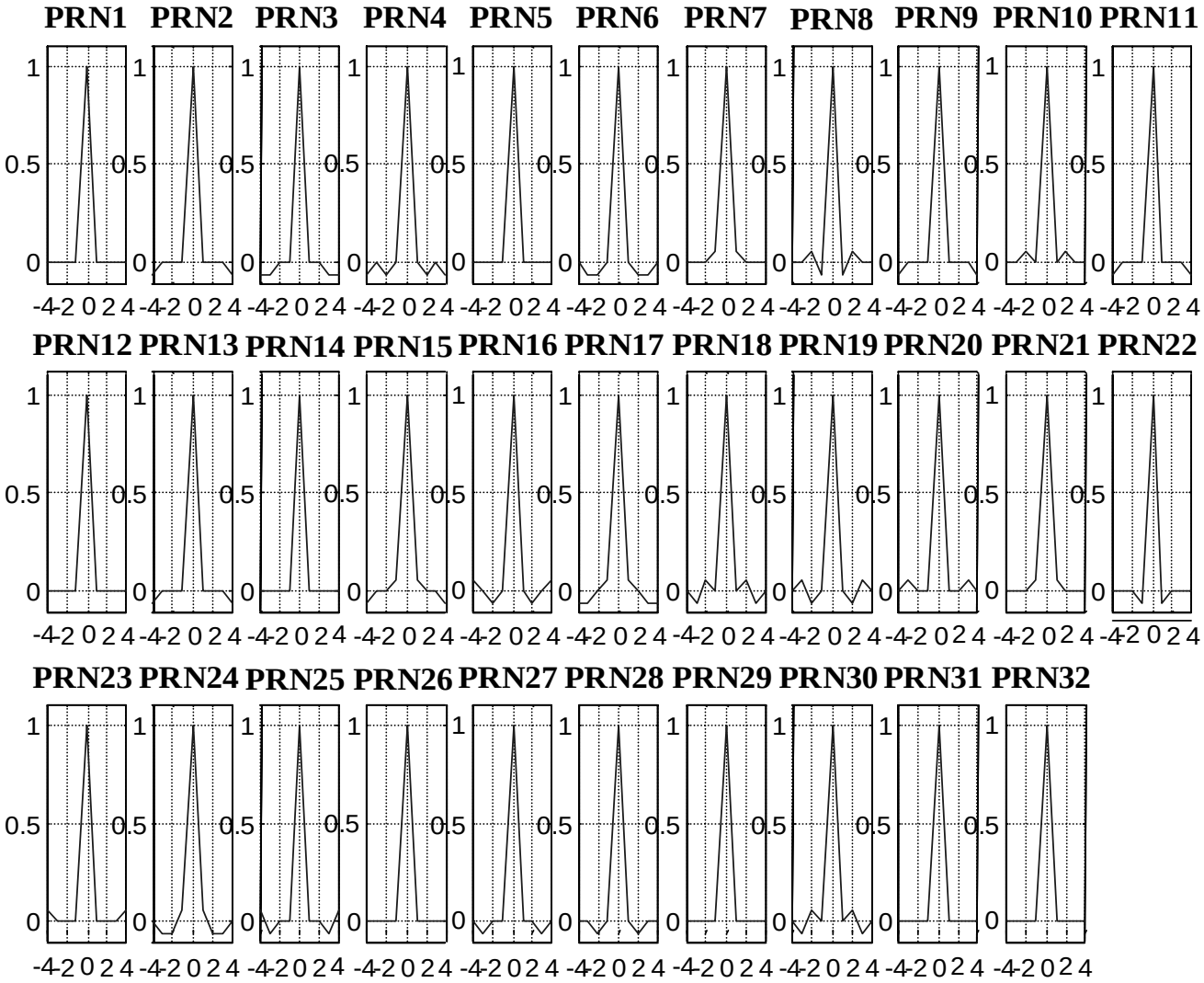

Figure D-1 Normalized Autocorrelation Peaks and Near-Peak Sidelobes for Current GPS PRNs

Bibliography

[Akos97] Akos, D. M., *A Software Radio Approach to Global Navigation Satellite System Design*, Ph.D. Thesis, Ohio University, Athens, Ohio, 45701 May 1997.

[Akos00a] Akos, D. M., Phelts, R. E., Pullen, S., Enge, P., "Signal Quality Monitoring: Test Results," *Proceedings of the 2000 National Technical Meeting*, Institute of Navigation, San Diego, CA, January 2000, pp. 536-41.

[Akos00b] Akos, D. M., Phelts, R. E., Mitelman, A., Pullen S. Enge, P., "GPS-SPS Signal Quality Monitoring (SQM)," *Position Location and Navigation Symposium*, Conference Proceedings Addendum, IEEE PLANS, 2000.

[Akos00c] Akos, D. M., Phelts, R. E., Enge, P., "MDEs for SQM," Presentation to ICAO, Seattle, WA, May 2000.

[Anon] Anon, "Autocorrelation Sidelobe Considerations in the Characterization of Multipath," *IEEE TRANSACTIONS ON AEROSPACE AND ELECTRONIC SYSTEMS*, 1997 v 33, n 1, pp. 290-95.

[Apparicio] Apparicio, M., Brodie, P., Doyle, L., Rajan, J., Torrione, P., "GPS Satellite and Payload," in *Global Positioning System: Theory and*

Applications, B. W. Parkinson and J. J. Spilker (eds.), v 1 pp 209-244, American Institute of Aeronautics and Astronautics, Washington DC, 1996.

[Axelrad] Axelrad, P., Comp, C. J., MacDoran, P., "SNR-Based Multipath Error Correction for GPS Differential Phase," *IEEE Transactions of Aerospace and Electronic Systems*, Vol. 32 No. 2, April 1996.

[Bartone] Bartone, C., van Graas, F., "Ranging Airport Pseudolite for Local Area Augmentation," *IEEE PLANS, Position Location and Navigation Symposium*, 1998, pp. 479-86.

[Betz00a] Betz, J. W., "Effect of Narrowband Interference on Code Tracking Accuracy," *Proceedings of the 2000 National Technical Meeting, 2000: Navigating into the New Millennium*, 2000 v 1, pp. 16-27.

[Betz00b] Betz, J. W., Klodziejski, K. R., "Extended Theory of Early-Late Code-Tracking for a Bandlimited GPS Receiver," Submitted to: *Journal of the Institute of Navigation*, Accepted for Publication and revised May 2000.

[Braasch95] Braasch, M. S., "Multipath Effects," in *Global Positioning System: Theory and Applications*, B. W. Parkinson and J. J. Spilker (eds.), v 1 pp 547-568, American Institute of Aeronautics and Astronautics, Washington DC, 1996.

[Braasch96] Braasch, M. S., "GPS Multipath Model Validation," *Proceedings of Position Location and Navigation Symposium, IEEE PLANS 96*, pp. 672-8, 1996.

[Brenner] Brenner, M., Reuter R., Schipper, B., "GPS Landing System Multipath Evaluation, Techniques and Results," *Proceedings of the 1998 11th International Technical Meeting of the Satellite Division of the Institute*

of Navigation, ION GPS-98, Proceedings of ION GPS v 2 1998, v 1, pp. 999-1008.

[Brevik] Brevik, K., Forssell, B., Kee, C., Enge, P., Walter, T., "Estimation of Multipath Error in GPS Pseudorange Measurements," *Navigation*, Spring 1997, pp 43-52.

[Brodin] Brodin, G., Peter, D., "GNSS Code and Carrier Tracking in the Presence of Multipath," *International Journal of Satellite Communications* v 5 n 1, Jan-Feb. 1997, pp. 25-34.

[Brown] Brown, R. G., "Receiver Autonomous Integrity Monitoring," in *Global Positioning System: Theory and Applications*, B. W. Parkinson and J. J. Spilker (eds.), v 2 pp. 143-165, American Institute of Aeronautics and Astronautics, Washington DC, 1996.

[Bruce] Bruce, A. S., Van Dierendonck, A. J., Jakab, A., Townsend, B., "Detection of GPS Satellite Signal Failures in Satellite Based Augmentation Systems (SBAS)," *Proceedings of the IAIN World Congress*, 2000.

[Cahn] Cahn, C. R., Chansarkar, M. M., *Multipath Corrections for a GPS Receiver*, Proceedings of the 10th International Technical Meeting of the Satellite Division of the Institute of Navigation, ION-GPS-97, Part 1(of 2), Proceedings of ION GPS-97, 1997 v 1, pp. 551-57.

[Carson] Carson, B. A., *Communications Systems An Introduction to Signals and Noise in Electrical Communication*, Irwin McGraw-Hill, Boston, Massachusetts, 1986, pp. 26-55.

[Clark95] Clark, T., "GPS Antennas: De-Mystifying Multipath," Space Geodesy Branch Code 926.9, NASA/GSFC, Greenbelt, MD, March 5, 1995, pp. 1-10.

[Coenen] Coenen, A. J. R. M., de Vos, A. J., "FFT-Based Interpolation for Multipath Detection in GPS/GLONASS Receivers" *Electronics Letters*, v 28 n 19 Sept. 10, 1997, pp. 1787-788.

[Comp96] Comp, C. J., Axelrad, P., "An adaptive SNR-Based Carrier Phase Multipath Mitigation Technique," *Proceedings of the 1996 9th International Technical Meeting of the Satellite Division of the Institute of Navigation, ION GPS-96*. Proceedings of ION GPS v1 1996, pp. 683-697.

[Corrigan] Corrigan, T. M., Hartranft, J. F., Levy, L. J., Parker, K. E.., Pritchett, J. E., Pue, A. J., Pullen., S., Thompson, T., *GPS Risk Assessment Study*. The John's Hopkins University, Applied Physics Laboratory, VS-99-007, January 1999.

[Doris] Doris, D., Benhallam, A., "On Correlation Processes Reducing Multipath in the L1 GPS Receiver," *Proceedings of the 1996 9th International Technical Meeting of the Satellite Division of the Institute of Navigation, ION GPS-96*, Proceedings of ION GPS v 1 1996, pp. 699-708.

[Fuller] Fuller, R. A., *Geostationary Satellite Ranging and Datalink*, Ph.D. Thesis, Stanford University, Stanford, California 94305, June 2000.

[Edgar] Edgar, C., Czopek, F., Barker, B., "A Co-operative Anomaly Resolution on PRN-19," *Proceedings of the 2000 13th International Technical Meeting of the Satellite Division of the Institute of Navigation, ION GPS-2000*. Proceedings of ION GPS 2000, v 2, pp. 2269-271.

[El-Rabbany] El-Rabbany, A., "Temporal Characteristics of Multipath Errors," *Proceedings of the 1995 8th International Technical Meeting of the Satellite Division of the Institute of Navigation, ION GPS-95*. Proceedings of ION GPS, 1995 v.2, pp. 1493-497.

[El-Sayed] El-Sayed, G., Pachter, M., DeVilbiss, S. L., "Design of GPS Receiver Code and Carrier Tracking Loops for Multipath Mitigation," *Proceedings of the 1998 11th International Technical Meeting of the Satellite Division of the Institute of Navigation, ION GPS-98*. Proceedings of ION GPS 1998, v 2, pp. 1041-1053.

[Enge95] Enge, P. K., Van Dierendonck, A. J., "Wide Area Augmentation System," in *Global Positioning System: Theory and Applications*, B. W. Parkinson and J. J. Spilker (eds.), v 2 pp. 117-142, American Institute of Aeronautics and Astronautics, Washington DC, 1996.

[Enge97] Enge, P. K. Farmer, D., Schipper, J. F., "Adaptive Multipath Equalization," United States Patent, Patent Number: 5,630,208, May 13, 1997.

[Enge99] Enge, P. K., Phelts, R. E., Mitelman, A. M., "Detecting Anomalous signals from GPS Satellites," ICAO, GNSS/P, Toulouse, France, 1999.

[Eissfeller] Eissfeller, B., Winkel, J. O., "GPS Dynamic Multipath Analysis in Urban Areas," *Proceedings of the 1996 9th International Technical Meeting of the Satellite Division of the Institute of Navigation, ION GPS-96*. Proceedings of ION GPS, 1996, v.1, pp 719-27.

[Gadallah] Gadallah, E-S. A., Pachter, M., DeVilbiss, S. L., "Design of GPS Receiver Code and Carrier Tracking Loops for Multipath Mitigation," *Proceedings of the 11th International Technical Meeting of the Satellite Division of the Institute of Navigation*, ION-GPS-98, Part 1(of 2), Proceedings of ION GPS-98, 1998 v 1, pp. 1041-54.

[Garin96] Garin, L., van Diggelen, F., Rousseau J-M., "Strobe and Edge Correlator Multipath Mitigation for Code," *Proceedings of the 1996 11th International Technical Meeting of the Satellite Division of the Institute*

of Navigation, ION GPS-98, Proceedings of ION GPS 1996, 1996 v 1, pp. 657-64.

[Garin97] Garin, L., Rousseau, J.-M., "Enhanced Strobe Correlator Multipath Mitigation for Code and Carrier," *Proceedings of the 10th International Technical Meeting of the Satellite Division of the Institute of Navigation, ION-GPS-97*, Part 1(of 2), Proceedings of ION-GPS, 1997 v l. 1, pp. 559-68.

[GEC] GEC Plessey Semiconductors (now Mitel Semiconductors), *Global Positioning Products Handbook*, August 1996.

[Glisic] Glisic, S., Vucetic, B., *Spread Spectrum CDMA Systems for Wireless Communications*, pp. 1-47, Artec House, Boston, MA, 1997.

[Hatch] Hatch, R. R., Keegan, R. G., Stansell, T. A., "Leica's Code and Phase Multipath Mitigation," *Proceedings of the 1997 10th International Technical Meeting of the Satellite Division of the Institute of Navigation, ION GPS-97*, Proceedings of ION GPS, 1997 v.1, pp. 217-225.

[Hegarty] Hegarty, C., Ericson, S., Van Dierendonck, A. J., McGraw, G., Fyfe, P., Kovach, K., "Status of RTCA Activities for the Future GPS Signal at L5," *Proceedings of the 2000 13th International Technical Meeting of the Satellite Division of the Institute of Navigation, ION GPS-2000*. Proceedings of ION GPS, 2000 v.2, pp. 2130-39.

[Jakab] Jakab, A., "An Approach to GPS Satellite Failure Detection," *Proceedings of the 1999 12th International Technical Meeting of the Satellite Division of the Institute of Navigation, ION GPS-99*, Proceedings of ION GPS, 1999 v.1, pp. 751-59.

[Kaplan] Kaplan, E. D., *Understanding GPS Principles and Applications*, Artech, Boston, Massachusetts, 1996.

[Kee] Kee, C., "Wide Area Differential GPS," in *Global Positioning System: Theory and Applications*, B. W. Parkinson and J. J. Spilker (eds.), v 2 pp. 143-165, American Institute of Aeronautics and Astronautics, Washington DC, 1996.

[Klobuchar96] Klobuchar, J. A., "Ionospheric Effects on GPS," in *Global Positioning System: Theory and Applications*, B. W. Parkinson and J. J. Spilker (eds.), v 1 pp. 485-515, American Institute of Aeronautics and Astronautics, Washington DC, 1996.

[Kumar] Kumar, R., Lau. "Deconvolution Approach to Carrier and Code Multipath Error Elimination in High Precision GPS," *Technology and Operations: Partnership for Success in Navigation, Proceedings of the 1996 National Technical Meeting, Institute of Navigation*, 1996, pp. 729-37.

[Laxton] Laxton, Mark C., DeVilbiss, Stewart L., "GPS Multipath Mitigation During Code Tracking," *Proceedings of the American Control Conference*, 1997 v.3, pp.1429-1433.

[LGFSpec] *Specification: Performance Type One Local Area Augmentation System Ground Facility*. U.S. Federal Aviation Administration, Washington, D.C., FAA-E-2937, Sept, 21, 1999.

[Macabiau00a] Macabiau, C., Chatre, E., "Impact of Evil Waveforms on GBAS Performance," *Position Location and Navigation Symposium, IEEE PLANS*, 2000.pp. 22-9.

[Macabiau00b] Macabiau, C., Chatre, E., "Signal Quality Monitoring for Protection of GBAS Users Against Evil Waveforms," *Proceedings of the 2000 13th*

International Technical Meeting of the Satellite Division of the Institute of Navigation, ION GPS-2000, 2000.

[Macabiau00c] Macabiau, C., Chatre, E., Working Papers: 19-24, Global Navigation Satellite System Panel (GNSSP), Working Group B (WG-B), Seattle, WA, May-June 2000.

[Mattos] Mattos, P. G., "Multipath Elimination for the Low-Cost Consumer GPS," *Proceedings of the 1997 10th International Technical Meeting of the Satellite Division of the Institute of Navigation, ION GPS-96, Part 1(of 2), ION GPS*-97, Institute of Navigation, 1997 v 1, pp. 665-71.

[McGraw] McGraw, G. A., Braasch, M. S., "GNSS Multipath Mitigation Using Gated and High Resolution Correlator Concepts," *Proceedings of the 12th-Internatinal Technical Meeting of the Satellite Division of the Institute of Navigation, ,"* ION GPS-99, pp. 333-42, 1999.

[Mitelman98] Mitelman, A., Phelts, R. E., Akos, D. M., "LAAS Monitoring for a Most Evil Satellite Failure," 1998 ION National Technical Meeting, *Proceedings of the 1994 National Technical Meeting*, 1998, pp 129-34.

[Mitelman00] Mitelman, A., Phelts, R. E., Akos, D. M., "A Real-Time Signal Quality Monitor for GPS Augmentation Systems," ION GPS-2000 *Proceedings of the 13th-Internatinal Technical Meeting of the Satellite Division of the Institute of Navigation*, 2000.

[Moelker] Moelker, D., "Multiple Antennas for Advanced Multipath Mitigation and Multipath Direction Finding," *Proceedings of the 1997 10th International Technical Meeting of the Satellite Division of the Institute of Navigation, ION GPS-97*. Proceedings of ION GPS, 1997 v.1, pp. 541-550.

[Montalvo] Montalvo, A., Brown, A., "Comparison of Three Multipath Mitigation Approaches for GPS Receivers," *Proceedings of the 1995 8th International Technical Meeting of the Satellite Division of the Institute of Navigation, ION GPS-95*. Proceedings of ION GPS, 1995 v.2, pp. 1511-520.

[Ndili] Ndili, A., *Robust Autonomous Signal Quality Monitoring*, Ph.D. Thesis, Stanford University, Stanford, California 94305, August 1998.

[Nelson] Nelson, L. M., Akselrad, L. M., Etter, D., "Adaptive Detection of code Delay and Multipath in a Simplified GPS Signal Model," *Proceedings of the 1997 10th International Technical Meeting of the Satellite Division of the Institute of Navigation*, ION GPS-97 v1, pp 569-80.

[Onwubiko] Onwubiko, C. O., *Foundations of Computer-Aided Design*, pp. 196-207, St. Paul, MN, USA, West Publishing Company, 1989.

[Oppenheim] Oppenheim, A. V., Schafer, R. W., *Discrete-time Signal* Processing, Prentice Hall, Englewood Cliffs, New Jersey, 1989, pp. 403-513,713-721.

[Parkinson95] Parkinson, B. W., Enge, P. K., "Differential GPS," in *Global Positioning System: Theory and Applications*, B. W. Parkinson and J. J. Spilker (eds.), v 2 pp. 3-50, American Institute of Aeronautics and Astronautics, Washington DC, 1996.

[Peterson] Peterson, B., Bruckner, D., Heye, S., "Measuring GPS Signals Indoors," *Proceedings of the 1997 10th International Technical Meeting of the Satellite Division of the Institute of Navigation*, ION GPS-97 v1, pp 615-24.

[Phelts] Phelts, R. E., Enge, P. K., "The Case For Narrowband Receivers," *ION National Technical Meeting*, San Diego, CA, January 2000.

[Ray99a] Ray, J. K., "Use of Multiple Antennas to Mitigate Carrier Phase Multipath in Reference Stations," *Proceedings of the 1999 13th International Technical Meeting of the Satellite Division of the Institute of Navigation, ION GPS-99*. Proceedings of ION GPS v1 1999, v 1, pp. 269-79.

[Ray99b] Ray, J. K., Cannon, M. E., "Code Range and Carrier Phase Multipath Mitigation Using SNR, Range and Phase Measurements Mitigation in a Multi-Antenna System," *Proceedings of the 1999 13th International Technical Meeting of the Satellite Division of the Institute of Navigation, ION GPS-99*. Proceedings of ION GPS v1 1999, v 1, pp. 713-24.

[Shively99a] Shively, C., Brenner, M., Kline, P., "Multiple Ground Tests Protecting Against Satellite Correlation Symmetry Faults in LAAS," (Revision 3), RTCA SC-159, 1999.

[Shively99b] Shively, C. A., "Derivation of Acceptable Error Limits For Satellite Signal Faults in LAAS," *Proceedings of the 1999 13th International Technical Meeting of the Satellite Division of the Institute of Navigation, ION GPS-99*. Proceedings of ION GPS v1 1999, v 1, pp. 761-70.

[Shively00] Shively, C. A., Braff., R., "An Overbound Concept for Pseudorange Error from the LAAS Ground Facility," MITRE Product MP 00W0000138, July 2000.

[Sleewaegen] Sleewaegen, J., "Multipath Mitigation, Benefits from Using the Signal-to Noise Ratio," *Proceedings of the 1997 International Technical Meeting of the Satellite Division of the Institute of Navigation,* ION GPS-97, v 1 1997, pp. 531-40.

[Spilker94a] Spilker, J. J., "GPS Signal Structure and Theoretical Performance," in *Global Positioning System: Theory and Applications*, B. W. Parkinson and J. J. Spilker (eds.), v 1 pp. 57-119, American Institute of Aeronautics and Astronautics, Washington DC, 1996.

[Spilker94b] Spilker, J. J., "Fundamentals of Signal Tracking Theory," in *Global Positioning System: Theory and Applications*, B. W. Parkinson and J. J. Spilker (eds.), v 1 pp. 245-327, American Institute of Aeronautics and Astronautics, Washington DC, 1996.

[Spilker95] Spilker, J. J., "Interference Effects and Mitigation Techniques," in *Global Positioning System: Theory and Applications*, B. W. Parkinson and J. J. Spilker (eds.), v 1 pp. 717-771, American Institute of Aeronautics and Astronautics, Washington DC, 1996.

[Stockmaster] Stockmaster, M. H., Tsui, J. B. Y., Akos, D. M., "Passive Ranging Using the GPS," *Proceedings of the 1998 11th International Technical Meeting of the Satellite Division of the Institute of Navigation, ION GPS-98*. Proceedings of ION GPS v1 1998, pp 915-21.

[Townsend94] Townsend, B., Fenton, P., "A Practical Approach to the Reduction of Pseudorange Multipath Errors in a L1 GPS Receiver," *Proceedings of the 7th International Technical Meeting of the Satellite Division of the Institute of Navigation*, Proceedings of ION GPS-94, 1994 v l pp. 143-48.

[Townsend95] Townsend, B., Fenton, P., Van Dierendonck, K., van Nee, R. D. J., "L1 Carrier Phase Multipath Error Reduction Using MEDLL Technology," *Proceedings of the 1995 8th International Technical Meeting of the Satellite Division of the Institute of Navigation, ION GPS-95*. Proceedings of ION GPS v 2 1995, pp. 1539-544.

[Van Dierendonck92] Van Dierendonck, A. J., Fenton, P., Ford, T., "Theory and Performance of Narrow Correlator pacing in a GPS Receiver," *NAVIGATION, Journal of the Institute of Navigation*, 1992 v 39 n 3, pp. 265-83.

[Van Dierendonck95] Van Dierendonck, A. J., "GPS Receivers," in *Global Positioning System: Theory and Applications*, B. W. Parkinson and J. J. Spilker (eds.), v 1 pp. 329-407, American Institute of Aeronautics and Astronautics, Washington DC, 1996.

[Van Dierendonck97] Van Dierendonck, A. J., Braasch, M. S., "Evaluation of GNSS Receiver Correlation Processing Techniques for Multipath and Noise Mitigation," *Navigation and Positioning in the New Age, Proceedings of the 1997 National Technical Meeting, Institute of Navigation*, 1997, pp. 207-15.

[Van Dierendonck99a] Van Dierendonck, A. J., McGraw, G. A., Erlandson, R. J., Coker, R., "Cross-Correlation of C/A Codes on GPS/WAAS Receivers," *Proceedings of the 1999 12th International Technical Meeting of the Satellite Division of the Institute of Navigation, ION GPS-99*. Proceedings of ION GPS, 1999 v.2, pp. 581-590.

[Van Dierendonck99b] Van Dierendonck, "Effects of CW Interference and Testing," Presentation to RTCA, SC159, WG4a, January, 18-21, 1999.

[Van Dierendonck00] Van Dierendonck, A. J., Akos, D., Pullen, S., Phelts, R. E. Enge, P., "Practical Implementation Considerations in the Detection of GPS Satellite Signal Failure," *Proceedings of the 2000 National Technical Meeting*, Institute of Navigation, June 2000.

[van Nee92a] van Nee, R. D. J., "Multipath Effects on GPS Code Phase Measurements," *NAVIGATION, Journal of Navigation*, 1992 v 39 n 2, pp. 177-90.

[van Nee92b] van Nee, R. D. J. "Reducing Multipath Tracking Errors in Spread-Spectrum Ranging Systems," *Electronics Letters*, v 28 n 8, April 9 1992, pp. 729-31.

[van Nee94a] van Nee, R. D. J., Siereveld, J., Fenton, P., Townsend, B. R., "The Multipath Estimating Delay Lock Loop: Approaching Theoretical Accuracy Limits," *IEEE*, 1994, 246-51.

[van Nee94b] van Nee, R. D., J., "The Multipath Estimating Delay Lock Loop," 1994 ION National Technical Meeting, *Proceedings of the 1994 National Technical Meeting*, 1994.

[Weill] Weill, L. R., "Achievable GPS Multipath Mitigation Performance Using Dual Civil Frequencies," 1999 ION National Technical Meeting, *Proceedings of the 1999 National Technical Meeting*, 1999, pp 181-91.

[Weill94] Weill, L., "C/A Code Pseudorange Accuracy – How Good Can It Get?" *Proceedings of the 1994 7th International Technical Meeting of the Satellite Division of the Institute of Navigation, ION GPS-94*. Proceedings of ION GPS, 1994, v.1, pp. 133-41.

[Weill97] Weill, L. R., "GPS Multipath Mitigation by means of Correlator Reference Waveform Design," *Navigation and Positioning in the Information Age, Proceedings of the National Technical Meeting*, Proceedings of the 1997 National Meeting, pp. 197-206.

[Zhadanov] Zhadanov, A., Vietsel, V., Zhodzishsky, M., Ashjee, J., "Multipath Error Reduction in Signal Processing," *Proceedings of the 1999 13th International Technical Meeting of the Satellite Division of the Institute of Navigation, ION GPS-99*. Proceedings of ION GPS 1999, v 1, pp. 1217-223.